Queen Mary University of London

School of Engineering and Materials Science

Final Technical Report

Design of UAV with Morphing Wing for Natural Disaster Management

Students:

180035328	Arisa Supawaree
180400744	Emran Rahmat
170208279	Mark Lapitan
170469696	Mohammad Z Khan
170283449	Rosemary Rifaat
180486988	Saaqib Asif-Jussab
180193721	Shovethan Murugathas

Supervisors:

Prof. Vassili Toropov and Dr Ranjan Vepa

MAT7400 – Research and Design Team Project

Master of Engineering Project Report

MAT7400 – Research and Design Team Project

May 2022

DECLARATION

This report entitled:

Design of UAV with Morphing Wing for Natural Disaster Management- Technical Report

was composed by Arisa Supawaree, Emran Rahmat, Mark Lapitan, Mohammad Z Khan, Rosemary Rifaat, Saaqib Asif Jussab and Shovethan Murgathas and is based on our own work. Where the work of the others has been used, it is fully acknowledged in the text and in captions to table illustrations. This report has not been submitted for any other qualification.

Name: Arisa Supawaree, Emran Rahmat, Mark Lapitan, Mohammad Z Khan, Rosemary Rifaat, Saaqib Asif Jussab and Shovethan Murgathas

Signed:

Date:

Queen Mary
University of London

Specific Learning Differences Cover Note

Student ID: 180193721

Date Diagnosis Report Received: 28/Feb/2019

Guidelines for markers assessing coursework and examinations of students diagnosed with Specific Learning Differences (SpLDs).

As far as the learning outcomes for the module allow, examiners are asked to mark exam/essay scripts sympathetically, ignoring the types of errors that students with SpLDs make and to focus on content and the student's understanding of the subject.

SpLDs may affect student performance in written work in the following ways:

- Spelling, grammar and punctuation may be less accurate than expected
- Organisation of ideas may be confused, affecting the overall structure of written work, despite including appropriate and interesting content
- Proof reading may be weak with some errors undetected, particularly homophones and homonyms which can avoid spell checkers

Under examination conditions, these difficulties are likely to be exacerbated, particularly towards the end of scripts.

When marking, please ensure the following guidance is adhered to:

- Scan the text for content to gain an overview of the work, to avoid making a judgement based on the structure alone or any minor spelling and grammar errors
- Do not comment solely on spelling and grammar issues, SpLD students are usually aware of this already. If you feel this is a major problem which has affected the sense of the writing, then please encourage the student to use their study skills support from DDS to help with this.
- Include positive and constructive comments amongst the feedback so that students can acknowledge their strengths but work with specialist study skills tutors on developing new strategies for areas of difficulty.
- Use clear English providing specific examples of what is right or wrong, to ensure that the student knows what to improve upon for future work

Colleagues in Schools and Institutes are asked to encourage students with specific learning differences to access the support provided by the Disability and Dyslexia Service (http://www.dds.qmul.ac.uk/dyslexia/) if they have any concerns about a students work.

For more information regarding marking guidelines see the Institutional Marking Practices for Dyslexic Students (http://adshe.org.uk/wp-content/uploads/marking_guidelines_for_good_practice.docx) on the DDS webpage.

Disability and Dyslexia Service
http://www.dds.qmul.ac.uk/ (http://www.dds.qmul.ac.uk/)

Disability and Dyslexia Service
Room 3.06, Francis Bancroft Building
Queen Mary University of London
Mile End Road
London
E1 4NS

Acknowledgements

The team would like to take this opportunity to give sincere and heartfelt thanks to the people that helped with the completion of this project. The group would like to thank the project supervisors Prof. Vassili Toropov and Dr Ranjan Vepa, for their constant support and guidance, without which this report could not have been completed.

Abstract

This project will involve the design and development of a UAV designed for natural disaster management. This report is split several categories, topology optimisation of wing and rib, aerodynamics and morphing, propulsion system, and control system and automation.

The topology optimisation section of this report will use Altiar (HyperWork and Optistruct) to optimise the internal structure of the wing as well as wing ribs. The optimisation will use minimise compliance methodology (minimising weight whilst maximising stiffness) to iteratively remove elements that do not contribute to supporting the load path, thus only material vital to the structural integrity remains. The topology optimisation results were then interpreted to design an optimised internal structure of the wing.

The wing analysis in this study is divided into two major sections: aerodynamics and morphing wing. For aerodynamics, different mathematical software was used to investigate the aerodynamic behaviour and airflow around the UAV at cruise conditions. The results obtained were then used to determine the optimum aerofoil and its geometry as well as the structure of the wing. The morphing will analyse and investigate the aerodynamic characteristics of a morphing wingtip as well analysing the structure of the wing. The dynamic response of the morphing wingtip was obtained by assuming two plunging modes and the stress, strain, total deformation, and the resonant frequency of the wing structure, were found.

The propulsion system design was focused on the sizing, designing of propellers, batteries, and motors. Four propellers were used for cruise and four different ones were used for the takeoff and landing. Two different approaches were taken for the blade angle distribution design. The performances of both designs were assessed using JBLADE and compared to literature, and a final optimal design chosen. The vertical takeoff and landing propellers were simulated on ANSYS Fluent to obtain the optimal rotational speed and compared to the theoretical value obtained through the theoretical model blade element momentum theory.

The control system section can be divided into two parts, the control system simulation, and the implementation research for the autopilot and hardware solutions. The control system can be split into two areas, the morphing dynamics and the thrust control system, which were made in Simulink and its results analysed. A PID controller was implemented and tuned for the control systems and was simulated to analyse the effect it has. The implementation of the control system was discussed using different topics. There were several options for every

implementation issue, so solutions were discussed along with their advantages and disadvantages and the final option was presented.

Contents

List of Abbreviations

2D	2 dimensional
3D	3 dimensional
AC	Alternating Current
AI	Artificial Intelligence
AOA	Angle of Attack
API	Application Programming Interface
BEM	Blade Element Momentum
BLDC	Brushless DC
CAD	Computer-Aided-Design
CPP	Controllable-Pitch Propeller
DC	Direct Current
DES	Detached eddy simulation
ESC	Electronic Speed Controller
ESC	Electronic Speed Controller
FE	Finite elements
FoM	Figure of Merit
FPP	Fixed-Pitch Propeller
GPS	Global Positioning System
HTS	High Temperature Superconducting
IGBT	Insulated Gate Bipolar Transistor
INS	Internal Navigation System

iOS	Iphone Operating system
JSON	JavaScript Object Notation
LIB	Lithium-Ion Battery
LiDAR	Light Detection and Ranging
Li-ion	Lithium Ion
LiPo	Lithium Polymer
MDO	Multi-Disciplinary Optimisation
NACA	National Advisory Committee for Aeronautics
NASA	National Aeronautics and Space Administration
OMP	Optimal Microstructures with Penalisation
PMAD	Power Management and Distribution
RAMP	Rational Approximation of Material Properties
RANS	Reynolds-Averaged Navier Stokes
ROS	Robot Operating System
SAR	Synthetic Aperture Radar
SIMP	Solid Isotropic Materials with Penalisation
SNS	Satellite Navigation System
SOTA	State of The Arts
TCP	Transmission Control Protocol
TO	Topology Optimisation
UAV	Unmanned Aerial Vehicle
VTOL	Vertical Take-Off and Landing

List of Symbols

$\boldsymbol{Chord_{Tip}}$	Chord Length at the wing tip
$\boldsymbol{Chord_{Root}}$	Chord Length at the wing root
$\boldsymbol{C_D}$	Coefficient of Drag
$\boldsymbol{C_{di}}$	Coefficient of Induced Drag
$\boldsymbol{Cd_0}$	Parasitic Drag
$\boldsymbol{D_i}$	Induced Drag
$\boldsymbol{C_L}$	Coefficient of Lift
$\boldsymbol{v}$	Velocity
$\boldsymbol{\rho}$	Density
$\boldsymbol{\mu}$	Dynamic Viscosity of the Fluid
$\boldsymbol{L}$	Lift
$\boldsymbol{L'}$	Lift per unit span
$\boldsymbol{D}$	Drag
$\boldsymbol{b/s}$	Wing span
$\boldsymbol{A}$	Area
$\boldsymbol{AR}$	Aspect Ratio
Γ	Circulation Distribution
$\propto_{\mathbf{eff}}$	Effective angle of attack
$\propto_{\mathbf{i}}$	Induced angle of attack
$\propto$	Geometric angle of attack
$\boldsymbol{e}$	Oswald efficiency
$\boldsymbol{\delta}$	Induced factor/Lift efficiency Factor

λ	Taper Ratio
Re	Reynolds Number
J	Advance Ratio
n	Propeller Rotational Speed (rev/s)
d	Propeller Blade Diameter
T_{cruise}	Thrust Required for Cruise
C_T	Thrust coefficient
C_P	Power Coefficient
ω	Propeller/Rotor Disk Angular Speed (rad/s)
$\dot{W}_{shaft}$	Shaft Power
Q	Torque
η_P	Propeller Efficiency
S	Reference Wing Area
f	Equivalent Parasite Area
S_{wet}	Wetted Surface Area
C_f	Skin Friction Coefficient
L_c	Characteristic Length
W_{TO}	Takeoff Weight
P_{cruise}	Power Required for Cruise
P_{inst}	Installed Power
β	Twist Angle
φ	Inflow Angle
C_{Lmax}	Maximum Coefficient of Lift

$\boldsymbol{r/R}$	Radial Position over Propeller Radius
$\boldsymbol{V_{rel}}$	Relative Wind Velocity
$\boldsymbol{V_{w}}$	Forward Wind Velocity
$\boldsymbol{V_{rot}}$	Rotational Velocity
V	Voltage
I	Current
R	Wire internal resistance
$\boldsymbol{P_{req}^{VTOL}}$	Vertical take-off power required
$\boldsymbol{I}$	Moment of inertia
m	Propeller mass
$\boldsymbol{P_{2}}$	Upstream propeller disk pressure
$\boldsymbol{P_{3}}$	Downstream propeller disk pressure
$\boldsymbol{V_{2}}$	Upstream propeller disk velocity
$\boldsymbol{V_{3}}$	Downstream propeller disk velocity
$\boldsymbol{A_{disk}}$	Propeller disk area
a	Induction factor
$\boldsymbol{\ddot{p}}$	Roll acceleration
$\boldsymbol{\ddot{q}}$	Pitch acceleration
$\boldsymbol{\ddot{r}}$	Yaw acceleration
$\boldsymbol{\phi}$	Roll angle
$\boldsymbol{\theta}$	Pitch angle
$\boldsymbol{\Psi}$	Yaw angle
$\boldsymbol{m}$	mass

$\boldsymbol{V_b}$	Linear velocity of the origin of the UAV
$\boldsymbol{\omega}$	Angular velocity of the origin of the UAV
$\boldsymbol{F_{ext}}$	Extra force
$\boldsymbol{F_E}$	Total external forces acting on the UAV
$\boldsymbol{M_{ext}}$	Extra moment
$\boldsymbol{F_E}$	External moment acting on the UAV
$[\overline{\boldsymbol{\omega}}]$	3D skew-symmetric matrix
$\boldsymbol{J}$	Inertia tensor of the aircraft
$\boldsymbol{d_{cm}}$	Position of the CM within the body frame
$[\overline{\boldsymbol{d}}]$	3D skew-symmetric matrix
$\boldsymbol{h/b}$	Non-dimensional plunging degree of freedom at the section
$\boldsymbol{\alpha}$	Non-dimensional pitching degree of freedom at the section
$\boldsymbol{W_{to}}$	Take off weight
$\boldsymbol{W_{pl}}$	Payload weight
$\boldsymbol{W_{structure}}$	Structural weight
$\boldsymbol{V_{stall}}$	Stall speed
$\boldsymbol{W_s}$	Wing loading
$\boldsymbol{T_w}$	Thrust loading
$\boldsymbol{\widetilde{M}_a}$	Dynamic inertia matrix
$\boldsymbol{\widetilde{C}_a}$	Aerodynamic stiffness matrix
$\boldsymbol{\widetilde{K}_a}$	Aerodynamic damping matrix
$\mathbf{M}$	Mass matrix
$\boldsymbol{\ddot{U}}$	Acceleration

$\mathbf{K}$	Stiffness matrix
$\mathbf{U}$	Displacement
$\boldsymbol{\varphi}$	Mode shapes
$\boldsymbol{CM_{X-Fuselage}}$	Centre of mass of the fuselage
$\mathbf{u_t}$	turbulent eddy viscosity
$\boldsymbol{\varepsilon}$	dissipation rate of turbulent kinetic energy
$\boldsymbol{\sigma_\varepsilon}$, $\boldsymbol{\sigma_k}$, $\mathbf{C_{1\varepsilon}}$, $\mathbf{C_{2\varepsilon}}$	empirical coefficients
$\tilde{\mathbf{v}}$	working variable
$\mathbf{S}$	vorticity magnitude

Section A (Group)

Introduction to Research Problem

The world is affected by natural disasters every year, mainly the earthquakes. They can come in a wide range of forms and severity. They are the cause of many deaths and destruction of infrastructure around the world. This mean that disaster management is very important as it is needed to reduce human casualties. These earthquakes have larger effect on countries which are less economically developed and result in a high level of economical damage due to the destruction of infrastructure and livelihoods. The earthquake in Haiti in 2021 had a magnitude of $7.2M_W$ on the richter scale resulting in the deaths of 2,248 people and left 650,000 people needing immediate aid and relief (International Medical Corps, 2021).

With the severity of natural disasters, and the number of earthquakes around the world being high, the development of a way to deal with these occurrences and provide aid to areas which are affected is needed urgently. The areas that are affected by this natural phenomenon tend to be hard to reach after the occurrence due to the destruction of major roots into the cities and destruction of infrastructure. This means that the relief and delivery of aid to the areas is extremely difficult. This difficulty can be overcome using UAV as they will have the ability to reach this area without the need of all the infrastructure and major roots. The use of UAV will also mean that the aid can be delivery quicky due to them being air born and the reduced risk of human error due to there not being a need of a pilot. The automation of these UAV will also benefit as it will further reduce the amount of human error due to a computer or AI overseeing all the tasks.

Aims & Objectives

The main aims and objectives must be defined due to the broad scope of this project; these will be broken down into their respective discipline: Structures Analysis with Topology Optimisation, Aerodynamics and morphing analysis, Propulsion system and Stability and Control system. The main aims for this project are as follows:

- To design a high-lift UAV that meets the required criteria to successfully complete the mission
- To enhance the aerodynamic performance of the UAV by implementing a morphing wing
- To design an all-electric propulsion system for the UAV
- To design and implement an autonomous control system

- To optimise the internal structure of the wing

These aims will be achieved by completing the following objectives:

- To conduct market research on UAVs that are currently commercially available
- To perform static and modal analysis on the structure of the wing using Ansys Fluent
- To model the dynamics of a morphing wingtip using MATLAB and Simulink
- To assess the dynamic behavior of the wing using CFD and XFLR5
- To analyse the propeller performance using JBLADE, XFOIL and Ansys fluent.
- To optimise the internal structure by using Altair HyperWorks, HyperMesh, and Optistruct.
- To understand the requirements to make the UAV autonomous thus, enabling it to operate self sufficiently

Methods Used

In this section, the methods used for each of the sections within the report will be discussed. Altair Hyper works software (OptiStruct and Hypermesh) were used to for the Topology Optimisation. Aerodynamic forces were taken into consideration by using the XFLR code. The analysis was then interpreted to create a valid structural design for the wing rib and internal structure of the wing, which was then designed on SolidWorks. Ansys is an engineering mathematical software which models simulations and numerically solving complex engineering problems. In this report, Ansys Fluent is an industry-leading fluid simulation which optimizes the product performance. Ansys Fluent was used for CFD and static and model analysis and VTOL propeller analysis. Furthermore, when designing the optimised propeller, the aerofoil analysis software *XFOIL* was used to find the stall angle of the NACA 0010 aerofoil which determined the maximum angle of attack and thus the twist distribution along the propeller. The propeller analysis software *JBLADE* was then used to simulate the various propeller designs and analyse performance characteristics such as propeller efficiency, coefficient of thrust, and coefficient of power.

Matlab and Simulink were used for the dynamic response of the morphing wingtip and the control system design. The morphing wingtips were simulated on Simulink to help understand the effect of $\overline{U}$ on the dynamic response of the morphing wingtips. Simulink was the main software used for all the simulations and control system design as well as the PID controller implementation. A companion Matlab script was written to calculate and define all the necessary parameters. All results were taken directly from Simulink and analysed in this report.

Principle Findings and Project Outcomes

The principle findings, outcomes, and conclusions for each respective component of the project are highlighted below.

Structure and Topology

Topology Optimisation on the Wings and Wing Ribs were successfully performed using Altair Hyperwork and Optistruct, with the objective to minimise compliance. From the analysis clear structural components could be identified, such as spar, stringers, and ribs. Spar was present in the upper portion of the wing and were thickest near the wing root where bending moment is largest. Similarly, Ribs appear to be clustered towards the wing root where bending moment is largest, frequency of ribs decreases towards the wing tip. Stringers were also identified from the analysis and were connected closely to the ribs. The wing ribs were also optimised the results showcased I beams in the centre of the wing rib, with truss like structures close to the tip of the wing, where most of the material was distributed. Analysis of the results were then interpreted to create a valid structural design for the optimised wing ribs and internal structure of the wing.

Aerodynamics and Morphing

In the aerodynamic part, the flow and aerodynamic behaviour around the wing was analysed by using CFD and XFLR5 softwares. Firstly, two different simulations regarding the aerofoil characteristics were obtained from XFLR5, where an aerofoil with a thickness of 12% was determined to be the most suitable one as it will provide a greater lift to drag ratio. Subsequently, by using the same software, a simulation based on three aerofoil was performed to compare the results; it was determined that the best aerofoil was NACA4412, as it has a greater generation of lift, and it can withstand harsh angle of attack due to its camber ratio geometry of 4%. Finally, based on the wing analysis, the wing structure that was chosen was a tapered wing, the reason of this choice was based on its aerodynamic stability and its high lift to drag ratio. Furthermore, the tapered wings have a smaller wingtip thus, minimal drag will be experienced. In addition to this, by using the CFD software, the UAV was simulated to validate the conclusion obtained from the XFLR5 data.

In the morphing part, the dynamics of the morphing wingtip was analysed as well as the structure of the 3D wing. It was concluded that firstly, the dynamic response for the morphing wing tip consisted in three lines: black, blue and red, where the red and blue line stabilised and the black line diverged as the simulation time increased. Secondly, the static analysis highlighted that the maximum and minimum stress and strain was located at the root and tip of the wing, respectively. Whereas in the total deformation, the maximum and minimum were experienced on the tip and root of the wing, respectively. Also, it was determined that the converged solution for the total deformation, stress and strain occurred at around 3000 elements with a value of 0.0721m, 3510000 Pa and 0.00077 m/m, respectively. Finally, modal analysis was performed on the wing to determine the resonant frequency at 5 different mode shapes, it was observed that all modes experienced pure bending and that mode 5 experienced the largest deformation with a value of 0.57537m at a frequency of 37.924Hz.

Propulsion System

For the propulsion system, sizing calculations were used to determine the thrust requirements for each propeller and therefore the required diameter, as well as the power requirement for battery selection and motor selection based on torque and power requirement. This sizing showed that lithium polymer batteries and brushless DC motors were the most suitable choices for the design. The propeller design optimisation carried out was based on the cruise phase of flight. Two methods were then carried forward to determine the blade angle distribution. The first involved using distribution commonly found in UAV propeller designs, and the other determined the variation through the use of stall control. Both designs were analysed using the software known as *JBLADE* to determine propeller efficiency and C_T and C_P variation with advance ratio. It was concluded that the propeller design based on stall control was the optimal one and provided a peak efficiency of 0.93 when compared to the peak of 0.82 shown for the initial design. The peak C_T for the optimised design was 0.85 when compared to the initial design's 0.65, showing better thrust production. The number of blades was found to not have a great effect on the propeller performance, and thus a two-bladed design should be taken forward as it adds the least weight to the UAV. The simulations showed great agreement with the sizing calculations, with the value of thrust produced by the propellers agreeing within 5.6%.

Additionally, a folded propeller was designed for the vertical takeoff and landing phase of flight using SolidWorks in order to reduce drag effects. The propeller was then numerically optimised using both William Froude's theory and the blade element momentum theory. The propeller was then simulated in Ansys fluent to analyse and confirm findings. The theoretical calculation provided an optimal rotational speed of $650\,rpm$. However, the computational fluid dynamics simulation displayed an increased rotational speed requirement of $700\,rmp$, which shows a percentage difference of 7.14%.

Control Systems

The control systems were modelled using Matlab and Simulink using the dynamic equations and thrust equations. The systems worked successfully and were proven to work using the PID tuning. It was found that the PID controller's introduction helped to manipulate the response of the system in a successful way so that the control systems could be implemented into the UAV model in the future. The simulations without PID controllers also yielded interesting conclusions about the stability of the current design. Currently, the UAV is not stable in the x-axis acceleration and this could be taken into account in the future when a model could be created. Overall, the results of the Simulink control system were successful, as the response was able to be changed in an effective way so that the UAV could stabilise itself around a reference value. This was due to the implementation and tuning of a PID controller.

Section B

1. Project Overview (Group)

1.1. Workflow Package

This study is composed by three phases: Initial Conceptual Design, Determining System Requirements and Final Design and Optimisation; Figure 1 highlights the flow chart diagram for this project. The design and requirements phases consisted of a group effort in which the weight estimation and sizing was determined and discussed. Subsequently, the analysis and optimisation of the conceptual design was done in respect to each discipline as shown below. Finally, the Final Design and Optimisation Phase was carried out by gathering the analysis, optimisation and principal findings for each discipline to finalise the conclusion; this explains the optimised design and the possible improvements of the project.

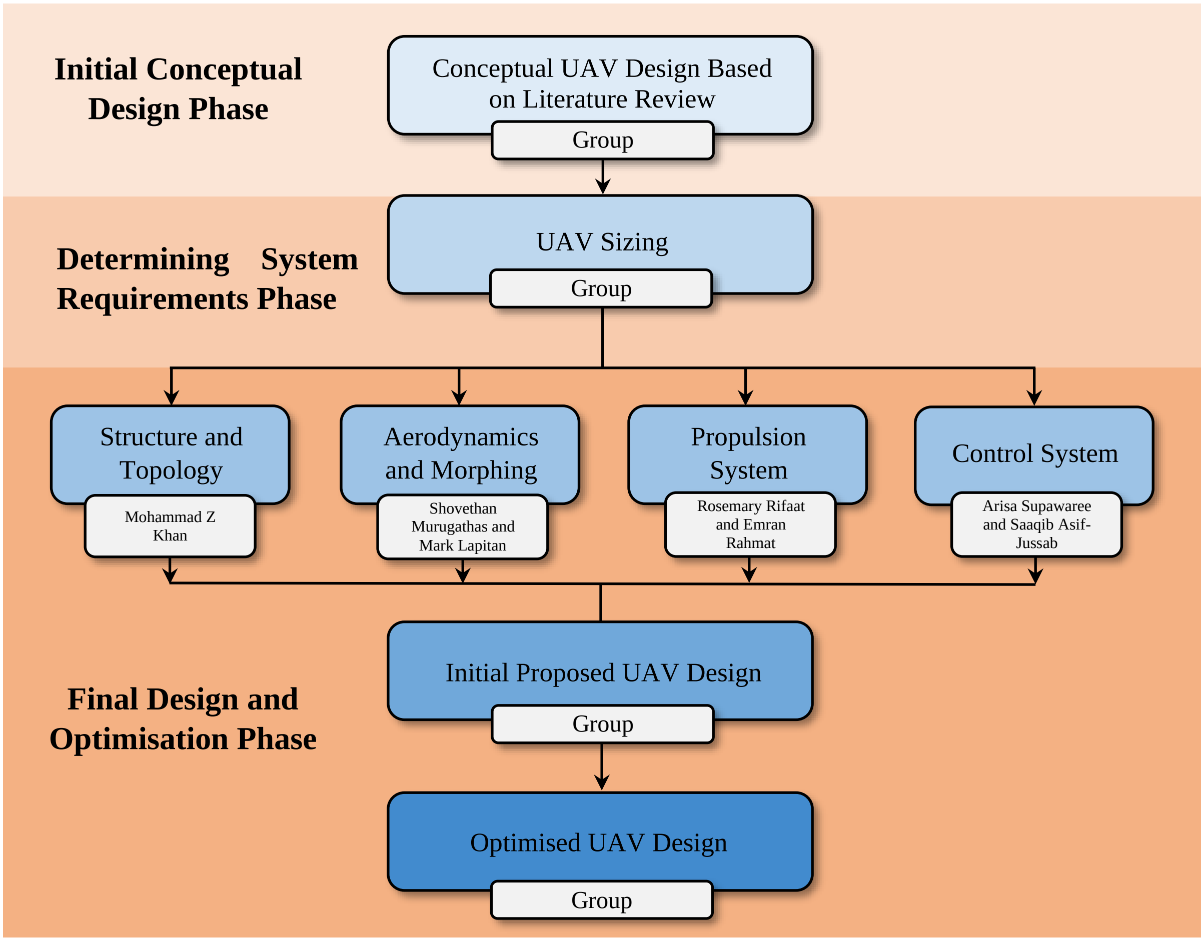

Figure 1- Workflow Package

1.2. Conceptual Design

One of the main aims of this project, is about designing and optimizing a UAV with a purpose of search and rescue missions. When constructing the final design UAVs, the following important factors are considered:

- High strength to weight ratio
- Fracture toughness
- Lift-to-drag ratio
- Corrosion resistant
- Environment Friendly
- Low Cost

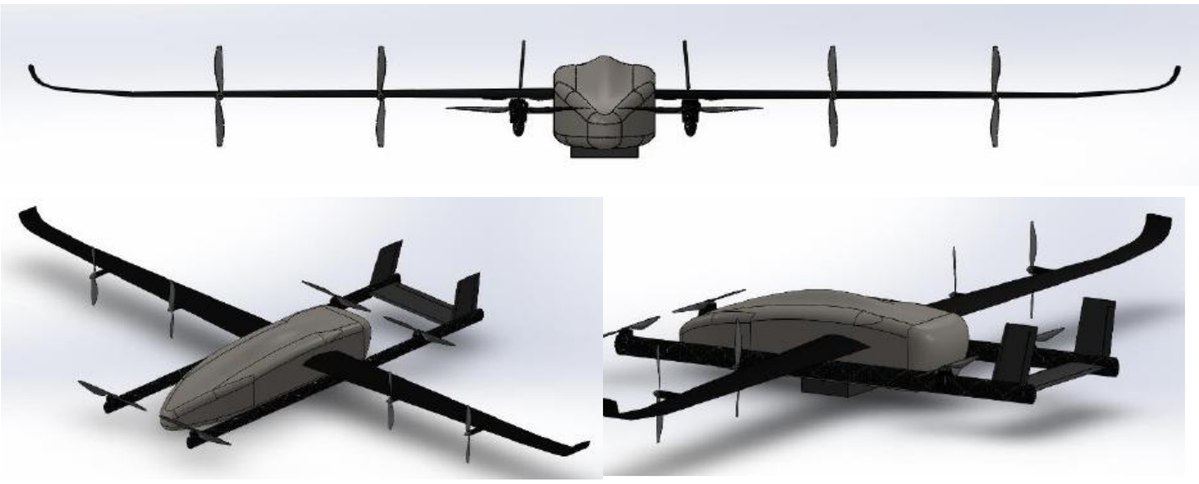

Figure 2- Multiple views of Soildworks model of UAV

As shown in Figure…, the final design is an autonomous all-electric UAV with a morphing wing design. The UAV is designed in a VTOL structure with 4 vertical and 4 horizontal propellers. The VTOL structure also improves maneuverability making it ideal for the UAV to be able to weave through urban areas with tall buildings and obstacles as well as dense forests. In a VTOL formation, the drone is able acquire some benefits over a conventional drone or plane, most notably, its ability to expand its range and making it more efficiency. The range is further expanded because the drone is lightweight as its main body is made from carbon fiber, meaning that the drone can stretch the battery power further and extending the range.

The UAV is planned to have a payload of 10kg, all of which will be the weight of the aid delivery package. This is one of the main advantages of the UAV that is being created as the UAV is somewhat small but can still carry a decently sized payload further, meaning that the UAV operator does not need to set the drone off close to the disaster zone (which may be difficult to get to otherwise). This makes the aid delivery response times quicker as more aid is able to be delivered in larger quantities. This structure would allow the UAV to fly with a speed of 100km/h and cover a range of 80km -100km. The vertical propellers allow the UAV to take-off and land vertically, eliminating need for a runway which makes it ideal to be deployed in natural disaster zones as the space needed for a runway may not be available.

1.3. Maximum Take-off Weight

Methods of estimating the size mass and power of an aircraft intended to meet specific performance and mission requirements are of significant importance to aircraft design (Tayan, 2017). The most popular methodology for aircraft sizing was introduced by Roskam (1986), which uses derives empirical equations from an initial weight estimation from previous aircraft data, however, this method could not be used in this project for various reasons. Firstly, these equations do not consider the unique nature of FW-VTOLs, which take off using a separate hover system, and cruises like a normal fixed-wing aircraft. The fact that take-off and landing use an alternative system means there is less loading on the wing during this phase than a fixed-wing aircraft. Additional reasons Roskam's method cannot be used is the fact our UAV is electric, whilst Roskam's methodology is for fuel aircraft, as well as the fact our UAV is outside of the size range of existing data.

The total mass of an aircraft is the sum of all its components, thus the sum of the payload plus the sum of the empty aircraft.

$$W_{TO} = W_{PL} + W_{Structure} \quad (1)$$

The first step in achieving accurate and reliable measurements for the sizing of the aircraft is to estimate aircraft weight, which is done by analyzing data from existing aircraft. The total payload is estimated in equation 1 as 18KG, which comprises of 10Kg of emergency supplies, 2KG estimate for Camera and hardware needed for the control system, as well as 6KG for propulsion systems and margin of error.

$$W_{PL} = 10KG + 2KG + 6KG = 18KG \quad (2)$$

Whilst the mass of the payload can be calculated implicitly from the design requirement (Tayan, 2017), assumptions have to be made in order to estimate the weight of the structure. Gundlach (2014) suggests using 25%-35% mass fraction for the structure of an FW-UAV, Tayan (2017) adjust this figure to 30%-40% to account for additional structural elements to support VTOL propulsion. Our VTOL will use the upper end of Tayan's estimation for structure mass facture as our UAV will need to support not only VTOL but distributed propulsion, which adds an extra 2 propellers to the wing, increasing the load on the structure.

$$W_{TO} = 18KG + (0.35)(18) = 24.3KG \tag{3}$$

1.4. Mission Plan

The formulation of a detailed mission plan is necessary to complete the next step of the sizing calculation. The mission plan is given below in Table 1 and Figure 3. Stall speed is the slowest speed a plane can fly to maintain level flight is crucial for the stability of the aircraft. To design an appropriate mission plan. Stall speed must be calculated using Equation 4. Both parts of the flight, the initial delivery of supplies as well as the return flight are flown in standard atmospheric

$$V_{Stall} = \sqrt{\frac{2W}{\rho A C_{LMAX}}} \tag{4}$$

A C_{LMAX} of 1.5 is assumed, as well as a 1.56M^2 wing area, which is taken from (Bergmann et al., 2021) for an all-electric UAV with a similar payload. Technical data of our UAV is initially assumed from previously designed UAVs, in particular (Bergmann et al., 2021), which designed a UAV of a similar specification.

$$V_{Stall} = \sqrt{\frac{2(24.3)(9.81)}{(1.225)(1.56)(1.5)}} = 12.89\frac{m}{s} = 46.4\ km/h \tag{5}$$

Table 1 - Mission plan (segments)

	Segment	Vertical Speed (m/s)	Horizontal Speed (m/s)	Altitude
1	Take-off position	0	0	0
2	Take-off hover and transition from hover to fixed-wing flight	2.5	0 to 1.2*Vstall	60-120
3	Accelerate and climb to cruise speed	2.5	1.2Vstall - 100kmh	120
4	Cruising at 70-75KPH	0	100kmh	120
5	Decelerate and descend	2.5	100-1.2Vstall	120-60
6	The transition from fixed-wing flight to hover, landing.	2.5	1.2Vstall - 0	60-0
7	Unloading of supplies,	0	0	0
8	Take-off hover and transition from hover to fixed-wing flight	2.5	0 to 1.2*Vstall	60-120
9	Accelerate and climb to cruise speed	2.5	0 to 1.2*Vstall	65-100
10	Cruising at 70-75KPH	0	100kmh	120
11	Decelerate and descend	2.5	100-1.2Vstall	65-100
12	The transition from fixed-wing flight to hover, landing.	2.5	1.2Vstall - 0	60-0

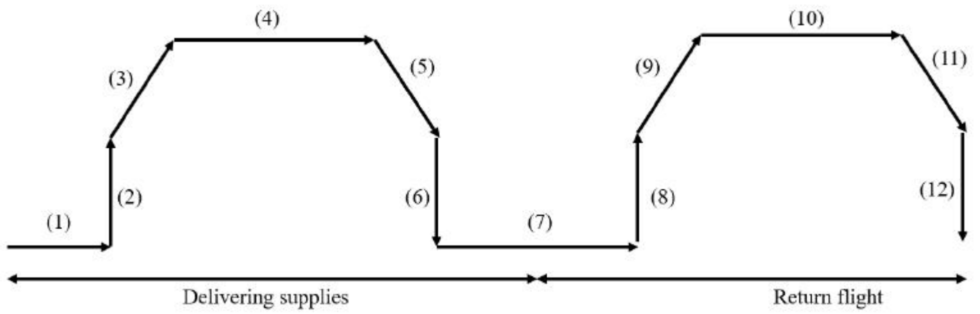

Figure 3: Mission Plan

1.5. Wing Loading

Calculating Wing loadings at each segment of our flight plan is necessary to size the UAV. The methodology used is that off (Tayan, 2017).

$$WS = \frac{1}{2}V^2\rho CL_{Max} \tag{6}$$

The main proponent of a VTOL UAV is that a long runway, since initially the UAV will only have a vertical component of velocity. The vertical velocity is estimated to be 2.5 M/s, yielding a Wing loading of 4.59 Kg/m^2. This low figure for wing loading is understandable, as in this phase of the flight there is no horizontal component of velocity, and vertical velocity is initially very small. This value is valid for 1-2 and 5-6 on the flight plan.

$$WS = \frac{1}{2}V^2\rho CL_{Max} = \frac{1}{2}(2.5)^2(1.225)(1.2) = 4.59\ Kg/m^2 \tag{7}$$

One the aircraft reaches an altitude of 60M, the UAV begins to accelerate horizontally and vertically until it reaches its cruising speed. The wing loading for this phase of the flight is shown in Equation 8.

$$WS = \frac{1}{2}V^2\rho CL_{Max} = \frac{1}{2}(15.7)^2(1.225)(1.8) = 181.17\ Kg/m^2 \tag{8}$$

The highest wing loading occurs in the cruise phase of the flight, where the UAV is cruising at 27.8 m/s resulting in a total wing loading of 560.03 Kg/m^2.

$$WS = \frac{1}{2}V^2\rho CL_{Max} = \frac{1}{2}(27.8)^2(1.225)(1.8) = 568.03\ Kg/m^2 \tag{9}$$

1.6. Thrust loading

Thrust-to-weight ratio or thrust loading is the efficiency factor for the total aircraft propulsion and it is directly proportional to the acceleration of the aircraft, meaning that the higher the thrust loading, the greater the acceleration experienced by the aircraft. Furthermore, a high thrust loading will have a greater excess thrust thus, resulting in a higher rate of climb.

By using the assumption mentioned in the previous sections, the thrust loading for their corresponding wing loading can be calculated by using the equation below:

$$\frac{T}{W} = qC_{d0}\frac{1}{\frac{W}{S}} + k\frac{1}{q}\frac{W}{S} \tag{10}$$

(Where $\frac{T}{W}$ is the thrust loading in kg/m^2; $\frac{W}{S}$ is the wing loading in kg/m^2; q is the dynamic pressure in Pa; Cdo is the zero-lift coefficient; k is the induced drag coefficient)

To calculate the thrust loading using equation 10, the following parameters will need to be calculated: q, Cdo and k. Firstly, the dynamic pressure can be calculated by using equation 11; assuming that the density of air, ρ. is equal to 1.225 for the height stated in the mission profile.

Table 2: Velocity and dynamic pressure for each segment

Segments	**Velocity (m/s)**	**Dynamic pressure (Pa)**
Takeoff/Landing - Phase 1	2.5	3.8
Takeoff/Landing - Phase 2	26.8	439.9
Loiter	13.9	118.3
Cruise	27.8	473.4

Sample Calculation (Takeoff/Landing – Phase 1)

$$q = \frac{\rho v^2}{2} = \frac{1.225(2.5)^2}{2} = 3.8\ Pa \tag{11}$$

(Where q is dynamic pressure in Pa; v is the velocity in m/s (depending on segment); ρ is the density of air in kg/m^3)

Secondly, assuming that the model is a single jet aircraft, the Oswald's number and the lift coefficient can be taken as the values shown below.

Table 3: Oswald's number and lift coefficient values used

Oswald's number ($\boldsymbol{e}$)	0.825
Lift coefficient ($\boldsymbol{C_l}$)	1.2 – 1.8

The induced drag k can be calculated by using the equation below:

$$C_{di} = \frac{{C_l}^2}{\pi ARe} = \frac{1.2^2}{\pi(20.2)(0.825)} = 0.0275 \tag{12}$$

Finally, by using the values obtained the thrust loading for each segment can be calculated, this is shown in *Table 4*

Table 4: Thrust loading for each section

Segments	Wing loading (kg/m^2)	Thrust loading (kg/m^2)	Dynamic pressure (q)	Induced drag (k)	Cl
Takeoff/Landing - Phase 1	4.6	0.05	3.8	0.028	1.2
Takeoff/Landing - Phase 2	181.2	0.07	439.9	0.028	1.2
Loiter	212.7	0.12	118.2	0.062	1.8
Cruise	845.9	0.12	473.4	0.062	1.8

Sample Calculation (Takeoff/Landing – Phase 1)

$$\frac{T}{W} = qC_{d0}\frac{1}{\frac{W}{S}} + k\frac{1}{q}\frac{W}{S} = 3.8(0.023)\frac{1}{4.6} + (0.028)\frac{1}{3.8}(4.6) = 0.05\ kg/m^2 \quad (13)$$

1.7. Selection of Wing Aerofoil

Assuming steady level flight L = W, and that the UAV is in cruise condition, the aerofoil of the wing was determined. By using the equation below and the data from the previous sections, the Cl at cruise condition can be calculated

$$C_l = \frac{2W}{\rho V^2 A} = \frac{2(32 * 9.81)}{1.225(27.778)^2(1.56)} = 0.43 \quad (14)$$

Using the C_l value obtained, it was determined that the NACA 4412 was a suitable aerofoil for the design of the wing.

2. Topology Optimisation of Wing and Wing Rib - Mohammad Z Khan (170469696)

2.1. Introduction

Continuously evolving requirements for the aviation industry, as well as aggressive weight targets, has allowed for substantial progress in the field of aeronautical engineering (Ameduri, S. and Concilio, 2020). The above conditions have resulted in the increasing integration of advanced computer aided-optimization methods into the avionic design process, to achieve lighter and more efficient designs (Altair Engineering, 2011).

One optimisation technique that has become increasingly prevalent in aeronautical and automotive engineering is Topology Optimization (TO); which is used to find the optimal distribution of materials across a certain design area under given constraints (Elelwi, 2021). TO determines load-bearing components from individual elements within the structure, and iteratively removes material that do not contribute to supporting the load path, thus only material vital to support the structure is left behind (Walker, 2013). Since only material that is irrelevant to structural integrity is removed, TO results in weight savings without compromising structural integrity. This process is illustrated in Figure 4.

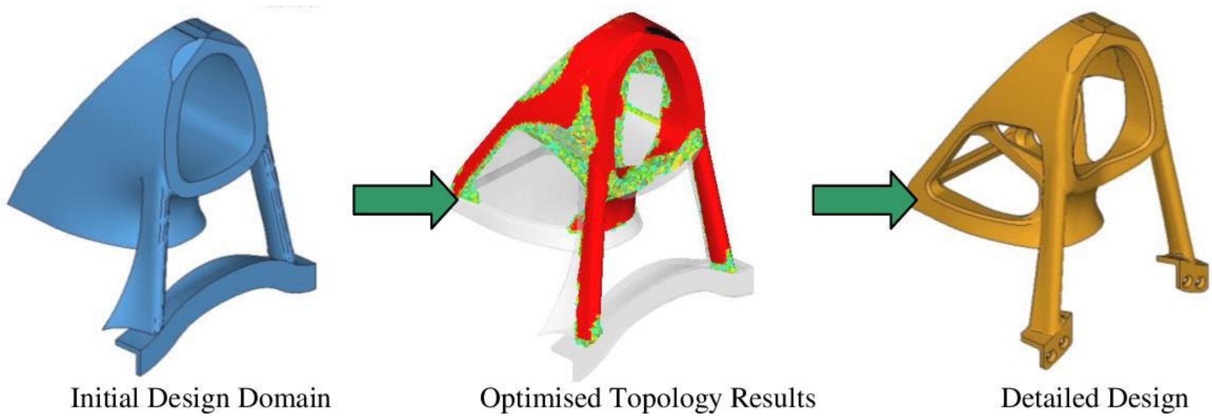

Figure 4: Topology Optimisation Process and Results (Zhou, 2011)

Industrial applications of TO have seen rapid growth, and have generated promising results; Airbus was able to achieve a 40% weight reduction on a group of A380 leading edge ribs by performing TO (Altiar Engineering, 2011).

2.1.1. Aims, Objectives & Rational

The aim of this investigation is to optimise the internal material distribution for the wing of UAV designed in the previous section of this report, as well as to optimise the wing rib component. To achieve this, the following objectives must be met:

- Develop a strong understanding of the fundamental concepts and principles behind TO.
- Become proficient in Altair HyperWorks, HyperMesh, and Optistruct.
- Apply TO theory to Optimise wing and wing rib.
- Obtain justifiable constraints, forces to apply to wing model.
- Analyse TO results, identify improvements that can be made to wing design.
- Interpretate TO results to create valid structural design on Soildworks.

A fundamental roadblock to the electrification of aircrafts, and the wider aerospace industry is the significant discrepancy in the energy densities between fuel and batteries (Kammermann, 2020), which results in electric aircrafts being 25% - 40% heavier according to the Transportation Electrification Community (2015). Whilst research is consistently being done to increase the energy density of batteries, another effective approach towards the electrification of aircrafts is to reduce the weight of other components in the aircraft i.e., wings, fuselage etc.

Additionally, in the application of UAVs for search and rescue application, reduced weight can result in a larger range, or the ability to carry a larger payload, both features can significantly enhance the commercial viability of our UAV.

2.1.2. Internal Structure of Aircraft Wing

An important pre-requisite to understanding TO in the context of the aviation industry is the internal structure of an aircraft wing. The wing is comprised of three structural components, which work in tandem with each other to support the aerodynamic forces acting on the wing during flight (Megson, 2017).

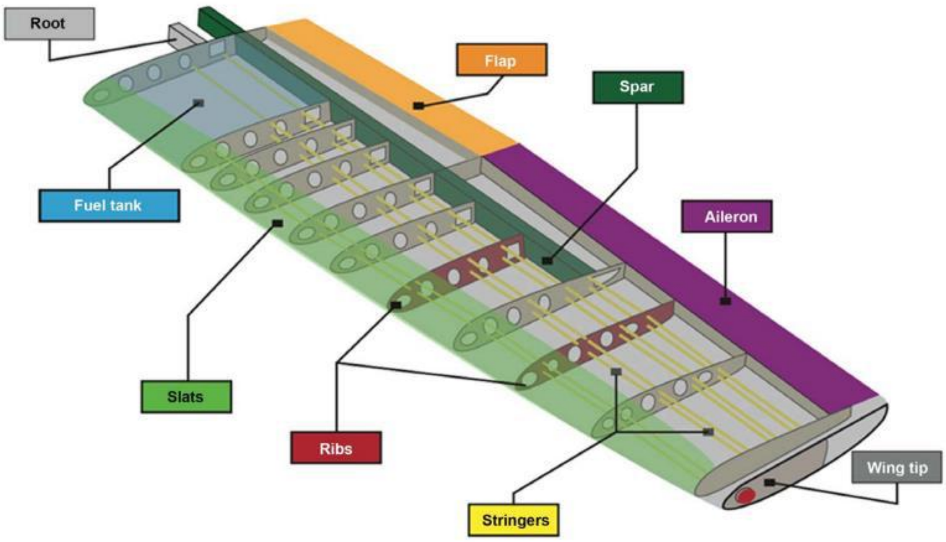

Figure 5: Internal Structure of Aircraft Wing (Hicks and Henne, 1978)

These three components are as follows (Hoang, 2015):

Wing Spars – Longitudinal components of wing, which are typically arranged to form an I-beam.

Stringers- Longitudinal component which performs similar function to Spar; carry axial loads that arise from bending in the wing. Stringers are spaced laterally through the wing, from the fuselage to the wing tip.

Ribs – Ribs are spaced along the span of the wing, and are attached perpendicularly at frequent intervals, they usually have the same shape as the aerofoil.

Analysing the results of the TO, should show clear signs of the above structural components. The current wing is made of a single solid mass, therefore having unnecessary weight that is insignificant to the structural integrity of the wing. Removing this excess material should result in significant weight reduction.

2.2. Topology Optimisation

Before solving, an optimisation formulation must be made which consists of an objective function, constraints, and design variables. Design variables uniquely identify the design and can be anything that influences the performance of the structure (Toropov & Muller, 2022). The objective function is the response from the structure (i.e., mass, stress, compliance) that is being maximised or minimised, whilst constraints are limitations on performance characteristics, to ensure that the simulation is realistic. Formal mathematical representation of a general optimization problem can be given as:

$$\begin{array}{lll} \text{Minimise} & f(x) & \\ \text{Subject to} & g_j(x) \leq 0 & j = 1,2, \ldots\ldots, n_j \\ h_k(x) = 0 & k = 1,2, \ldots\ldots n_k. & \end{array} \tag{15}$$

Where X are the design variables, f is the objective function, and g and h are constraints.

As described previously, TO reduces unnecessary weight by iteratively removing elements that are irrelevant to the structural load, therefore only structurally relevant elements are left behind, which are critical to the load path. Initially, this was achieved by the discretization of a domain into a grid of finite elements called isotropic solid microstructures, each element is either filled with material or emptied, depending on if the element in question is structurally relevant. The density distribution is discrete, and each element has a binary value; the problem can be formulated as (Bendsøe and Sigmund, 2003):

$$\rho = 1 \; or \; \rho \approx \; 0 \tag{16}$$

An example of this can be observed below in Figure 6, which demonstrates the optimized material layout of a loaded beam, solid elements with densities $\rho_{(e)}$ =1 are black, whereas the void elements with $\rho_{(e)}$ = 0 are removed.

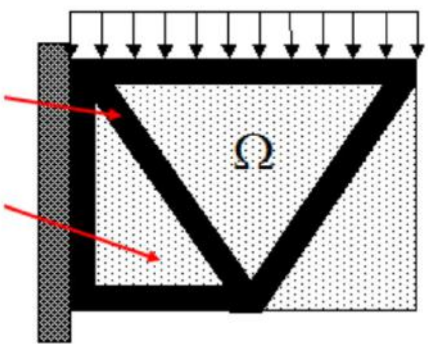

Figure 6:Discrete Optimization of beam (Dassault Systèmes, 2020)

Whilst discrete solutions are preferred, it is noteworthy to consider that an optimisation that only deals with discrete variables is not realistic when dealing with large number of design variables (Hoang, 2015). Therefore, it is necessary to introduce continuous relative density distribution for more complex problems. The SIMP (Solid Isotropic Material with Penalization) method, allows for continuous density distribution whilst pushing the solver to produce a more discrete solution. In the SIMP method each finite element has a relative density, which is related to the module of elasticity, with some penalization. The SIMP method can be stated mathematically as:

$$E = \rho^p E_0 \tag{17}$$

Where E_0 is module of elasticity, and P is penalisation factor.

The penalisation factor diminishes contribution of intermediate densities (grey elements), and therefore defines to what extent the optimizer pushes a solution to having hard or void elements only i.e., the higher the penalisation factor the lower the intermediate densities. (Massachusetts Institute of Technology, 2013).

Whilst there are other methods for material distribution, such as Rational Approximation of Material Properties (RAMP), and Optimal Microstructures with Penalisation (OMP); the SIMP methods remains the most popular since it is the most computationally efficient as well as the fact it can be used without prior knowledge of microstructures (Rozvany, 2007). Furthermore, the SIMP method is used in Altair Opti Struct which is the optimizer we will be using for this investigation.

The iterative process used in Opti struct can be seen below in Figure 7. The initial step is to analyse the Finite Element (FE) model with respect to the objective function and constraints. If none of the constrains has been violated, however the objective function has not been reached, the FE model is adapted, and another FE analysis is conducted. Once the mode converges to the objective function the solver treats the design as fully optimised, and the final FE model is displayed.

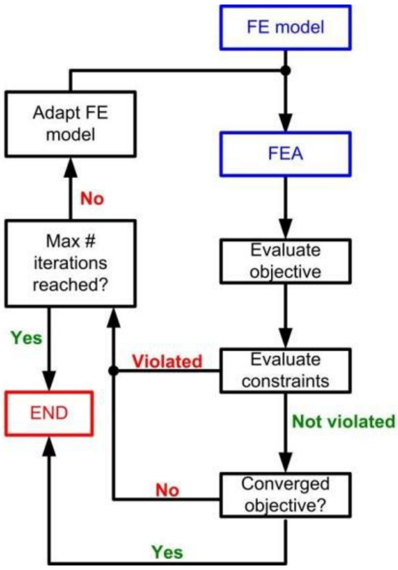

Figure 7: Flowchart for Optimisation Algorithm (Christensen, 2015)

2.3. Topology Optimisation of Global Wing Structure

2.3.1. Force Estimation

To estimate aerodynamic forces acting on the wing the XFLR5 code is used. The wings are remodelled on XFLR5, and a simulation was run with cruise conditions of 20m/s and a 7 ° angle of attack. The coefficient of lift was given for different points along the wing, which was then converted to lift using the following equation (Nasa,2009):

$$Lift = \frac{\mathrm{CL}\rho V^2}{2} \tag{18}$$

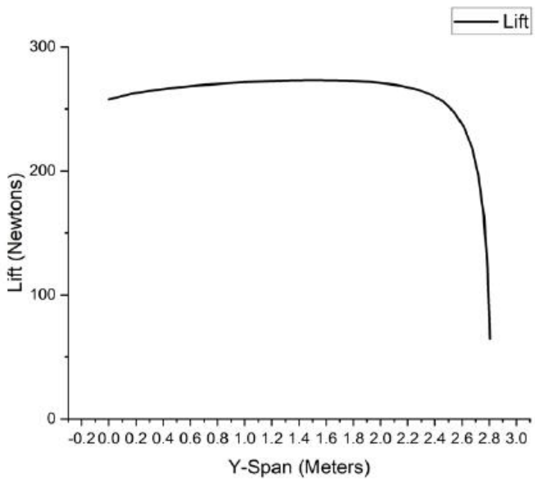

Figure 8: Lift distribution from XFLR5 simulation at 20m/s and 7°AOA

Figure 8 shows the lift distribution at across the wingspan. For most of the wingspan (up to 2.2m) the lift is between 220N and 240N, and rapidly drops towards the wing tip. To keep the simulation simple, it is assumed that the maximum value for lift recorded (273.15N) will be uniformly distributed across the surface of the wing. The Federal Aviation Administration recommend a safety factor of 1.5 for external loads acting on a system (Federal Aviation Administration, 2008), although for this report a much higher safety factor of 2.3 will be used. This is to factor in the added load on the wings from the VTOL structure and distributed propulsion. The drag force acting on the wing was assumed to be a third of that of the lift.

$$Lift\ = 273.13N\ \times 2.3\ \times 9.8 = 6156.35N \tag{19}$$

$$Drag = 6156.35\ \times \frac{1}{3} = 2052.12N \tag{20}$$

2.3.2. Meshing Process

The error '2 edges failed nodal set up' was encountered upon importing the model from SolidWorks into Hypermesh. Additionally, there was some difficulty meshing the size of the wing, which was solved by scaling up the model so larger sized elements could be used. Initially a 2D mesh was created which was subsequently converted into 3D hex mesh, using the Solid Map function. A Hexahedral mesh is used as it is more economical in terms of number of elements, when compared to Tetrahedral mesh, therefore easier to compute.

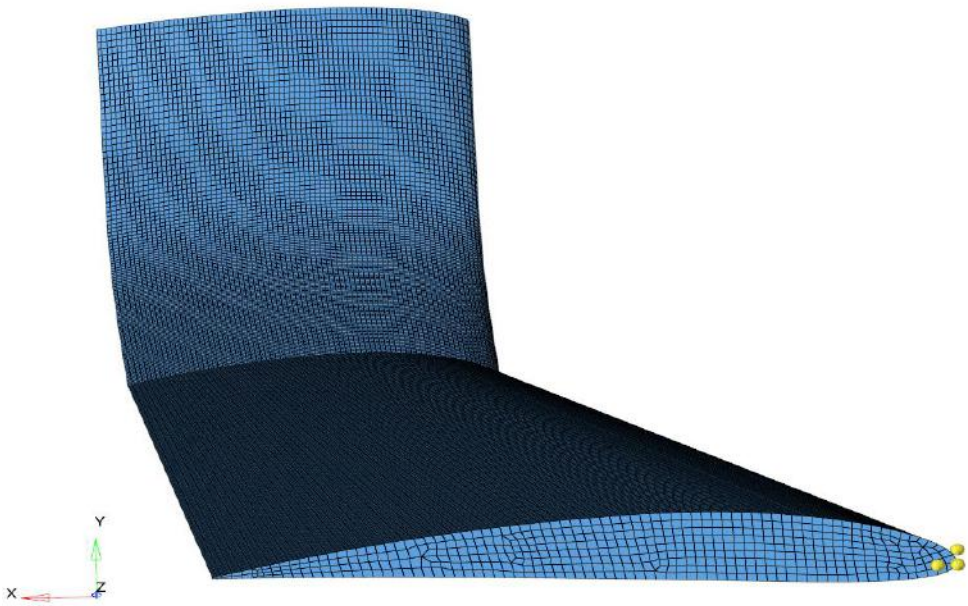

Figure 9: Sideview of meshed wing

Table 5: Summary of Meshing Information

Element Size	50mm
Number of Elements	281502
Nodes	325420
Mesh Type	Hexahedral

The objective function of the investigation was to minimise the compliance whilst limiting the volume fraction to 30%. In other words, the simulation should converge to a solution which reduces the weight whilst maximising the stiffness. A penalisation factor of 1.25 was selected, the objective function can be stated mathematically as:

$$\begin{gathered}\text{Minimize compliance}\\ \text{Subject volume fraction} < 0.30 \\ \rho_L \leq \rho_i \leq 1 \\ \rho_i \; relative\ density\ of\ each\ solid\ element\ in\ the\ designable\ space\end{gathered} \tag{21}$$

The wing was constrained in a manner that represents normal flight conditions where deflection is possible at the tip of the wing, however not the root which is attached to the fuselage. Thus, the Root Chord was constrained for all degrees of freedom; whilst the tip was constrained for rotation and unconstrained in deflection. RBE3, which is an interpolation element, is used to distribute the loads calculated earlier on the wingspan. Since the model had to be scaled up, due to issues with meshing, the forces were also scaled up accordingly.

The criteria for simulations were the following:

1. Noticeable aircraft structural aspects such as spars, stringer and ribs can be identified.
2. Structural members can be seen such as I beam and truss like systems.

Should both criteria be met, relevant suggestions can be implemented to reduce the weight of the aircraft, whilst maintaining structural integrity. A concern in TO is that designs concepts are not manufacturable, thus manufacturing constraints can be used to limit size shape and direction of the material distribution (Bontoft & Toropov, 2018). There are several different methods within OptiStruct, for instance member size control can allow control over the simplicity of the final design. Minimum and maximum member size control, penalise formation of small and large members respectively, thus providing a form of quality control over the solution (Altair Hyperwork, 2022). Additionally, OptiStruct allows users to impose draw directional constraints along the X, Y and Z axis which can enables structural member to be seen clearly. A combination of minimum and maximum member size control and direction constrains were used in the simulations, in addition to a control simulation with no manufacturing constraints.

2.3.3. Results and Discussion

The first simulation was run without any manufacturing constraints and converged to a solution after 14 iterations, the results can be observed in Figure 10. The material distribution can be interpreted as a single spar like structure, with most of the material towards the upper surface of the wing. Additionally, the width of the spar is of significance, since it is thickest at the root of the wing and becomes much thinner towards the wing tip. Towards the lower surface a second spar or stringer can be identified which is entirely separate to the first.

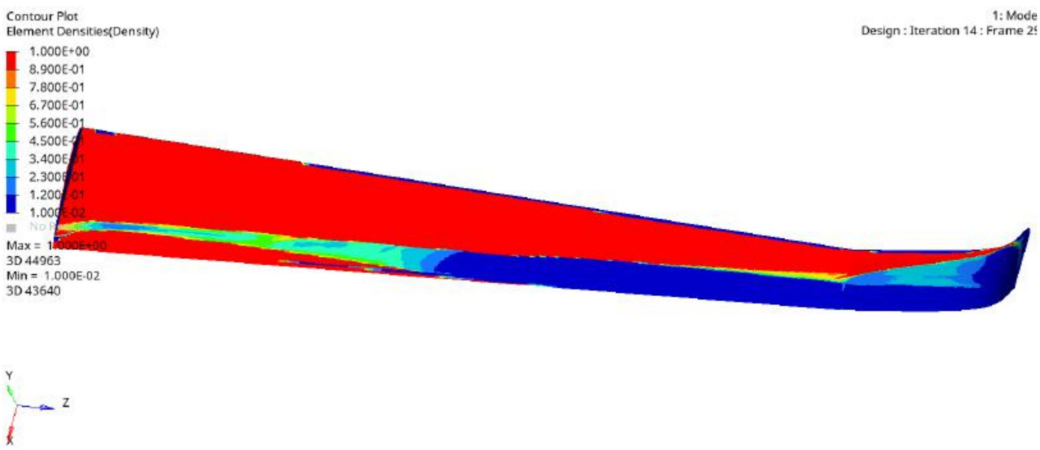

Figure 10: Contour plot of element density for simulation without any manufacturing constraints

In the second simulation manufacturing constraints were used in the form of member size control and can be observed in Figure 11. The MINDIM and MAXDIM functions were used to set a minimum dimension size of 50 and a maximum of 150. Similar to Figure 10 a large single spar like structure is present in the upper portion of the wing, with greater material distribution towards the root of the wing. This is indicative of greater bending moment at the root of the wing, thus more material is allocated in this region. The utility of using manufacturing constraints is clear when comparing Figure 10 with Figure 11, as along with the spar like structure, ribs are also present in the contour plot.

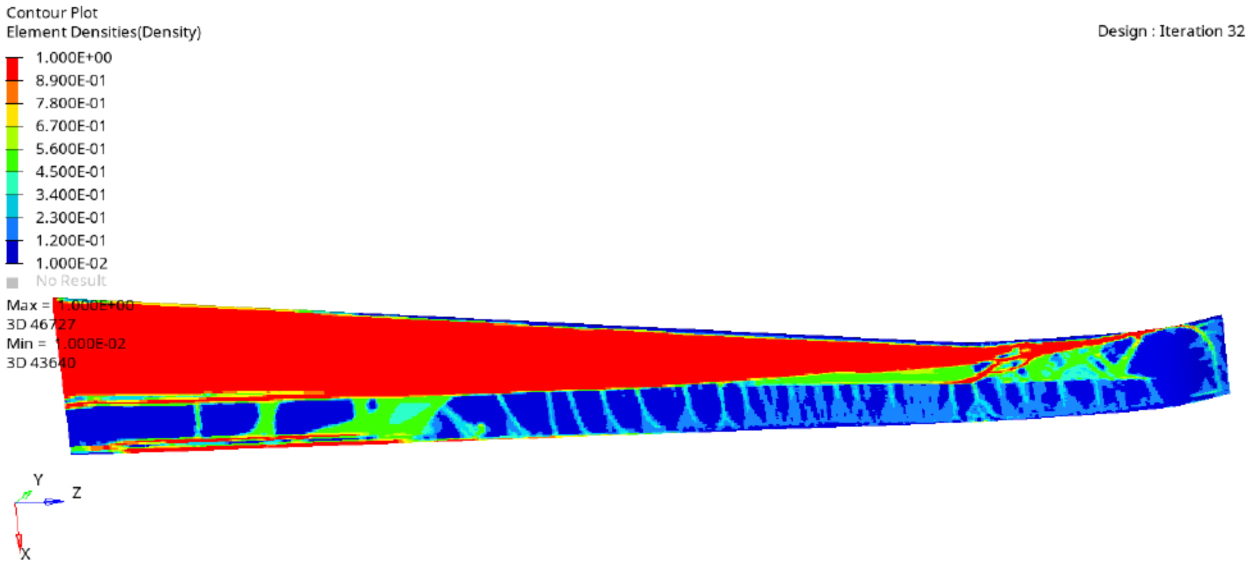

Figure 11:Contour plot of element density for simulation with MINDIM 50 and MAXDIM150

It is noteworthy that the wing rib distribution is not uniform; towards the wing root ribs appear to be much thicker than the ribs near the wing tip. This can be interpreted as either one large rib, which is much thicker than the ribs close to the wing tip, or a cluster of ribs of uniform thickness. The conventional interpretation is a cluster of ribs in close proximity to each other, since designing ribs of various thickness is impractical. In the middle portion of the wing, ribs appear to be spread out, and cluster again closer towards the wing tip. The clustering of wing ribs near the wing root and wing tip are distinctly different; the ribs close to the wing tip are clearly separated, whereas ribs near the root appear as one structure. The difference in frequency of wing ribs is indicative of the bending moment experienced by the wing; in areas where bending moment is large ribs are clustered to provide maximum support (close to the root). However, in the middle part of the wing ribs have less frequency and significant gaps.

Additionally Figure 12 which shows the side view of the same simulation, showcases clear I-Beam structures in increasing frequency towards the upper third of the wing, this mirrors the material distribution in Figure 10, where most of the material is located towards the upper portion of the wing. The I-beam support throughout the wing can also be interpretated as wing ribs, which are spread across the wingspan that give the wing its aerodynamic shape.

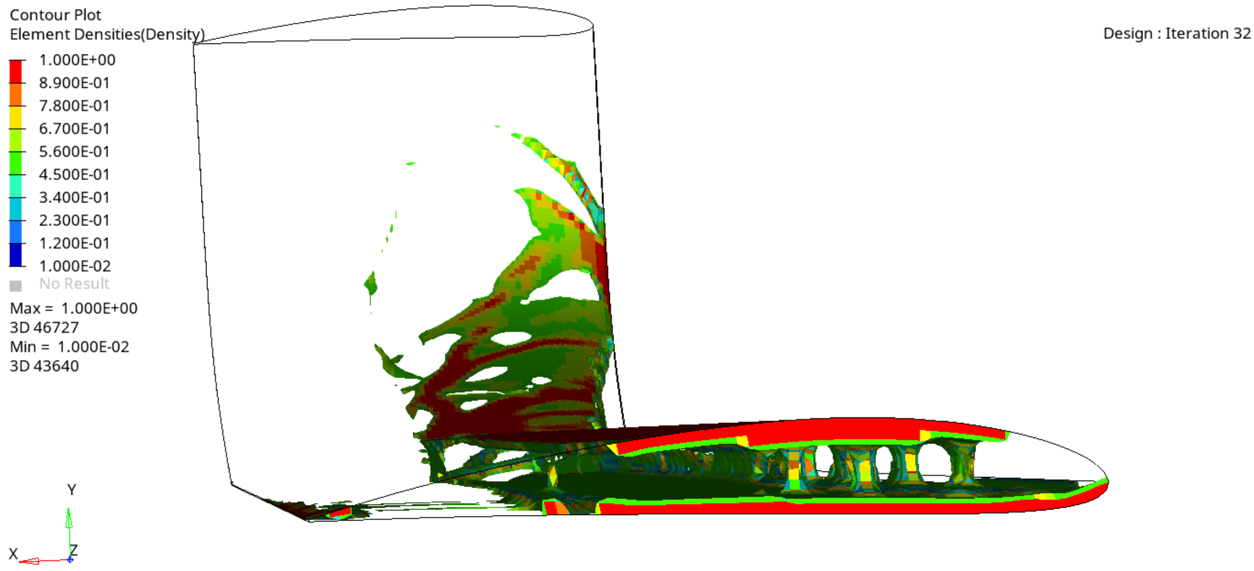

Figure 12: Contour plot of element density for simulation with MINDIM 50 and MAXDIM150 (Sideview)

A third simulation with MINDIM of 50 and MAXDIM of 200 was also run, however results were very similar, and no new conclusions could be drawn, therefore results are included in the appendix.

The next set of simulations were run with draw dimensional constraints in the X, Y and Z axis. The draw constraint in the X axis yielded a contour plot in Figure 13; the material distribution can be interpreted as a stringer, for reasons such as location, thickness, and connectivity to ribs. Stringers are thin rods that are placed laterally throughout the internal material of a wing to support the axial load. The material distribution is not as thick as the material distributions present in Figure 10 and 11, which is evident of a stringer as it is much thinner than spars. Furthermore, the Spars Figure 10 and 11 get much thinner towards the wing tip whereas the material distribution in Figure 13 is of a much more uniform thickness which indicates this element is a stringer not a spar. Additionally, the ribs appear to be so closely attached to the stringer close to the wing tip it appears to be one structure, it is hard to separate the boundary of the stringer and ribs. This again points towards the material distribution representing a stringer, since one of the main functions of the stringer is to provide structural connectivity by connecting the ribs to each other and the stringer.

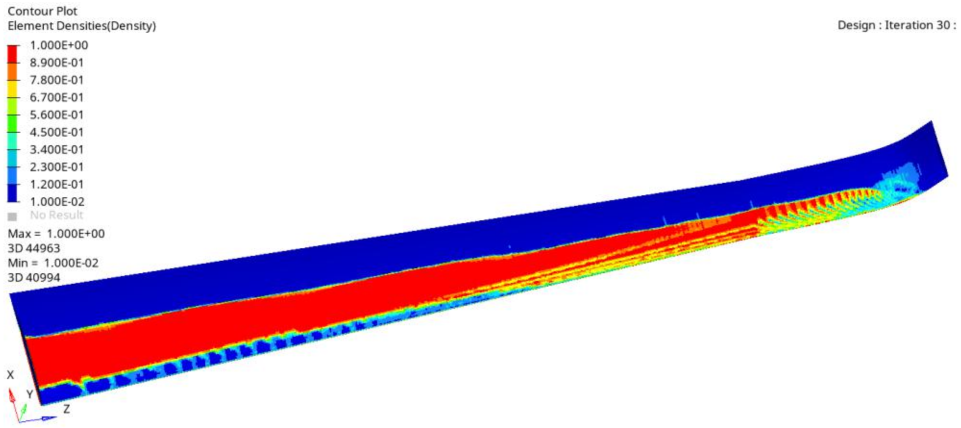

Figure 13: Contour plot of element density for simulation with draw constraint in the X axis

The simulation results for the draw constraint in the Y- direction is shown in Figure 14. The material is distributed similar to Figure 10 and 11, showing a spar like structure towards the upper area of the wing, with material density tapers off towards the wing tip. A feature that is unique for Figure 14, in comparison with previous contour plots, is the breaking of the spar into two distinct parts towards the wing tip. Soundarya (2018) states that the majority of wings do not have a single spar but in fact multiple, whilst previous contour plots demonstrated single spar structures, Figure 14 provides evidence for a dual spar layout.

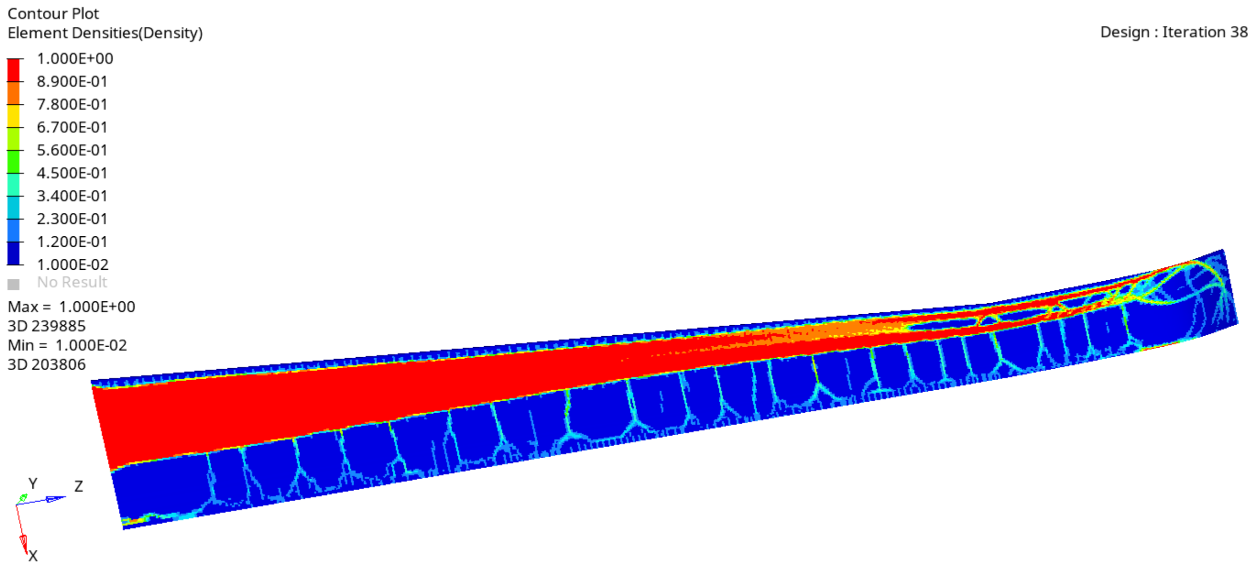

Figure 14: Contour plot of element density for simulation of Draw Constraint on Y axis

Figure 15 below, shows a thin rod like structure in the centre of the wing which indicates the presence of a stringer. The material distribution is relatively uniform, and slowly becomes thinner towards the end of the wing tip. Furthermore, the fluid web-like manner in which ribs are attached signify a stringer since there is much more connectivity than contour plots which indicates spars.

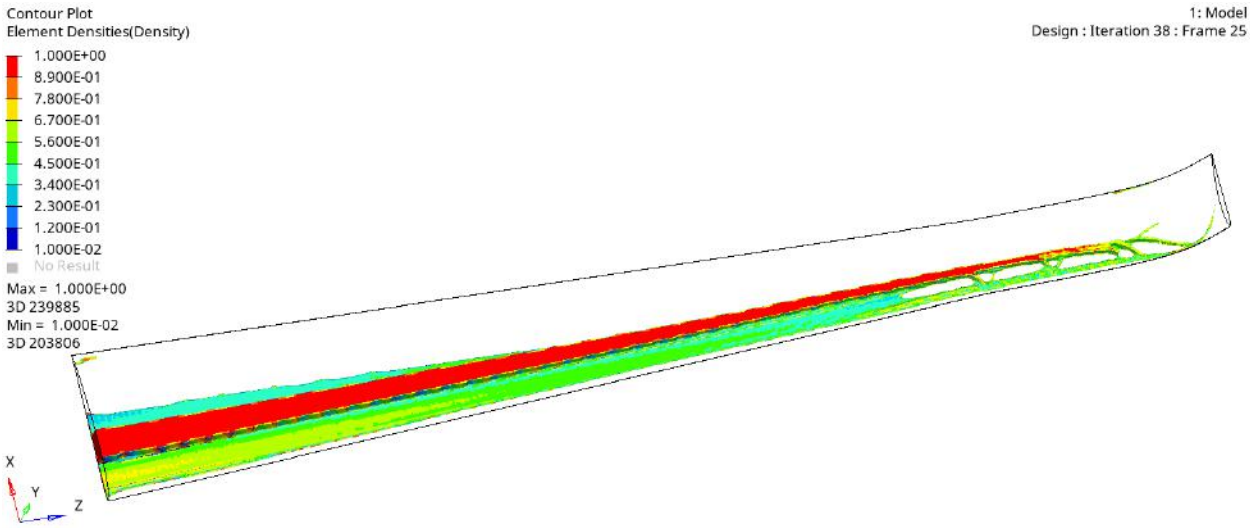

Figure 15: Contour plot of element density for simulation of Draw Constraint on Y axis

Figure 16 shows the results for the simulation with draw constraint in the Z axis. The material distribution begins with one mass which eventually breaks up into three parts. This contour plot is of limited use since the material distribution appears to be fractured and broken towards the wing tip, thus overall providing limited insight in comparison with other simulations.

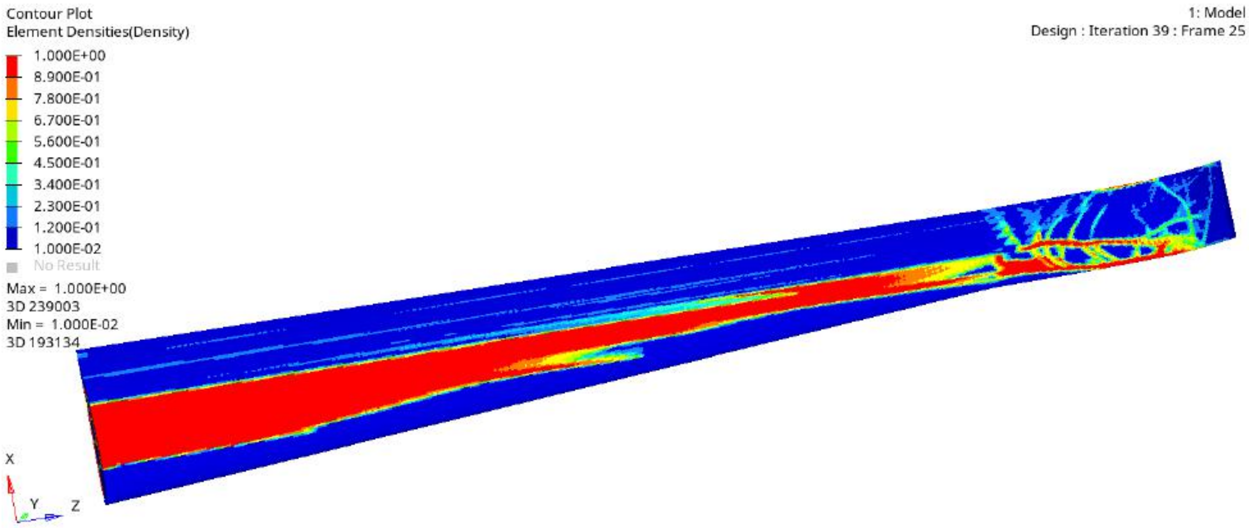

Figure 16: Contour plot of element density of Draw constraint on Z axis

2.3.4. Conclusion, Limitations and Future Work

Various conclusions can be drawn from the results of the simulations and relevant suggestions can be made and implemented to minimise the weight of the wings whilst improving its structural integrity. Figures 10,11 and 14 pointed to a spar like structure at the upper portion of the wing, which is thickest at the wing root, becoming thinner as it approaches the wing tip. Therefore, this portion of the wing can be classed as of high structural significance, which must be reflected in higher material distribution. Whilst Figure 14 provided some indication of a dual spar layout, the majority of results indicated a single spar should be used.

Ribs were also noticeable in Figures11,13,14 and 15. Ribs appear to be clustered towards the wing root where bending moment is largest, frequency of ribs decreases in the middle area of the wing, and then increases again towards the wing tip, however not to the same magnitude as the wing root.

Stringers can be identified from Figures 13, 15 and 16; and can be differentiated from the spars due to location, thickness, and connectivity to ribs. Whilst spars are located in the upper portion of the wing, stringers are placed laterally throughout, additionally stringers resemble thin rods whereas spar are more like thick I beam structures. Additionally, stringers are used to provide the wing with structural connectivity and connect the ribs to each other and the stringer, this is reflected in the fact the boundary between the stringer and rib is unclear.

There are various methods in which our investigation could be improved in the future. Firstly, all the simulation had the same force vector applied, thus are all optimising for only bending. Wings are predominantly subject to bending force due to lift that keeps the aircraft aloft, however, significant twisting forces are also present during flight, which if not accounted for can cause failure. The contour plots fail to optimise for twisting, showing one straight longitudinal spar reduces the bending moment, however, does not reduce torsion. Reducing torsional force would require, beams to be placed longitudinally as well as diagonally. Due to time constraints, simulations which account for torsion were not completed, this could be useful in future work. Including torsional forces in the objective function, would allow the solver to optimise for a more accurate solution, which could be included as such:

$$
\begin{gathered}
\text{Minimize compliance} \\
\text{Subject volume fraction} < 0.30 \\
\rho_L \leq \rho_i \leq 1 \\
\sigma \text{ max} = 150 \text{ MPA} \\
\tau_{Max} = 100MPA
\end{gathered}
\tag{22}
$$

An optimisation problem, which considers multiple forces, would converge to a more complete and accurate solution.

Another method to improve that could be implemented in future works is varying volume fraction and SIMP number to obtain the optimal combination, that will converge to the most accurate results. Furthermore, when meshing hexahedral elements and 50mm element size was selected, to make the optimisation easier to compute. Employing a machine with much stronger computational power would allow simulations to be run with finer element size and use of tetrahedral elements which would increase the accuracy of results. Additionally applying multiple manufacturing constrains simultaneously could have been explored i.e., having constrains on dimension size and extrusion at once.

2.4. Topology Optimisation of Wing Rib

Ribs provide the wing with aerodynamic shape and structural support. TO in the previous section show ribs located across the wingspan; clustered together at the wing root and uniformly distributed towards the wing tip. Whilst spars and stringers are rod like strucutres, there is limited room to use topology optimisation to futher optimise, however literature such asWalker(2013), Segarra (2014), Sandhiya (2016) Soundary (2015) have demonstrated that performing TO on wing ribs can result in significant reduction of wing weight.

2.4.1. Procedure

The wing rib co-ordinates are the same as the NACA 4412 aerofoil, which are imported from Aerotools (2022); the Z co-ordinates which are all zero are added to import into Soildworks, co-ordinates can be found in the appendix. The insert curve, tool is then used to create a 2D model.

The 2D model was then meshed in hyper mesh, using the automesh feature. Mesh element size was set at 1mm, to yield precise material distribution, the element type QUAD 4 is used. Additionally, two non design space circles are used to connect the stringers to the ribs.

Figure 17: Meshed wing rib

2.4.2. Force Calculation

The aerodynamic forces used in the previous section of this report are significantly scaled down since force will be divided amongst all aspects of the wing (skin, stringers, spars, and multiple ribs). Thus, only a small fraction of the force will be acting on the individual ribs. The RBE3 element, was again used to distribute the force, with drag force assumed as 1/3 of lift. The degrees of freedom constrained in X, Y and Z axis.

2.4.3. Results and Discussion

In total 5 simulations were done, with the minimum dimension parameter being increased:

1) No constraints
2) Mindim = 4 mm
3) Mindim = 8 mm
4) Mindim = 16 mm
5) Mindim = 32 mm

Ultimately, the simulation with Mindim 8 is selected shown in Figure 18, since it has the lowest number of elements with intermediate densities. Contour plots for other simulations can be found in the appendix.

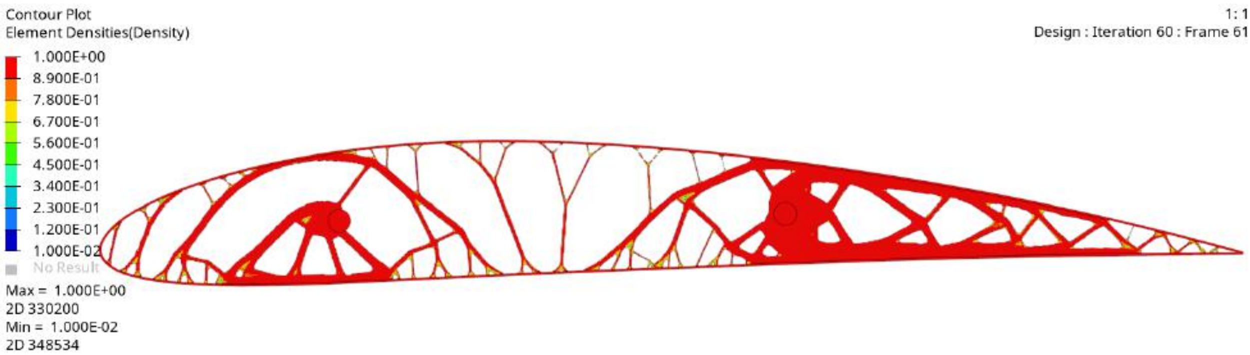

Figure 18: Contour plot for Simulation with MINDIM 8mm

Analysing the material distribution shown in Figure 18 various conclusions can be drawn regarding the optimal structure of a wing rib. Firstly, it is evident from the contour plots that tip of the rib is where the material is heavily distributed, in a truss like support structure similar to a web. Much of the material from the centre of the wing rib has been removed and appears to be supported by thin I-beams, providing further validation to the previous simulation, as I beam were also present in Figure 12.

In order to validate the results stress tests were conducted, OSSmooth function allows the final design geometry to be extracted in CAD format which can then be used for Finite element analysisVisual representation of the stress analysis can be seen from Figure 19 & 20 below, whilst Table 6 shows the results.

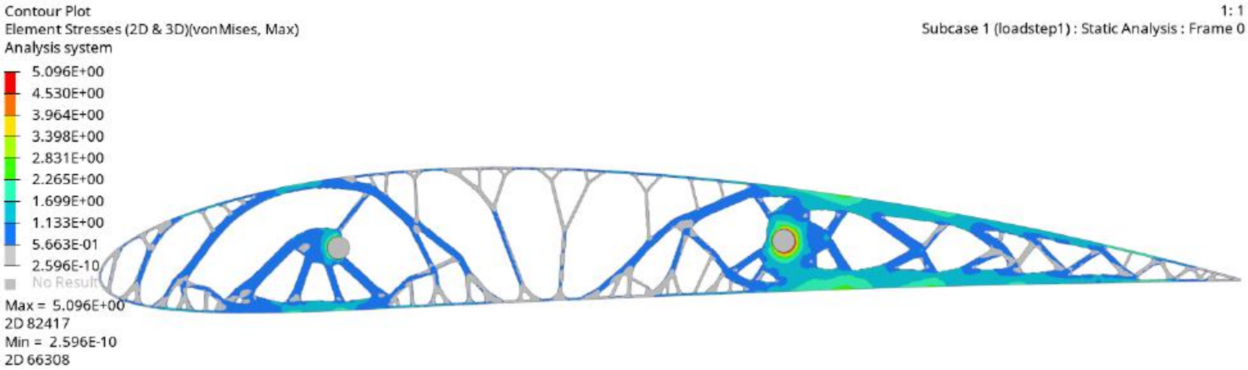

Figure 19: Visual representation of stress test for optimized wing rib

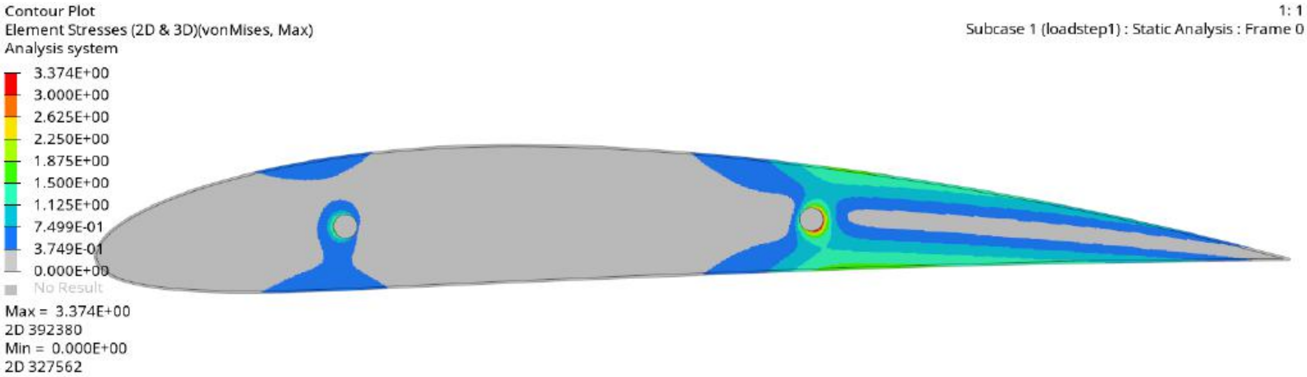

Figure 20- Visual representation of stress test for original wing rib

Table 6-Summery of data from stress test

	Original design	**Optimized design**
Stress, MPa	3.37	5.096
Displacement, mm	0.06176	0.08937
Mass, kg	2.22	0.81

A vast amount of material can be saved on each wing rib, as shown in Table 1, the original design weight 2.2Kg whereas the optimised rib weighed 0.81Kg, which represents a 63.5 % percentage decrease. The wingspan of one wing is 2.81m; Assuming each wing has 5 ribs clustered towards the root, and a further 10 ribs which are uniformly distributed towards the wing tip as shown in Figure 11 from the material distribution graphs in the previous section. The total weight saving is equivalent to 20.85 Kg.

$$Weight\ saving = (15\ \times 2.22kg) - (15 \times 0.81) = 20.85KG \tag{23}$$

Additionally, whilst neither design reaches its yield strength it is important to consider the fact that the optimised ribs experienced more stress and displacement. This is since the TO analysis was directly converted into a design; rather than being interpreted by an engineering team, to use the analysis to redesign the component, which is the common approach.

2.5. Interpretation of TO as Valid Structural Design

Manual interpretation of TO results are necessary to create realistic CAD models with valid structural designs that can be manufactured. The objective of the simulations run in this report are to minimise compliance whilst maximising stiffness, however in real application trade-offs need to be made to ensure the design can be manufactured. TO analysis can often suggest solutions which cannot be manufactured into a valid structural design, e.g., Figure 18 shows very thin I-beams across the wing rib which would be impractical and difficult to manufacture. Thus, analysis from the TO results will be used to the optimised internal structure for the UAV wing.   Figures 18 & 19 demonstrate the CAD model for the wing rib, whilst Figures 21 & 22 show the final optimised internal structure of the wing. Design decisions based on topology analysis are presented in Table 7 & 8.

Table 7 Design decisions with analysis from TO for wing ribs

Design Implementation	Reasoning from TO
Minimum Material Distribution in Centre	From Figure 18, minimal material distribution in the centre is observed, which is supported by very thin I-Beams. Thus, a cut out in the centre of wing rib can be used to reduce weight, there will still be significant weight distribution above and below the cut-out, for structural support.
Thick Material Distribution at Tip	The majority of material is distributed towards the tip of the rib, which demonstrates its structural significance, in the CAD design significant amount of material is allocated towards the tip.
Circular support and material distribution towards on the left side	A circular support structure can be seen on the left side rib, as well as heavier material distribution than the centre. Therefore, a small circular cut out is used in the design.
Two Circular holes	Two circular holes are needed for stringer.

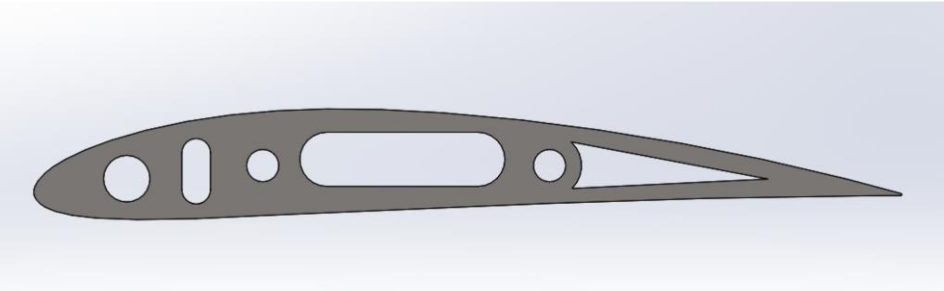

Figure 21: Front view of optimized wing rib

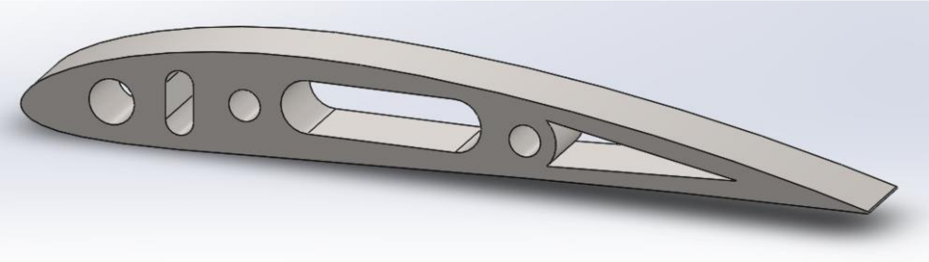

Figure 22: Isometric view of Optimized Wing Rib

Table 8: Design decisions with analysis from TO for wing

Design Implementation	Reasoning from TO
Dual-Spar	A large spar like support can be interpreted from Figures 10,11 and 14. TO suggest the spar should be tapered and decrease in length towards the tip, this is since the bending moment is largest closest to the root. This analysis in impractical to implement into a design that can be manufactured, as constructing a specialised spar that is tapered will increase cost, therefore an ordinary spar that is uniform in thickness will be used. Furthermore, Figure 14 provided evidence of two spars in close proximity to each other, this was implemented in our design, distributing the load across two structures can decrease the probability of failure.
Stringers	Stringers are present in Figures 13, 15 and 16. All evidence of stringers suggests rods are uniformly thin across the wingspan. Stringer are necessary to provide structural connectivity, which is evident Figure 10 where stringer are so closely attached to ribs they appears to be one structure.
Variable rib distribution	Wing ribs appeared most frequently in TO results, with ribs clearly present in Figures 11,13,14 and 15. Figure 11 suggests variable rib distribution with ribs clustered towards the root, to provide maximum support where element density is highest, the number of ribs and proximity decrease towards the wing ribs. This design is practical from a cost and structural prospective. Using ribs only where they are necessary will mean only the minimum number of ribs have to be produced and used, whereas having ribs spread uniformly will result in ribs in areas where they are not required. Ribs are placed 0.12m from each other towards the root, and 0.56 meters from each other towards the tip.

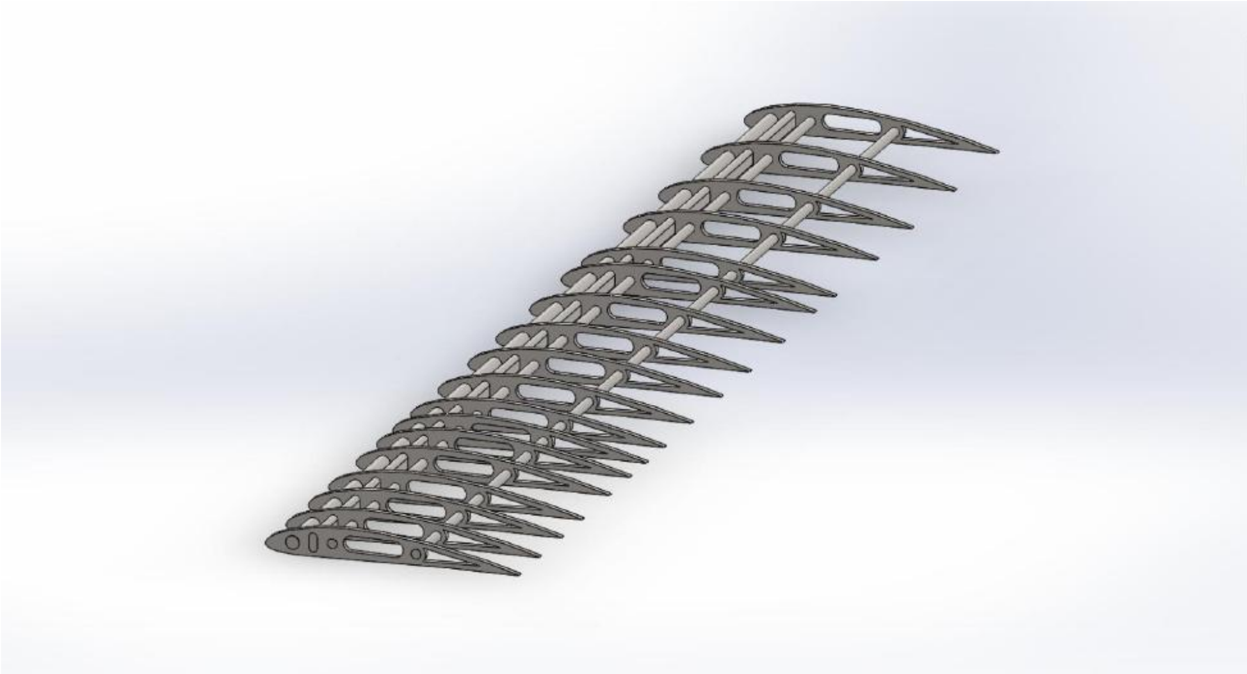

Figure 23: Isometric view of optimized wing structure

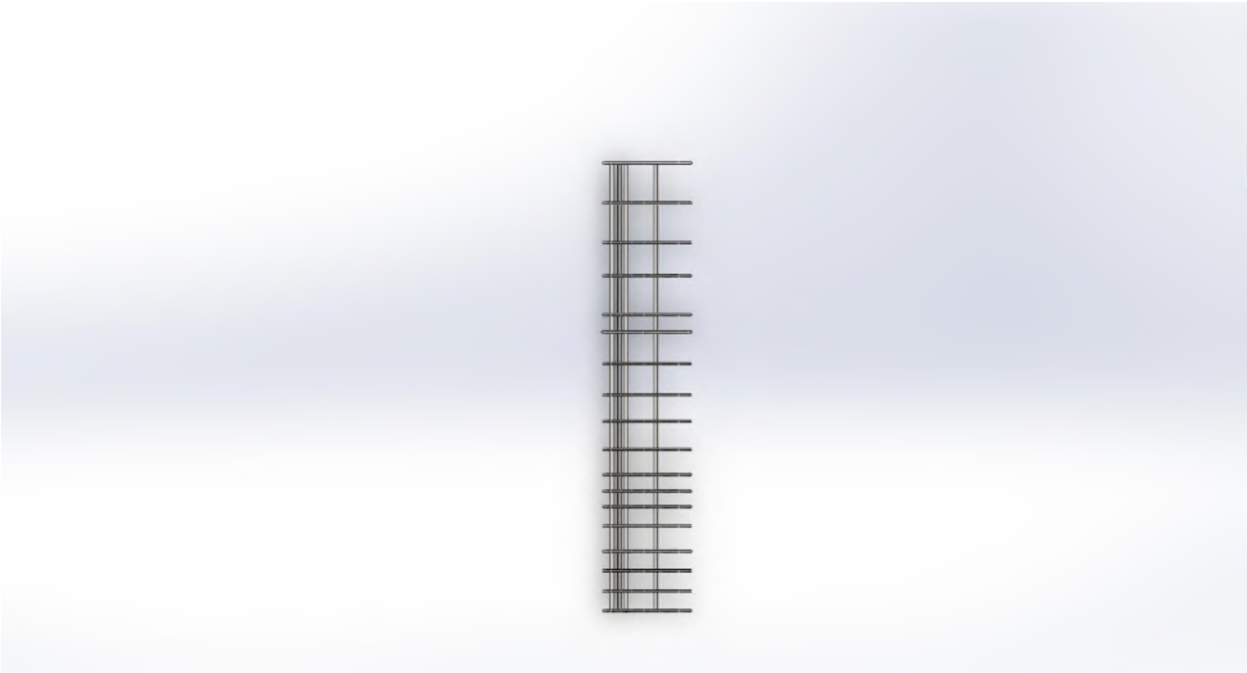

Figure 24: Top view of internal structure of wing demonstrating variable rib distribution

2.6. Conclusion

Optimisation was successfully performed using Altair's Opti Struct solver, with the objective being to minimise the weight while optimising structural strength. Clear structural components can be seen from the simulations, which we can use to make informed decisions regarding the internal material distribution for the wing. One of the primary objectives was to identify structural wing elements such as ribs, spars, and stringers, which was achieved.

The second aspect of the study focused on optimising the shape of the wing ribs. The results showcased I beams in the centre of the wing rib, with truss like structures close to the tip of the wing, where most of the material was distributed. The study proved optimisation of wing ribs can result in further weight savings, whilst maintaining structural integrity. Analysis of the results of the TO were interpreted to design an optimised internal structure of the wings in Soildworks.

In terms of improving the results achieved, and future work various measures can be taken. Firstly, the optimisation framework used did not consider twisting forces, thus our optimisation converged to a solution which only considers bending moment. This is inaccurate as significant twisting forces can be present during flight. In the future, having an optimisation framework which considers multiple factors such as torsion, bending moment and different flight conditions will converge to a more accurate solution. Additionally, using a more powerful computer would allow for smaller mesh element size improving the accuracy of our results.

Whilst structural components have been successfully identified, the next step would have been to run shape and size optimisations to investigate the optimum location for components, i.e., determining the optimum angle and location to place ribs and spars would increase structural strength with zero weight increase.

3. Morphing Wingtip - Mark Lapitan (170208279)

3.1. Introduction

3.1.1 Aims and objectives

The aims of this section are to investigate and analyse the aerodynamic characteristics of a morphing wingtip, to demonstrate the benefits of morphing and to analyse the 3D wing structure created in Solidworks by performing static and modal analysis, by using Ansys Fluent.

To achieve the aims for this analysis, the following objectives will be completed:

- To model and simulate the dynamics equations of the morphing wingtip by using MATLAB & Simulink and understand the response given by the Simulink diagram.
- To understand the dynamic behaviours and characteristics of structures when performing modal analysis
- To perform mesh convergence on the total deformation, stress and strain of the results obtained in Ansys Fluent.

3.1.2 Rationale

The idea of manipulating the geometry or shape of a wing, started with the Wright Brothers' airplane, where actuating cables were used to change the twist of the wings thus, enabling the pilot to control roll (Barbarino et al., 2011). The design of a conventional fixed wing UAV restricted the potential benefits that could be obtained by using a more variable or deformable wing. In today's modern era, most UAVs have implemented morphing wings to enhance flight performance at different stages of flight (Gamboa et al., 2007). The primary purpose of implementing morphing devices into air vehicles was to solve the design conflicts that arise between high and low speed flight, where the aircraft transitions into the following speed regimes: Transonic, supersonic, and hypersonic (Weisshaar, 2013). The proposed UAV morphing wing concept is a promising design that will allow the UAV to enhance flight performance under different flight conditions; this configuration will essentially increase the aspect ratio (AR) during climb as well as decrease drag during cruise. The morphing wingtip will consist of a hinge mechanism which is controlled by an actuating system.

3.2 Background theory

3.2.1. Morphing

3.2.1.1. Morphing applications

The main aim of implementing morphing in UAVs is to efficiently and effectively complete multi-objective mission roles thus, increasing the cost effectiveness of manufacturing multiple mission specific aircraft. Based on Friswell and Inman (2006), there are four applications of morphing:

- To enhance flight performance
- To improve range by decreasing drag
- To control flutter
- To increase stealth and flight control

To achieve these effects, the UAV will need to undergo shape change for each application as it will require different types of morphing.

3.2.1.2. Morphing types and mechanisms

According to Juan Carlos Gomez and Garcia (2011), shape morphing of a structured wing can be classified into three major categories, which are: Planform alteration, out of plane transformation and aerofoil adjustment. These categories will involve the change or manipulation of the parameters shown in the image below.

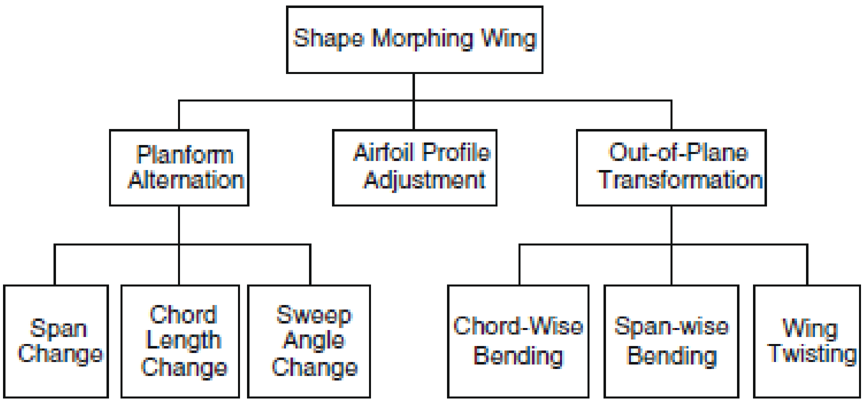

Figure 25: Morphing categories (A Y N Sofla et al., 2010)

3.2.1.2.1. Planform alteration

Planform alteration involves the change of span, chord length and sweep angle; each parameter will involve a different geometric alteration, these are shown in Figure 26.

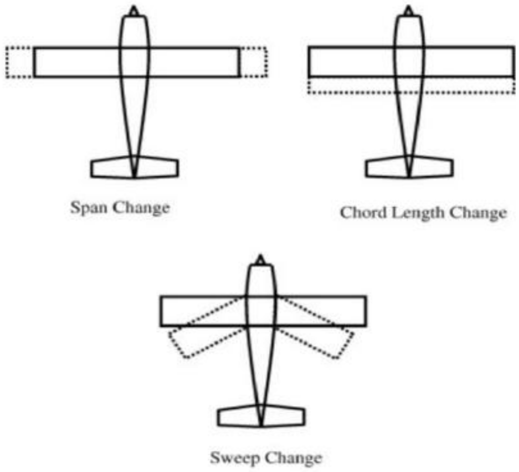

Figure 26: Planform alteration (A Y N Sofla et al., 2010)

Firstly, the variable wingspan is used to enhance flight performance and improve the overall manoeuvrability of the UAV. According to Barbarino et al. (2011), increasing the wingspan, increases the aspect ratio and wing area, resulting in an increase in lift and decrease in drag due to the decrease of spanwise lift distribution for the same lift. As a result, the endurance and range of the UAV is significantly enhanced. Although it provides these benefits, wing-root bending moment could potentially increase due to the increase in wingspan, thus aerodynamic and aeroelastic characteristics should be considered during the designing phase. Whereas by decreasing the wingspan, the UAV will increase its manoeuvrability as well as its speed at cruise condition (Ajaj et al., 2012).

The system used for this type of morphing is the telescopic mechanism which includes the following key components: several actuators that are used to change the wingspan and its control system, a system of structural elements to support aerodynamic loads of the wing and a type of skin that allows the transformation whilst maintaining the shape of the wing. This transformation is shown in the figure below (Samuel and Pines, 2007).

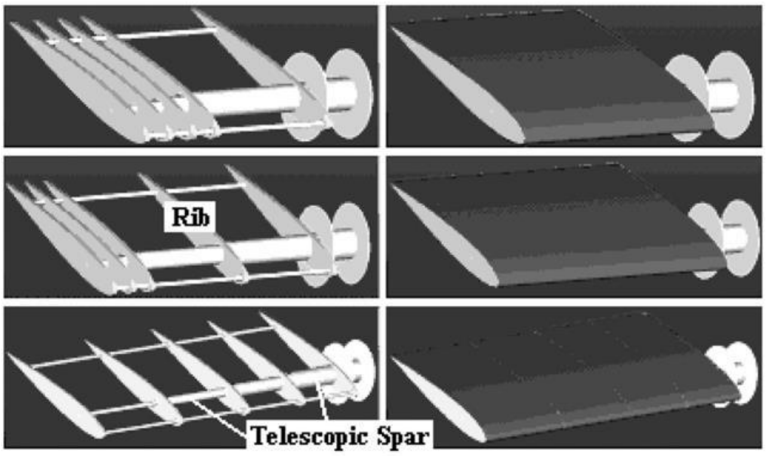

Figure 27: Telescopic mechanism (Samuel and Pines, 2007)

Secondly, the chord length morphing is used to decrease the drag developed on a wing, to increase lift and lift to drag ratio by increasing the chord length of the wing; achieved by removing the gap and maintaining the smoothness of the wing's surface. This is usually caused due to leading or trailing edge flaps, which are used for conventional aircraft to increase chord length, Figure 28 displays the chord morphing (Zaini and Ismail, 2016).

The mechanism used for this morph is the rack and pinion actuation system which is powered by stepper motors; similarly, to the wingspan morphing, a skin that enables the transformation without compromising the shape of the wing is required.

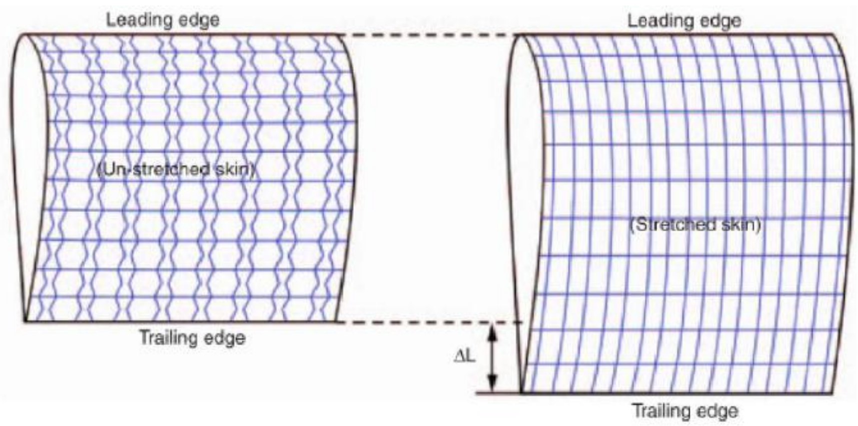

Figure 28: Chord morphing (Zaini and Ismail, 2016)

Finally, according to Zaini and Ismail (2016), sweep morphing is used to enhance flight performance and the lift to drag ratio, which is achieved by adjusting the sweep angle. This allows the UAV to meet different requirements for different flight conditions such as: take-off, climb, cruise, and descent as the AR and wing area is changed to enable an efficient operation.

Similarly, to the chord morphing, the rack and pinion mechanism could be used, this will allow the wings to move backwards when the servo motor moves forwards. This is due to the moment produced from the hinge on the servo, which is caused when the servo moves through the track, this is shown in Figure 29 (Prabhakar, Prazenica and Gudmundsson, 2015).

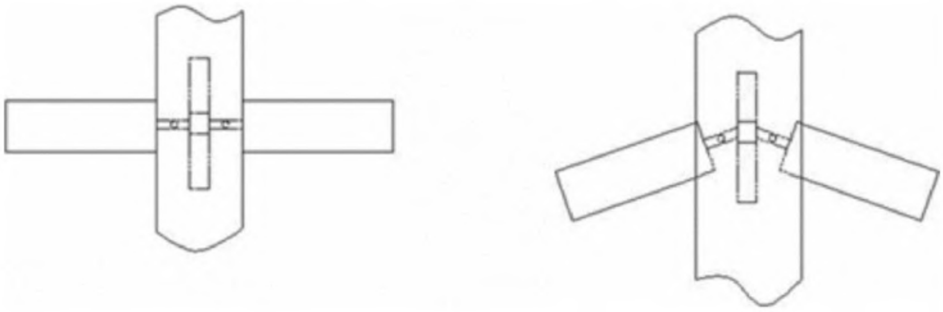

Figure 29: Sweep morphing (Prabhakar, Prazenica and Gudmundsson, 2015)

3.2.1.2.2. Aerofoil adjustment

Aerofoil adjustment is used to control the aerodynamic loading, when transitioning from laminar to turbulent flow; it involves the change of the wing profile, in this case thickness, which does not impose a significant change in the wing camber (Hee, 2012). The mechanism used for aerofoil adjustment involve linear translational actuators and skin that allows the deformation without undergoing deformation, where the actuators will allow the expansion and contraction of the deformation (Austin et al., 1994).

3.2.1.2.3. Out of plane transformation

Out of plane transformation involves wing twisting, chord and spanwise bending, these transformations are shown in Figure 30.

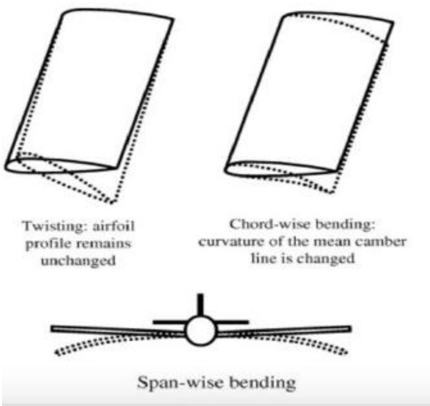

Figure 30: Out of plane transformation (A Y N Sofla et al., 2010)

Firstly, wing twisting morphing is used to enhance the control ability of the UAV, which provides effective roll, yaw, and pitch control. Furthermore, by varying the twist, the UAV can provide a greater coefficient of lift compared to a baseline wing. According to Detrick and Washington (2012), the system used involves the kinematic mechanism and piezoelectric actuator; the rib sections of the wing will be connected by hinges, enabling the rotation of the arms due to its moment, this is shown in Figure 31.

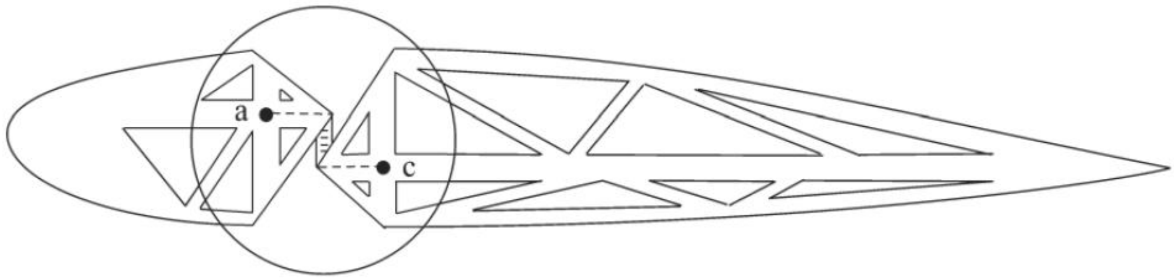

Figure 31: Twisting morphing (Detrick and Washington, 2012)

Secondly, chord wise bending is used to enhance and provide better control and roll authority compared to ailerons; by changing the curvature of the mean camber line, the wing's surface will be smooth and continuous, thus reducing the aerodynamics loses as well as decreasing power consumption (Zaini and Ismail, 2016). Similarly, span wise bending is also used to enhance flight performance and control of the UAV; controlling the spanwise bending could potentially decrease the induced drag and improve lateral stability, as well as stall characteristics. The mechanism used for this morph is the use of active materials that act as an actuator, which can be activated by using either thermal or electrical input to activate the bending process.

3.2.1.3. Use of structures and materials to implement morphing

According to Sun et al. (2016) study, the implementation of traditional materials and structures in morphing resulted in an increase of cost and maintenance hours, this is due to the heavy and complex structures that was required to perform the morphing. Therefore, to overcome this problem, smart materials and structures were considered due to their adaptive capabilities. The following advantages proves that smart materials are a viable option to be used for the morphing:

- High energy density
- Ease to control
- Variable stiffness
- The ability to tolerate large amounts of strain

3.2.1.3.1 Material

The material for the morphing skin of a wing needs to have the sufficient robustness to support the aerodynamic loads experienced due to the flight speed increase, as well as being able to withstand the combination of the following forces: compression, tensile and compression forces (Etches et al., 2008). In addition, high strain capabilities and recovery rates are needed to maintain the shape of the wing after morphing is performed. As mentioned previously, smart materials have the capabilities to meet the requirements needed for the morphing wing.

The most common smart materials that could be used for the skin are shape memory alloys and polymers, and electro-active polymers. Firstly, shape memory alloys, known as SMA, is a metallic alloy which has a shape memory effect ability, this is triggered by applying heat, enabling the material to return to its original shape after deformation. Furthermore, it is a highly elastic material, meaning that it can support a greater applied load without undergoing plastic deformation or failure.

Similarly, shape memory polymers, known as SMP, have similar capabilities and has the shape memory effect but, this ability can only be triggered by external stimulus such as electricity and light. Although it only exhibits a macroscopic recovery; during this stage the material transitions from a glassy to an elastic state and the stiffness of the material changes from high to a low Youngs Modulus. This change makes it suitable to be used as a morphing skin as the glassy state could withstand aerodynamic loads and the elastic state could allow high deformations (Sun et al., 2016).

Finally, electro-active polymer, known as EAP, by applying electricity, the material can undergo a significant geometric change, where the strain can be up to 300%.

3.2.1.3.2. Structures

The structure to implement morphing wingtips requires to be light, load-carrying and shape adaptable (Wang et al., 2016). According to Sun et al. (2016), there are two structure that can meet these requirements: multi-stable structures and corrugated structures. Multi-stable structures have multiple stable states and can transition between states at a rapid rate; this change occurs when the structure is stimulated. Whereas corrugated structures are suitable for folding and bending due to its great expansion or contraction.

3.2.1.3.1. Controlled Hinge mechanism: Active hinge stiffness

According to Kidane and Troiani (2020), there are three possible concepts that will actuate the folding winglet mechanism, these are: hinge line actuator, system of pulley gears, and a worm gear system. The hinge line actuator concept 1 aims to develop the required rotational torque by using hinge line actuators, this is seen in Figure 32; due to the required space and location of the actuator, the winglet area is compromised as well as the safety of the actuation system, as the likelihood of damage is increased due to its exposure when landing or taking off (Mills and Ajaj, 2017).

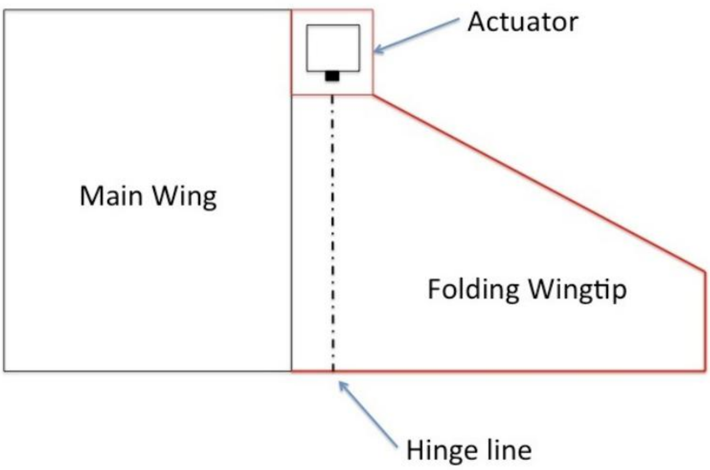

Figure 32: Hinge line actuators (Mills and Ajaj, 2017)

Whereas the system of pulley gears concept 2 aims to maximise the winglet area by incorporating the actuation components inboard, this is shown in Figure 33; the actuation torque to the hinge line is transferred by using the system of timing pulley and belts. Although, frequent maintenance is required to ensure the belt tensioning leading to an increase of cost due to its maintenance.

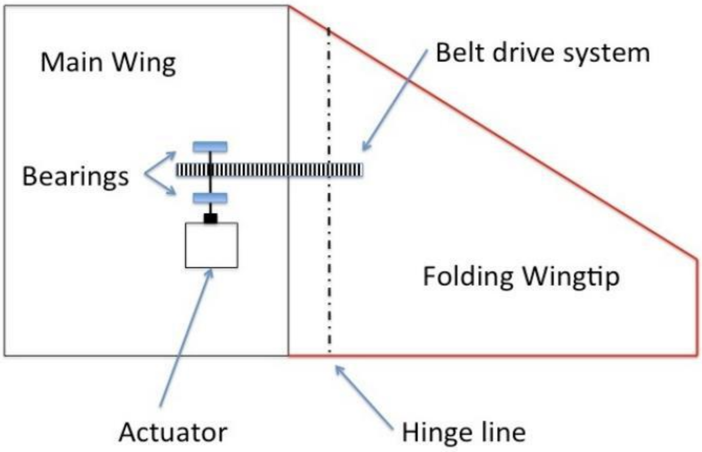

Figure 33: System of pulley gears (ibid)

Similarly, to the system of pulley gears concept 2, the worm gear system concept 3 also aims to maximise the winglet area; the torque is transferred by using the worm drive which acts to gear the system and thus, developing greater torques as shown in Figure 34. This will allow the use of smaller and less powerful actuators, thus reducing the cost of the system.

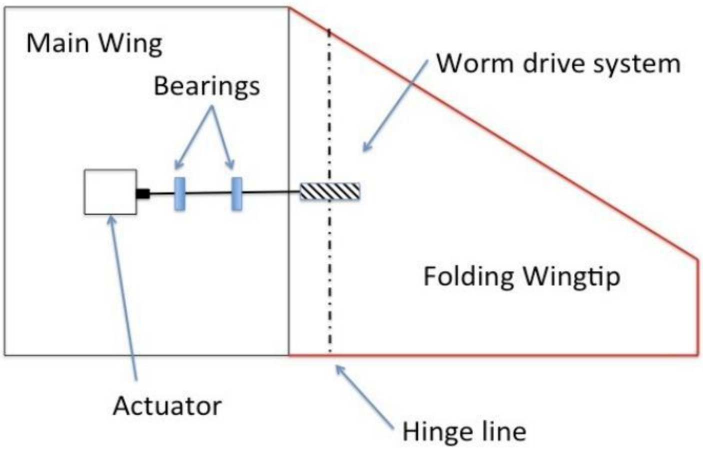

Figure 34: Worm gear system (ibid)

3.2.1.4. Aerodynamics of wingtip

3.2.1.4.1 Aerodynamics of Morphing Wingtips: The Quasi steady approach

To start with, the aerodynamics of the morphing wingtip differs from that of a conventional aircraft, this is due to the centre of mass not being coincident with the body-frame origin. To model this, the morphing UAV requires to be treated as a single body, but relaxing the condition of rigidity, meaning that the centre of mass and inertia tensor varies. According to Yang et al. (2020), the centroid dynamics equation can be expressed by Equation (24) and (25); knowing that the centre of mass of the initial configuration is the body frame origin.

$$m\dot{V}_b = F_E - m[\overline{\omega}]V_b + F_{ext} \tag{24}$$

$$J\dot{\omega} = M_E - [\overline{\omega}]J\omega + M_{ext} \tag{25}$$

In addition to this, the restraining forces and moments need to be considered and subtracted from the previous equation to achieve equilibrium and complete the dynamics of the morphing wingtip. By assuming an incompressible flow-field, the governing dynamical equation of a typical aerofoil section given in Equation (26), can be used to derive the equation of motion in the absence of any external disturbances, where the restraining forces are structural spring forces and aerodynamic lift.

$$\begin{bmatrix} 1 & x_\alpha \\ x_\alpha & \dfrac{I_\alpha}{mb^2} \end{bmatrix} \begin{bmatrix} \dfrac{\ddot{h}}{b} \\ \ddot{\alpha} \end{bmatrix} + \begin{bmatrix} \dfrac{k_h}{m} & 0 \\ 0 & \dfrac{k_\alpha}{mb^2} \end{bmatrix} \begin{bmatrix} \dfrac{h}{b} \\ \alpha \end{bmatrix} + \frac{1}{\mu}\left(\widetilde{M_a} \begin{bmatrix} \dfrac{\ddot{h}}{b} \\ \ddot{\alpha} \end{bmatrix} + \widetilde{C_a} \begin{bmatrix} \dfrac{\dot{h}}{b} \\ \dot{\alpha} \end{bmatrix} + \widetilde{K_a} \begin{bmatrix} \dfrac{h}{b} \\ \alpha \end{bmatrix} \right) = \begin{bmatrix} 0 \\ 0 \end{bmatrix} \tag{26}$$

(Where h(y)/b is the non-dimensional plunging degree of freedom at the section; α(y) is the pitching degree of freedom at the section)

Where the dynamic inertia ($\widetilde{\mathrm{M}_a}$), the aerodynamic stiffness ($\widetilde{\mathrm{C}_a}$) and aerodynamic damping matrices ($\widetilde{\mathrm{K}_a}$) are shown by the equations below.

$$\widetilde{M_a} = \begin{bmatrix} 1 & -a \\ -a & \left(a^2 + \frac{1}{8}\right) \end{bmatrix} \tag{27}$$

$$\widetilde{C_a} = \frac{U}{b}\begin{bmatrix} 0 & 1 \\ 0 & 1 - \left(\frac{1}{2} + a\right) \end{bmatrix} + 2\frac{U}{b}C(k)\begin{bmatrix} 1 \\ -\left(\frac{1}{2} + a\right) \end{bmatrix}\begin{bmatrix} 1 & \left(\frac{1}{2} - a\right) \end{bmatrix} \tag{28}$$

$$K_a = 2C(k)\left(\frac{U}{b}\right)^2 \begin{bmatrix} 1 \\ -\left(\frac{1}{2} + a\right) \end{bmatrix}\begin{bmatrix} 0 & 1 \end{bmatrix} \tag{29}$$

By assuming pure plugging and quasi steady strip theory, the following two parameters α and $\frac{h}{b}$ are replaced by $[\theta_j(y)]\ \alpha$ and $[\eta_j(y)]h/b$. Giving the equation below.

$$m\begin{bmatrix} 1 & x_\alpha \\ x_\alpha & r_\alpha^2 \end{bmatrix}\begin{bmatrix} [\eta_j(y)]\frac{\ddot{h}}{b} \\ [\theta_j(y)]\ \ddot{\alpha} \end{bmatrix} + \begin{bmatrix} K_h & 0 \\ 0 & K_\alpha \end{bmatrix}\begin{bmatrix} [\eta_j(y)]\frac{h}{b} \\ [\theta_j(y)]\ \alpha \end{bmatrix} + m\begin{bmatrix} \bar{L}b \\ \bar{M} \end{bmatrix} = \begin{bmatrix} 0 \\ 0 \end{bmatrix} \tag{30}$$

Where $\begin{bmatrix} \bar{L}b \\ \bar{M} \end{bmatrix}$ is represented by the equation below.

$$\begin{bmatrix} \bar{L}b \\ \bar{M} \end{bmatrix} = \frac{1}{\mu}\left(\widetilde{M_a}\bar{U}^2 \begin{bmatrix} [\eta_j(y)]\frac{\ddot{h}}{b} \\ [\theta_j(y)]\ddot{\alpha} \end{bmatrix} + \widetilde{C_a}\bar{U}^2 \begin{bmatrix} [\eta_j(y)]\frac{\dot{h}}{b} \\ [\theta_j(y)]\dot{\alpha} \end{bmatrix} + \widetilde{K_a}\bar{U}^2 \begin{bmatrix} [\eta_j(y)]\frac{h}{b} \\ [\theta_j(y)]\alpha \end{bmatrix} \right) \tag{31}$$

Subsequently, Equation (32) is obtained by multiplying the first equation by $\eta_i(y)$ and the second equation by $\theta_i(y)$, which is then integrated over the span.

$$m\begin{bmatrix}\langle\eta^2\rangle & \langle\eta,\theta\rangle x_\alpha\\ \langle\eta,\theta\rangle x_\alpha & \langle\theta^2\rangle r_\alpha^2\end{bmatrix}\begin{bmatrix}\frac{\ddot{h}}{b}\\ \ddot{\alpha}\end{bmatrix}+\begin{bmatrix}K_h\langle\eta^2\rangle & 0\\ 0 & K_\alpha\langle\theta^2\rangle\end{bmatrix}\begin{bmatrix}\frac{h}{b}\\ \alpha\end{bmatrix}+m\begin{bmatrix}\langle\bar{L}b,\eta\rangle\\ \langle\overline{M},\theta\rangle\end{bmatrix}=\begin{bmatrix}0\\0\end{bmatrix} \quad (32)$$

$\begin{bmatrix}\bar{\mathrm{L}}\mathrm{b}\\ \overline{\mathrm{M}}\end{bmatrix}$ can be expressed similarly to Equation (31) by using the matrices and vectors shown below.

$$\langle\eta^2\rangle=\frac{1}{s}\int_0^s\eta_i(y)\,\eta_j(y)dy \quad (33)$$

$$\langle\eta,\theta\rangle=\frac{1}{s}\int_0^s\eta_i(y)\,\theta_j(y)dy \quad (34)$$

$$\langle\theta^2\rangle=\frac{1}{s}\int_0^s\theta_i(y)\,\theta_j(y)dy \quad (35)$$

$$\langle\bar{L}b,\eta\rangle=\frac{1}{s}\int_0^s\bar{L}b\,\eta_i\,(y)dy \quad (36)$$

$$\langle\overline{M},\theta\rangle=\frac{1}{s}\int_0^s\overline{M}\,\theta_i\,(y)dy \quad (37)$$

Subsequently, these are then multiplied and integrated over the span, giving the equation below.

$$\begin{bmatrix}\langle\eta,\bar{L}b\rangle\\ \langle\theta,\overline{M}\rangle\end{bmatrix}=\frac{1}{\mu}\left(\widetilde{M_a}\overline{U}^2\begin{bmatrix}\frac{\ddot{h}}{b}\\ \ddot{\alpha}\end{bmatrix}+\widetilde{C_a}\overline{U}^2\begin{bmatrix}\frac{\dot{h}}{b}\\ \dot{\alpha}\end{bmatrix}+\widetilde{K_a}\overline{U}^2\begin{bmatrix}\frac{h}{b}\\ \alpha\end{bmatrix}\right) \quad (38)$$

Where the $(\widetilde{M_a}\overline{U}^2)$, $(\widetilde{C_a}\overline{U}^2)$ and $(\widetilde{K_a}\overline{U}^2)$ are shown by the equations below.

$$\widetilde{M_a}\bar{U}^2 = \begin{bmatrix} \langle\eta^2\rangle & -a\langle\eta,\theta\rangle \\ -a\langle\eta,\theta\rangle & \left(a^2+\frac{1}{8}\right)\langle\theta^2\rangle \end{bmatrix} \tag{39}$$

$$\widetilde{C_a}\bar{U}^2 = \bar{U}\begin{bmatrix} 0\langle\eta^2\rangle & \langle\eta,\theta\rangle \\ 0\langle\eta,\theta\rangle & \left(\frac{1}{2}-a\right)\langle\theta^2\rangle \end{bmatrix} + \frac{\bar{U}}{2}\begin{bmatrix} 4\langle\eta^2\rangle & 2(1-2a)\langle\eta,\theta\rangle \\ -2(1+2a)\langle\eta,\theta\rangle & -(1+2a)(1-2a)\langle\theta^2\rangle \end{bmatrix} \tag{40}$$

$$K_a\bar{U}^2 = \bar{U}^2\begin{bmatrix} 0\langle\eta^2\rangle & 2\langle\eta,\theta\rangle \\ 0\langle\eta,\theta\rangle & -(1+2a)\langle\theta^2\rangle \end{bmatrix} \tag{41}$$

Assuming that the wing is only oscillating in two plunging modes, the first bending mode can be represented by Equation 42:

$$\eta_1 = \left(\frac{y}{s}\right)^2 - \frac{2(n-1)}{n+1}\left(\frac{y}{s}\right)^{n+1} + \frac{n(n-1)}{(n+2)(n+1)}\left(\frac{y}{s}\right)^{n+2}, \text{with } n = 2 \tag{42}$$

and the gull-wing or canted wing mode is represented by,

$$\eta_2 = \frac{(y-y_h)}{(s-y_h)}, \qquad y_h \le y \le s, \eta_2 = 0, 0 \le y \le y_h \tag{43}$$

The first bending mode can be approximated as shown in Equation (44); assuming that the oscillations are small in amplitude and that there is no torsion mode.

$$\eta_1 = \left(\frac{y}{s}\right)^2 - \frac{2}{3}\left(\frac{y}{s}\right)^3 + \frac{1}{6}\left(\frac{y}{s}\right)^4, \text{with } \theta_1 = 0 \tag{44}$$

By defining the following,

$$\langle \eta_1^2 \rangle = \frac{1}{s}\int_0^s \eta_i(y)\,\eta_j(y)dy = \int_0^s \left(\left(\frac{y}{s}\right)^2 - \frac{2}{3}\left(\frac{y}{s}\right)^3 + \frac{1}{6}\left(\frac{y}{s}\right)^4\right)^2 d\left(\frac{y}{s}\right) =$$

$$= \frac{1}{5} + \frac{4}{63} + \frac{1}{324} + \frac{1}{21} - \frac{2}{9} - \frac{1}{36} = \frac{26}{405} = J_{11} \tag{45}$$

$$\langle \eta, \theta \rangle = \frac{1}{s}\int_0^s \eta_i(y)\,\theta_j(y)dy = \int_0^s 0\ \times \left(\left(\frac{y}{s}\right) - \frac{1}{2}\left(\frac{y}{s}\right)^2\right) d\left(\frac{y}{s}\right) = 0,$$

$$\frac{1}{s}\int_0^s \eta_i(y)\ dy = \frac{1}{5}, \frac{1}{s}\int_0^s \theta_i(y)\ dy = 0 \tag{46}$$

$$\langle \theta^2 \rangle = \frac{1}{s}\int_0^s \theta_i(y)\,\theta_j(y)dy = 0 \tag{47}$$

$$\langle \eta_2 \rangle = \frac{1}{s}\int_0^s \eta_j(y)dy = \frac{s-y_h}{s}\int_{y=y_h}^{y=s} \left(\frac{y-y_h}{s-y_h}\right) d\left(\frac{y-y_h}{s-y_h}\right) =$$

$$= \frac{1}{2}\frac{s-y_h}{s}\left(\frac{s-y_h}{s-y_h}\right)^2 = \frac{1}{2}\frac{s-y_h}{s} = J_2 \tag{48}$$

$$\langle \eta_1 \times\ \eta_2 \rangle = \frac{1}{s}\int_0^s \eta_i(y)\,\eta_j(y)dy = \int_{y=y_h}^{y=s} \left(\left(\frac{y}{s}\right)^2 - \frac{2}{3}\left(\frac{y}{s}\right)^3 + \frac{1}{6}\left(\frac{y}{s}\right)^4\right)\ d\left(\frac{y}{s}\right) = J_{12} \tag{49}$$

The exact integral evaluation is shown in Equation (50),

$$\langle \eta_2 \times\ \eta_2 \rangle = \frac{1}{s}\int_0^s \eta_i(y)\,\eta_j(y)dy = \frac{s-y_h}{s}\int_{y=y_h}^{y=s} \left(\frac{y-y_h}{s-y_h}\right)^2 d\left(\frac{y-y_h}{s-y_h}\right) =$$

$$\frac{s-y_h}{3s}\left(\frac{s-y_h}{s-y_h}\right)^3 = \frac{s-y_h}{3s} = J_{22} \tag{50}$$

Thus, the equation of motion in the absence of any external disturbance can be represented by,

$$\begin{bmatrix} J_{11} & J_{12} \\ J_{12} & J_{22} \end{bmatrix} \begin{bmatrix} \frac{\ddot{h}_1}{b} \\ \frac{\ddot{h}_2}{b} \end{bmatrix} + \frac{1}{m} \begin{bmatrix} J_{11} & J_{12} \\ J_{12} & J_{22} \end{bmatrix} \begin{bmatrix} \frac{k_{h1} h_1}{b} \\ \frac{k_{h2} h_2}{b} \end{bmatrix} + \frac{1}{\mu} \left(\widetilde{M_a} \begin{bmatrix} \frac{\ddot{h}}{b} \\ \ddot{\alpha} \end{bmatrix} + \widetilde{C_a} \begin{bmatrix} \frac{\dot{h}}{b} \\ \dot{\alpha} \end{bmatrix} + \widetilde{K_a} \begin{bmatrix} \frac{h}{b} \\ \alpha \end{bmatrix} \right) = \frac{L_g b}{5} \begin{bmatrix} 1 \\ 5J_2 \end{bmatrix} \tag{51}$$

Where the dynamic inertia ($\widetilde{M_a}$), the aerodynamic stiffness ($\widetilde{C_a}$) and aerodynamic damping matrices ($\widetilde{K_a}$) are shown by the equations below.

$$\widetilde{M_a} = \begin{bmatrix} J_{11} & J_{12} \\ J_{12} & J_{22} \end{bmatrix} \tag{52}$$

$$\widetilde{C_a} = 2\bar{U} \begin{bmatrix} J_{11} & J_{12} \\ J_{12} & J_{22} \end{bmatrix} \tag{53}$$

$$K_a = \bar{U}^2 \begin{bmatrix} 0 & 0 \\ 0 & 0 \end{bmatrix} \tag{54}$$

By rearranging, F can be obtained as,

$$m \begin{bmatrix} \frac{\ddot{h}_1}{b} \\ \frac{\ddot{h}_2}{b} \end{bmatrix} = F = - \begin{bmatrix} \frac{k_{h1} h_1}{b} \\ \frac{k_{h2} h_2}{b} \end{bmatrix} + \frac{m}{\mu} \left(\begin{bmatrix} \frac{\ddot{h}}{b} \\ \ddot{\alpha} \end{bmatrix} + 2\bar{U} \begin{bmatrix} \frac{\dot{h}}{b} \\ \dot{\alpha} \end{bmatrix} \right) + \frac{mb}{5} \begin{bmatrix} J_{11} & J_{12} \\ J_{12} & J_{22} \end{bmatrix}^{-1} \begin{bmatrix} 1 \\ 5J_2 \end{bmatrix} L_g \tag{55}$$

(Where k_{h1} is the wing stiffness in the first bending mode; k_{h2} is the hinge-stiffness in the canted wing mode)

3.2.2. Structural analysis

3.2.2.1. Modal analysis

According to Karabulut (2021), modal analysis is a technique that can be used in ANSYS fluent to analyse the dynamic behaviour and characteristics of structures; it outlines the limit of the system's responses. It is considered as the most fundamental of all dynamic analysis as well as being the basis of other dynamic analysis such as harmonics, response spectrum and random vibration. The aims of using modal analysis are:

- To determine the mode shapes and natural frequencies of the system
- To determine if there are rigid modes in the system by evaluating the connections between components
- To determine the correct constraints of the system
- To determine the system's behaviour under dynamic loads

Modal analysis calculates the frequency at which the amplitude goes to infinity; this occurs when the frequency vibrates close to the resonant frequency (ibid). The natural frequencies and their respective mode shapes (such as bending, torsion mode) can be determined by using the linear equation of motion for free undamped vibration (Ansys, 2022).

$$[M][\ddot{U}] + [K][U] = [0] \tag{56}$$

(Where [M] is the mass matrix; $[\ddot{U}]$ is the acceleration; [K] is the stiffness matrix; [U] is the displacement)

By assuming harmonic motion [U] and $[\ddot{U}]$ can be expressed by the following equations.

$$[U] = \varphi \sin(\omega t - \theta) \tag{57}$$

$$[\ddot{U}] = -\varphi\omega^2 \sin(\omega t - \theta) \tag{58}$$

Subsequently, the eigenvalue problem can be obtained by substituting Eq (57) and (58) into Eq(56),

$$([K] - \omega^2[M])\ \varphi = 0 \tag{59}$$

By solving the first part of this equation, which is $([K] - \omega^2[M])$ the natural frequency can be obtained and by solving the second part, which is φ the mode shapes can be determined. Where the eigenvalues are ω^2(the natural frequency) and the eigenvectors are φ (mode shapes). Thus, the natural frequency can be obtained by using the following equation

$$f_i = \frac{\omega_i}{2\pi} \tag{60}$$

(Where the eigenvectors represent the mode shapes at frequency f_i)

3.3. Designed eVTOL UAV

3.3.1 Selected morphing and mechanism

Based on the UAV's application, which involve the UAV to search for survivals and drop supplies, the most suitable category for the EVTOL UAV would be planform alteration; the parameter involved is the span. The benefits of changing the span are that the range and endurance are increased thus, enhancing flight performance. This is essential as it will increase the search radius and thus, increasing the chances of success.

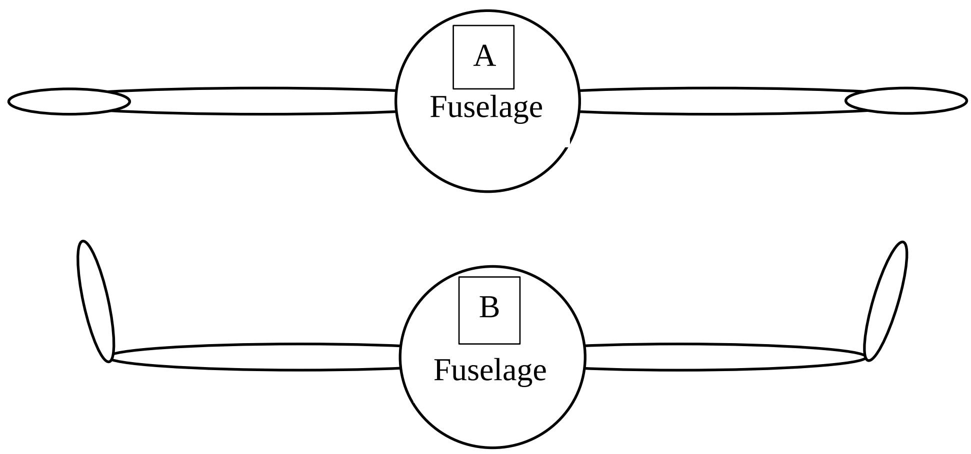

Figure 35: (A) Fully extended wingtips and (B) morphed wingtips

The change of span will be achieved by morphing the wingtip, this will consist of two forms (A) and (B), as shown in Figure 35; (A) will be during climb and descent stage and (B) will be during the cruise stage.

This will create a new geometry whilst maintaining high aerodynamic performance; as a result, the AR will change affecting the climb rate, stall angle and lateral stability. As well as enhancing the overall control when the eVTOL is in form (B), as it will eliminate the presence of wingtip vortices, thus reducing the possibility for the wingtip to stall. Stall is an aerodynamic condition in which results in flow separation and leads to an abrupt loss of lift and altitude, an increase in drag and in extreme cases losing control of the aircraft completely.

The folding wingtip involves the use of hinges that connect two sections of the wing, allowing the UAV to change its cant angle. As mentioned previously, there are three mechanism that could be used for the morphing wingtip; Figure 36 summarises the advantages and disadvantages of each mechanism.

The pros/cons of each concept are shown in Figure 36.

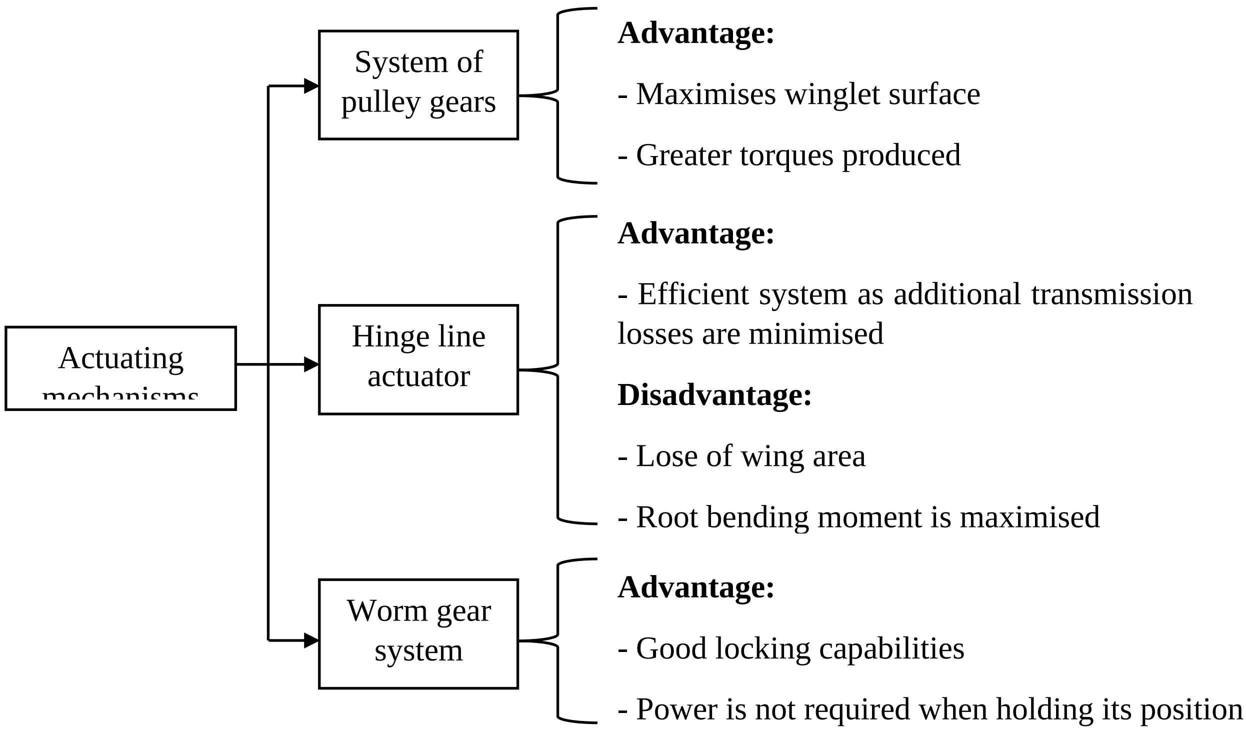

Figure 36: Pros and cons of each concept

As shown below in Table 9, to select the optimal concept, a decision matrix was created where the following requirements were considered based on the eVTOL UAV design: cost, effectiveness, complexity, robustness, and weight. The importance of each requirement was rated from 1 to 5, 1 being the least important and 5 being the most important. This will be then multiplied by how well each concept meet the requirement which will be rated from 1 to 5, 1 being the least and 5 being the best, which will then be summed to obtain the totals. Based on the total scores, concept 3, the worm gear system is the optimal solution to meet these requirements.

Table 9 – Decision matrix

	Cost	**Effectiveness**	**Complexity**	**Robustness**	**Weight**	**Totals**
Importance	3	3	2	2	4	
Concept 1	2	4	4	1	3	40
Concept 2	1	4	4	3	2	37
Concept 3	4	4	4	5	2	50

One important factor that needs to be considered is the space between the tip of the main wing and the root of the winglet; this is a critical region as the gap will enable airflow to escape through thus, reducing the overall efficiency (ibid). To overcome this problem a form of skin could be used to completely cover the region, this will be further explained in the next section.

3.4. Methodology

3.4.1. Morphing Simulation: Simulink and MATLAB approach

3.4.1.1 Calculated Modelling parameters

Table 10 - UAV initial data

Battery	**Value**	**Wing**	**Value**	**Fuselage**	**Value**
Mass (kg)	10.725	Mass (kg)	6	Mass (kg)	10
Length (m)	0.218	Length (m)	2.5	Length(m)	1.77859
Width (m)	0.12			Diameter (m)	0.52272
				Volume (kg/m^3)	0.28743

The position vectors for each component can be taken with respect to a frame of reference centred on the tail of the UAV. These are shown in the table below.

Table 11 - Position vector of each component

Component	Position Vector (m)
Battery	[3.0, 0 , 0.53]
Port wing root	[1.6, 0 , 0.32]
Starboard wing root	[1.6, 0 , 0.32]

3.4.1.2. Inertia tensor

According to Yang et al. (2020) the inertia tensor of the UAV can be represented by

$$J = \begin{bmatrix} I_{xx} & 0 & -I_{xz} \\ 0 & I_{yy} & 0 \\ -I_{xz} & 0 & I_{zz} \end{bmatrix} \tag{61}$$

(Where J is the inertia tensor; I_{xx}, I_{yy}, I_{xz} and I_{zz} are the mass moment of inertia)

To begin with, the centre of mass of the fuselage can be calculated by using the formula below (Smith, 2020)

$$CM_{X-Fuselage} = \frac{\int_0^{1.77859} mpl_{fus} \cdot xdx}{\int_0^{1.77859} mpl_{fus}dx} = \frac{\int_0^{1.77859} \left(\frac{10}{1.77859}\right) x}{\int_0^{1.77859} \frac{10}{1.77859}\ dx} =$$

$$= \frac{[2.8112x^2]_0^{1.77859}}{\left[\frac{10}{1.77859}x\right]_0^{1.77859}} = \frac{8.8929}{10} = 0.8893\ m \tag{62}$$

Therefore, the centre of mass of the fuselage is located at [0.8893, 0, 0]

Subsequently, knowing that the total mass of the system as stated previously is 32kg, the centre of mass can be determined.

Table 12 – Product of masses and its coordinates

Component	$\boldsymbol{m_i \cdot x_i}$	$\boldsymbol{m_i \cdot z_i}$
Battery	32.175	5.684
Fuselage	8.893	0
Port wing root	9.6	1.92
Starboard wing root	9.6	1.92
TOTAL	60.268	9.524

By using the values from Table 12 and the total mass, the centre of mass can be determined (ibid)

$$x_{cg} = \frac{\sum \boldsymbol{m_i \cdot x_i}}{\sum m} = \frac{60.268}{32} = 1.88\, m$$

$$y_{cg} = 0 \tag{63}$$

$$z_{cg} = \frac{\sum \boldsymbol{m_i \cdot z_i}}{\sum m} = \frac{60.268}{32} = 0.30\, m$$

Knowing this, the mass moment of inertia with respect to the centre of mass are taken

Table 13 - Mass of inertia components

Component	$\boldsymbol{r_x}$	$\boldsymbol{r_z}$	$\boldsymbol{m_i \cdot {x_i}^2}$	$\boldsymbol{m_i \cdot {z_i}^2}$	$\boldsymbol{m_i \cdot x_i \cdot z_i}$
Battery	1.12	0.23	13.5	0.57	3.96
Fuselage	-0.99	-0.30	9.80	0.9	2.97
Port wing root	-0.28	0.02	0.47	0.0024	0.009
Starboard wing root	-0.28	0.02	0.47	0.0024	0.009
TOTAL			24.2	1.47	6.95

The mass moment of inertia is given by

$$I_{xx} = \sum(\boldsymbol{m_i} \cdot \boldsymbol{z_i}^2 + \boldsymbol{m_i} \cdot \boldsymbol{y_i}^2) = 1.47\ m^4 \tag{64}$$

$$I_{yy} = \sum(\boldsymbol{m_i} \cdot \boldsymbol{x_i}^2 + \boldsymbol{m_i} \cdot \boldsymbol{z_i}^2) = 24.2 + 1.47 = 25.67\ m^4 \tag{65}$$

$$I_{zz} = \sum(\boldsymbol{m_i} \cdot \boldsymbol{x_i}^2 + \boldsymbol{m_i} \cdot \boldsymbol{y_i}^2) = 24.2\ m^4 \tag{66}$$

$$I_{xz} = \sum(\boldsymbol{m_i} \cdot \boldsymbol{x_i} \cdot \boldsymbol{z_i}) = 6.95\ m^4 \tag{67}$$

Hence the inertia tensor of the UAV is:

$$J = \begin{bmatrix} 1.47 & 0 & -6.95 \\ 0 & 25.67 & 0 \\ -6.95 & 0 & 24.2 \end{bmatrix} \tag{68}$$

3.4.1.3 Dynamics of the wing tip

To model the dynamics of the wing tip, the morphing UAV was treated as a single body but with a relaxing condition of rigidity, which means that it is a single body with a variable centre of mass and inertia tensor. Therefore, the centroid dynamics can be modelled and simulated in MATLAB & Simulink by using the equation below (Yang et al., 2020).

$$\mathrm{m}\dot{\mathrm{V}}_\mathrm{b} = \mathrm{F_E} - \mathrm{m}[\overline{\omega}]\mathrm{V_b} + \mathrm{F_{ext}} \tag{69}$$

$$\mathrm{J}\dot{\omega} = \mathrm{M_E} - [\overline{\omega}]\mathrm{J}\omega + \mathrm{M_{ext}} \tag{70}$$

To start the simulation, the dynamic equations shown above must be rearranged by making the higher derivative the subject, this is shown in Equation (71) and (72).

$$\dot{V}_b = \frac{F_E}{m} - [\overline{\omega}]V_b + \frac{F_{ext}}{m} \tag{71}$$

$$\dot{\omega} = \frac{M_E}{J} - [\overline{\omega}]\omega + \frac{M_{ext}}{J} \tag{72}$$

Equation (47) and (48) can be represented by the Simulink diagram shown below which does not include the expanded equation of F_{extra} and M_{extra}, respectively.

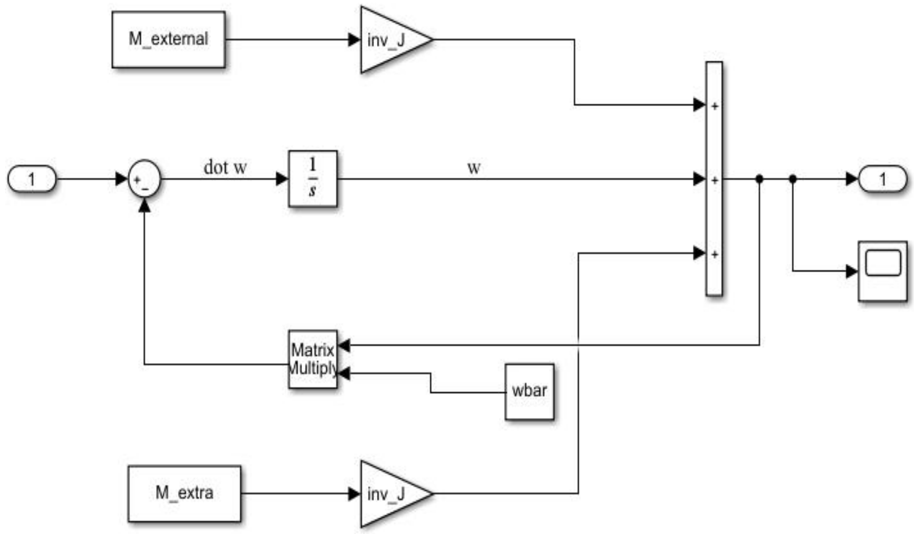

Figure 37: Dynamics without M

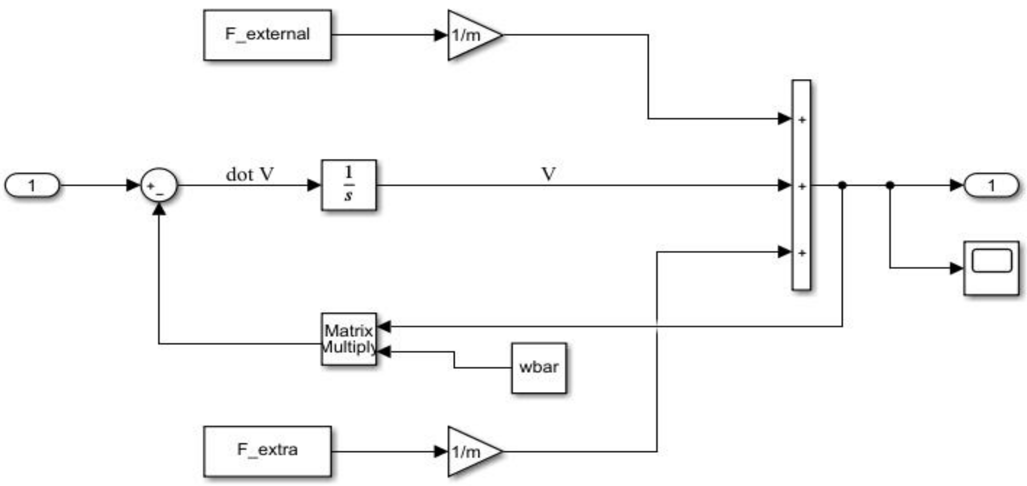

Figure 38: Dynamics without F

F_{extra} and M_{extra} are the extra force which originated from the morphing and can be expressed by the following formulas.

$$F_{ext} = -m\ddot{d}_{cm} - m[\overline{\omega}]d_{cm} - m[\overline{\omega}]^2 d_{cm} - 2m[\overline{\omega}]d_{cm} \tag{73}$$

$$M_{ext} = -\dot{J}\omega - m[\overline{d_{cm}}](\overline{\omega}V_b + \dot{V}_b) - \int [\overline{d}]\ddot{d}dm - [\overline{\omega}] \int [\overline{d}]\dot{d}dm \tag{74}$$

By substituting Equation (73) and (74), into Equation (71) and (72), respectively. The following is obtained.

$$\dot{V}_b = \frac{F_E}{m} - [\overline{\omega}]V_b - \ddot{d}_{cm} - [\overline{\omega}]d_{cm} - [\overline{\omega}]^2 d_{cm} - 2[\overline{\omega}]d_{cm} \tag{75}$$

$$\dot{\omega} = \frac{M_E}{J} - [\overline{\omega}]\omega + \frac{-\dot{J}\omega - m[\overline{d_{cm}}](\overline{\omega}V_b + \dot{V}_b) - \int[\overline{d}]\ddot{d}dm - [\overline{\omega}] \int[\overline{d}]\dot{d}dm}{J} \tag{76}$$

Similarly, to show the Simulink diagram that represent the equations above, the highest derivative should be the subject as Simulink can only integrate. These are shown in the equations below; the following parameters were assumed to be 0 to ensure that the simulations run: F_E and M_E, these will be included in a later stage.

$$\ddot{d}_{cm} = \frac{F_E}{m} - [\overline{\omega}]V_b - [\overline{\omega}]d_{cm} - [\overline{\omega}]^2 d_{cm} - 2[\overline{\omega}]d_{cm} - \dot{V}_b \tag{77}$$

$$\ddot{d} = J\dot{\omega} - M_E + J[\overline{\omega}]\omega + \dot{J}\omega + m[\overline{d_{cm}}](\overline{\omega}V_b + \dot{V}_b) + [\overline{\omega}] \int [\overline{d}]\dot{d}dm + \int [\overline{d}] \tag{78}$$

Thus, giving to the Simulink diagram without including the forces:

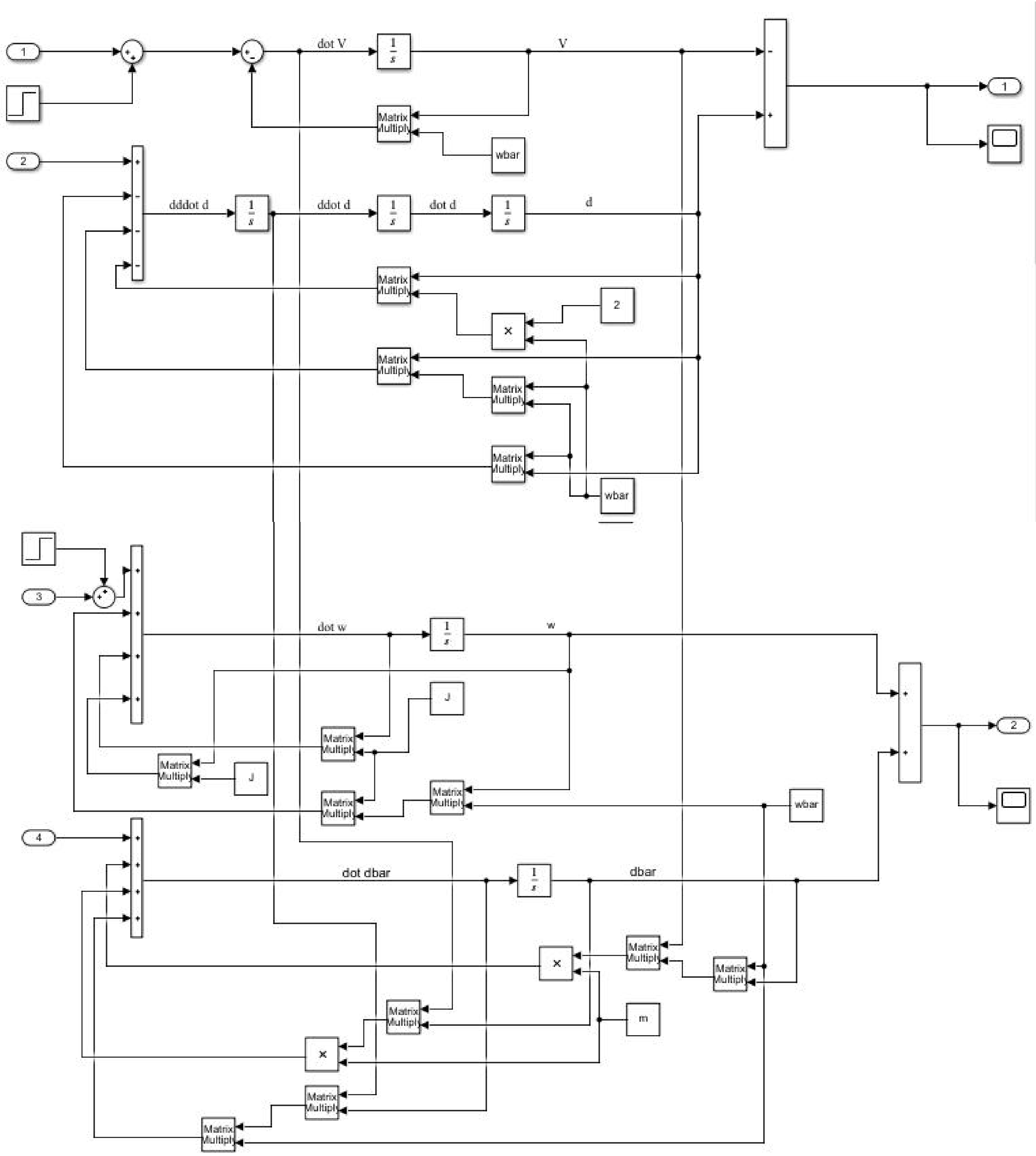

Figure 39: Dynamics without F and M

Finally, to complete the dynamics of the morphing wingtip, the external forces which can be represented by the following equation

$$m\begin{bmatrix}\frac{\ddot{h}_1}{b}\\ \frac{\ddot{h}_2}{b}\end{bmatrix} = F = -\begin{bmatrix}\frac{k_{h1}h_1}{b}\\ \frac{k_{h2}h_2}{b}\end{bmatrix} + \frac{m}{\mu}\left(\begin{bmatrix}\frac{\ddot{h}}{b}\\ \ddot{\alpha}\end{bmatrix} + 2\bar{U}\begin{bmatrix}\frac{\dot{h}}{b}\\ \dot{\alpha}\end{bmatrix}\right) + \frac{mb}{5}\begin{bmatrix}J_{11} & J_{12}\\ J_{12} & J_{22}\end{bmatrix}^{-1}\begin{bmatrix}1\\ 5J_2\end{bmatrix}L_g \tag{79}$$

(Where k_{h1} is the wing stiffness in the first bending mode; k_{h2} is the hinge-stiffness in the canted wing mode)

By rearranging the equation above,

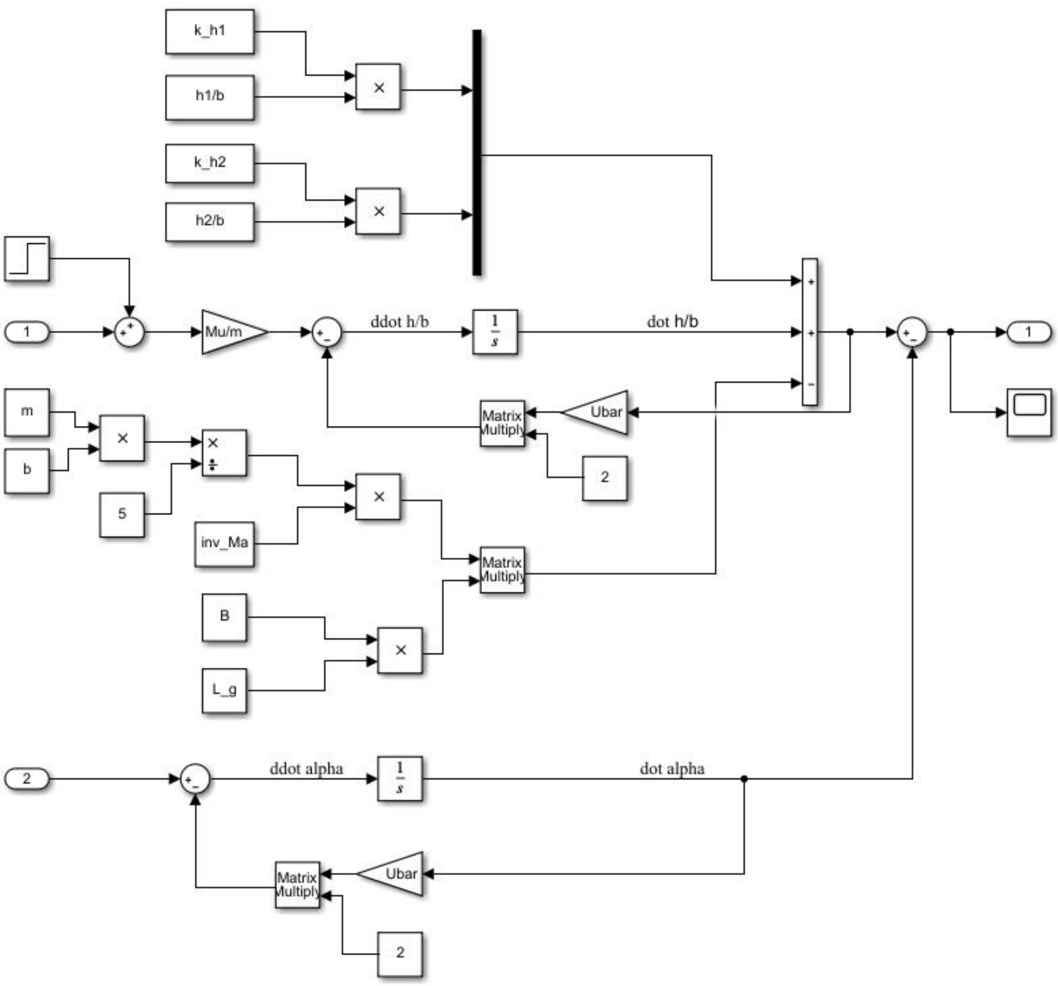

Figure 40: Forces which includes the two plunging modes

$$\begin{bmatrix} \frac{\ddot{h}}{b} \\ \ddot{\alpha} \end{bmatrix} = \frac{\mu}{m}\left(F + \begin{bmatrix} \frac{k_{h1}h_1}{b} \\ \frac{k_{h2}h_2}{b} \end{bmatrix} - \frac{mb}{5}\begin{bmatrix} J_{11} & J_{12} \\ J_{12} & J_{22} \end{bmatrix}^{-1}\begin{bmatrix} 1 \\ 5J_2 \end{bmatrix} L_g \right) - 2\bar{U}\begin{bmatrix} \frac{\dot{h}}{b} \\ \dot{\alpha} \end{bmatrix} \tag{80}$$

By subtracting the restraining force, which is the total external force in this case, the dynamics of the morphing wingtips can be represented by the Simulink below; the restraining forces are structural spring forces and aerodynamic lift.

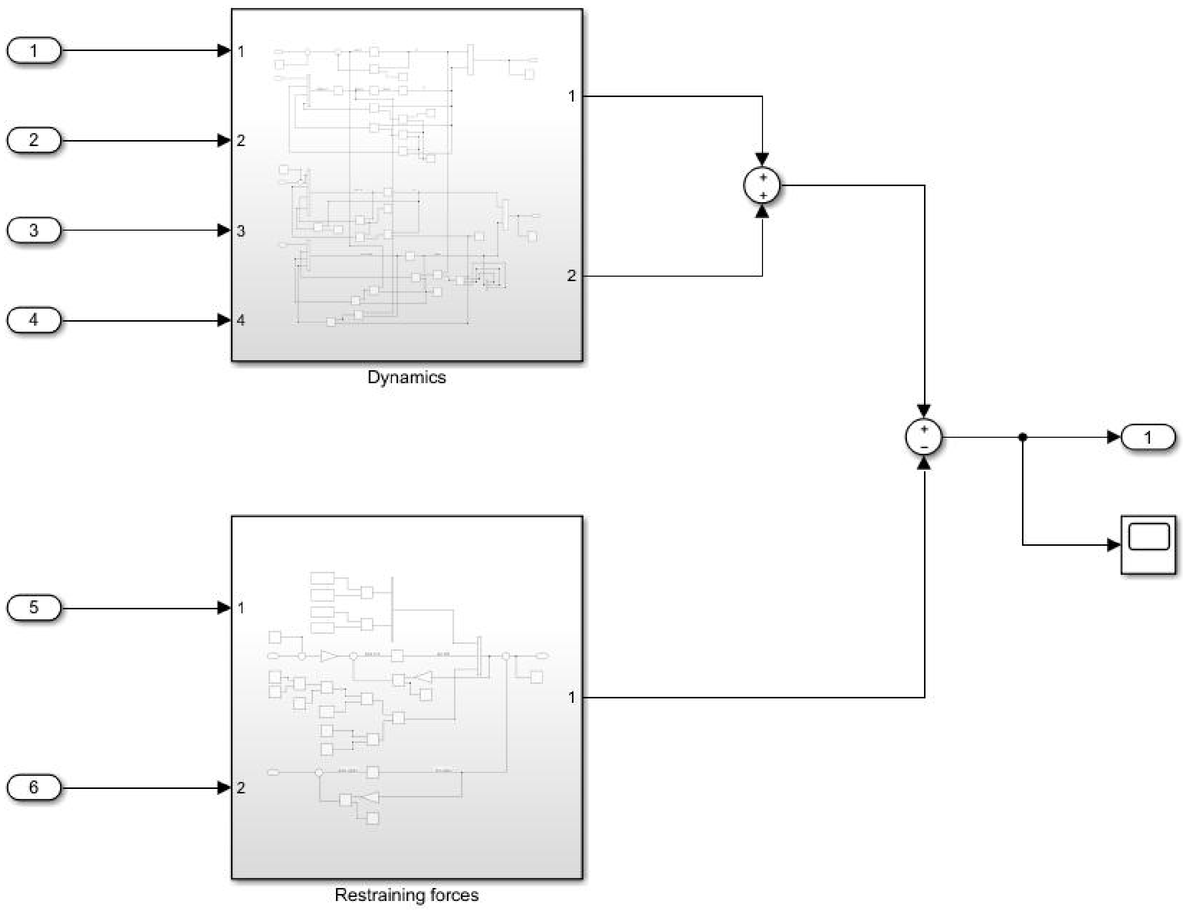

Figure 41: Dynamics of the morphing tip

3.4.2. Static and modal analysis: 3D wing structure

3.4.2.1. General procedure

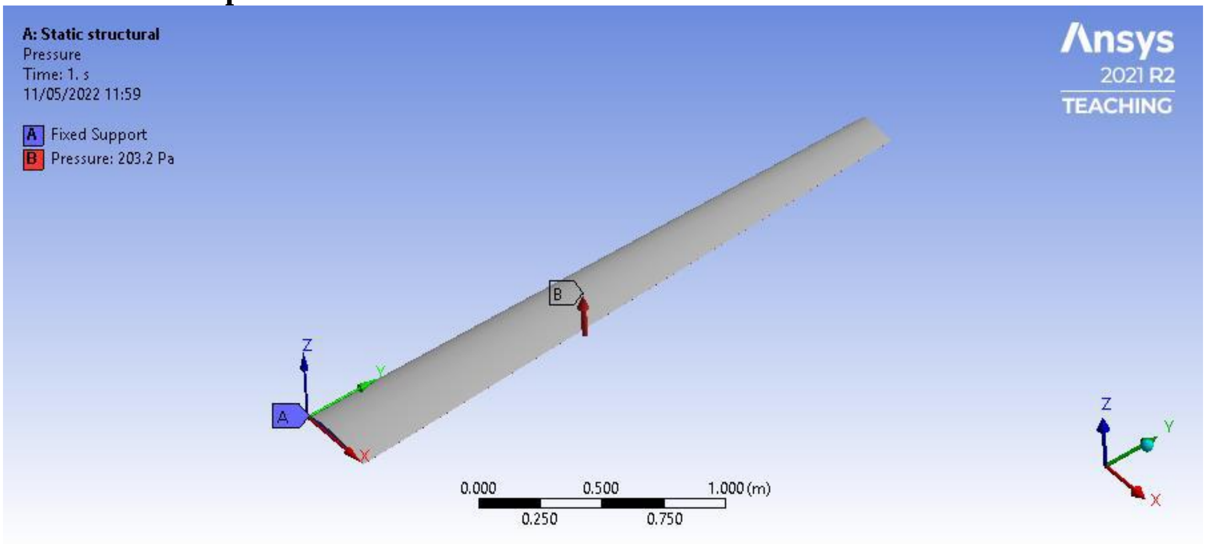

Figure 42: Pressure load and boundary condition applied on the wing

To begin with, as mentioned in the previous sections, the 3D structure of the wing was sketched in Solidworks by using the dimensions stated previously. Subsequently, it was then imported to the static structural analytical system from Ansys Fluent. Once done, the next step was to define the material properties of the wing by using Table 14 and the engineering data sources provided by Ansys.

Table 14 - Carbon fiber

Youngs Modulus (GPa)	395
Poisson ratio	0.26

Next, a boundary condition and pressure were applied on the 3D structure of the wing as shown in Figure 42; these were a fixed support at the end of the aerofoil and a pressure of 203.2 Pa which was applied at the bottom surface of the wing, respectively. The fixed support was placed at the end of the wing as it is attached firmly with the fuselage and the pressure was applied at the centre, at the bottom surface, assuming that it is the location where the total pressure acts (Das and Roy, 2018). Subsequently, to start the mesh phase, the mesh was defined as dominant hexahedral with a starting global seeding of 0.06m which was then decreased by 0.01m until 0.02 was reached. The contour plots will be shown in the Section 3.5, Results and discussion.

3.5. Results and Discussion

The main aims were to investigate and analyse the aerodynamic characteristics of a morphing wingtip, to demonstrate the benefits of morphing and to analyse the 3D wing structure created in Solidworks by performing static and modal analysis by using Ansys Fluent.

These were achieved by firstly, the Simulink diagram representing the dynamics of the morphing wingtip was created using MATLAB & Simulink and the background theory covering the benefits of the morphing wingtip was discussed. Secondly, the structure was statically analysed by observing the structural behaviour in terms of total deformation, stress and strain; contour plots, graphical and tabulated results were discussed. Finally, the dynamic behaviour was analysed by performing modal analysis, where the frequencies and their mode shape were determined. These will be further explained in the sections below.

3.5.1. Morphing Simulation: Simulink and MATLAB approach

3.5.1.1. MATLAB code for the parameters

Figure 43 displays the input parameters used to run the simulation of the dynamics of the morphing wing tip.

```
%%Parametrs
clc;clearvars;
%Variables
Ubar = 10; % Ubar=U/b

%Constants
m = 20; % Mass of the aircraft
wbar = [0 0 0; 0 0 -0.01; 0 0.01 0];  %angular velocity assuming a slowly rolling wing
b = 2.8; %Span of the wing in m
k_h1= 40000; %Wing stiffness in the first bending mdoe
k_h2= 80000; %Hinge-stiffness in the canted wing mode
L_g = 0.01;
h1 = 0.5;
h2 = 0.5;
Pi = pi;
Rho = 1.225; %Density of air

%Calculated constants
J = [1.47 0 -6.95; 0 25.67 0 ;-6.95 0 24.2]*1.0e-01; %Inertia tensor matrix
dotJ = diff(J);
inv_J = inv(J);
J_11 = 26/405;
J_12 = sqrt(26/405)* 86./405;
J_22 = 172./405;
J_2 = 86./405;
B = [1 ; 5*J_2];
M_a = [J_11  J_12; J_12 J_22];
inv_Ma = inv(M_a);
M = [(k_h1*h1)./b ; (k_h2*h2)./b];
Mu = (m./(Rho*Pi*b.^2));
```

Figure 43: Input parameter

3.5.1.2 Dynamic response of the morphing wingtip

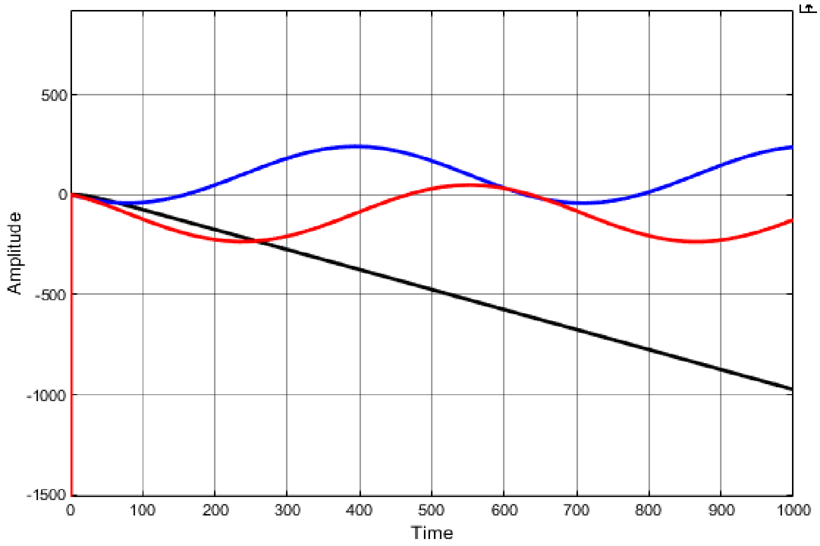

Figure 44 - Dynamic response (Stop time 1000s)

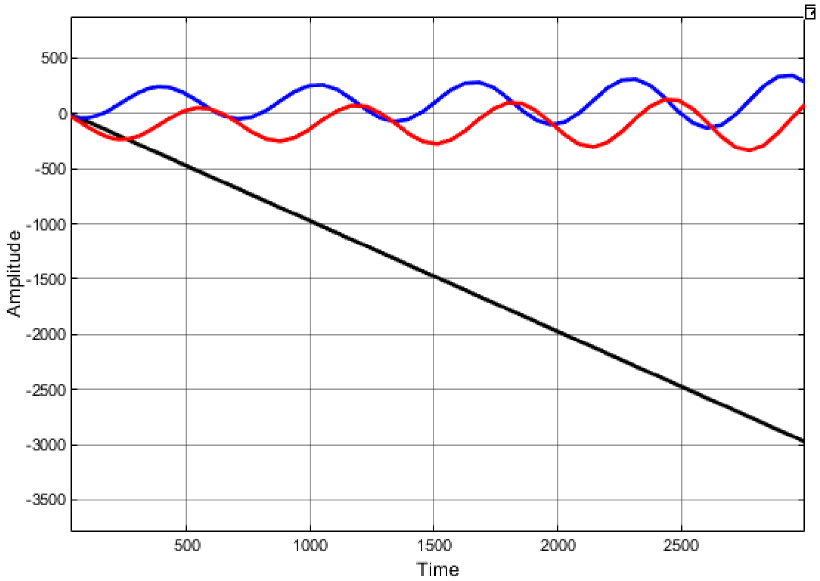

Figure 45: Dynamic response (Stop time 3000s)

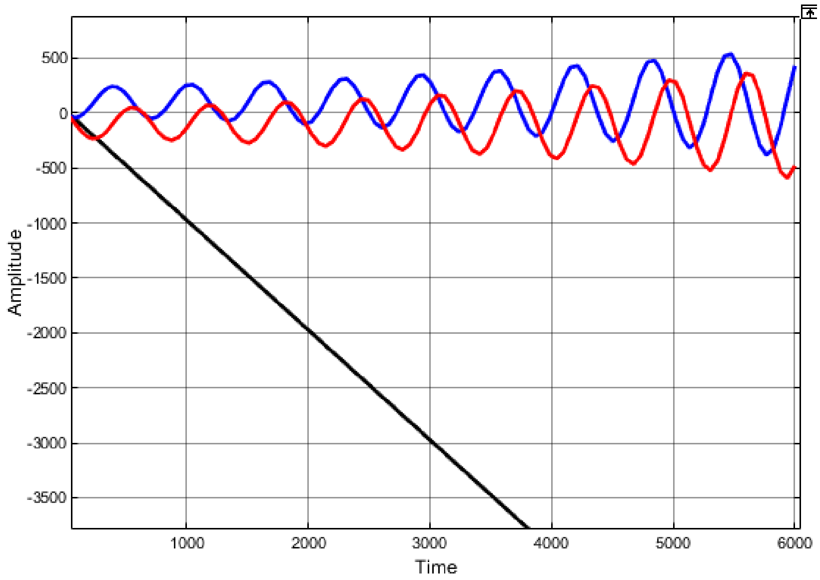

Figure 46: Dynamic response (Stop time 6000s)

Figure 44, 45 and 46, displays the dynamic response from the morphing wingtip, where three lines are observed: red, blue and black. It can be observed that as the time of the simulation increases, the behaviour of each line begins to change drastically. The red and blue line seemed to experience an increase in amplitude which is slowly stabilising, resembling a sine wave; the two oscillations seem to be travelling at a 90 degree out of phase from each other. Whereas the black line is diverging in a highly rapid rate.

During the modelling of the Simulink, multiple difficulties were encountered such as: dimensionality problems, having only one variable per path line and ensure that the right multiplication block was used. These problems were solved, and the response given by the final Simulink seemed to provide a result.

However, the result obtained could not be changed, regardless of the change of Ubar and U. This was observed after investigating and testing the response of each output, this was viewed by using the scope block. Therefore, it was determined that an unknown error was within the Simulink diagram of either the dynamics or restraining forces, which has caused the result to not be affected by the change of parameter. Although the error was noticed based on the investigation, after reviewing the connections of the Simulink diagram no error was found. Furthermore, the Simulink did not provide any suggestion regarding the error that caused the dynamic output to remain unchanged so the analysis of the dynamic response with varying Ubar and U was not possible.

3.5.2. Static and modal analysis: 3D wing structure

3.5.2.1. Static analysis

In this section, the 3D structure of the wing will be analysed by using Ansys fluent. The aim is to statically analyse the structure of the wing without the motion of time and observe its structural behaviour in terms of total deformation, stress and strain (Zakuan, Aabid and Khan, 2019).

3.5.2.1.1. Mesh convergence

According SimuTech Group (2020), the creation of an appropriate mesh and performing mesh convergence is crucial for engineering as it has a significant effect on the accuracy, computational time and convergence of the result obtained. It has a significant role to the engineering field as it provides the solution of complex partial differential equations, where hand calculation would not be practical.

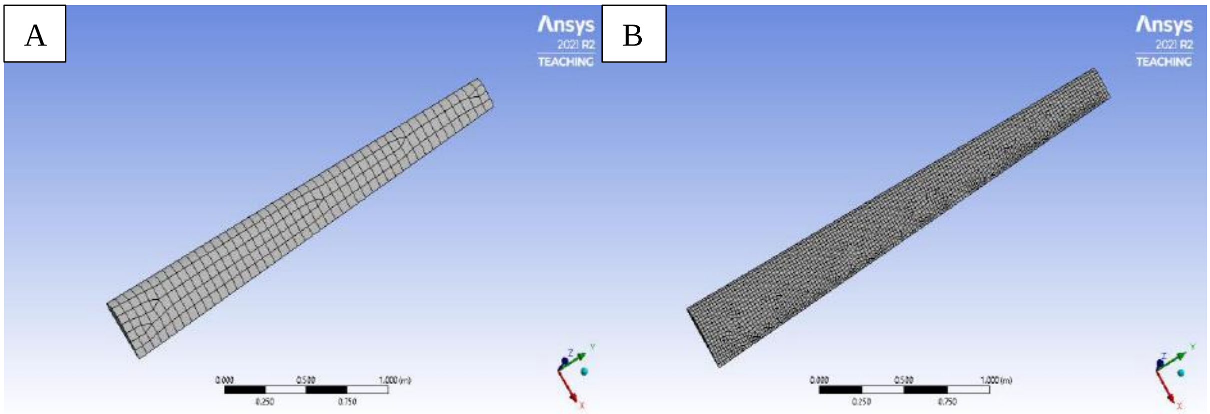

Figure 47: (A) Coarse mesh and (B) Fine mesh

Mesh convergence is achieved by reducing the global size from 0.06 to 0.02m, with a decrement of 0.01m, this was performed for the following three parameters: total deformation in the z-direction, stress and strain variation. Figure 47 displays the coarse and fine mesh, where 0.06m and 0.02m as the global size, respectively. The element used for this mesh was hexahedral as it decreases the computational time whilst maintaining accuracy of the results obtained.

Table 15 - Mesh convergence

Global seeding	Number of elements	Number of nodes	Total deformation (m)	Equivalent elastic strain	Equivalent von-Mises stress (Pa)
0	0	0	0	0	0
0.06	372	1755	$7.37x10^{-2}$	$7.80x10^{-4}$	$3.65x10^{6}$
0.05	377	2294	$7.29x10^{-2}$	$7.96x10^{-4}$	$3.68x10^{6}$
0.04	789	4003	$7.24x10^{-2}$	$7.86x10^{-4}$	$3.62x10^{6}$
0.03	2916	10210	$7.21x10^{-2}$	$7.70x10^{-4}$	$3.51x10^{6}$
0.02	7188	25872	$7.21x10^{-2}$	$7.70x10^{-4}$	$3.51x10^{6}$

As seen in Table 15, by decreasing the global size, the number of elements and node increases; a finer mesh will provide a better capture of stress gradients across the element, therefore increasing the accuracy of the result (ibid). Although, this leads to an increase in complexity, thus having longer computational times. The results obtained for the total deformation, stress and strain of the model have converged to a solution with a value of 0.0721m, 3510000 Pa and 0.00077, respectively. These results are graphically represented by Figure 48, 49 and 50.

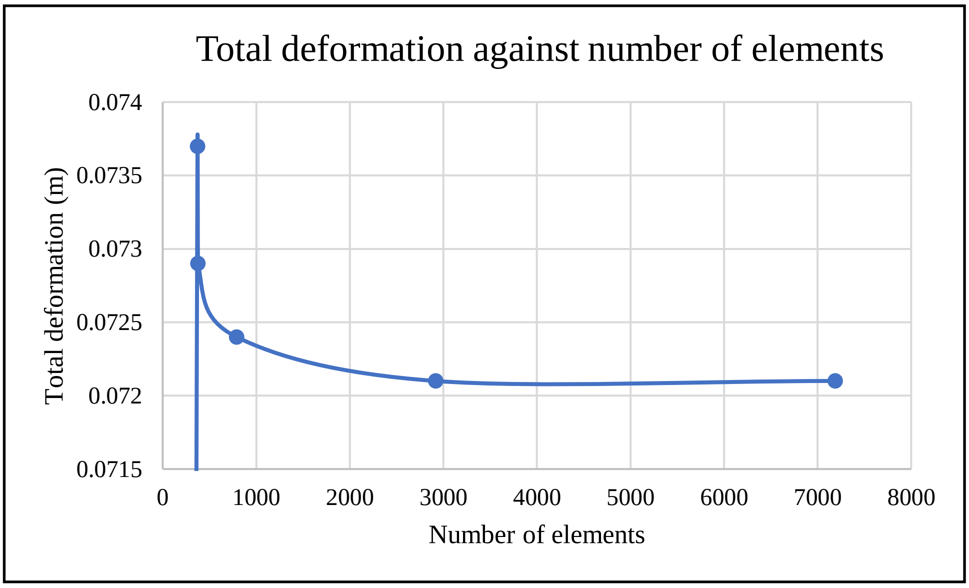

Figure 48: Total deformation convergence

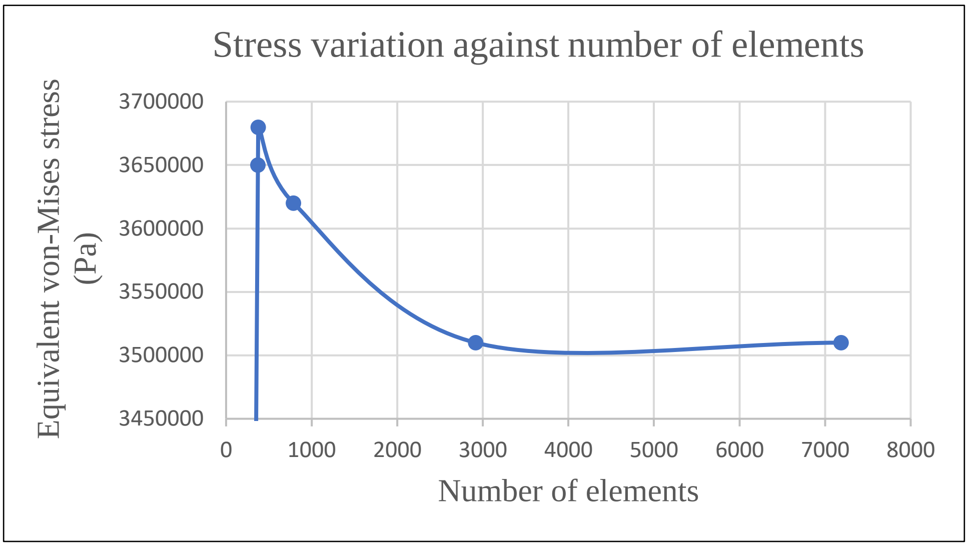

Figure 49: Stress convergence

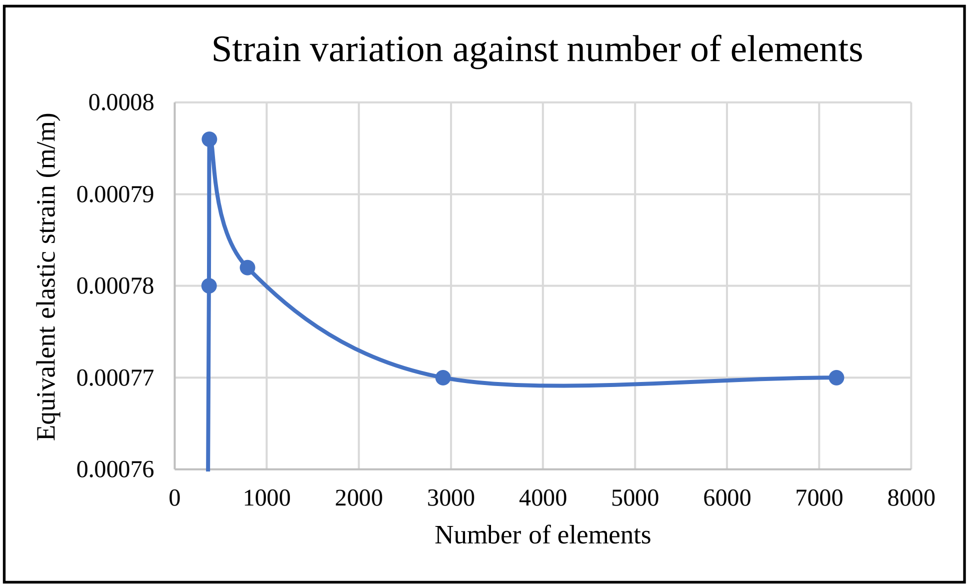

Figure 50: Strain convergence

Figure 48, 49 and 50 highlights the convergence of the total deformation, stress and strain; by observing the graphs, convergence occurs at round 3000 elements and 10000 nodes. Although the simulation includes up to 7000 elements and 26000 nodes, the solution has not changed, or minimal change have been noticed which further indicates that the simulation fully converged to a solution. This means that further refinements will only increase the cost and computational time as the result obtained will not change any further.

3.5.2.1.1.1. Total deformation in the y direction

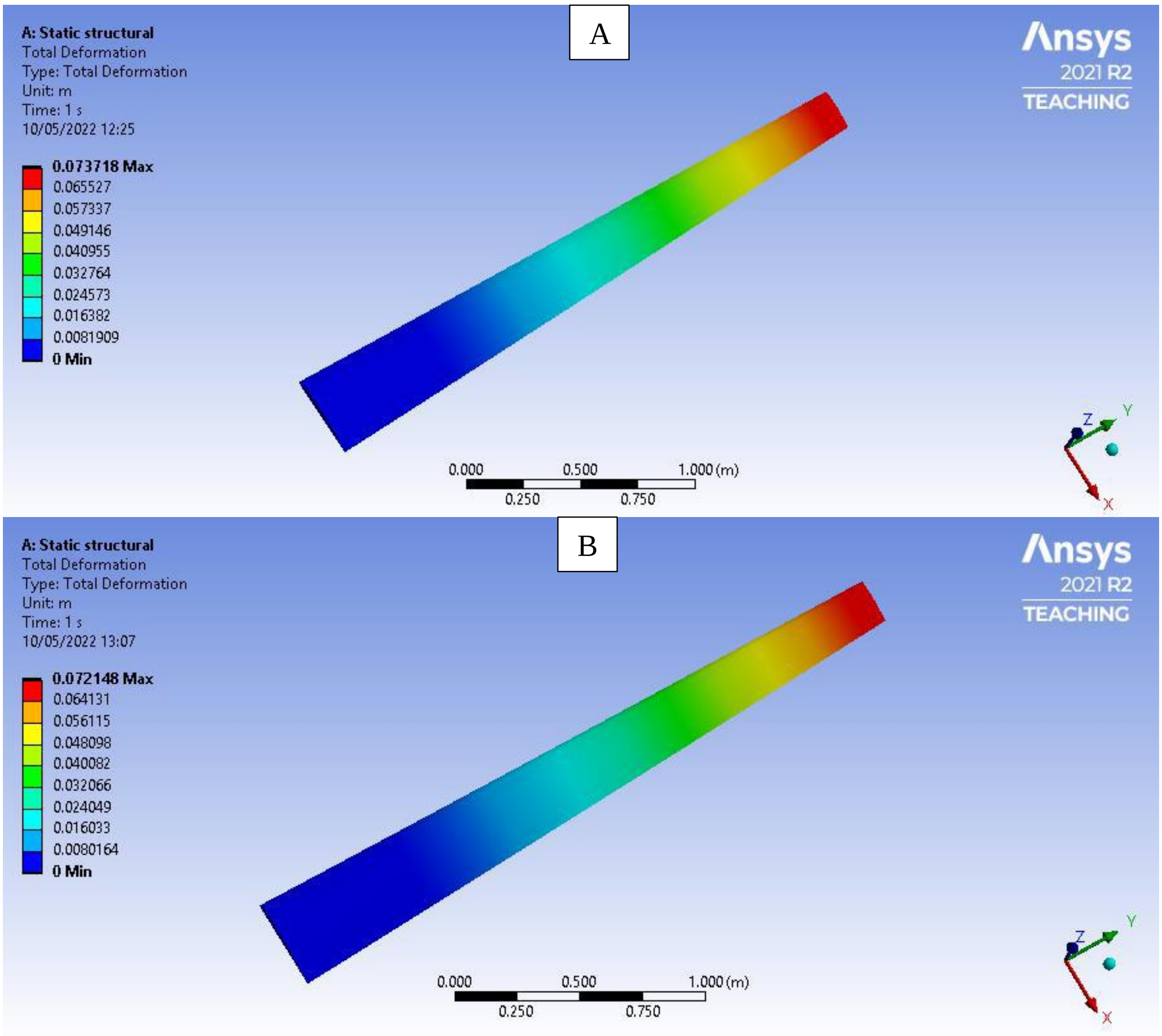

Figure 51: (A) Coarse mesh and (B) Fine mesh

The total deformation of the 3D wing structure can be seen in Figure 51; where the colours represent the magnitude, the warmer the colour the greater the magnitude. This deformation was obtained after the wing was subjected to a pressure load and a fixed support was applied at one of the ends of the wings as explained previously. According to Aabid et al. (2021), deformation gradually increases for each component as it moves away from the support; Figure 51B supports this as the lowest deformation is located at the root of the wing, near the fixed support, and the location in which the wing structure experiences the largest deformation is at the wingtip, further away from the fixed support, with a value of 0.072148m. This value can be considered reasonable for a wing of 2.8m.

3.5.2.1.1.2. Stress variation

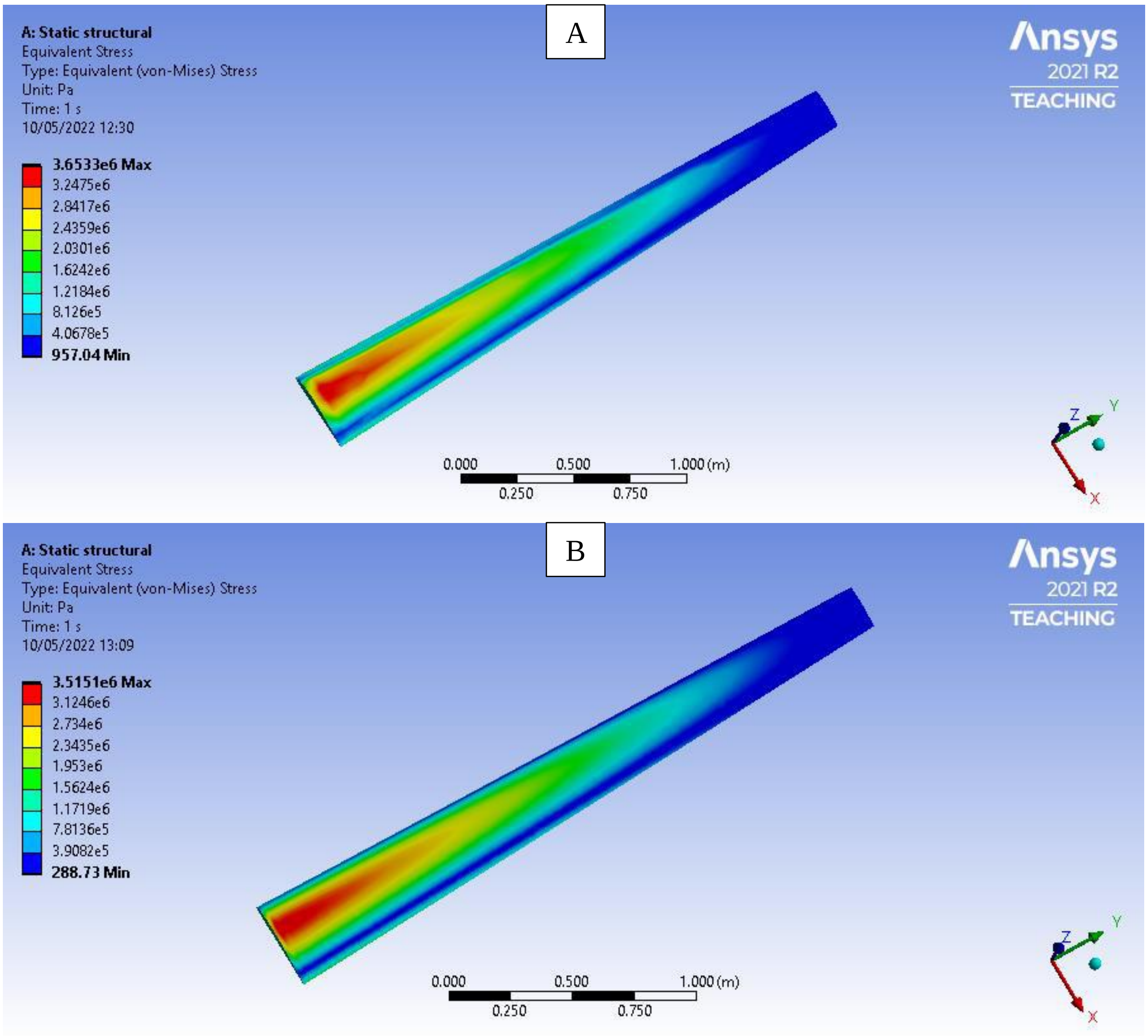

Figure 52: (A) Coarse mesh and (B) Fine mesh

Based on the study of Rogers (2018), efficient structures should display an evenly distributed stress across the wing. As seen in Figure 52, the stress decreases from root to tip, as the maximum stress is located at the root highlighted in red with a value of 3.51MPa and the lowest stress is located at the tip with a value of 288.73Pa, highlighted in blue. In addition, higher stress areas indicated by the warmer colours signifies the likelihood of that part failing first whereas, the lower stress areas indicated by the colder colours signifies the excess strength which is unused (ibid). Furthermore, by comparing the maximum stress obtained across the wing and the yield strength of the material, it can be determined whether the structure can sustain the loads or structural failure occurs.

According to the elastic failure theories and based on the maximum stress obtained of 3.51MPa, it can be determined that the 3D structure can sustain the loads as it does not exceed the yield strength of the material used for the structure (Atmeh, Hasan and Darwish, 2010).

1.5.2.1.1.3. Strain variation

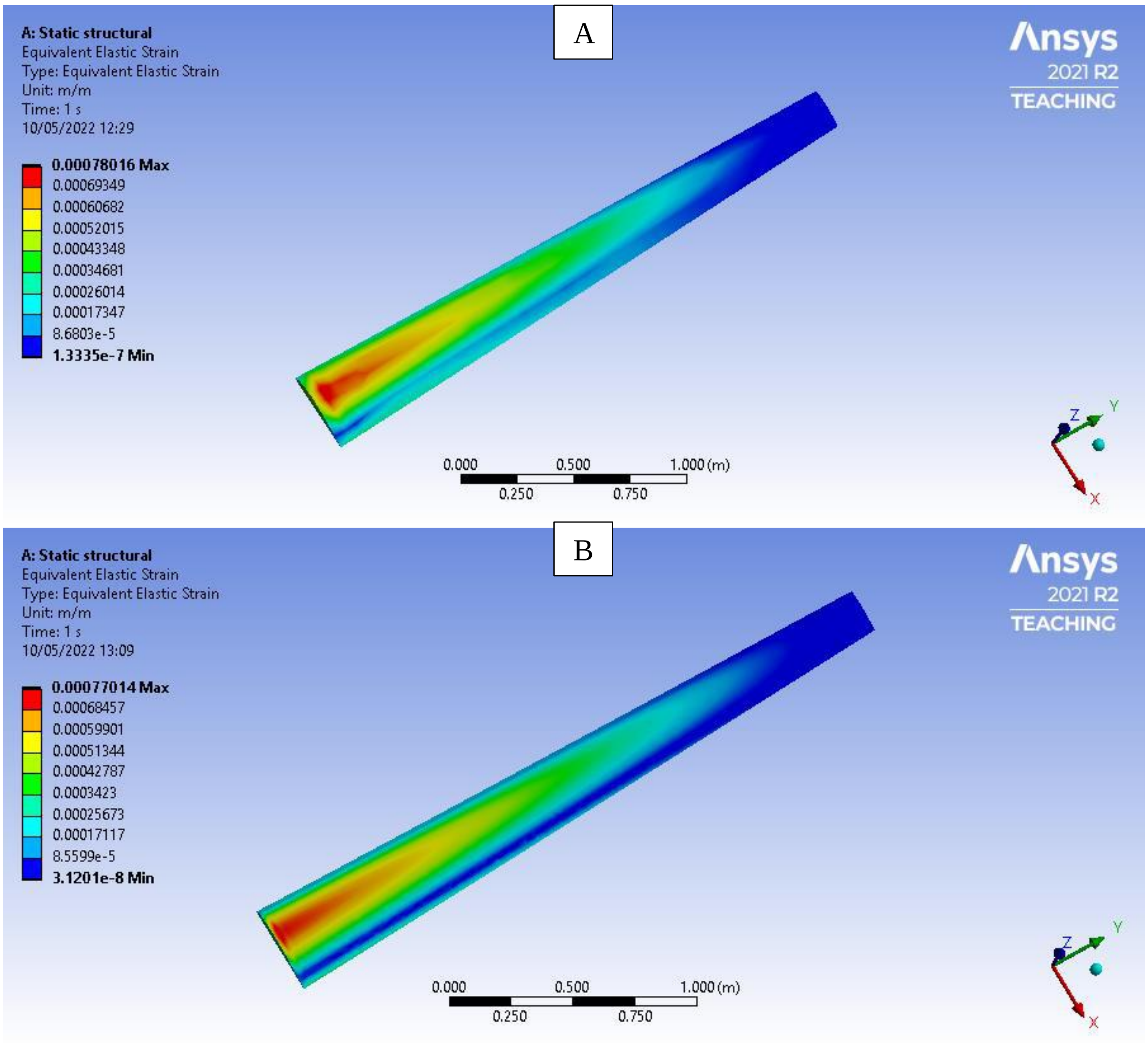

Figure 53: (A) Coarse mesh and (B) Fine mesh

Similarly, Von-Mises strain decreases from root to tip, as the maximum strain is located at the root highlighted in red with a value of $7.70\text{x}10^{-4}$ m/m and the lowest strain is located at the tip with a value of $3.1\text{x}10^{-8}$ m/m, highlighted in blue. The Von-Mises strain is the ratio between the deformation and the original length; as the strain increases, the strength and stiffness of the material also increases.

3.5.2.2. Modal analysis

Modal analysis is a tool used in engineering to understand the limits of the system's response; by performing this analysis, the resonant frequencies and their respective mode shapes can be determined. This is essential because as the frequency comes close to the resonant frequency, the amplitude of the response approaches infinity (Harish, 2016). As a result, the structure will experience the following deformations at different frequencies shown from Figure 54 to 58.

In this section, the 3D structure of the wing will be analysed by using Ansys fluent. The aim is to perform modal analysis to determine the shuddering features such as natural frequencies and their mode shapes (bending or torsion mode) (Zakuan, Aabid and Khan, 2019). The mesh that was used to perform modal analysis was the fine mesh with a global size of 0.02m.

3.5.2.2.1 Mode 1

As seen in Figure 54, the deformation type of the first mode shape is bending; its deformation deflects in the positive Z-axis with a total deformation of 0.47936m. This occurs at a frequency of 1.9201Hz.

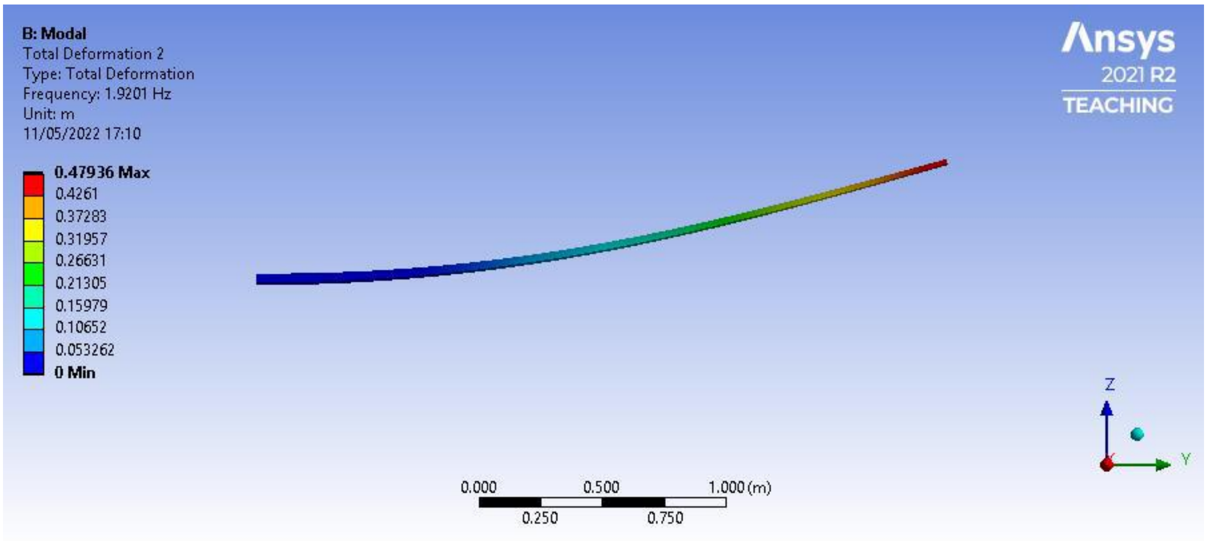

Figure 54: Mode 1

3.5.2.2.2 Mode 2

As seen in Figure 55, the deformation type of the second mode shape is bending; its deformation deflects in the positive Z-axis with a total deformation of 0.54746m. This occurs at a frequency of 8.1013Hz

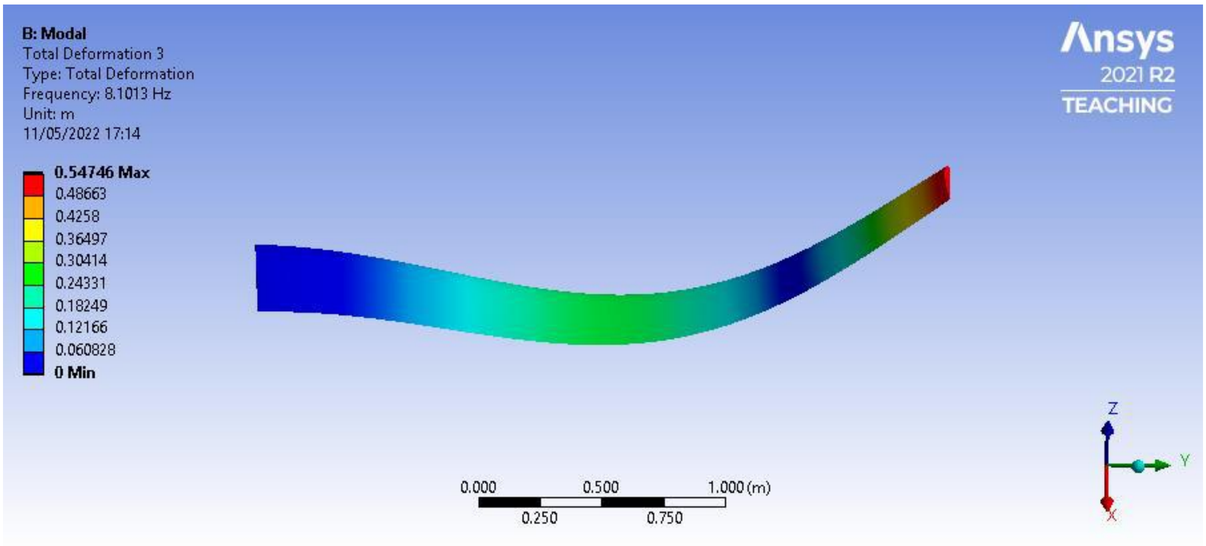

Figure 55: Mode 2

3.5.2.2.3 Mode 3

As seen in Figure 56, the deformation type of the third mode shape is bending; its deformation deflects in the positive X-axis with a total deformation of 0.47903m. This occurs at a frequency of 14.862Hz.

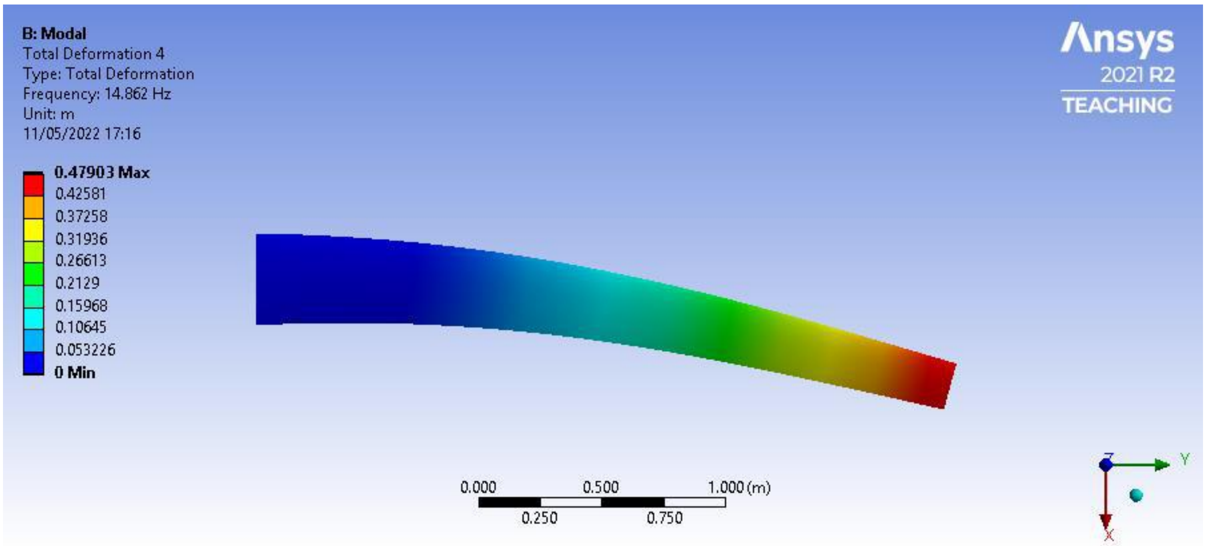

Figure 56: Mode 3

3.5.2.2.4 Mode 4

As seen in Figure 57, the deformation type of the fourth mode shape is bending; its deformation deflects in the positive Z-axis with a total deformation of 0.56748m. This occurs at a frequency of 20.098Hz.

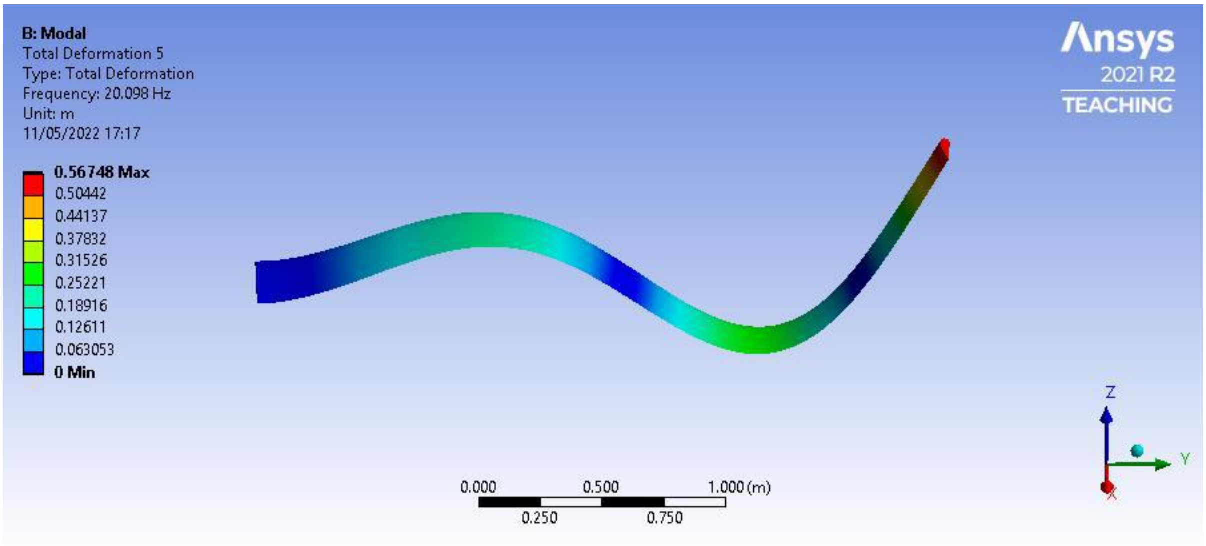

Figure 57: Mode 4

3.5.2.2.5 Mode 5

As seen in Figure 58, the deformation type of the fifth mode shape is bending; its deformation deflects in the positive Z-axis with a total deformation of 0.57537m. This occurs at a frequency of 37.924Hz.

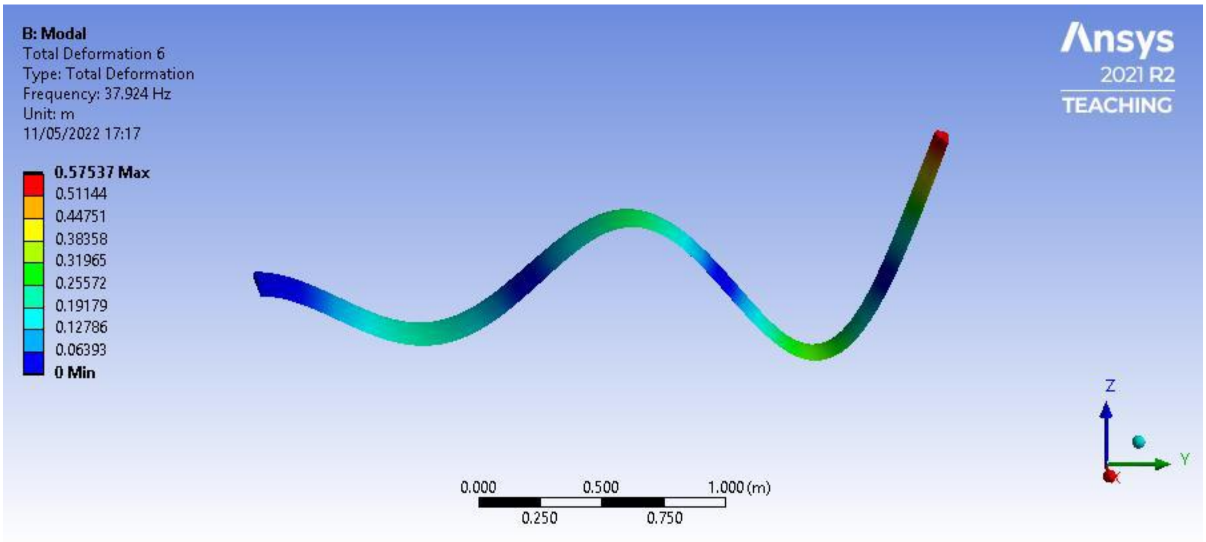

Figure 58: Mode 5

3.5.2.2.6. Analysis

Table 16 - Results for modal analysis

Mode shape	Frequency (Hz)	Direction of deflection	Largest deformation (m)	Type of deformation
1	1.9201	Z-axis	0.47936	Bending
2	8.1013	Z-axis	0.54746	Bending
3	14.862	X-axis	0.47903	Bending
4	20.098	Z-axis	0.56748	Bending
5	37.924	Z-axis	0.57537	Bending

As seen in from Figure 54 to 58, each mode shapes experiences pure bending mode as seen in Table 16. Furthermore, it is observed that all modes experience the deformation at the tip of the wing as there is no support to resists and overcome the applied load.

***** PARTICIPATION FACTOR CALCULATION ***** X DIRECTION

MODE	FREQUENCY	PERIOD	PARTIC.FACTOR	RATIO	EFFECTIVE MASS	CUMULATIVE MASS FRACTION	RATIO EFF.MASS TO TOTAL MASS
1	1.92008	0.52081	-0.12300E-01	0.003181	0.151287E-03	0.101176E-04	0.455793E-05
2	8.10127	0.12344	0.10010E-01	0.002589	0.100198E-03	0.168185E-04	0.301872E-05
3	14.8616	0.67287E-01	3.8669	1.000000	14.9526	1.00000	0.450488
4	20.0979	0.49757E-01	-0.11336E-02	0.000293	0.128498E-05	1.00000	0.387134E-07
5	37.9236	0.26369E-01	0.24114E-02	0.000624	0.581482E-05	1.00000	0.175187E-06
sum					14.9529		0.450496

***** PARTICIPATION FACTOR CALCULATION ***** Y DIRECTION

MODE	FREQUENCY	PERIOD	PARTIC.FACTOR	RATIO	EFFECTIVE MASS	CUMULATIVE MASS FRACTION	RATIO EFF.MASS TO TOTAL MASS
1	1.92008	0.52081	-0.88648E-01	1.000000	0.785854E-02	0.563663	0.236759E-03
2	8.10127	0.12344	-0.20748E-01	0.234047	0.430475E-03	0.594540	0.129692E-04
3	14.8616	0.67287E-01	0.43074E-01	0.485898	0.185537E-02	0.727618	0.558981E-04
4	20.0979	0.49757E-01	0.47699E-01	0.538070	0.227520E-02	0.890810	0.685463E-04
5	37.9236	0.26369E-01	-0.39017E-01	0.440132	0.152232E-02	1.00000	0.458640E-04
sum					0.139419E-01		0.420037E-03

***** PARTICIPATION FACTOR CALCULATION ***** Z DIRECTION

MODE	FREQUENCY	PERIOD	PARTIC.FACTOR	RATIO	EFFECTIVE MASS	CUMULATIVE MASS FRACTION	RATIO EFF.MASS TO TOTAL MASS
1	1.92008	0.52081	3.8708	1.000000	14.9835	0.556073	0.451417
2	8.10127	0.12344	-2.6313	0.679762	6.92350	0.813022	0.208589
3	14.8616	0.67287E-01	0.10761E-01	0.002780	0.115800E-03	0.813026	0.348877E-05
4	20.0979	0.49757E-01	1.7929	0.463187	3.21458	0.932327	0.968477E-01
5	37.9236	0.26369E-01	-1.3504	0.348852	1.82345	1.00000	0.549363E-01
sum					26.9451		0.811793

Figure 59: Modal analysis raw data

The participation factor and effective mass of each model in the X, Y and Z axis; it determines the contribution of that mode has to the response of the structure; this is shown in Figure 32 (Ansys, 2021). Furthermore, as seen in Figure 59, mode 1, 2,4 and 5 are contributing significantly to the total deformation experienced in the Z-axis, this is due to their large value for the participation factor and effective mass whereas, mode 3 is contributing more to the X-axis; meaning that, mode 1,2 4 and 5 are more susceptible to get exciting vibration excitation on the Z-axis and mode 3 is more susceptible to get exciting vibration excitation in the X-axis (ibid). In addition, by knowing this information, it will for the design assessment as the mode shape and resonant frequency is.

3.5.3. Limitations

In the dynamics of the morphing wingtips, the quasi-steady approach was used to derive the equation of motion in the absence of any external disturbances; it assumes that the wing is a flat plate and that the wing stiffness is idealised. This might cause some error in terms of accuracy as the aerodynamic forces simulated in the Simulink model does not reflect the flow physics of a conventional wing. Furthermore, according to Brunton and Rowley (2013), the major simplification Theodorsen’s modelling approach was considered when modelling the forces which assumes that the flow is incompressible and inviscid; this assumption loses accuracy at low Reynolds number.

3.5.4. Possible improvements and future works

To improve this section, the following needs to be done: firstly, the validation of the experimental results should be obtained to increase the reliability of the results obtained. Secondly, for the structural static analysis, different mesh types could have been used with different discretisation to compare which method is the most accurate. Finally, for the modal analysis more mode shapes could have been simulated to compare and understand more the dynamic behaviour and characteristic of structures.

Future work to be conducted in this study:

- To further analyse the Simulink diagram obtained and thus, solve the error given by the system. This will enable the output of the dynamic response to vary as the Ubar or U is changed, therefore the effects of Ubar or U on the dynamic response could be evaluated.
- To include the moment of an actuator thus, providing a more sensible dynamic result.
- To perform flutter analysis of the eVTOL UAV and therefore, optimise the wing configuration and enhance the design.

- To analyse the ribs and spars under aerodynamic loads by using ABAQUS software to optimise the structure of the 3D wing

3.6. Conclusion

To summarise, this report analysed the dynamics of the morphing wingtip by modelling the dynamics in MATLAB Simulink and assuming two plunging modes to represent the external forces as well as, performing static and modal analysis of the 3D wing structure created in Solidworks.

The main conclusions made in this study are written below:

- The dynamic response for the morphing wing tip consisted in three lines: black, blue and red. It was determined that the blue and red line, resemble sine waves travelling out of phase from each other; these seemed to slowly stabilise as the time of the simulation was increased. Whereas the black line further diverged into the negative axis.
- The total deformation, stress and strain have converged to a solution at around 3000 elements with a value of 0.0721m, 3510000 Pa and 0.00077 m/m. Looking at the convergence graphs, by reducing the global size, the number of elements increases thus, increasing the accuracy of the result obtained.
- The mode shapes obtained from the modal analysis experience pure bending, where mode 1,2,4 and 5 deflected in the Z-axis and mode 3 deflected in the X-axis. The mode that experienced more deformation was mode 5 with a value of 0.57537m.
- The total deformation is experienced at the tip of the wing as there is no support to resist or overcome the applied load, whereas the root experiences the lowest deformation due to its distance from the support. However, by observing the stress contours it is seen that the opposite occurs as the maximum stress is located at the root and the minimum stress is located at the tip.
- The stress obtained from the static analysis was 3.51MPa, this value is well below the yield strength, thus structural failure would not occur.

4. Aerodynamic Design - Shovethan Murugathas (180193721)

The final wing design of the Unmanned Aerial Vehicle (UAV) was developed by analysing the 2D and 3D wing designs for greater efficiency and performance.

4.1 Introduction

4.1.1 Aim and Objectives

This chapter aims to produce a final wing design for the UAV by investigating the aerodynamic characteristics by using mathematical engineering softwares like SolidWorks, XFLR5 and Ansys Fluent. To successfully construct this report, the following objectives will be achieved:

- Using XFLR5 multiple XFoil analyses will be used to identify the optimum aerodynamic aerofoil for the UAV.
- From the desired aerofoil, Wing analysis will be conducted to understand the aerodynamics characteristics of the wing and to calculate the aerodynamic load for the wings using XFLR5.
- From the dimension parameters, SolidWorks will be used to design the morphing wing and attach it to the UAV's fuselage.
- Computational Fluid Dynamics simulations will be run to understand the aerodynamic characteristics of the air flow around the UAV's wing and fuselage.
- This report will be constructed with all the research, consisting of both experimental and theoretical results.

4.1.2 Rationale

In the past 50 years, the aviation industry has advanced drastically, especially in aircraft performance and efficiency. UAVs are used in many applications, such as military, delivery of aid kits and more. This project is about an autonomous all-electric UAV with a morphing wing design for the delivery of aid kits to survivors of natural disasters. Natural disasters result in extreme flight conditions so UAVs are useful in getting a birds-eye view of the scene and can navigate in challenging terrains to deliver first aid kits. UAVs could assess the damage zone and help coordinate first responders to plan effectively.

In the modern era, the development of UAVs being fully electric is significant as it has changed the aviation industry by paving the future path of air travel to be greener and more eco-friendly. However, pioneers have discovered methods of changing the geometry of the wing using mechanisms to increase the UAV's aerodynamic properties under different operating conditions (Bil, Massey and Abdullah, 2013). According to Galantai (2010), for a morphing wing, the flow characteristics over an aerofoil can dramatically change the magnitude of lift and drag compared to a fixed wing. It is expected that successful morphing wings will generate a high degree of adaptability, manoeuvrability, and aerodynamic efficiency. Therefore, when developing the wing design for the UAV, a morphing design is more suitable for its purpose in extreme conditions than a fixed wing. After designing the morphing wing, computational softwares can be used to simulate a UAV's aerodynamic efficiency and to enhance the optimum wing design.

4.2. Background Theory

A UAV's main structural component is the wing as this affects the aerodynamics and performance of the vehicle. Various geometries and sizes can be employed for designing a UAV's wings based on their intended use such as for defence and rescue. According to Alejandro Hugo, and Darío Rodríguez (2018), the wing geometry and operating speed for the mission have an impact on the aerodynamic properties, affecting the longitudinal stability of the UAV. Wings can be designed with a straight or curved leading or trailing edge and others can be tapered so that the wingtip is narrower than the root. Generally, modern wingtips are designed to be a curve or a point to minimize drag and turbulence.

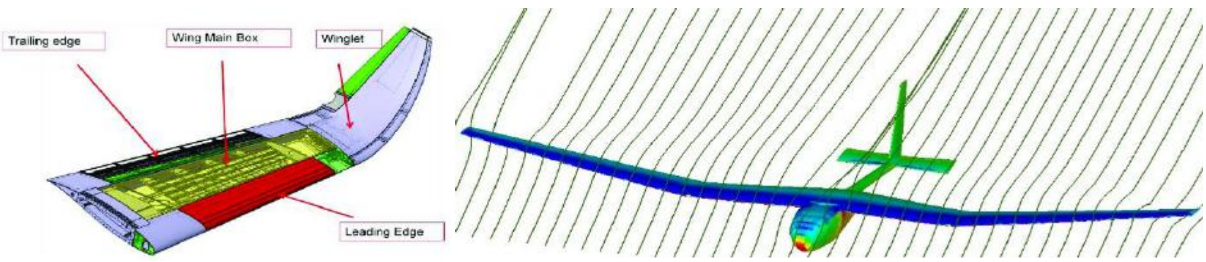

Figure 60: Wing Structure (left) (Messina, 2018) and UAV Aerodynamic Analysis (right) (Hanleyinnovations.com, 2014)

UAVs have an aerodynamic load acting on the wing due to the aerodynamic pressure differences and viscous forces. When the UAV is flying at high velocities, it becomes dynamically unstable due to the development of turbulence on the wing's surface. Engineers have reported that when the temperature of the aircraft increases during flight, the structural load bearing capacity decreases due to the buckling phenomenon (Zhang and Bisagni, 2021). The Civil Aviation Authority has enforced engineers to conduct multiple dynamic and static stability and aerodynamic analyses as shown in Figure 60 to investigate if the UAV is capable to complete the task in extreme conditions.

4.2.1 Morphing Wing

In the aviation industry modern aircrafts are designed with morphing wings to increase adaptability for extreme flight conditions. The word ‘morph’ originates from the Greek word ‘morphos’ which translates to ‘shape’ but in the current English language, it is defined as the ‘ability to transform shape or structure’ (Sofla, A.Y.N et al. 2010). Pioneers have proved that morphing wings have increased an aircraft’s performance significantly. The morphing wings allow the UAV to adapt to extreme flight conditions whilst increasing the aerodynamic efficiency. According to Sofla, A.Y.N et al. (2010), there are many types of morphing wings such as span-wise, variable-sweep, forward-sweep, backward-sweep, folding and twisting. Each type of morphing has a different significance and purpose for flight. These alterations optimise the aerodynamics for specific flight conditions such as take-off, landing and cruise.

After discussing the types of morphing wings in SOTA, it was concluded that the spanwise and folding morphing wings will increase the UAV’s performance. Span-wise morphing is the variation in the dimensions of the wing according to the flight conditions. Barbarino et al. (2011) said that by changing the dimensions, the aspect ratio changes which affects the aerodynamic efficiency. When the wingspan increases, the UAV’s aspect ratio increases as does the UAV’s flight endurance and lift. The folding morphed wing is bio-inspired by birds as they can fold and tuck their wings to create a new wing geometry while maintaining its aerodynamic performance. When the UAV’s wings are folded, the geometry and the aspect ratio are altered, thus affecting the climb rate, stall angle and laterally stability. Lockheed Martin has researched and proved that UAVs with folding wings have positively affected the lateral and longitudinal stability during take-off and landing as the wingtip vortices are significantly reduced thereby keeping the possibility of stall minimum (Li et al., 2018). Therefore, the use of folding wings on the UAV would increase the flight range and endurance which increases the chance of completing the mission.

4.2.2 Aerodynamics

The concept of airflow patterns around aerofoil and wings is a complex theory to understand but it is crucial in fundamental aerodynamics. On an aircraft, the four main aerodynamic forces acting on the wing are drag, lift, thrust and weight. These aerodynamic forces enable us to calculate moments, giving a greater understanding of the motion of air flow around the wing. As shown in Figure 61, thrust is a mechanical force exerted in the direction of motion of the aerofoil from the leading edge and drag is the force exerted opposing the direction of motion from the trailing edge. Thrust is generated from the propulsion system of the UAV and drag is the resistance force and is proportional to the flight speed. The lift force and weight are exerted perpendicular to the drag force from the upper and lower surface of the aerofoil respectively

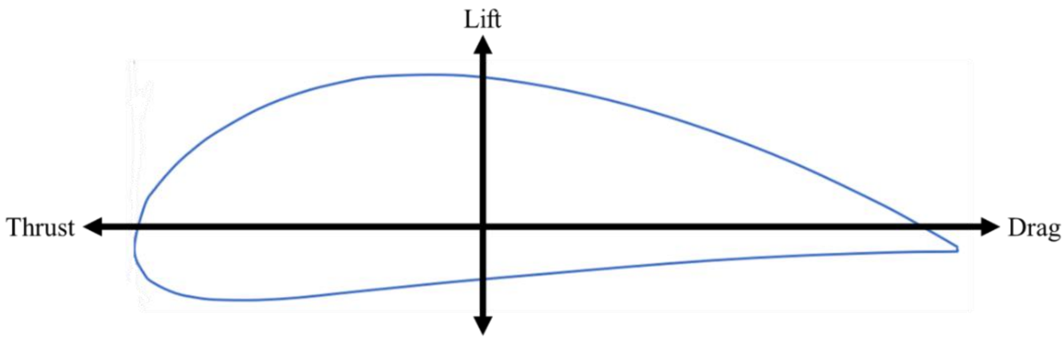

Figure 251: Aerodynamic Forces acting on an NACA4412 aerofoil

Airflow around a UAV wing can be characterised into three main types of boundary layers: laminar, transitional, and turbulent. When the airflow and pressure distribution are equal above and below the surface, it is known as laminar flow. Figure 62 shows that when the angle of attack increases at the leading edge, the airflow is laminar but at the trailing edge the flow develops into a turbulent flow, creating laminar separation. The stability of the boundary layer increases when the transition from laminar to turbulent flow occurs towards the trailing edge. This is known as the transitional boundary layer. Due to the pressure difference, the flow on the upper surface at the leading edge is laminar. Based on Crivellini et al. (2014), Figure 62 shows when the flow travels along the surface, the flow separates resulting in a laminar separation bubble as the laminar boundary layer has low kinetic energy, creating a shear layer. The free stream flow conserves momentum during the separation where the flow later becomes turbulent when joining at the trailing edge. (Abbott et al,. 1959). When the aerofoil is at the critical stall angle, the flow is turbulent, and the UAV becomes in free-fall. If the point of the transition flow occurs towards the leading edge than the trailing edge, the aerofoil reaches its stall angle quickly which means that the drag increases and lift decreases. This is an extremely dangerous manoeuvre in aviation.

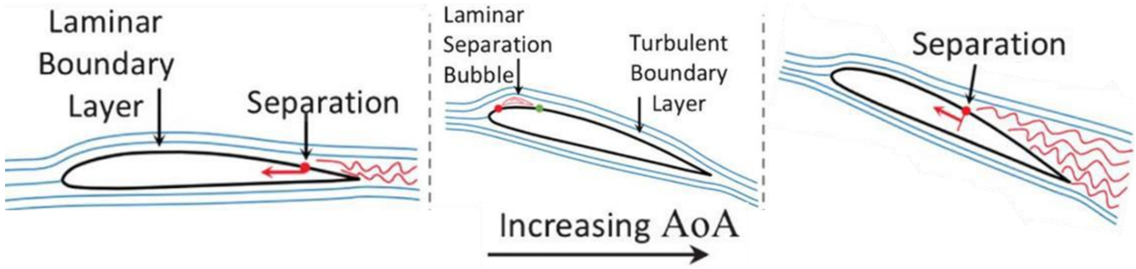

Figure 62: Boundary layer at different angle of attack (Winslow et al., 2018)

4.2.2.1 Lifting Line Theory

In real-life, the airflow over a UAV wing is three-dimensional compared to the airflow around an aerofoil as it is two-dimensional as explained above. When there is a high and low pressure of airflow on the lower and upper surface respectively, the lift force is generated along the wing due to the pressure gradient. Figure 64 shows that along with the wingspan high pressure airflow travels towards the wingtip, creating a vortex. Based on Reid, (2020), a vortex is a spiral of high-pressure air, which dissipates behind the wing to generate induced lift by a circulation of airflow. This concept of circulation induced lift is known as the Lifting-Line Theory.

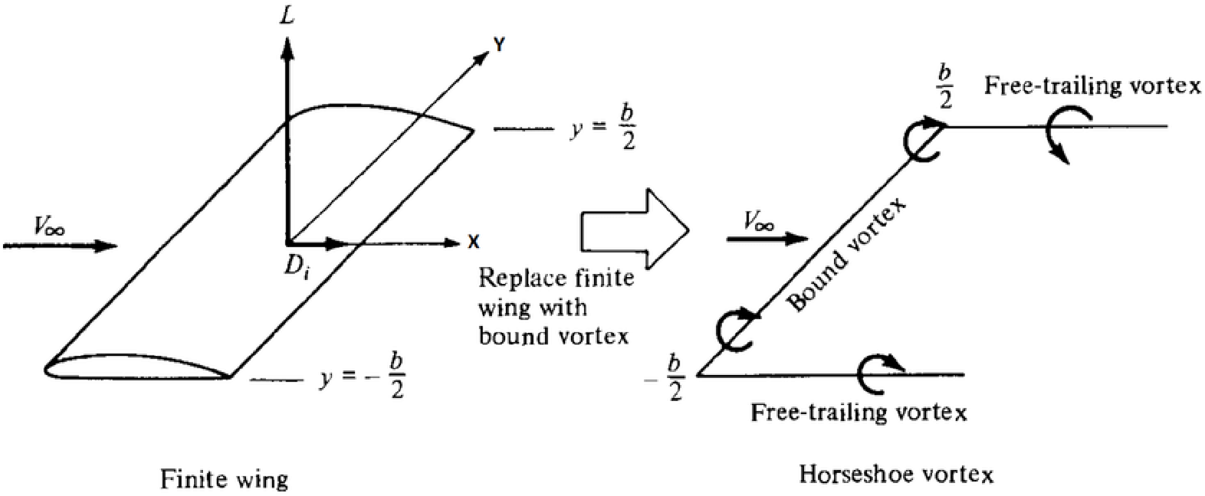

Figure 63: Circulation along the wingspan (Jose Rodolfo Chreim, 2016)

Ludwig Prandtl established the 'Lifting Line Theory' in the 1900s to calculate the circulation of airflow along the wingspan. He hypothesized that for a 2D finite wing, each spanwise section generates a lift which is equivalent to the circulation generated for each section of a 3D infinite wing (Corda S, 1958). For each region of the 3D wing, the relative velocity of the circulation allows calculating the perpendicular vertical lift force generated. This is known as the Kutta-Joukaswi two-dimensional vortex lifting law (Milne-Thomson, L. M. (1973). Equation 81 is used to calculate the lift distribution for each three-dimensional wing region. In this equation, L′(y) is the lift per span, ρ is the fluid density, V is the free stream velocity, and (y) is the circulation distribution.

$$L'(y) = \rho V_\infty \Gamma(y) \tag{81}$$

As shown in Figure 63, using Equation 81, the lift distribution over a three-dimensional wing can be calculated by integrating the lift per span of the 3D wing.

$$L = \int_{-\frac{b}{2}}^{\frac{b}{2}} L'(y)dy \ = \ \rho V_\infty \int_{-\frac{b}{2}}^{\frac{b}{2}} \Gamma(y)dy \tag{82}$$

4.2.2.2 Drag

Drag is a resistance force generated by the vortex which opposes the direction of the UAV's motion. Ludwig Prandtl has demonstrated that the drag force can be calculated from the lift generated as the lift distribution is directly proportional to the induced angle of attack as shown in Equation 83 and Figure 64.

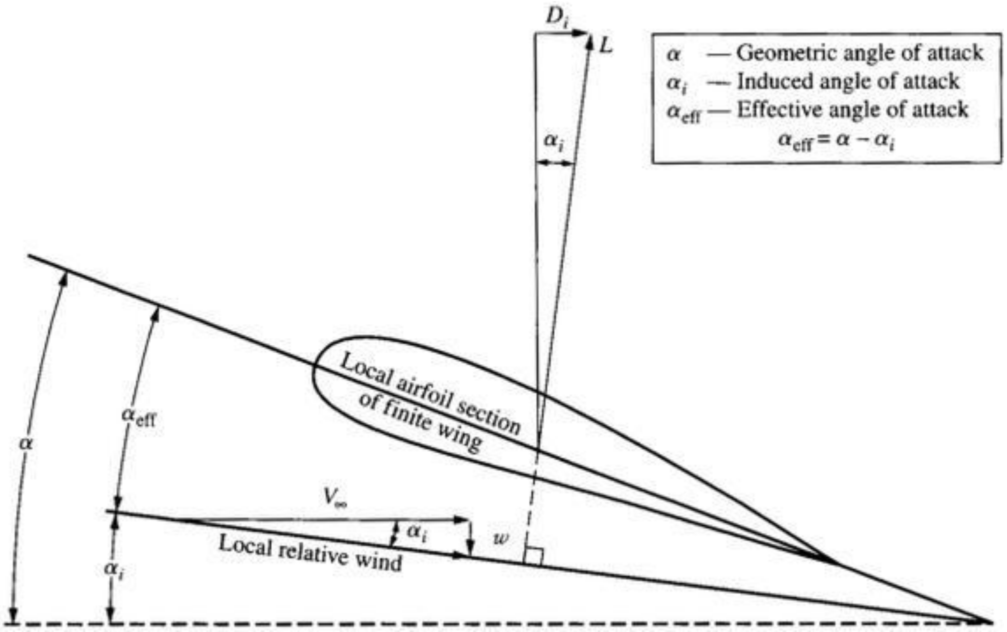

Figure 64: Relationship between Lift and Induced angle of attack (Anderson et al, 2001)

$$\propto_i = \frac{C_L}{\pi e AR} \tag{83}$$

The coefficient of lift is denoted as 'C_L' and the induced angle of attack is denoted as '$\propto_i$' in Equation 83. In the same equation, 'e' is denoted as the Oswald efficiency number otherwise known as the span efficiency factor. The Oswald efficiency number determines the change in drag to lift ratio across a three-dimensional wing as the geometry of the wing is related to the aspect ratio which affects the aerodynamic efficiency while the aspect ratio is the proportion between the wingspan and the mean chord of the wing. According to Corda S, (1958). Prandtl experimented to measure the drag force on seven rectangular wings by varying the aspect ratio to give a better understanding of the effects of aspect ratio and drag. In his investigation, he concluded that when the aspect ratio increases, lift generated across the wing increases with drag reducing at the root. In 1902, Samuel Langley stated that a craft 'of fixed size and weight would need less propulsive power the faster it flew' due to the induced drag creating a greater lift to drag ratio (Fehrm, B., 2017). The induced drag is directly proportional to the lift force as shown in Equation 84 and Figure 64 because the energy of the airflow is converted into the downward force at the vortices for the wingspan.

$$D_i = L \propto_i = L \frac{C_L}{\pi eAR} \tag{84}$$

$$C_{di} = \frac{{C_L}^2}{\pi eAR}$$

The total drag coefficient is calculated by:

$$C_D = C_d + C_{di} = C_d + \frac{{C_L}^2}{\pi eAR} \tag{85}$$

According to equation 85, the total drag coefficient is proportional to the lift coefficient squared. For a symmetrical aerofoil wing, the lift and drag coefficient will be zero as the pressure distributed above and below the wing will be balanced as there is no pressure gradient. However, for an unsymmetrical, cambered aerofoil wing, the lift to drag ratio will be greater than one because when the aspect ratio and the span efficiency vary, the pressure around the wing changes, respectively.

4.3. UAV's Preliminary Design Requirements

The preliminary parameters for the UAV have been decided as the purpose of our UAV is to help first responders with search and rescue missions in the aftermath of natural disasters. First responders say that the 'chance of survival is drastically reduced within the first 72 hours' which would result in death. The UAV will entail deploying emergency aid and searching for survivors via infrared thermography. To complete these difficult missions, the UAV must be aerodynamically efficient to fly in extreme conditions such as in strong wings and forecasts and designed to have a high strength to weight ratio and fracture toughness.

Structural integrity is a key factor when designing the UAV as the wing should be about to withstand the take-off weight and load weight without being damaged or deformed. According to Megson, T.H., (1990), a UAV should be able to carry two types of loads which are the ground load and air load. The ground load is the weight of the UAV when landing without the payload while the air load is the combination of the payload and the aerodynamic load on the UAV. To withstand these loads, the UAV should be designed with an optimum material which improves the durability and the efficiency of flight (Findlay et al.,2002). Fatigue, fracture, and deformation are key factors causing the structural failure in the UAV, which would increase the loss of lives as time is of the essence in critical situations. To ensure these factors do not affect the flight, certain design parameters for the UAV are fixed as shown in Table 17.

Table 17: UAV's design requirements

Parameters	Requirements
Structural Type	VTOL
Number of Propellers	4 Vertical and 4 Horizontal
Flight Range	80km - 100km
Flight Endurance	100 mins – 110mins
Flight Speed	100kmh
Payload	10kg

4.4. Aerofoil Design Choices

The aerofoil is the wing profile, a specific cross-section shape for a UAV's wing. This design parameter is particularly a crucial factor as it determines the correct aerodynamic characteristic for its performance. The aerofoil determines the approximate lift, drag, stall and flow for the UAV. National Advisory Committee for Aeronautics (NACA) has established a variety of aerofoils with different profiles based on the chord length, dimensions and positioning of the maximum camber and maximum thickness as shown in Figure 65. NACA divided the profiles into 4 or 5 digits aerofoils. The first number is the maximum camber in the percentage of the chord, the second and third digits are the distance from the leading edge to the maximum camber in tenths in the chord while the fourth and fifth digits are the maximum thickness of the aerofoil as a percentage of the chord.

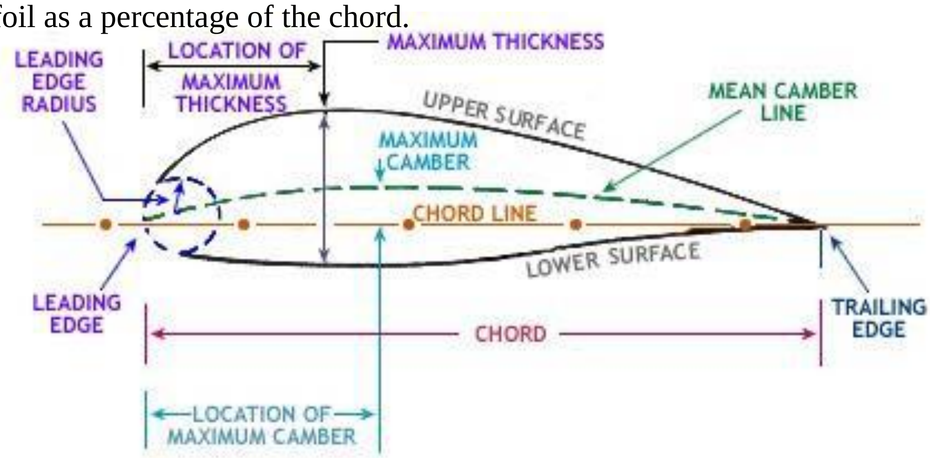

Figure 65: Aerofoil design characteristics (Geometriccae Engineering Services, 2018)

The thickness of the aerofoil affects the aerodynamic efficiency. For a UAV, an aerofoil with the minimum thickness would be beneficial as the weight of the wing decreases but this would decrease the structural integrity of the wing. Based on Somers, (2005), when the aerofoil thickness increases, the stiffness increases and the sensitivity to root-bending moments decreases, reducing the possibility of structural failure. However, aerodynamically a thicker aerofoil would not be efficient as it would generate greater drag as the number of vortices produced will increase. Changing the aerofoil thickness affects the point of transition between laminar to turbulent flow (Dongli et al., 2015). The transitional region must be nearer to the trailing edge than the leading edge so the flow around the aerofoil is mostly laminar. To a certain thickness, the flow separation can be resisted which reduces the chance of the UAV stalling and losing its stability.

4.4.1 Aerofoil Thickness analysis

The appropriate aerofoil thickness was determined by running an aerodynamic analysis using XFLR5. XFLR 5 is a computational software analysing aerofoils and the 3D design of wings using the Lifting Line Theory and 3D Panel Method. Six symmetrical aerofoils were chosen from the NACA aerofoil directory with thicknesses varying from 6% to 16% of the thickness. On XFLR5, the 2D cross-section of the NACA aerofoils was designed to run an 'XFoil Direct Analysis'. The parameters set for this analysis are shown below in Table 18.

Table 18 - XFoil Direct Thickness Analysis parameter

Parameter	
Velocity	100kmh
Reynold Number	2000,000
Angle of Attack	-20°to 20°

Figure 66 is a graph showing the effect of the aerofoil's efficiency whilst varying the aerofoil's thickness at a different angle of attack varying from -20° to 20°. It is evident that as the aerofoil thickness increases, the lift to drag ratio and angle of attack increase. This is because the radius of the leading edge of the aerofoil increases making it smoother, creating the laminar bubble to resist the flow of separation according to Chang, (1970). However, Figure 66 shows that as the angle of attack increases, the lift-to-drag ratio decrease. This is because when the aerofoil thickness increases, the flow separation occurs at the trailing edge creating vortex drag. Comparing all aerofoils, the NACA0006/NACA0008/NACA0010 would be the least suitable aerofoil for the UAV as it does generate a maximum lift and drag. Specifically, the NACA0006 and NACA0008 cannot be considered because the aerofoils reach their critical stall angle quickly which is extremely dangerous for our UAV's purpose. However, the NACA0012, NACA0014 and NACA0016 aerofoils have produced comparable results as they reach the optimum lift-to-drag ratio of around 90. All three aerofoils would be suitable for the UAV as they would be aerodynamic. However, a UAV is a light aircraft and one of its main parameters is weight as the UAV should be able to manoeuvre smoothly and rapidly.

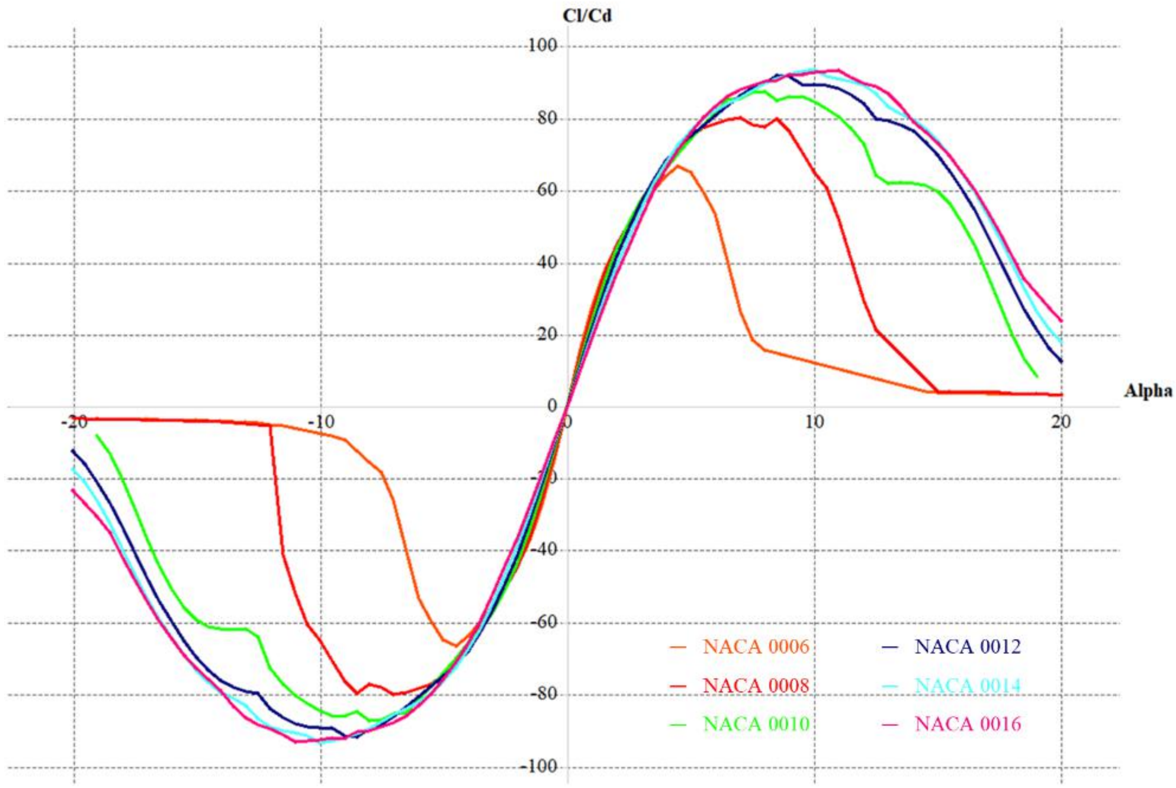

Figure 66: Lift-to-drag ratio for symmetrical aerofoils at different thickness from XFLR5

For extreme flight conditions, the UAV's wing structural integrity must be rigid as it should be able to withstand aerodynamic loads. The gross mass of the UAV exceeds its limits when the aerofoil increases which is caused by the increase in thickness. As the result, the wing could undergo deformation and structural failure which affects the aerodynamic efficiency. Caesar Wiratama, (2021), the author evaluated eight symmetrical aerofoils from NACA0006 to NACA0020 for every 2% thickness for lift-to-drag ratio at various angles of attack between -20° to 20° The external source Figure 67 shows a similar trend to Figure 66. These research results validate my results, making them dependable and thus can be used to select the suitable thickness of the aerofoil.

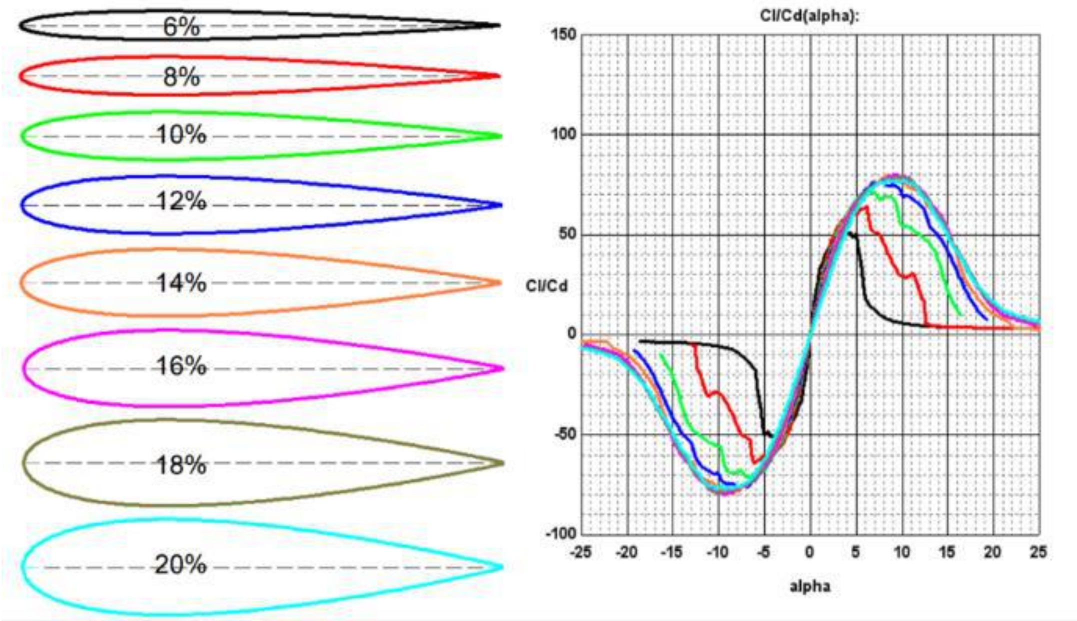

Figure 67: Lift-to-drag ratio for different thickness of symmetrical aerofoils (Caesar Wiratama, 2021)

To conclude the NACA0012/NACA0014/NACA0016 aerofoil has similar aerodynamic characteristics therefore it is sensible to use the aerofoil with the minimum thickness. Therefore, an aerofoil with a maximum thickness of 12% would be selected for the UAV.

4.4.2 Types of 2D NACA Aerofoil geometry

For the UAV, it is decided to choose an aerofoil from the NACA directory. As explained above, the NACA aerofoil should have a thickness of 12%. To investigate which aerofoil would be suitable for the UAV's wing, three aerofoils were chosen varying from symmetrical to asymmetrical where the aerofoil is cambered. The three chosen aerofoils are NACA0012, NACA2412, and NACA4412 as displayed in Figure 68.

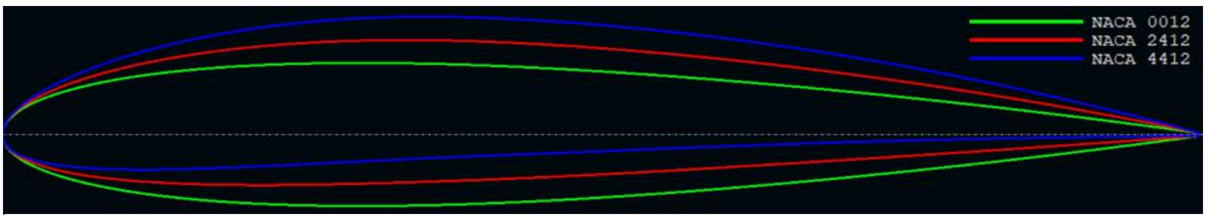

Figure 68: 2D cross-sectional view of the three NACA aerofoils designed on XFLR5

The suitable NACA aerofoil was determined by running an aerodynamic analysis using XFLR5. On XFLR5, the three chosen aerofoils were designed to run 'XFoil Direct Analysis' to compare the aerodynamic characteristics. The same parameter was set for analysis from Table 18.

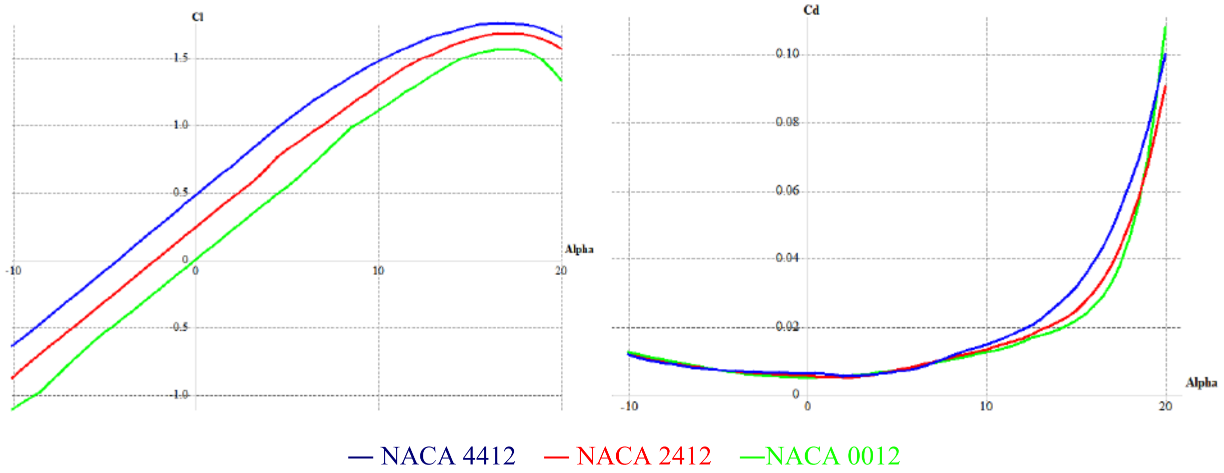

Figure 69: Coefficient of Lift (right) and Drag (left) at varying angle of attack

From the XFLR5 computation, Figure 69 shows the coefficient of lift and drag at a different angle of attack for different aerofoils, from this data it is evident that each aerofoil exhibits distinctive characteristics. As seen in Figure 69, NACA4412 aerofoil generated a greater lift at the same angle of attack in comparison to the NACA0012 and NACA2412 aerofoils as the graph proves that NACA4412, NACA2412 and NACA0012 have a lift coefficient of 1.72, 1.68 and 1.55, respectively. Figure 69 represents the drag coefficient for each aerofoil at a different angle of attack. All three aerofoil have a similar coefficient of drag between the angle of attack of -10° and 10°. At 20°, NACA0012 has a greater drag than the NACA4412 and NACA2412 has a drag coefficient of 1 and 0.92, respectively.

NACA4412 has a camber ratio of 4% which is greater compared to the other aerofoil which affects the UAV’s aerodynamic performance because when the camber ratio of the aerofoil increases there is a greater pressure gradient, causing the greater lift to be generated. This is due to the difference in momentum of airflow around the aerofoil. In the late 1800s, Philip W F, et al (2000) said ‘aerofoils with better curvatures, produce better lift coefficients and aerodynamics efficiency’ which supports the results from Figure 69. It is assumed that when the UAV is flying under cruise conditions, the angle of attack is 0°. This graph clearly shows that when the aerofoil is at an inclination of 0°, the NACA4412, NACA2412 and NACA0012 have a lift coefficient of 0.5, 0.25 and 0, respectively. NACA0012 generated no lift due to the pressure gradient being zero because the pressure on the upper and lower surface of the aerofoil was counteracted equally whereas the other aerofoil had a pressure gradient due to the cambered geometry of the aerofoil.

The aerofoil with a greater camber at the trailing edge is more aerodynamically efficient when travelling at a Reynold number of $2X10^6$. At a high Reynolds number, the aerodynamic coefficient is higher because of the kinematic viscosity of the airflow. Across the aerofoil, the air modules collide multiple times generating momentum when the energy in the airflow is too high to dissipate (Jain, Sitaram and Krishnaswamy, 2015). Therefore, eddy currents are produced on the wing, generating turbulence when the angle of attack increases to induce lift. At this high Reynold number, the graph shows that all the aerofoils have the same critical stall angle of 17° at different coefficients of lift because the boundary layer of separation is assumed to be towards the trailing edge. Ravi Jain and Usman Mohammad (2018), the authors simulated the NACA0012 and NACA4412 on CFD using the K-epsilon model with a Reynold Number of $3x10^6$ to compare the aerodynamic performance. The external results show a similar coefficient to the results from the XFLR5 simulations. For the NACA4412 aerofoil, at the angle of attack 5° and 10° have a lift coefficient of 1 and 1.5, respectively. As the aerodynamic values are like my results, therefore the results produced are valid and precise. From both figures displaying the coefficients of lift and drag, it is shown that the NACA4412 aerofoil is the most suitable aerofoil for the UAV due to its aerodynamic characteristics.

4.4.3 XFLR Wing analysis with the desired aerofoil

From the 2D aerofoil analysis, the results prove that the NACA4412 aerofoil is the most efficient and suitable aerofoil for the UAV's wing due to its cambered geometry. A wing is three-dimensional and there are several types of geometry such as elliptical, rectangular, and tapered. Using the XFLR5, a 3D wing was designed using the NACA4412. However, in this analysis, the elliptical wing was not experimented with as the Aeronautic Society mentions that the Supermarine Spitfire was designed with an elliptical wing which had a uniform lift distribution causing the aircraft to stall instantaneously, potentially losing its stability and control (Ackroyd, J., 2013). Therefore, a rectangular and tapered wing was designed using the desired aerofoil for a 'wing and plane analysis' by changing the 'offset2' and 'chord2' parameters as shown in Figure 70.

	y (m)	chord (m)	offset (m)	dihedral(°)	twist(°)	foil	X-panels	X-dist	Y-panels	Y-dist
1	0.000	0.370	0.000	0.0	0.00	NACA 4412	300	Cosine	300	-Sine
2	2.810	0.370	0.000		0.00	NACA 4412				

	y (m)	chord (m)	offset (m)	dihedral(°)	twist(°)	foil	X-panels	X-dist	Y-panels	Y-dist
1	0.000	0.370	0.000	0.0	0.00	NACA 4412	300	Cosine	300	-Sine
2	2.810	0.185	0.185		0.00	NACA 4412				

Figure 70: Rectangular (above) and Tapered (below) wing design dimensions

Assuming the UAV is at cruise, the free stream velocity was fixed as 27.778ms^{-1} (~100kmh) at the angle of attack of 0°. In this simulation, the 'Lifting Line Theory' model was used to calculate the lift distribution and the downwash drag generated across the wingspan.

4.4.3.1 NACA4412 Rectangular Wing

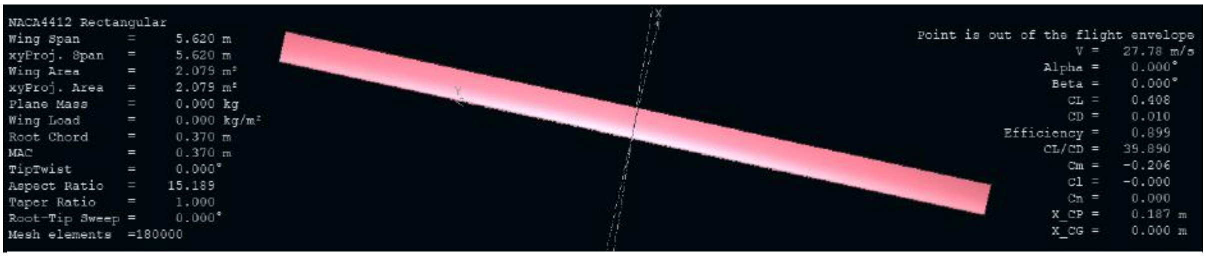

Figure 71: 3D Rectangular NACA4412 Wing with theoretical parameters

Theoretical Calculations using the computation parameters in Figure 71.

Aspect Ratio:

$$\mathrm{AR} = \frac{\mathrm{s}^2}{\mathrm{A}} = \frac{5.62^2}{2.0794} = 15.189 \tag{86}$$

Taper Ratio:

$$\lambda = \frac{\mathrm{Chord_{Tip}}}{\mathrm{Chord_{Root}}} = \frac{0.37}{0.37} = 1 \tag{87}$$

Lift Efficiency Factor:

$$\delta = \frac{1 - \mathrm{e}}{\mathrm{e}} = \frac{1 - 0.899}{0.899} = 0.11235\ (5\mathrm{s.f}) \tag{88}$$

Lift Induced Drag using equation 84:

$$\mathrm{Cd_i} = \frac{\mathrm{Cl}^2}{\pi \mathrm{AR}}(1 + \delta) = \frac{0.408^2}{\pi(15.189)}(1 + 0.11235) = 0.0038804\ (5\mathrm{s.f})$$

Parasitic Drag ($\mathrm{Cd_0}$):

$$\mathrm{Cd_0} = \mathrm{C_d} - \mathrm{Cd_i} = 0.010 - 0.0038804 = 0.0061196\ (5\mathrm{s.f}) \tag{89}$$

Total Drag:

$$\mathrm{D} = \frac{1}{2}\rho \mathrm{v}^2 \mathrm{s} \mathrm{C_d} = \frac{1}{2}(1.225)(27.778^2)(5.62)(0.01) = 26.561\mathrm{N} \tag{90}$$

Total Lift Distribution:

$$L = \frac{1}{2}\rho v^2 s C_l = \frac{1}{2}(1.225)(27.778^2)(5.62)(0.408) = 1083.7\text{N} \tag{91}$$

To calculate Circulation (Γ) using equation 83:

$$L = \rho V_\infty \int_{-\frac{b}{2}}^{\frac{b}{2}} \Gamma(y)dy$$

$$\frac{L}{\rho V_\infty} = \Gamma\left(\frac{b}{2}\right) - \Gamma\left(-\frac{b}{2}\right) = \Gamma\left(\frac{b}{2} + \frac{b}{2}\right) = \Gamma(b)$$

$$\Gamma = \frac{L}{\rho V_\infty b} = \frac{1083.7}{(1.225)(27.778)(5.62)} = 5.667\text{m}^2\text{s}^{-1}$$

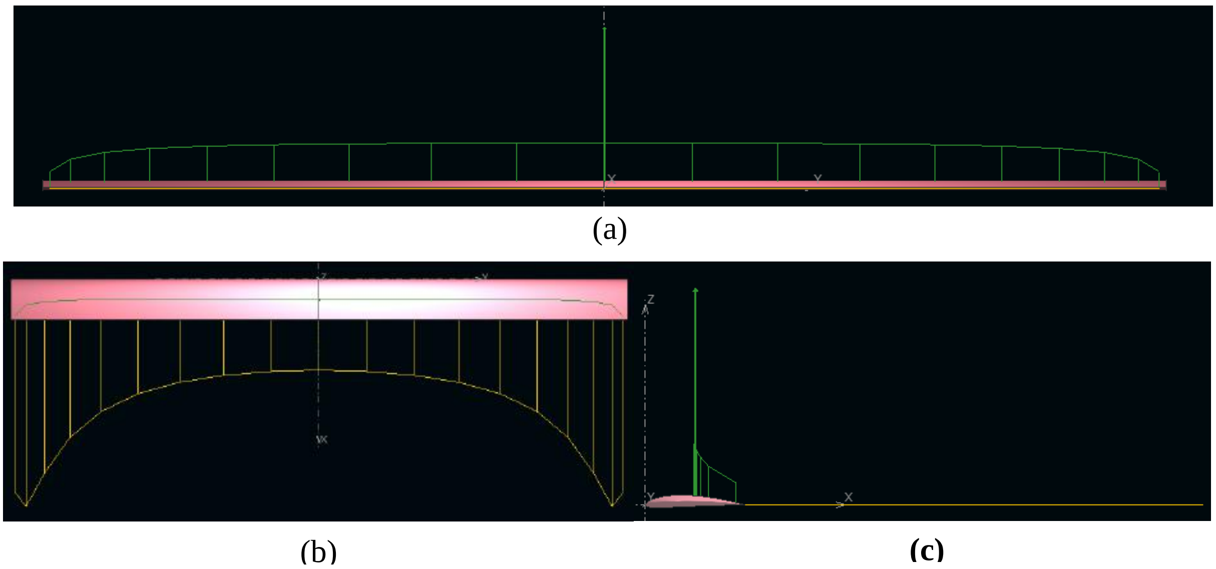

Figure 72: 3D Wing analysis of NACA4412 Rectangular, (a) is front view, (b) is the top view, (c) is a cross-sectional view. Green arrow is the lift distribution and Yellow arrow is the induced drag

4.4.3.2 NACA4412 TAPERED WING

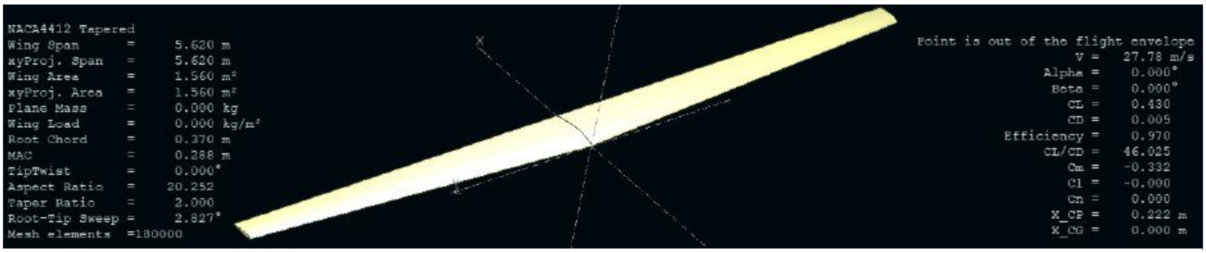

Figure 73: 3D Tapered NACA4412 Wing with theoretical parameters

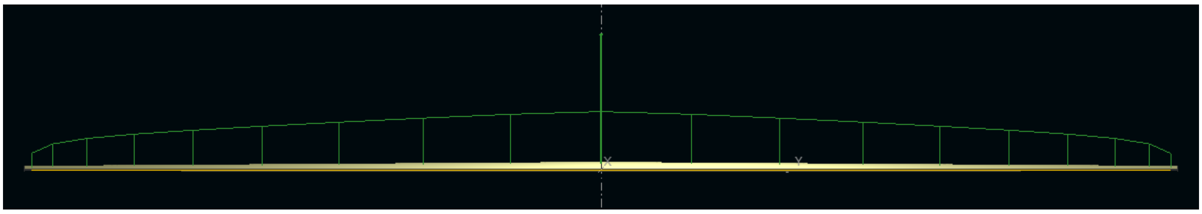

(a)

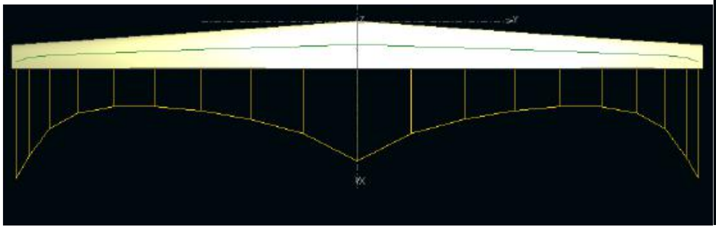

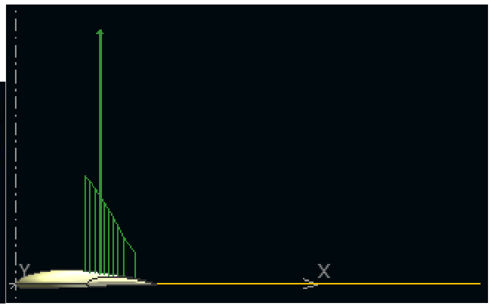

(b) (c)

Figure 74: 3D Wing analysis of NACA4412 Tapered, (a) is front view, (b) is the top view, (c) is a cross-sectional view. Green arrow is the lift distribution and Yellow arrow is the induced drag

Using Equations 88 to 91 and the XFLR5 results, the aerodynamic characteristics are calculated theoretically and presented in Table 18.

After choosing the desired aerofoil, a rectangular and a tapered wing were analysed to develop a greater understanding of the aerodynamic load distribution generated across the wingspan.

Table 18: NACA4412 Wing theoretical calculations based on XFLR5 parameters

	NACA4412 Wing	
	Rectangular	Tapered
Aspect Ratio	15.189	20.252
Taper Ratio	1	0.5
Lift efficiency Factor	0.11235	0.030928
Lift Induced Drag	0.0038804	0.00299604
Parasitic Drag	0.0061196	0.0060040
Total Drag (N)	26.561	24.490
Total Lift (N)	1083.7	1170.1
Circulation (m^2s^{-1})	5.667	6.119

The rectangular and tapering were modelled with taper ratios of 1 and 0.5 respectively to compare which wing geometry would be aerodynamically suitable for a UAV.

Figures 71 and 73 from the XFLR5 wing analysis were used to determine the aerodynamic theoretical hand calculations. Table 18 shows that the tapered wing has a greater lift than the rectangular wing as the circulation of airflow is higher than the latter wing with values of 6.110 m^2s^{-1} and 5.667 m^2s^{-1}, respectively. As shown in Equation 82, the total circulation produced along the wingspan is directly proportional to the total lift generated. The hand calculations support this theory as the taper wing and rectangular wing generated a total lift of 1170.1N and 1083.7N respectively which is shown in Figures 74a and 72a, respectively.

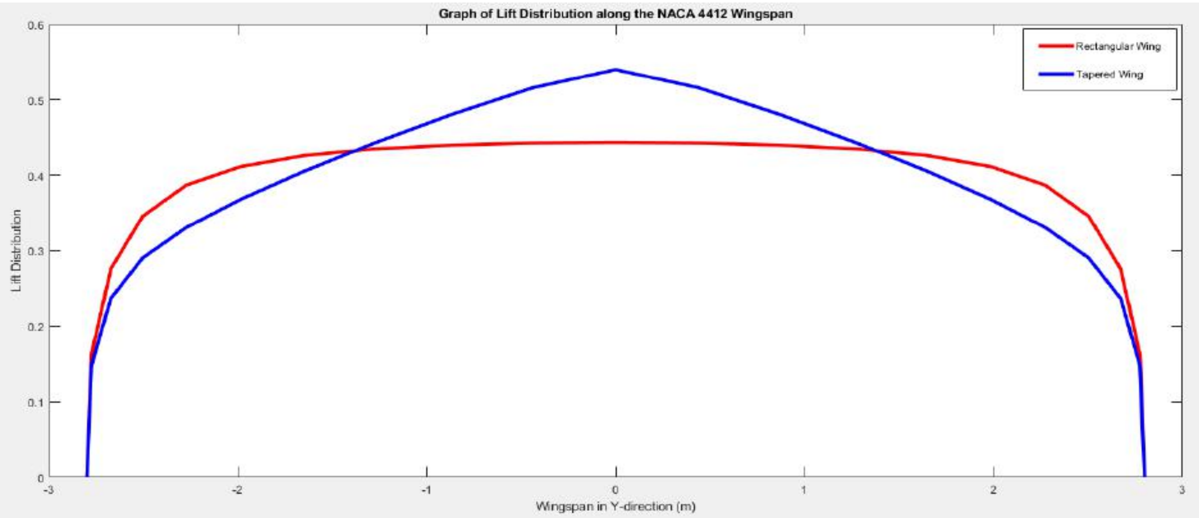

Figure 75: Graph of Lift distribution along the wingspan

Figure 75 graphically displays the lift distribution across the wingspan for both wings, similarly, shown in Figures 72a and 74a. The results show that the rectangular wing generated a uniform lift distribution along the wingspan until it reached the wingtips, and the generated lift quickly converges to zero. The first law of thermodynamics states that energy cannot be created or destroyed, so at the wingtips, the zero lift is converted into maximum drag as shown in Figures 72b and 74b (Abdul and Mousa, 2014). Compared to a rectangular wing, a tapered wing formed a non-uniform parabolic like lift distribution. Figure 74 illustrated that the tapered wing generates a maximum lift at the centre of the wingspan due to the adverse pressure gradient on the upper and lower surface, thus increasing the aerodynamic efficiency which is proved from the calculation as the tapered wing had a low lift efficiency factor of 0.03 whereas the rectangular wing has a lift efficiency factor of 0.11. According to Ibrahim et al. (2018), authors did numerical analyses using XFL5R at 10^6 Reynolds number on different tapered wing ratios ranging between 0.2 and 1.2 producing similar graphs. Figure 75 displays a slow decline in the lift towards the wingtips hence the size and the number of vortexes dissipated is reduced thus increasing the UAV's aerodynamic performance. From the wing analysis, it is evident that a tapered NACA4412 wing is more aerodynamically efficient than a rectangular NACA4412 wing.

The XFLR5 simulations on the aerofoils and the wing enabled us to choose the desired aerofoil and wing design. From the 'XFoil Direct Analysis', the NACA4412 was chosen as it is a cambered aerofoil with a maximum thickness of 12% as it would aid the UAV to be aerodynamically efficient. From the 'Wing Analysis', the NACA4412 tapered was chosen instead of the rectangular as it has a greater lift distribution on the wing, increasing the UAV's flight endurance.

4.5. Wing CAD on SolidWorks

SolidWorks is modelling computer-aided design which enables engineers to develop life size models. 2D and 3D models can be created to understand the final design of the object. Solidworks allows to modify and improve initial design plans. As part of the aerodynamic team, the 3D wing was constructed. From the XFLR5 computation results, the NACA4412 tapered wing is the desired design using the wing parameters in Table 20. The NACA4412 aerofoil XYZ coordinates in appendix are exported from the NACA aerofoil directory and imported into the 'XYZ curve coordinates'. The 2D aerofoil design surface was lofted by 2.20m to a tapered 2D aerofoil which was created on a separate plane. Then a tapered aerofoil was designed on the top plane. The aerofoil was lofted upwards by a height of 0.61m to create a morphing wingtip. The wingtip is domed with a 0.01m curvature to create a smooth wingtip. Once the NACA4421 wing was designed, the CAD was imported as a component was attached to the fuselage coincidentally. The wing CAD was mirrored on the x-axis to create another wing component. to attach to the other side of the fuselage. A design constraint was fixed on SolidWorks to ensure that the wing is parallel and coincident with the fuselage.

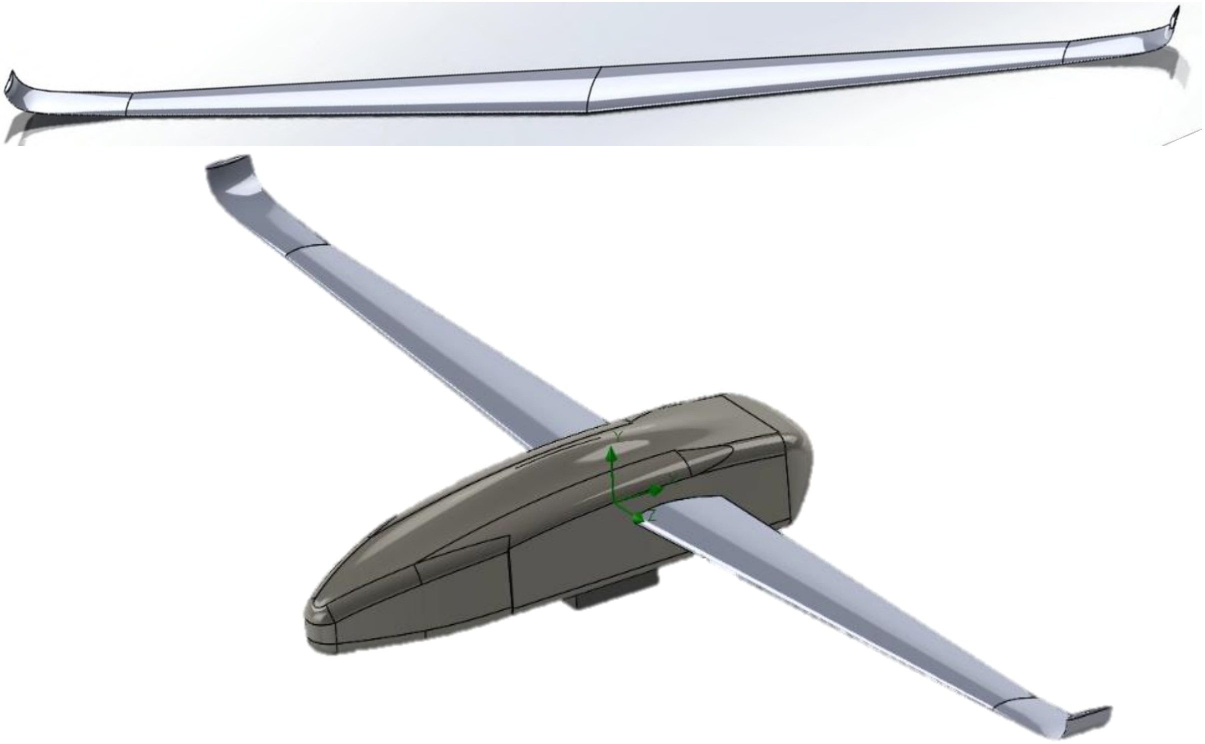

Figure 76: SolidWorks model of the NACA4412 wing and being connected to the fuselage

Table 20 – Wing Design Constraints

Wing Design Constraints	
Aerofoil Type	NACA4412
Wingspan	5.62m
Root Chord Length	0.3701m
Wing tip Length	0.1851m
Dome Curvature	0.01m
Aspect Ratio	20.25
Taper Ratio	2
Morphing Wing height	0.61m

4.6. Computational Fluid Dynamics

In the aerospace industry, computational fluid dynamic (CFD) software is frequently used by engineers to carefully understand the complexity of the airflow. CFD is a division of fluid mechanics which is combined with numerical analysis and data structures to analyse challenges with fluid flows internally and externally about the object. CFD produces accurate results for flows ranging from laminar to turbulent flows of subsonic to supersonic speeds.

Ansys is a 3D design mathematical engineering software which generates complex simulations for different purposes and aspects of engineering. In this technical report, 'Fluid Flow (Fluent)' was applied to model the airflow trajectory around the UAV. The SolidWorks design of the fuselage and NACA4412 wings were only imported to get accurate aerodynamic results of the UAV's main components.

On 'DesignModeler' an enclosure was created around the CAD with dimensions of 10m x 6m x 5m. The mesh was required to be generated for the enclosure and CAD. This enclosure was labelled using the 'Naming selection'. The 'inlet, outlet, air and UAV' was labelled on the mesh as these names will be used to set parameters for the results. The mesh size of 50mm was used to generate a fine four noded tetrahedral mesh.

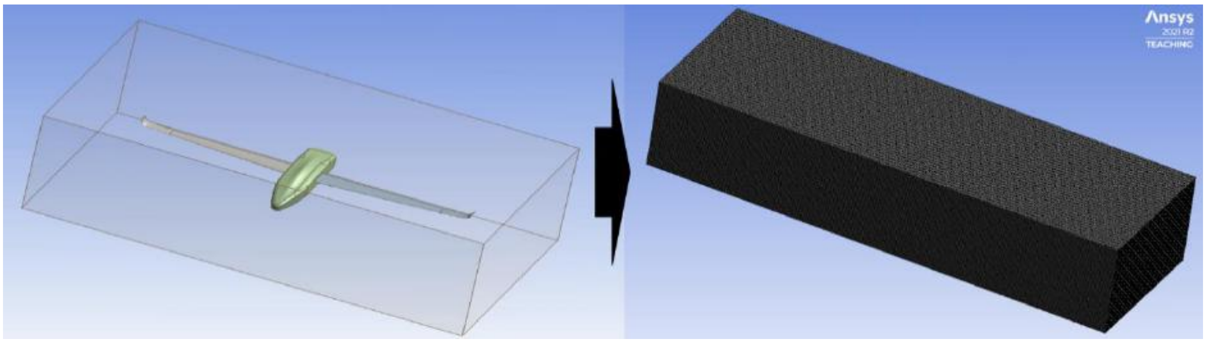

Figure 77: The enclosure is meshed to 50mm

4.6.1 CFD Numerical Method

After the mesh was created the parameters for, CFD simulations were set up. The enclosure and the solid were materialized with properties of air such as the density, ρ_{air} was taken to be $1.225kgm^{-3}$ and the material was chosen to be aluminium. The velocity of the airflow was fixed at 100kmh; therefore, the inlet free stream velocity was simulated at $27.7778ms^{-1}$. The airflow is assumed to be incompressible since the Mach number of the simulation is 0.03 which is below 0.3. Instead of using a density-based solver, a pressure-based solver is used because it produces more accurate results as the simulation is a low-speed incompressible flow (Enea. it, 2022). Density-based solvers are also valid and produce reliable simulations for high-speed incompressible flows with a Mach number greater than 0.3. A steady flow time was chosen instead of a transient flow time so the simulation can produce stable solutions with respect to time. According to Enea. it, (2022) a transient flow time could be applied however a Courant-Friedrichs-Lewy number must be calculated to be below 1 as this is not the case, and anomalies would be produced in data and contours plots.

4.6.1.1 Turbulent Model

A turbulent model must be chosen to run the simulation. There are two main types of turbulent models which are often used in CFD simulations. The two main types of models are K-epsilon (k-ε) and Spalart-Allmaras which will be discussed below.

4.6.1.1.1 K-epsilon model

K-epsilon is a two-equation model by two transport equations derived from the Reynolds Average Navier-Stokes equations, which simulates turbulent flow for the CFD simulation. (Stanford, n.d) The transport variables from these equations are the turbulent kinetic energy, where the energy in the turbulence is calculated, and the turbulent dissipation rate, where the rate of turbulent kinetic energy dissipation.

$$\frac{\partial k}{\partial t} + U_i \frac{\partial k}{\partial x_i} = \frac{\partial}{\partial x_i}\left(\frac{u_t}{\sigma_k}\frac{\partial k}{\partial x_i}\right) + u_t\left(\frac{\partial U_i}{\partial x_j} + \frac{\partial U_j}{\partial x_j}\right)\frac{\partial U_i}{\partial x_j} - \varepsilon \frac{\partial \varepsilon}{\partial t} + U_i \frac{\partial \varepsilon}{\partial x_i} \quad (92)$$

$$= \frac{\partial}{\partial x_i}\left(\frac{u_t}{\sigma_\varepsilon}\frac{\partial \varepsilon}{\partial x_i}\right) + C_{1\varepsilon}\frac{\varepsilon}{k}u_t\left(\frac{\partial U_i}{\partial x_j} + \frac{\partial U_j}{\partial x_j}\right)\frac{\partial U_i}{\partial x_j} - C_{2\varepsilon}\frac{\varepsilon^2}{k}$$

Whereas u_t is the turbulent eddy viscosity, ε is the dissipation rate of turbulent kinetic energy, σ_ε, σ_k, $C_{1\varepsilon}$, $C_{2\varepsilon}$ are empirical coefficients with fixed values depending on the simulation parameters.

4.6.1.1.2 Spalart-Allmaras Model

Spalart-Allmaras Model is one equation model which solves modelled transport equation for kinematic eddy turbulent viscosity. This model is designed for applications with wall bounded flows.

$$\frac{DF}{Dt} = \frac{\partial F}{\partial t} + (u \cdot \nabla)F \quad (93)$$

The transport equation can be written in the full form of the Spalart-Allmaras equation with three sections called Diffusion Production, and Destruction (All About CFD..., 2017). The diffusion operator is to achieve the aerodynamic flow oriented diffusion behaviour as the eddy viscosity is converted. The production operator increases the turbulent energy to increase the total viscosity and mean vorticity. The destruction operator is assumed that the eddy viscosity has the 'the ability of a turbulent flow to transport momentum' Nee and Kovaasznay, (1969).

$$\frac{\partial\tilde{v}}{\partial t}+\tilde{u_j}\frac{\partial\tilde{v}}{\partial x_j}=\underbrace{\frac{1}{\sigma}\left(\frac{\partial}{\partial x_i}(v+\tilde{v})+C_{b2}\frac{\partial\tilde{v}}{\partial x_j}\frac{\partial\tilde{v}}{\partial x_j}\right)}_{\text{Diffusion}}+\underbrace{C_{b1}\tilde{S}\tilde{v}}_{\text{Production}}-\underbrace{C_{w1}f_w\left(\frac{\tilde{v}}{d}\right)^2}_{\text{Destruction}} \tag{94}$$

Where $\tilde{v}$ is the working variable, $C_{b1}$and C_{b2} are constants, S is known as the vorticity magnitude.

The outer regions boundary layer is the decay of destruction as the behaviour is expressed in a function of f_w. The variable 'g' is a delimiter, preventing f_w becoming too large so the vorticity is not disregarded.

$$f_w(g) = g\left(\frac{1+C_{w3}^6}{g^6+C_{w3}^6}\right)^{\frac{1}{6}} \tag{95}$$

$$g = r+C_{w2}(r^6-r), \text{as } r = \frac{\tilde{v}}{\tilde{S}k^2d^2} \tag{96}$$

After comparing the study of both turbulent models, the K-epsilon model was chosen for the simulation because it produces accurate results for incompressible flow with complex geometry whereas Spalart-Allmaras produces accurate results for transonic flows over 2D designs.

As all the main aerodynamics parameters are inputted and ready for the simulation, the report files were created and saved for aerodynamic coefficients, pressure, and velocity. Before running the CFD simulation, all parameters were initialization. From the results produced, graphs and contours were created.

4.7. CFD Analysis

4.7.1 CFD Contour Plots

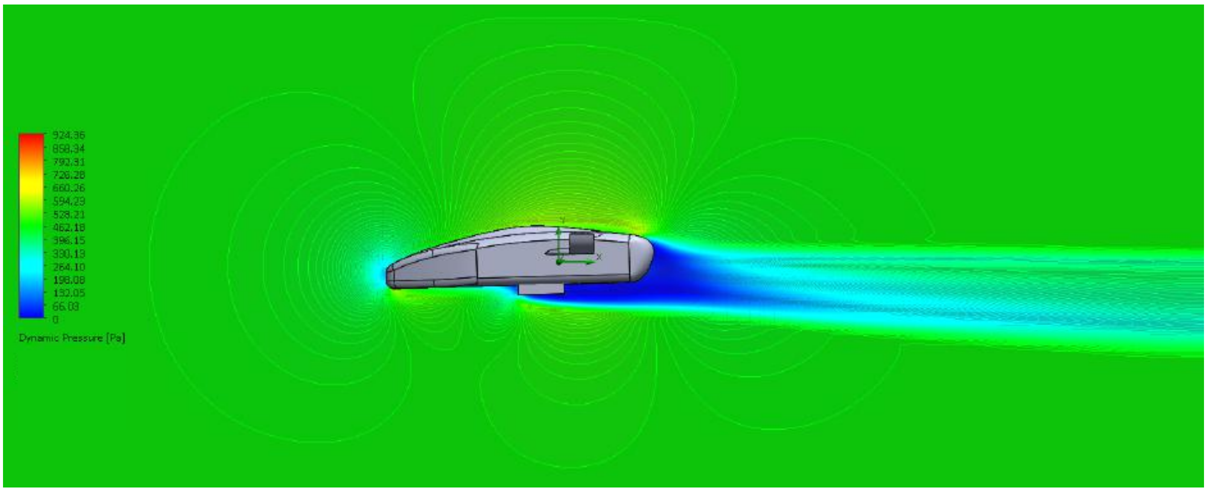

Figure 78: Dynamic Pressure Contour Plots our UAV's fuselage and NACA4412 wing

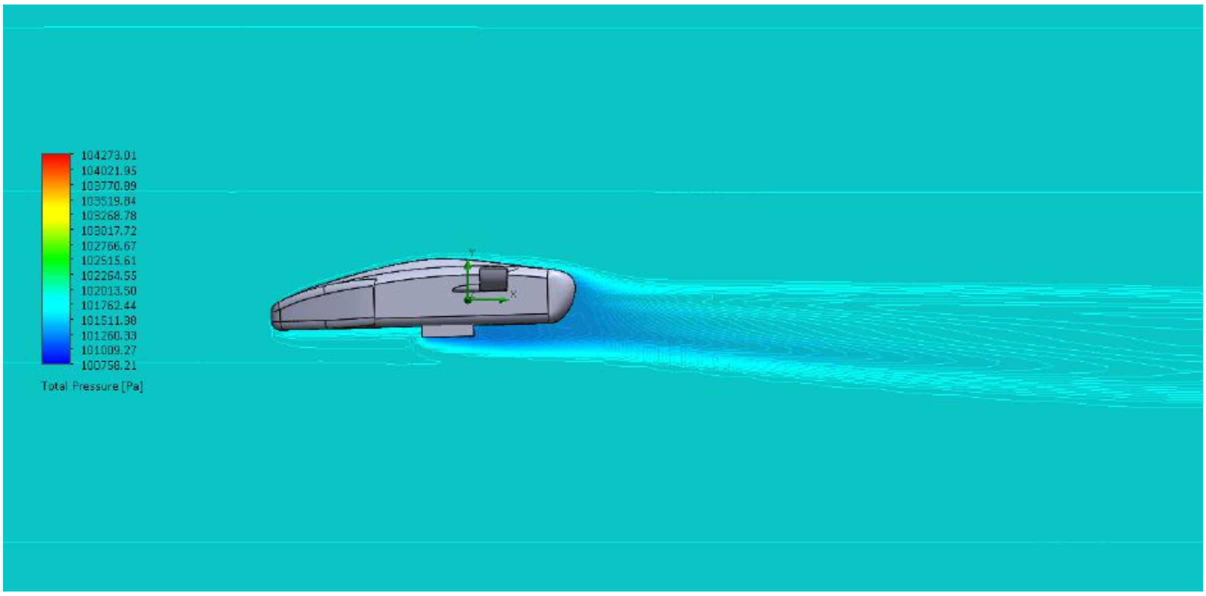

Figure 79: Total Pressure Contour Plots our UAV's fuselage and NACA4412 wing

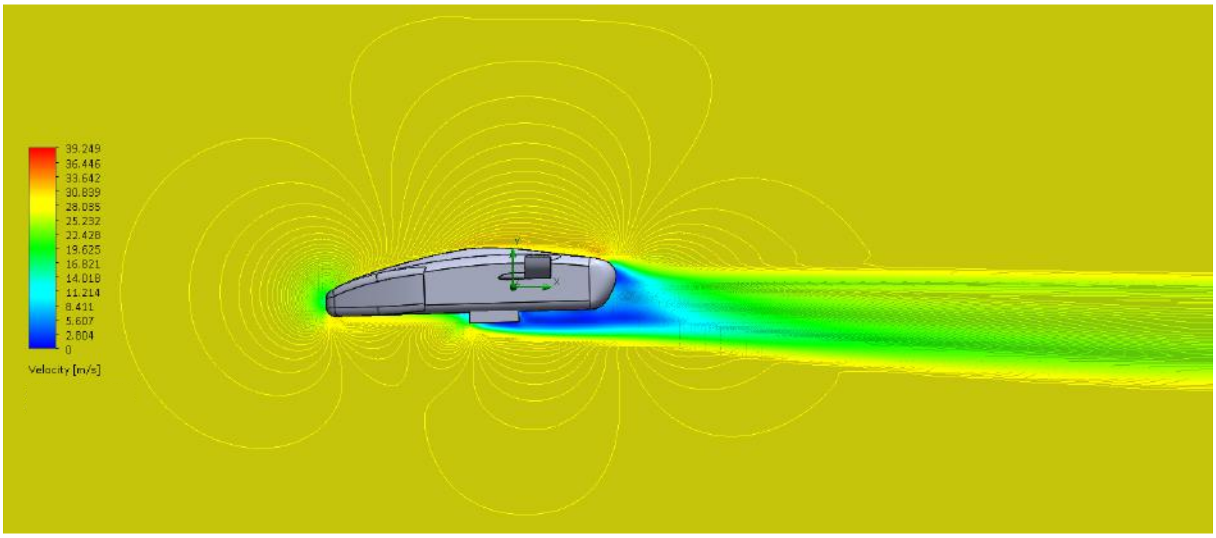

Figure 80: Velocity Magnitude Contour Plots our UAV's fuselage and NACA4412 wing

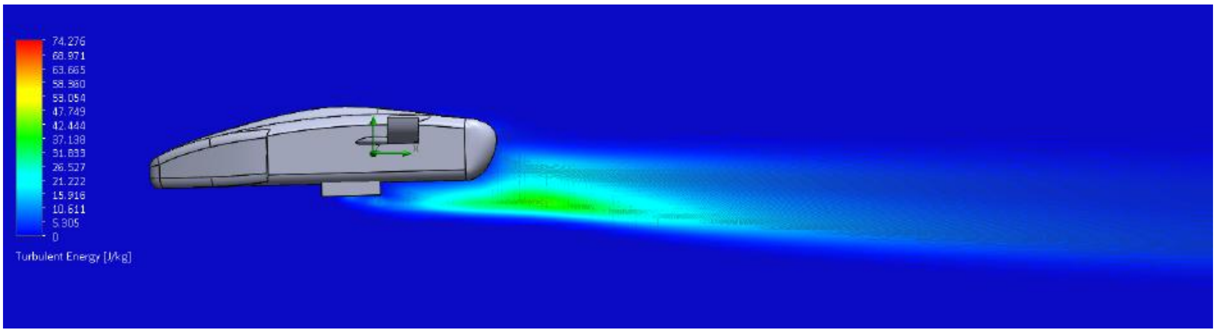

Figure 81: Turbulent Energy Contour Plots our UAV's fuselage and NACA4412 wing

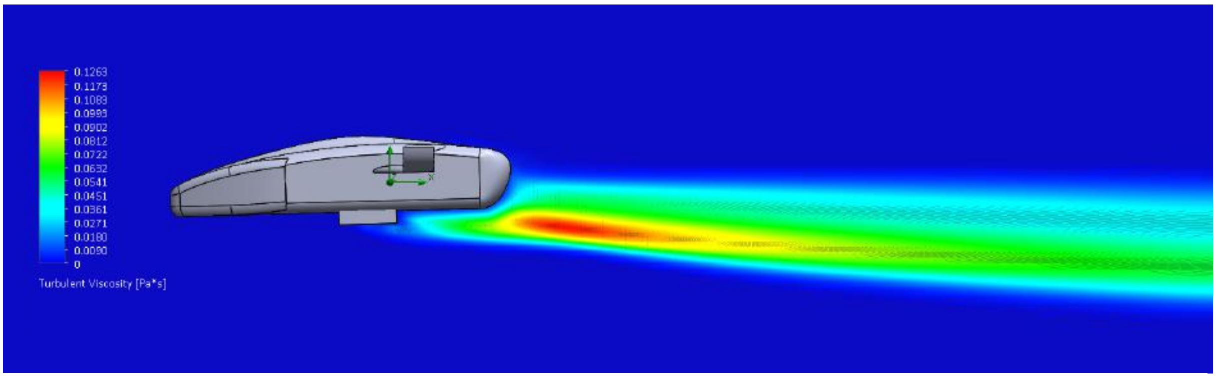

Figure 82: Turbulent Viscosity Contour Plots our UAV's fuselage and NACA4412 wing

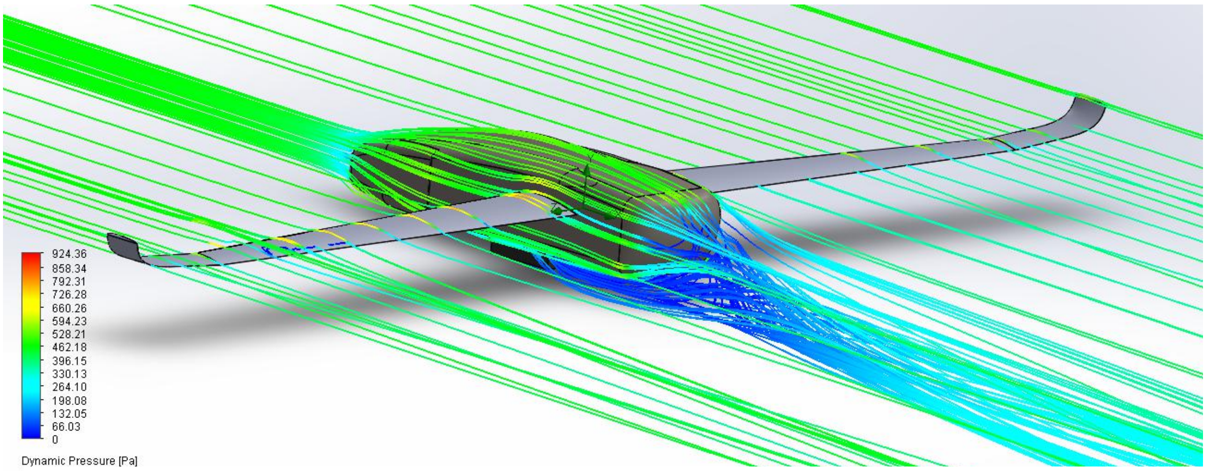

Figure 83: Flow trajectory of Dynamic Pressure

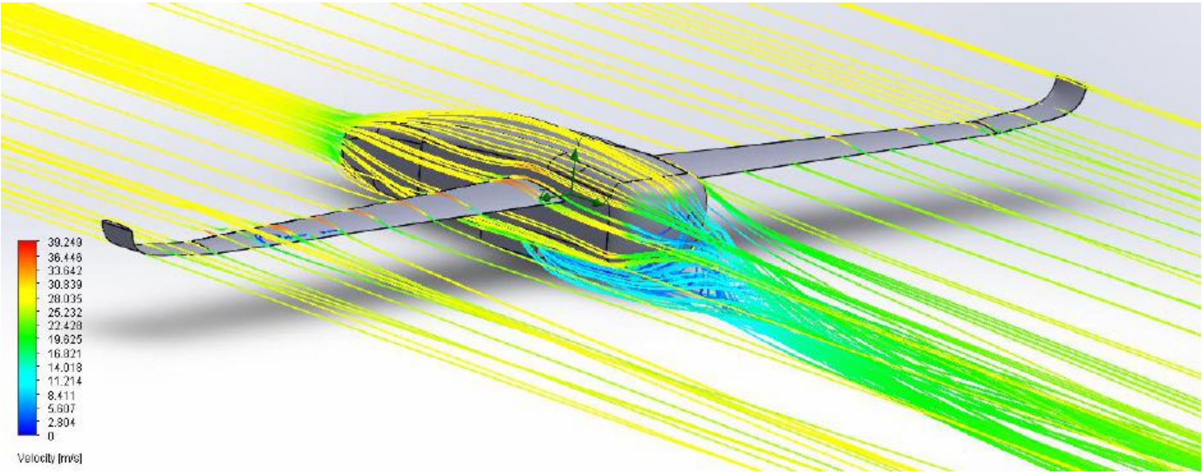

Figure 84: Flow trajectory of velocity Magnitude

4.7.2 Flow Trajectory Animation (Click on the factors to see the animation video on Google Chrome)

- Dynamic Pressure
- Turbulence Energy
- Velocity Magnitude

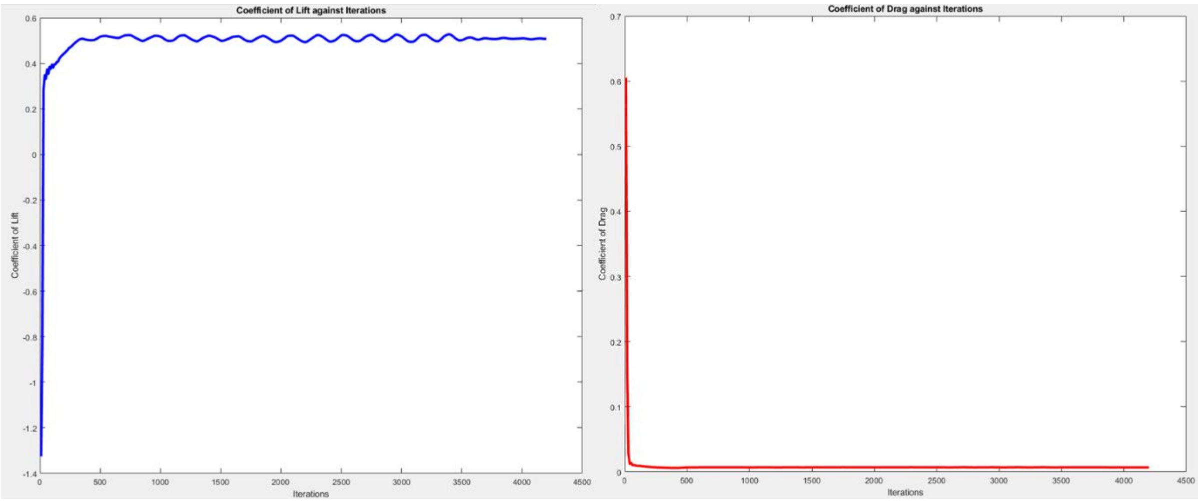

Figure 85: Graph representing the coefficient of lift (left) and drag (right) against the iterations

The CFD simulated results for the UAV's fuselage and the wing using the K-epsilon model. The contour plots are displayed in colours from varying red to blue, where red represents the greater magnitude and blue represents the low magnitude. Figures 78 and 79 illustrated the contour plots for the Total and Dynamic Pressure, respectively. The total pressure is the sum of static pressure and dynamic pressure which is the pressure on the airflow due to its motion. The contour shows that an amount of pressure is acting around the surface of the UAV. Around the UAV surface, the interval between each contour is small with a bright green shade, which suggests that as the dynamic pressure increases the airflow travelling towards the UAV as it measures the kinetic energy of the air flow. At the rear side of the UAV, a blue shade is displayed from the payload. This is because the payload changes the direction of airflow resulting in no static pressure being applied underneath the UAV. When the UAV is experimenting with the airflow at 100kmh, the flow is laminar at the nose of the UAV. However, at the back of the UAV, less total pressure is created as the air molecules reduce their kinetic energy and momentum. Figure 83 is the dynamic pressure trajectory on the CAD model which shows that the pressure around the UAV is uniform but on the NACA4412 tapered wing, the dynamic pressure has increased to yellow/red shade across the aerofoil as the airflow takes a longer time to travel across the chord. The pressure is higher at the root of the wing as the chordwise is longer compared to the tip. Arvind, P. (2013), the author performed a CFD analysis of dynamic and static pressure for the NACA4412 at various angles of attack, resulting in maximum dynamic pressure on the surface from the leading edge similarly to Figure 83. As the airflow travels towards the trailing edge and wingtip, the dynamic pressure decreases, with velocity also decreasing. Especially as the morphed wingtip, the flow trajectory is green which suggested the amount of drag and vortex generated has reduced, increasing the lift. The flow over the wing can be seen in the 'velocity magnitude' video. Figure 80 is a velocity magnitude contour, representing that the UAV travels forwards approximately with a velocity of 20ms^{-1}. At the tail of the UAV, the contour is green representing the velocity of the UAV relative to the airflow. Figure 84 is a velocity flow trajectory showing that the air flow around the UAV is 100kmh(27.8ms$^{-1)}$ as there are many yellow particle trajectories. At the nose and the tail of the UAV, the speed decreases to approximately 19ms^{-1} and 11.7ms^{-1}. The velocity is reduced significantly due to the increase in drag as shown in the turbulent contour plots.

Figures 81 and 82 are contour plots representing the turbulent energy and viscosity, respectively. The contours show that turbulence is generated at the tail of the UAV due to the payload as it is not designed aerodynamically. However, these figures show that turbulence decreases quickly as the contour intervals are closer together. The latter figure shows that the maximum viscosity is about tail of the UAV as there is a small shade of red. As the viscosity increases, resistance increases, resulting in turbulence as shown in Figure 80. Figure 85 are two graphs displaying the aerodynamic coefficients for this CFD simulation. The graph shows a maximum coefficient lift and drag at 0.38 and 0.04, respectively. Both results were accurate and reliable because the results from the XFLR5 wing analysis are approximately close in Figures 71 and 73. Although, the coefficient of lift is lower than the rectangular wing analysis and vice versa for drag. This is due to the geometry of the UAV's fuselage and payload. All contour plots showed that the payload box affects the aerodynamic characteristics, where turbulence is created, inducing drag.

4.8. Future Work

For aspiring pioneers, the next step is to conduct a multidisciplinary optimisation (MDO) via Hyper study; MDO allows to combine of the results of multiple engineering disciplines, such as structural, aerodynamic and aeroelasticity thus, obtaining a superior solution for the design to be optimised. Using the results from the CFD analysis, stress and strain analysis and topology analysis, MDO processes all the data within a constrained problem such as increasing aerodynamic characteristics, increasing stability and the structural integrity, etc. These mathematical models would be generated from the constraints to optimise the UAV's wing design. MDO would allow engineers to develop an optimal aerodynamic structure for the UAV. In addition, another step is to use Ansys Fluent and do the simulation for the whole UAV which would produce more accurate results.

4.9. Conclusion

The main purpose of this project is to design an autonomous, all-electric and high-lift UAV to transport a payload of a maximum of 10kg to a range varying from 80-100km in natural disasters under extreme flight conditions. In this mission, the most crucial component is the wing structure of the UAV therefore, different mathematical softwares were used to analyse and simulate the aerodynamic efficiency. In this report, the wing requirements were determined by running multiple XFLR5 simulations to produce valid data; an appropriate aerofoil was selected after considering the following factors: the symmetry, thickness, and camber of the aerofoil.

Four different simulations were obtained from analysing the aerofoil characteristics and the structure of the wing. Using the XFLR5, a symmetrical aerofoil with a variety of thicknesses ranging from 6% to 16% was examined. From the simulation results, the aerofoil with a 12% thickness would be suitable as it has a high lift-to-drag ratio and is lightweight which provides a big structural advantage for wings; it is said that as the thickness increases, the curvature of the leading edge is smoother, resulting in greater aerodynamic efficiency. Another 'XFoil Analysis' simulation was completed for three aerofoils with a thickness of 12% varying from symmetrical to camber, the three aerofoils were chosen to compare the aerodynamic characteristics were NACA0012, NACA2412, NACA4412. The graphical results displayed in Figure 69 prove that the NACA4412 aerofoil is the most suitable to be used for the UAV design, as it has shown a greater generation of lift and it was able to withstand harsh angle of attack due to its camber ratio geometry of 4%. This characteristic is an advantage as it aids the UAV tremendously during extreme flights at high Reynolds numbers. Therefore, it was confirmed that NACA4412 aerofoil is perfect to construct a wing. However, there are different types of wing geometry such as elliptical, rectangular and tapered, so the 3D wing analysis was programmed with the NACA4412 aerofoil. The wing analysis showed that the tapered wing was more aerodynamically stable and has a high lift-to-drag ratio, this is because the tapered wing had smaller wingtips resulting in minimum drag. From multiple XFLR5 simulations, it was confirmed that the tapered NACA4412 wing will be designed with a morphing wingtips on the UAV to improve the aerodynamic performance. Using SolidWorks, the tapered NACA4412 wing was designed with a morphed wingtip to run computational fluid dynamic analysis, where the airflow around the wing and fuselage were modelled to understand the aerodynamic characteristics.

The CFD analysis shows that the UAV performs aerodynamically at a high Reynolds number as the greater lift is generated and minimum drag is induced in the contour plots. At the morphing wingtips, the flow trajectory shows the vortex generated, increasing the aerodynamic characteristics of the UAV making it suitable to be used in extreme conditions. Therefore, the tapered NACA4412 Wing a wingtip is an ideal wing to be used on the UAV as the results and simulations generated are valid and accurate.

However, there were some limitations when running simulations. Engineers use XFLR5 to understand the aerodynamic characteristic of 2D aerofoils and 3D wings at low operating Reynolds numbers. However, the UAV was modelled at a Reynold number of $2x10^6$. Although the results produced were validated, more accurate results could be produced with a lower error if a low Reynold's number was used at an order of 4 or 5. The 'wing analysis' has some limitations to what the software can offer as the wing is designed to be straight but in modern aviation, complex wings with a twist and morph are used. Nevertheless, this analysis gave approximate aerodynamic characteristics. When the wing is designed, the number of panels in the x and y direction was fixed to 300 pixels which could be increased to refine the mesh to produce more accurate results. XFLR5 software enabled the desired aerofoil and wing geometry for the UAV to be identified. In addition to this, there were some limitations for the CFD simulations. Due to the complexity of the geometry, the four noded tetrahedron mesh size was fixed to 50mm as it wouldn't mesh at a smaller mesh size. To reduce anomalies being produced, the enclosure should use a smaller mesh size like $5x10^{-3}$mm and a different mesh shape like a hexahedron. This would reduce distortion on the edge and create a better mesh geometry. For the CFD simulation, k-epsilon, the turbulent model, was used instead of the Spalart-Allamaras model because the flow is incompressible, but the former model is not suitable for high Reynold numbers where the latter model produces more accurate results due to its transport equation. To compare the results and reduce the error, both models could have been implemented in the CFD simulation. Once these limitations are resolved, more accurate results will be produced with minimal error.

5. Propulsion System - Rosemary Rifaat (170283449) and Emran Rahmat (180400744)

5.1 Propulsion System Overview

The purpose of the propulsion system is to generate thrust in order to move the UAV forward. A typical propulsion system is made up of an energy source, like a battery, which stores energy and provides it to the mechanical energy converter, like a motor, which converts the chemical energy into mechanical energy, and a thrust converter, for example a propeller, uses this mechanical energy to rotate and generate thrust (Andersson and Wilkman, 2020). This section of the report focuses on the design and optimisation of the propulsion system and its respective components.

The propulsion system is required to be electrically powered and able to generate enough thrust in order to facilitate the delivering of aid within the 80-100km desired range. Each component must be suitably sized, and the rotational speed and blade angle distributions of the propellers should be optimised. The system should maximise aerodynamic efficiency and be suitable for application in natural disasters, i.e. there should be emphasis on design robustness in the event of component failure so that the UAV will still be able to deliver aid in a time-sensitive manner.

The expected outcomes of this project are to have designed each component of the propulsion system so that they meet the specified requirements and provide adequate performance which will be ensured through performance analysis and validated through literature.

5.1.1 Aims and Objectives

In order to achieve the expected outcomes, the following aims and objectives have been set out for the propulsion system.

Aims:

- Design an all-electric propulsion system
- Design optimised propellers with maximised performance

Objectives:

- Carry out sizing calculations to determine the required propeller diameter and power and speed requirements for the motors and batteries
- Design two propellers with different blade angle distributions and carry out performance analysis on them to determine the optimal design

- Select a suitable battery and motor configuration to power the propulsion system based on power requirements
- Design a folding propeller mechanism to be used during the cruise phase to improve UAV aerodynamic efficiency
- Analyse propeller design using Computational Fluid Dynamics (CFD)

Each component of the propulsion system will be designed and tested in this section of the report.

5.2 Propellers (Rosemary Rifaat)

5.2.1 Propeller Design Methodology

This section focuses on the design of the propellers used in the cruise phase of flight, with the findings being applicable to the design of the propellers used during takeoff and landing which will be discussed further in Section 7. An initial methodology was set out in order to achieve the design of optimised propellers suitable for use in this UAV application as shown in Figure 86.

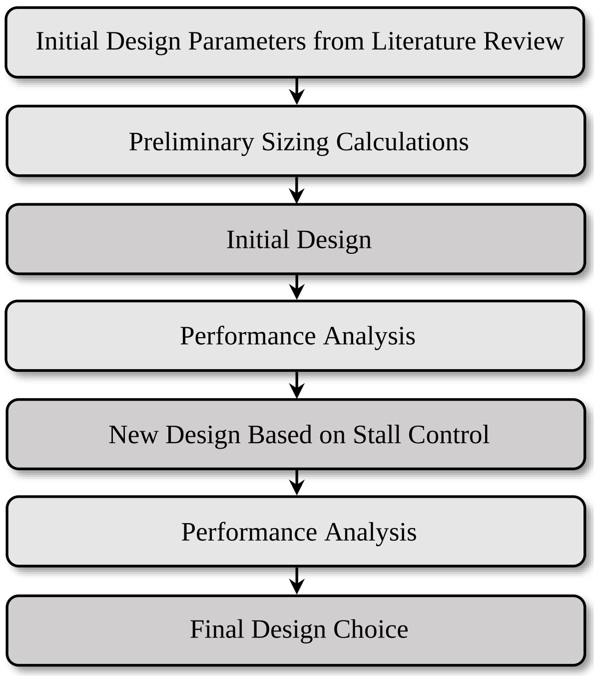

Figure 86: Flowchart of design methodology followed for propeller design

This methodology included combining previous findings from literature and newer research, along with calculations for the propulsion system requirements, such as sizing calculations, in order to obtain some base parameters to build the design on. The initial sizing and design of the propellers was carried out first so that a suitable motor and battery combination which could satisfy the thrust and power requirements of the propellers could be selected. Two approaches were then taken to design the blade angle distribution of the propellers, with one basing this distribution on existing UAV propeller designs and the other determining the variation through aerofoil propeller geometry analysis and the use of stall control. Both designs then underwent performance analysis using the software known as *JBLADE*.

5.2.2 Review of Previous Research

5.2.2.1 Open Rotors and Ducted Fans

In the literature review conducted, ducted fans were researched and considered for use in the UAV design due to some of their aerodynamic efficiency benefits among other reasons. Through further research and consideration, the decision to exclude them from the design has been made and will be discussed in this section.

One of the main advantages of having a ducted fan for this natural disaster application that was previously considered was that the inclusion of the duct itself would allow the UAV to manoeuvre close to obstacles with a reduced risk of damage to both the surroundings and the UAV itself (Muelaner, 2013). However, as the method of package distribution has been decided as having the UAV simply dropping the package off from a height without actually manoeuvring close to the ground, this advantage will not be of use and would be better suited to UAVs which intend to deliver their payload closer to the ground.

When considering existing VTOL UAV designs, ducted fans typically are not utilised, with open rotors being favoured. The inclusion of a duct inherently limits the diameter of the rotor as a large rotor would need a large duct which would add weight to the design. It is also desirable to maximise rotor diameter which can be seen in the relationship between shaft power, $\dot{W}_{shaft}$ in W, and propeller diameter, d, in m as expressed in the following equation:

$$C_P \equiv \frac{\dot{W}_{shaft}}{\rho n^3 d^5} \tag{97}$$

Where C_P is the power coefficient, ρ is the local air density in kg/m^3 and n is the propeller rotational speed in rev/s. It can be seen that the power consumed whilst driving a propeller is greatly dependent on the diameter of the propeller, with $\dot{W}_{shaft} \propto d^5$, therefore the diameter of the propeller should be maximised in order to increase efficiency.

Due to the aforementioned reasons, it was decided that the inclusion of ducted fans in this particular UAV design and application would not be of much benefit and thus, open rotors will be used alone.

5.2.2.2 Number of Blades

Previous research has indicated that changing the number of blades on a propeller does not affect propeller performance as significantly as blade angle does for example. In theory, increasing the number of blades leads to less efficient configurations as additional blades add weight to the design and a design which needs more blades to achieve the same or similar thrust production as a design with fewer blades is inherently less efficient. Increasing the number of blades has advantages such as producing less noise; however, the reduction of weight and improved performance is the most important factor in this UAV design.

As two-bladed propellers weigh less than propellers with more blades and the same diameter, and VTOL UAVs typically utilise two-bladed propellers, this will be carried forward in the design, however, propellers with different numbers of blades will be examined in terms of efficiency later on in this report in order to validate this decision.

5.2.2.3 Fixed Pitch Propellers and Controllable Pitch Propellers

Consideration has also been made in deciding between fixed pitch propellers (FPPs) and controllable pitch propellers (CPPs). One of the main advantages of using CPPs is that different pitches are optimal for different flight phases. Reducing propeller pitch is desirable for improving climb performance and thus low pitch propellers would be optimal for the takeoff and landing phases, and increasing the pitch is better suited to improving cruise performance (Heinzen, Hall and Gopalarathnam, 2015).

However, the design of this UAV will utilise four propellers for the vertical take-off and landing phase, and four different propellers for the cruise phase of flight, thus actively controlling the pitch of the propeller to optimise performance in each phase is not necessary. FPPs have a much simpler design which leads to less chance of mechanical failure and this, combined with the reason previously mentioned, has led to the decision to use FPPs.

5.2.3 Further Initial Design Considerations

5.2.3.1 Distributed Propulsion

Distributed propulsion is implemented for the cruise stage of flight for many reasons including potential improved overall efficiency, capabilities and robustness of the UAV (Kim, Perry and Ansell, 2018).

A distributed electric propulsion system, unlike more traditional models, allows propulsors to be electrically connected only to an energy source which allows for improved flexibility in design, placement and operation of the propulsors which could lead to improved performance (Kim, Perry and Ansell, 2018).

Many other VTOL UAV designs use four propellers and a single propeller at the back of the UAV, however, by using four separate propellers for the takeoff and landing phase and the cruise phase, there is less of a risk of crashing. This is because if failure were to occur with one of the components, it would not be as disastrous as there are more motors and propellers to continue the flight. This is especially important within this application as aid must be delivered in a timely fashion and so failures would lead to delays and could destroy aid packages. The design is made more robust by there being two propellers below each wing as if one propeller or motor fails, there will still be another propeller on the same wing and the thrust produced would not be as unsymmetrical as it would be if there were only one propeller on each wing. This therefore puts less pressure on each propeller/motor and reduces the reliance on them.

The distributed propulsion system is shown in Figure 87. A system of counter-rotation is used in order to ensure that the trust force acts right in between each propeller on both sides as shown by red arrows on Figure 88, rather than having a net resultant force that is offset. The propellers will turn towards each other which is a system witnessed on the Airbus A400M. This system also helps to reduce torque as counter-rotating propellers on each wing will cancel a left or right torque caused by all propellers turning clockwise or anti-clockwise respectively. Propellers 1 and 3 will be rotating clockwise and 2 and 4 will rotate anti-clockwise.

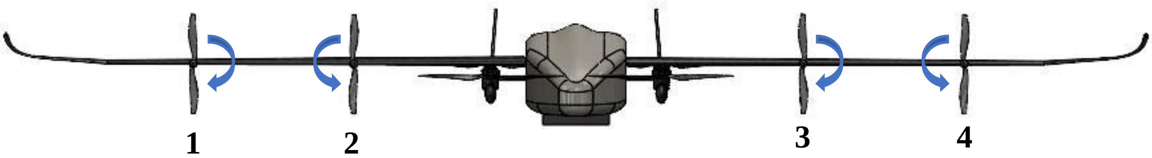

Figure 87: Distributed propulsion system - propeller counter-rotation

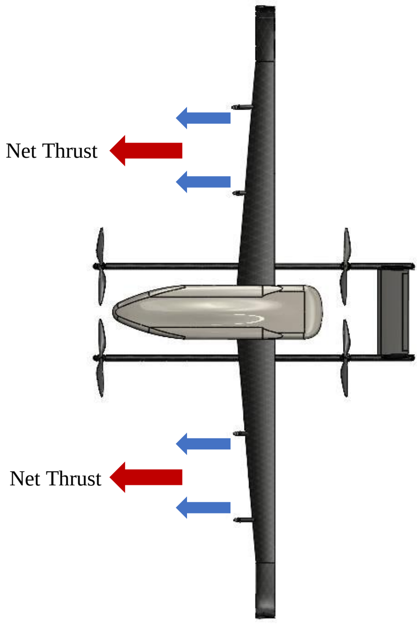

Figure 88: Thrust produced with counter-rotating propellers

5.2.4 Preliminary Propeller Sizing Calculations

In this section, the sizing calculations will be done for the four propellers used during cruise. The additional four propellers used for takeoff and landing will be sized later in this report.

5.2.4.1 Thrust and Required Diameter Calculations for Cruise

For a steady, level flight, the force balance is shown in Equation 98 where the thrust required for cruise, T_{cruise}, is equal and opposite to the drag, D, experienced by the UAV.

$$T_{cruise} = D \tag{98}$$

The required thrust can therefore be calculated using the equation for drag force experienced as shown in Equation 99, where ρ is local air density in kg/m^3, v is local air velocity in m/s, C_D is the drag coefficient, and S is the reference wing area in m^2.

$$T_{cruise} = \frac{1}{2}\rho v^2 C_D S \tag{99}$$

The drag coefficient can also be expressed as follows:

$$C_D = C_{D_0} + \frac{C_L^2}{\pi A e} + \Delta C_{D_0} \tag{100}$$

Where C_{D_0} is the zero-lift-drag coefficient, also known as the parasite drag coefficient, $\frac{C_L^2}{\pi Ae}$ is the induced drag with C_L being the lift coefficient with a value of 1.6, A being the aspect ratio with a value of 20.2, and e being Oswald's efficiency. ΔC_{D_0} is a term accounting for corrections to C_{D_0} during take-off and landing. As the aircraft can be assumed to have a 'clean' configuration, ΔC_{D_0} can be estimated to be zero as shown in Table 21. This 'clean' configuration also allows e to be estimated as $0.80 - 0.85$ and therefore will be taken as an average of 0.825 for further calculations.

Table 29: Estimates for ΔC_{D_0} and e (Roskam, 1997)

Configuration	ΔC_{D_0}	e
Clean	0	0.80-0.85
Take-off Flaps	0.010-0.020	0.75-0.80
Landing Flaps	0.055-0.075	0.70-0.75
Landing Gear	0.015-0.025	No effect

The final required thrust equation is therefore shown in Equation 101, with an additional 20% added as a correction factor for a conservative estimate.

$$T_{cruise} = 1.2\left(\frac{1}{2}\rho v^2\left(C_{D_0} + \frac{C_L^2}{\pi Ae} + \Delta C_{D_0}\right)S\right) \tag{101}$$

The zero-lift-drag coefficient is calculated using the equivalent parasite area, f, and the reference wing area (Roskam, 1997).

$$C_{D_0} = \frac{f}{S} \tag{102}$$

The equivalent parasite area can be found using Equation 103 where a and b are correlation coefficients and S_{wet} is the wetted surface area.

$$\log_{10} f = a + b\log_{10} S_{wet} \tag{103}$$

(Roskam, 1997)

The skin friction coefficient, C_f, must be calculated in order to find the values for coefficients a and b. This can be done using Equation 104.

$$C_f = \frac{0.455}{\log_{10} Re^{2.58}} \tag{104}$$

Where Re is the Reynolds number and is found using Equation 105.

$$Re = \frac{\rho v_p L_c}{\mu} \tag{105}$$

Where L_c is the characteristic length in m, v_p is the propeller speed in m/s, and μ is dynamic viscosity in kg/ms. The characteristic length in this case is the chord length which is taken as an approximate value of $0.1m$. The propeller speed is taken as an initial average of $150\ m/s$ for an aircraft like this. The value of dynamic viscosity is calculated by linear interpolation at 32^oC as this is the average high temperature in the Philippines (Worldbank.org, 2020). This linear interpolation provides a μ value of $1.87 \times 10^{-5}\ kg/ms$ (Engineeringtoolbox.com, 2022). Equation 105 then becomes:

$$Re = \frac{1.225 \times 150 \times 0.1}{1.87 \times 10^{-5}} = 9.83 \times 10^5 \approx 1 \times 10^6 \tag{106}$$

Using this value, C_f can be calculated using Equation 104.

$$C_f = \frac{0.455}{\log_{10} Re^{2.58}} = \frac{0.455}{\log_{10}(9.83 \times 10^5)^{2.58}} \approx 4.5 \times 10^{-3} \tag{107}$$

Table 22 can then be used to find the values of coefficients a and b and from this, $b = 1$ and linear interpolation gives a value of -2.3504 or a.

Table 210: Correlation coefficients for parasite area versus wetted area (Roskam, 1997).

C_f	a	b
0.0050	-2.3010	1.0
0.0040	-2.3979	1.0

S_{wet} must be found next and can be done so using Equation 108 where c and d are regression line coefficients and W_{TO} is the takeoff weight in lbs. W_{TO} is estimated to be $32kg$ which is multiplied by $9.81m/s$ to get roughly $314N$ which is equivalent to around $70.57lbs$.

$$\log_{10} S_{wet} = c + d \log_{10} W_{TO} \tag{108}$$

(Roskam, 1997)

Coefficients c and d may conservatively be estimated as 1.0892 and 0.5147 respectively for this case (Roskam, 1997) and therefore the wetted area can be calculated as follows:

$$\begin{gathered} \log_{10} S_{wet} = c + d \log_{10} W_{TO} = 1.0892 + 0.5147 \log_{10} 70.57 \\ S_{wet} \approx 110ft^2 \end{gathered} \tag{109}$$

Now, using Equation 102, the equivalent parasite area may be found.

$$\begin{gathered} \log_{10} f = a + b \log_{10} S_{wet} = -2.3504 + \log_{10} 110 \\ f \approx 0.50ft^2 \approx 0.05m^2 \end{gathered} \tag{110}$$

C_{D_0} may finally be calculated using these values:

$$C_{D_0} = \frac{f}{S} \approx \frac{0.05}{1.56} \approx 0.03 \tag{111}$$

It should be noted that the target UAV velocity is between $80 - 100km/h$ which is $22.22 - 27.78m/s$. In order for this estimate to be conservative, the higher bound of these values will be used. Combining all of these values, the required thrust for cruise may be calculated as shown below.

$$\begin{aligned} T_{cruise} = 1.2\left(\frac{1}{2}\rho v^2\left(C_{D_0} + \frac{C_L^2}{\pi Ae} + \Delta C_{D_0}\right)S\right) \\ \approx 1.2\left(\frac{1}{2} \times 1.225 \times 27.78^2\left(0.03 + \frac{1.6^2}{\pi \times 20.2 \times 0.825}\right)1.56\right) \\ \approx 70N \end{aligned} \tag{112}$$

Therefore, the thrust required for cruise phase of flight is approximately $70N$.

This power required to produce this amount of thrust, P_{cruise}, may then be calculated using Equation 113.

$$P_{cruise} = \frac{T_{cruise}v}{FoM} = \frac{70 \times 27.78}{0.7} \approx 2.7kN \tag{113}$$

(Tyan et al., 2017)

Where v is the air velocity which is $27.78m/s$, and FoM is the Figure of Merit which is the rotor efficiency and has a value of 0.7 for preliminary estimates (Sforza, 2014).

These required thrust and power values can be applied to determine the required diameter for each propeller. The two values may be split between the four propellers used during cruise which leads to roughly $17N$ of thrust produced by each propeller, with each propeller requiring around $685N$ of power.

The required diameter of each propeller can then be calculated using the empirical relation shown in Equation 114.

$$d = K(P_{inst})^{0.25} \tag{114}$$

(Kundu, 2010)

Where d is the diameter of the propeller in inches, K is a coefficient which can be taken as 22 for a two-blade propeller, and P_{inst} is the installed power in hp. $870N$ is equivalent to roughly 1.17 hp and therefore Equation 114 becomes:

$$d = 17(1.17)^{0.25} \approx 22in \; or \; 0.55m \tag{115}$$

5.2.5 Propeller Performance

There are several ways in which the performance of a propeller may be measured but the following equations allow some characteristics to be calculated for performance analysis (Martinez, 2014):

$$J \equiv \frac{v}{nd} \tag{116}$$

$$\eta_P \equiv \frac{Tv}{\dot{W}_{shaft}} = \frac{C_T}{C_P}J \tag{117}$$

$$C_T \equiv \frac{T}{\rho n^2 d^4} \tag{118}$$

Where J is the advance ratio which is a non-dimensional parameter which is the distance advanced by the propeller in one revolution (Martinez, 2014). C_T is the coefficient of thrust, T is the thrust force produced by the propeller in N and the propeller is driven by a device like a motor with shaft power $\dot{W}_{shaft}$ in W where $\dot{W}_{shaft} = Q\omega$ where Q being the torque in Nm and propeller rotational speed in rad/s may also be calculated as follows: $\omega = 2\pi n$. Power coefficient may also be calculated as shown previously. Combined, these are all used to find overall propeller efficiency η_P.

In order to validate the results obtained in later analysis, typical propeller performance characteristics were determined from literature and used as a comparison. Figure 89 shows typical propeller efficiency curves for various advance ratios and blade angles. Here, 0.75R denotes the blade angle at a position three-quarters of the propeller radius away from the hub. They can also be used as an initial guide to work out rotational speed requirements for different blade angles, with a target efficiency of $0.7 - 0.8$ being highlighted by the red region on the graph. The advance ratio equation can be rearranged to calculate the required rotational speed in order to achieve this efficiency range. An example calculation may be shown in Equation 119 for a blade angle of 15°, where the target advance ratio is $0.45 - 0.75$ based on Figure 89, and the airspeed and propeller diameter are $27.78 m/s$ and $0.55 m$ respectively.

.

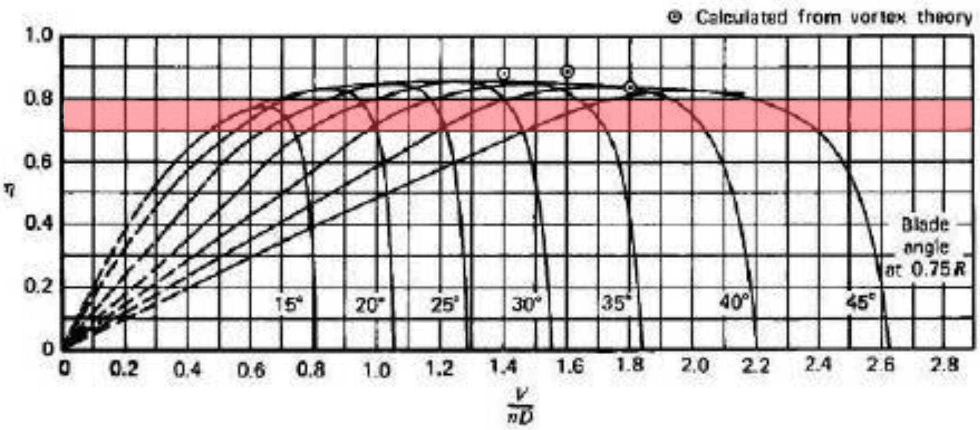

Figure 89: Propeller efficiency against advance ratio for a range of blade angles (Bronz, Moschetta and Hattenberger, 2012)

$$n = \frac{v}{dJ}$$

$$\text{Low } J \text{ range: } n = \frac{27.78}{0.55 \times 0.45} \approx 92\, rev/s \approx 6800\, rpm \tag{119}$$

$$\text{High } J \text{ range: } n = \frac{27.78}{0.55 \times 0.75} \approx 68\, rev/s \approx 4000\, rpm$$

This shows that a required rpm range of $4000 - 6800\ rpm$ is needed to achieve this efficiency. The same calculation is carried out for all blade angles shown in Figure 89 and the results are shown in Table 23. This can be used as a guide for motor sizing when considering different blade angles for the propeller design.

Table 211: Typical optimal advance ratio and rotational speed range for different blade angles

Blade Angle at 0.75R	J	Required rpm Range
15°	0.45-0.75	4000-6800
20°	0.55-1.00	3000-5600
25°	0.65-1.15	2700-4700
30°	0.80-1.40	2200-3800
35°	1.00-1.65	1800-3000
40°	1.20-1.90	1600-2600
45°	1.45-2.20	1400-2100

Figure 90 shows a propeller efficiency curve and coefficient of thrust and coefficient of power curves. These will also be used for comparison in order to validate the shape and range of values of the curves plotted.

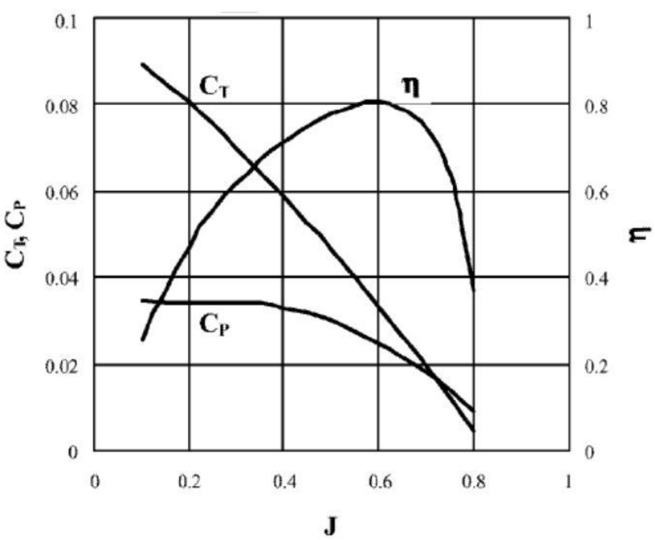

Figure 90: Typical propeller performance characteristic curves (Khan et al., 2000)

C_P and C_T graphs for various 3-bladed propellers were plotted from results in the 'NACA Technical Report 594' and validated using *JavaProp* software and can be seen in Figure 91. This shows slightly more fluctuation in results and will be kept in mind when analysing results.

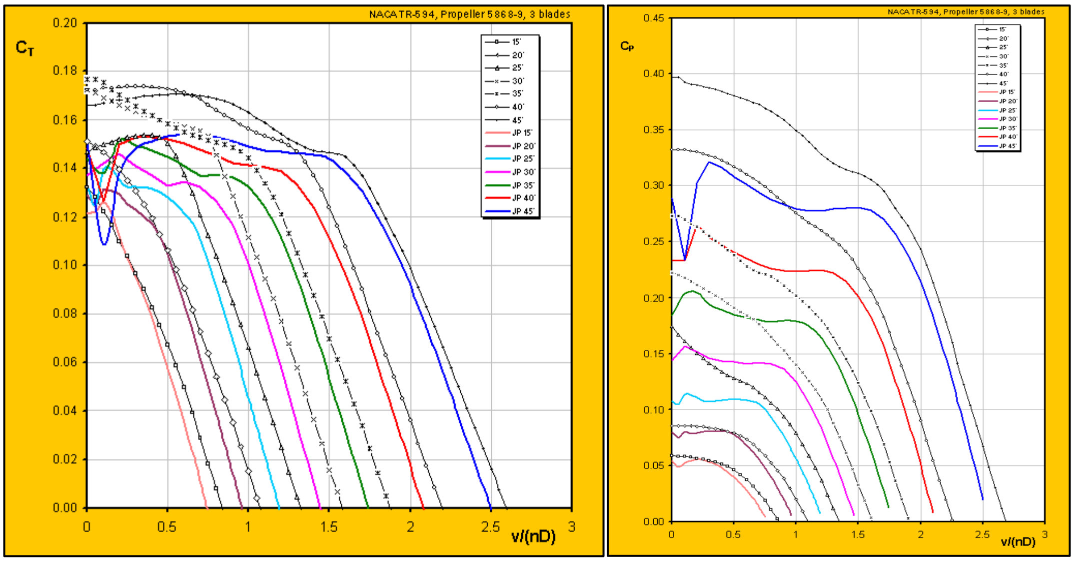

Figure 91: Propeller C_P and C_T plotted using JavaProp (Mh-aerotools.de, 2018)

5.2.6 Propeller Design and Performance Analysis

5.2.6.1 Aerofoil Profile Choice and Characteristics

The aerofoil chosen for the propeller design is the NACA 0010 as seen in Figure 92.

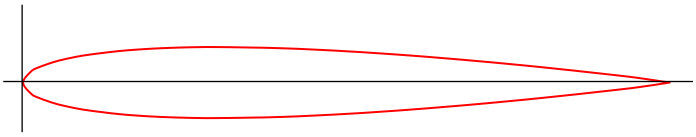

Figure 92: NACA 0010 aerofoil profile

It is a symmetrical aerofoil as the upper and lower surfaces are identical. Symmetrical aerofoils are typically used for propellers as they afford better lift-drag ratios for a wider range of velocities from the root to the tip of the propeller blade. Figure 93 shows the NACA 6412 aerofoil which is asymmetrical, and a comparison can be made between the performance of the two aerofoils as shown in Figure 94. The highest lift to drag ratio is achieved within a wider range of angle of attack for the symmetrical profile versus for the asymmetrical profile, i.e. the asymmetrical profile has a narrower efficient operating window.

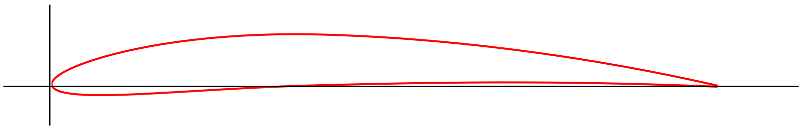

Figure 93: NACA 6412 aerofoil profile

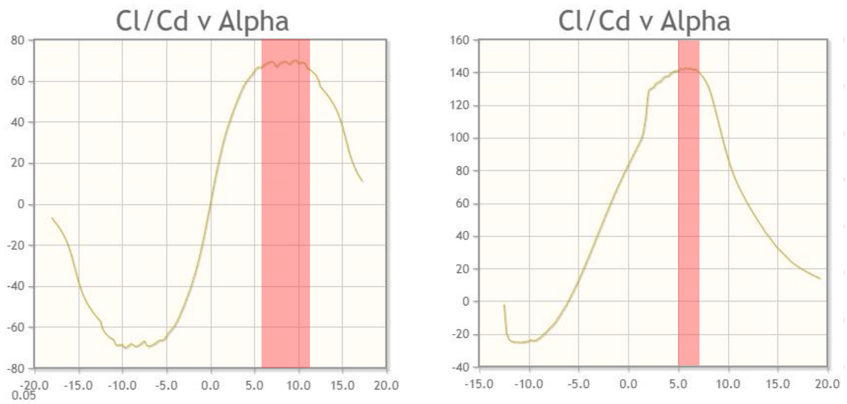

Figure 94: Example of lift to drag ratio against angle of attack for (left): NACA 0010 aerofoil and (right) NACA 6412 aerofoil (Airfoiltools.com, 2022)

A viscous simulation was run with a Reynolds number of 1×10^6 for the NACA 0010 aerofoil using *XFOIL* which is a programme that is used for the design and analysis of isolated aerofoils. Th polar plots of lift coefficient, C_L, and drag coefficient C_D, against angle of attack, α, for the NACA 0010 aerofoil were obtained for a set range of angle of attack between -20° and +20° at 0.25° intervals. As the flow is relatively low speed, the Mach number was kept as the default value of zero which takes the air as an incompressible ideal fluid as variations in density are negligible. The Ncrit value is a value used to model the fluid turbulence or roughness of the aerofoil. Table 24 is taken from *XFOIL* documentation and can be used to set the value for Ncrit for a particular analysis. In this case, a Ncrit value of 9 was used as this is the standard. The settings used and the aerofoil modelled in *XFOIL* is shown in Figure 95, and the resulting data obtained was plotted in *MATLAB* and can be seen in Figure 96 and Figure 97.

Table 212: Selection of Ncrit value for aerofoil simulations

Situation	Ncrit
Sailplane	12 to 14
Motorglider	11 to 13
Clean Wind Tunnel	10 to 12
Average Wind Tunnel	9
Dirty Wind Tunnel	4 to 8

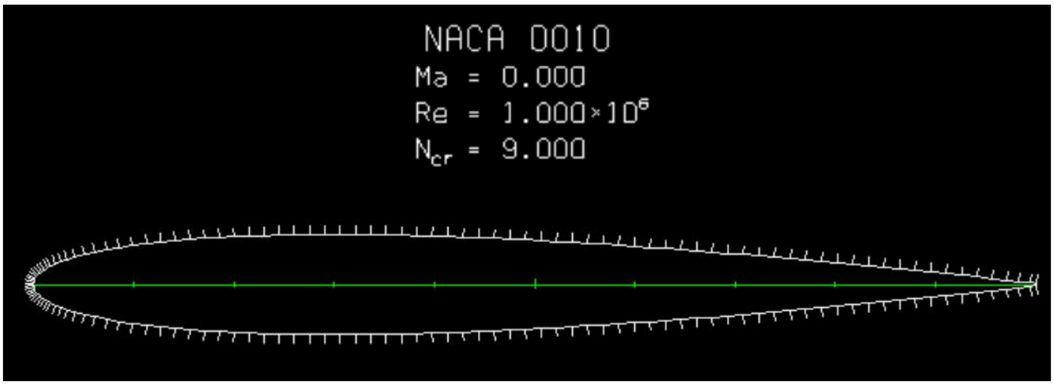

Figure 95: XFOIL aerofoil and settings used for polar simulations

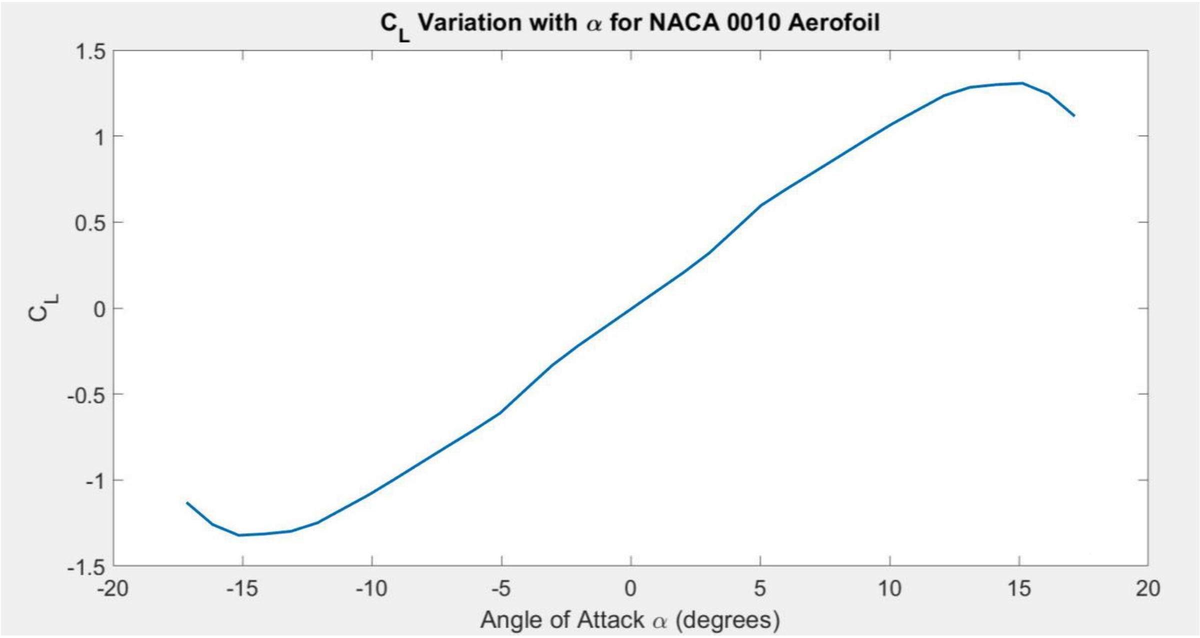

Figure 96: Lift coefficient variation with angle of attack for the NACA 0010 aerofoil

From this plot, it can be seen that the lift coefficient is zero at an angle of attack of zero as the aerofoil is symmetrical. The maximum lift coefficient, C_{Lmax}, past which point stall will occur, has a value of roughly 1.3 and occurs at an angle of attack of around 15°. This can therefore be considered the stall angle for this aerofoil.

Figure 97 shows that drag coefficient trend and at an angle of attack of 15°, C_D is approximately 0.04.

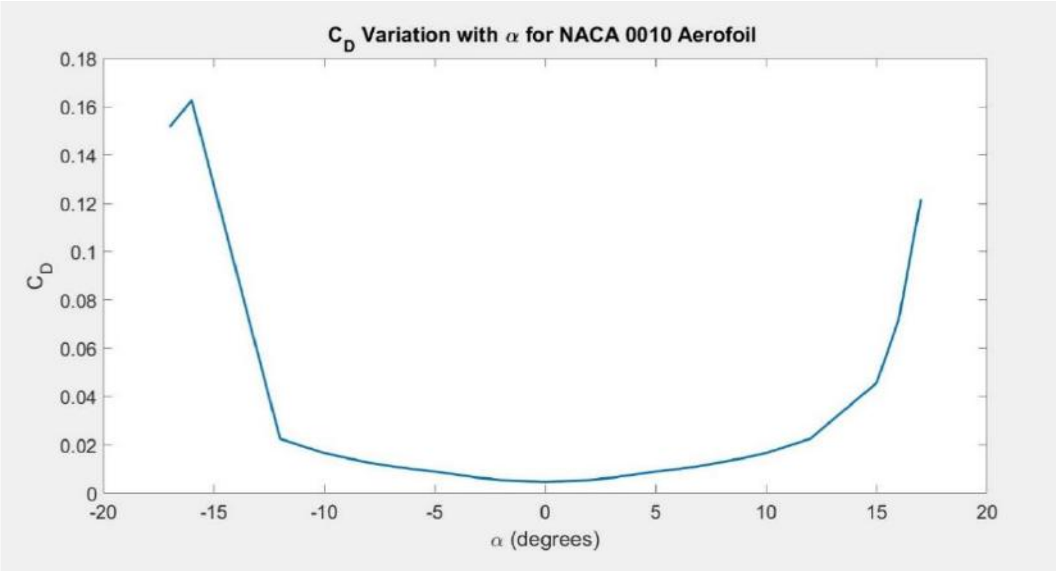

Figure 97: Lift coefficient variation with angle of attack for the NACA 0010 aerofoil

5.2.6.2 Initial Propeller Design

A preliminary design for a propeller was created using the NACA 0010 aerofoil and calculated required diameter. At this point, no specific calculations for angles were made and the stall angle was not taken into consideration as this was the first design. The blade angle is taken as the total angle that the aerofoil makes with a horizontal reference plane. The angles of an aerofoil will be discussed in more detail further on. The blade angle distribution used was based on a distribution commonly seen in UAV propeller designs, as shown in Figure 98.

Figure 98: Example of existing propeller design modelled for initial design (Joom.com, 2022)

To simplify this design, the propeller was split into three planes and a blade angle was assigned to each section to form a linear variation of blade angle for each blade section. If R is taken as the propeller radius and r is the radial position, an r/R of 0 represents the blade root and an r/R of 1 represents the blade tip. The blade angle distribution for this design is plotted in Figure 99 and the CAD model made in *SolidWorks* for the clockwise and anti-clockwise design is shown in Figure 10.

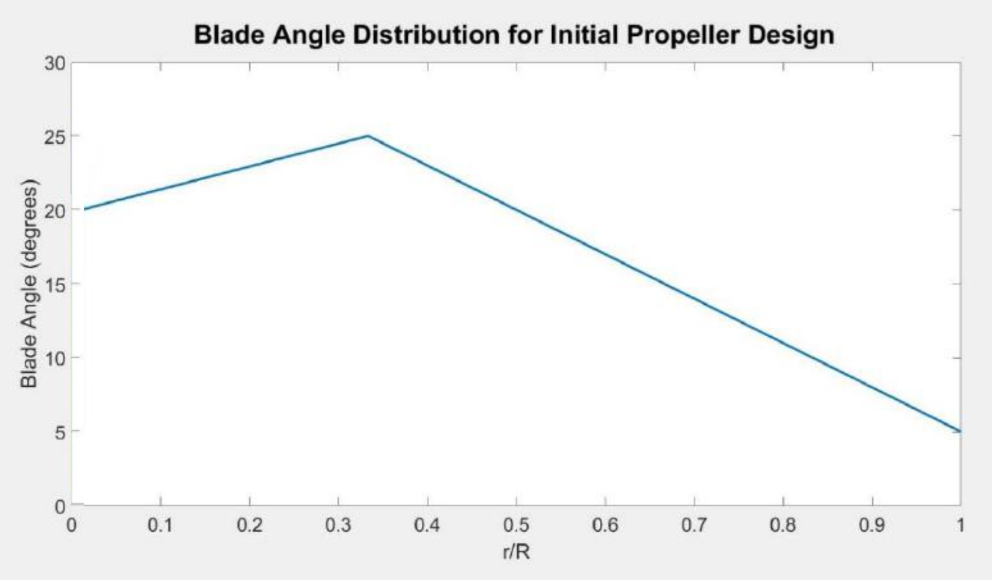

Figure 99: Blade angle distribution for initial propeller design

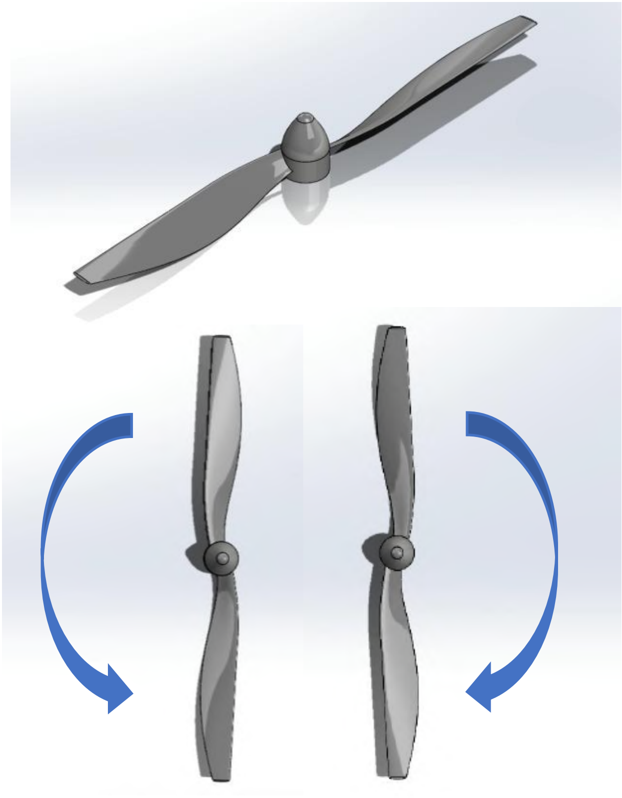

Figure 100: CAD model for initial propeller design. (Top) isometric view of propeller, (left) anti-clockwise propeller, (right) clockwise propeller

5.2.6.2.1 Initial Propeller Design Performance Analysis

The software known as *JBLADE* which is based on David Marten's *QBLADE* and André Deperrois' *XFLR5* was used to test certain performance characteristics of the propeller such as propeller efficiency and C_T and C_P variations with advance ratio. The two-bladed propeller tested can be seen in Figure 101 where the radius of each blade is $0.275m$ and the chord length is $0.02m$ at the root and tip, and $0.04m$ at an r/R of 0.33. This chord length variation across the propeller blade is shown in Figure 102.

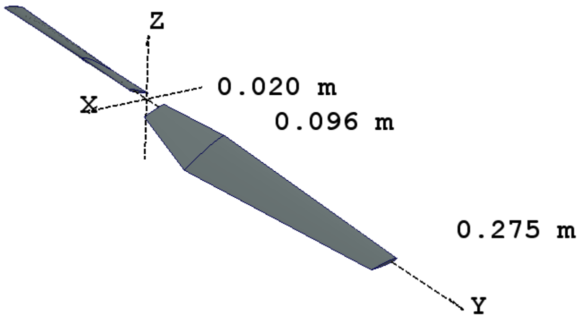

Figure 101: Initial propeller design modelled in JBLADE

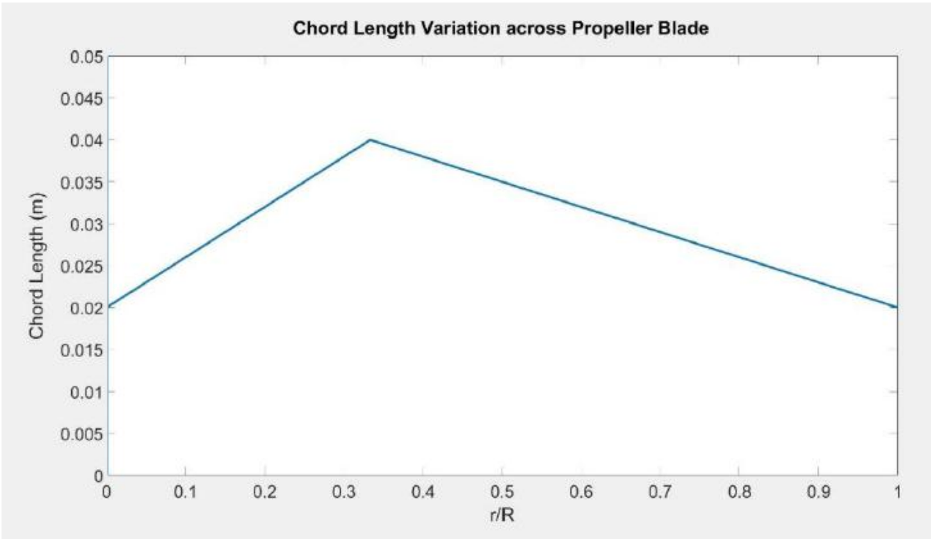

Figure 102: Aerofoil chord length variation across propeller blade

The blade angle at 0.75R for the initial design is $12.5°$ and a preliminary rotational speed of roughly $5000\ rpm$ was set for use in the simulations as a conservative estimate as this is within the average range of propeller speeds previously calculated based on typical efficiency curves. The optimal rotational speed for the propeller will be calculated after performance results are obtained and will be discussed later on.

Figure 103 shows the propeller efficiency curve for the initial propeller design. A maximum efficiency of 0.82 is achieved at an advance ratio of around 0.46. The curve follows the expected shape as the typical propeller efficiency curves and as the blade angle at 0.75R is 12.5°, the corresponding advance ratio range agrees with what is expected.

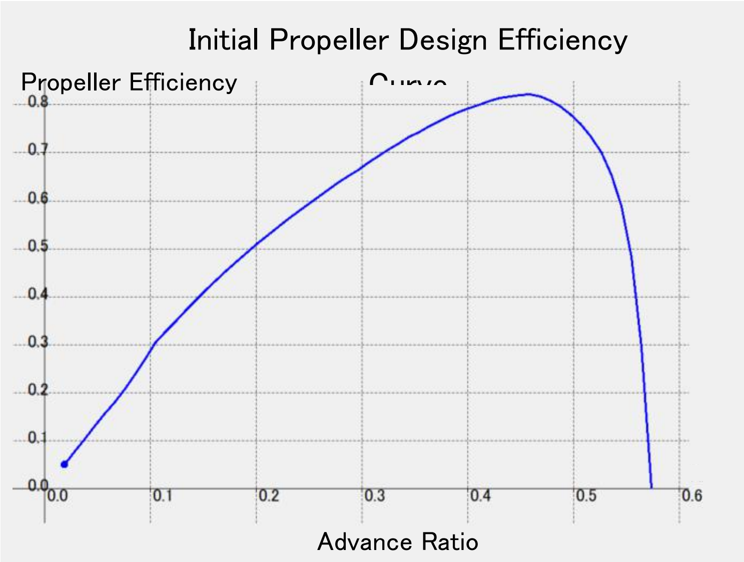

Figure 103: Initial propeller design efficiency curve

Taking the optimal efficiency, an advance ratio of 0.46 corresponds to an optimal rotational speed of 6600 rpm as shown in Equation 119 and the propeller C_T curve can be seen in Figure 104.

$$J = 0.46 : \; n = \frac{27.78}{0.46 \times 0.55} \approx 110 \, rev/s \approx 6600 \, rpm \tag{119}$$

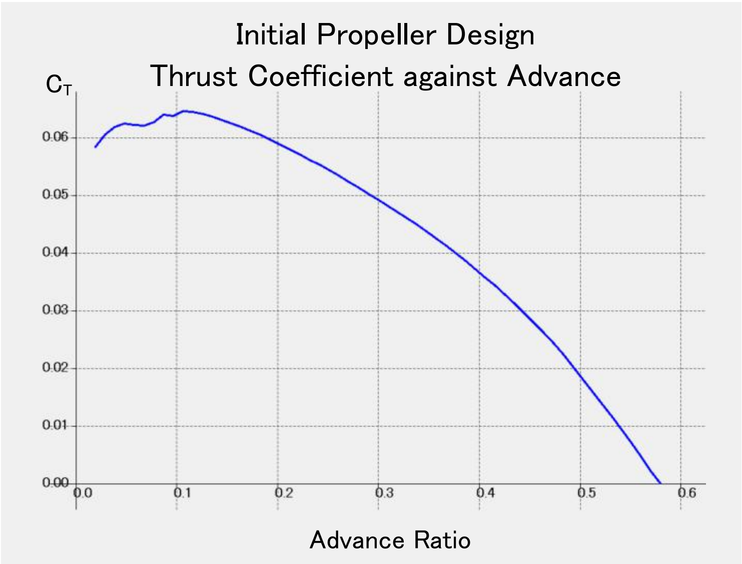

Figure 104: Coefficient of thrust variation with advance ratio for initial propeller design

A peak thrust coefficient of around 0.07 is shown. The curve follows a similar downwards trend to the typical curve with a similar C_T range, and there is an initial rise in value which is similarly shown in the *JavaProp* curves shown previously.

The C_P curve is shown in Figure 105 and once again, follows a similar trend in shape to the typical curve. For this curve, the power coefficient values start at half the value shown in the typical curve but at a similar to some of the *JavaProp* curves. The maximum C_P value achieved is approximately 0.024.

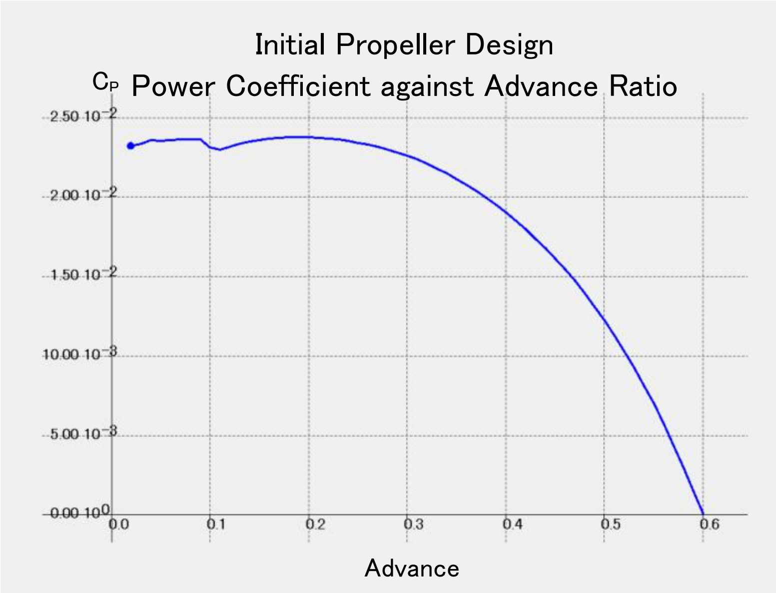

Figure 105: Coefficient of power variation with advance ratio for initial propeller design

Based on these performance characteristics, another approach will now be taken to attempt to design an optimised propeller with better performance, and comparisons will be made between the designs.

5.2.6.3 Propeller Design Optimisation

5.2.6.3.1 Propeller Geometry

Figure 106 shows the angles of a propeller, as well as its general geometry in relation to the propeller hub. The pitch angle is the angle that the horizontal rotational plane makes with the chord line of the aerofoil.

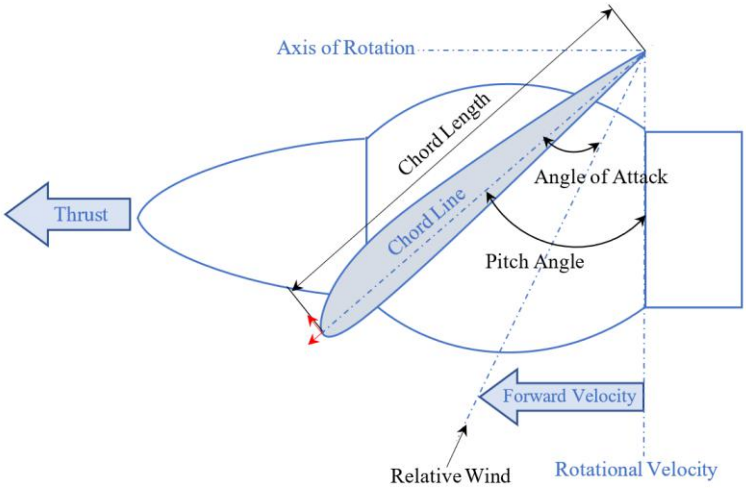

Figure 106: Propeller blade geometry

In order to better understand the other angles and directions being considered for propeller design, it is first important to understand why the angles of a propeller are important. The aerofoil profile is twisted along the length of the propeller blade in order to maintain a relatively constant and optimal angle of attack at any given section which will optimise lift performance and efficiency. The angles which are altered for propeller design are shown in Figure 107 which illustrates the flow geometry of an aerofoil. The net relative wind velocity vector, V_{rel} is the vector sum of the propeller blade's rotational velocity component, V_{rot}, which lies on the plane of rotation, and the forward velocity vector, V_w which takes into account both the air velocity far upstream of the rotor and also the induced air velocity ahead of the rotor (Vepa, 2020). The angle of attack, α, is the angle between the relative wind velocity direction and the chord line of the aerofoil, the twist angle, β, is the angle between the horizontal reference plane, which is in line with the rotational plane, and the chord line. Finally, the inflow angle, φ, is the angle between the horizontal reference plane, and relative air velocity. This angle is used to define the direction of the wind vector shown relative to the propeller's plane of rotation (Vepa, 2020).

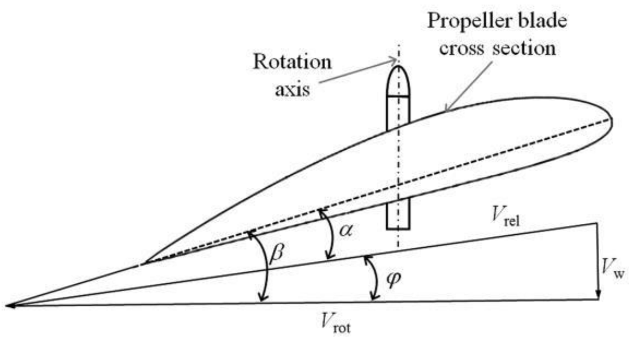

Figure 107: Geometry of an aerofoil (Vepa, 2020)

Propeller blades rotate which means that the speed at the tip will be higher than the speed at the root. As previously shown with how thrust is calculated for a propeller, thrust is directly proportional to air velocity squared and directly proportional to C_L, and therefore angle of attack up until the stall angle. The aim is to provide an optimal thrust along the span of the blade and therefore as the angular velocity is higher at the tip, the blade angle does not need to be as large as it will balance out. The tip of the blade inherently travels a further distance than the root during a rotation, also explaining why the blade angle should be greatest at the root of the propeller. The twist angle decreasing from root to tip will therefore allow an optimal thrust to be generated along the blade (Nasa.gov, 2021). If the blade angle was equal across the entire propeller, thrust and pressure would vary greatly across the blade which is highly undesirable, therefore it is very important to differ the blade angle for performance purposes. Additionally, Figure 107 shows that the aerofoil profile is shown with a twist. If it were not twisted, the normal to the blade axis would be parallel to the rotation axis, making the angle of attack negative. The aerofoil is twisted anti-clockwise in order to create a small positive angle of attack.

The twist angle can be calculated as follows:

$$\beta = \varphi + \alpha \tag{120}$$

5.2.6.3.2 Propeller Inflow Angle

In order to calculate the inflow angle, the wind velocity triangle shown in the aerofoil geometry diagram can be used as the rotational and forward components of velocity are known. Using trigonometric ratios to solve for φ, the following equation can be used:

$$\varphi = \tan^{-1}\left(\frac{V_w}{\omega r}\right) \tag{121}$$

Where V_w is forward wind velocity in m/s, ω is the angular velocity of the propeller in rad/s, and r is the radial position in m, i.e. the distance along the blade from the root at a given point. V_w is theoretically a combination of the velocity at which the UAV is moving and the induced velocity. The induced velocity can be calculated using the Blade Element Momentum (BEM) theory which combines the blade element and momentum theories in order to relate rotor performance to rotor geometry and can be used to assess the performance of propellers (El Khchine and Sriti, 2016). The BEM will be discussed in more detail in Section 7 but in this instance, the inclusion of the induced velocity will mean that the effective angle of attack calculated at each section will be lower, and thus can be ignored as this is a first approximation. Therefore in this case, V_w will be taken as the aircraft forward velocity which will be taken at the lower end of the cruise velocity range mentioned previously i.e. $22.22 m/s$ as this is the likely speed that the UAV will be moving forward at. The rotational speed will be taken as an initial estimate of $7000\ rpm$ as this is the rough average propeller speed for UAV VTOLs of this size (Palaia et al., 2019). This translates to roughly $733\ rad/s$. Equation 121 was used to calculate the inflow angle at various radial positions along the blade from root to tip using *MATLAB*. The plot of inflow angle against r/R is shown in Figure 108.

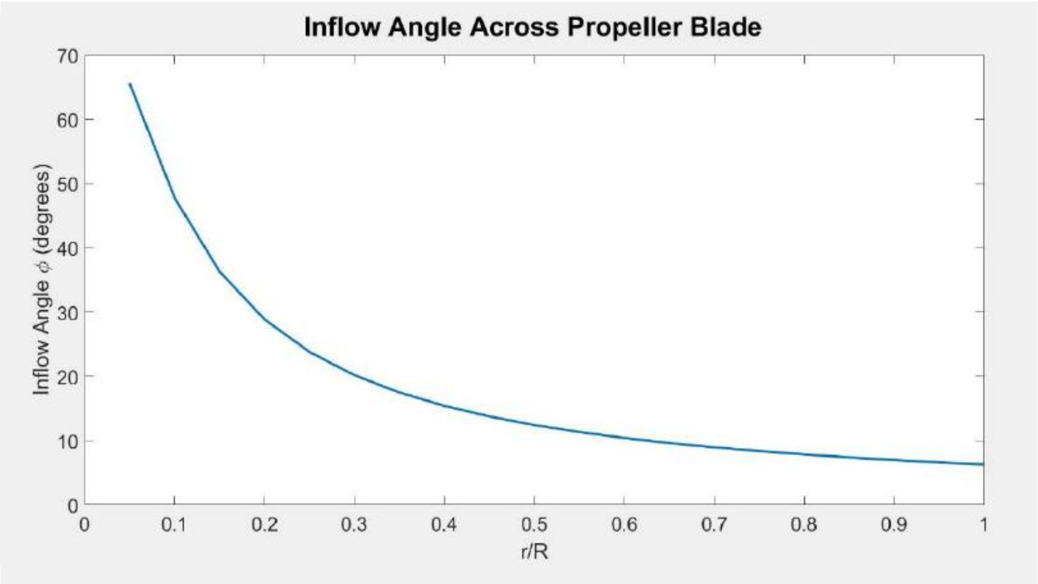

Figure 108: Inflow angle calculated across the length of the blade

The inflow angle ranges from around $66°$ to $6.3°$ and is maximum close to the root of the propeller and minimal at the tip. This is due to the speed at the tip of the propeller being much greater than at the root which makes the rotational component of the wind velocity vector much larger. Figure 109 shows that as this happens and the forward velocity does not change, the inflow angle decreases.

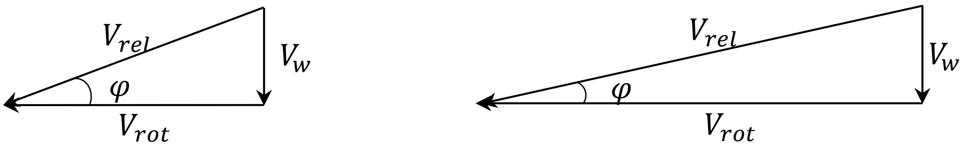

Lower Rotational Speed (Near Higher Rotational Speed (Near Tip)

Figure 109: Effect of increasing rotational velocity on inflow angle

5.2.6.3.3 Stall Control and Spanwise Twist Angle Distribution

In order to optimise the propeller design, stall control is utilised. The aim of the propeller is to produce maximum lift and therefore the lift coefficient should be close to the maximum value for the aerofoil denoted as C_{Lmax}. This corresponds to an angle of attack, known as the stall angle, and if the angle of attack exceeds this value, stall will occur. From the graph of C_L against α for the NACA 0010 aerofoil, C_{Lmax} was achieved at an angle of attack of $15°$, therefore for a conservative estimate, the angle of attack along the propeller blade should not exceed $14.5°$.

Using the inflow angle previously determined at each radial position and considering that the angle of attack should ideally always be below or around $14.5°$, the twist angle may be calculated using Equation 120. It is ideal to keep the twist angle roughly equal and below stall angle across the whole blade length, however, in this case, it can be seen that the inflow angle at near the root is actually quite large, an angle of attack of $14.5°$ here would result in a twist angle of around $86°$ which is very large considering that twist usually ranges between $0° - 90°$. The angle of attack near the root can therefore be lowered here to a small positive angle of around $3°$ for example as the root of the blade has a much less significant impact on the performance of the propeller than the tip and therefore a low angle of attack will not make much difference. The aerofoils along the remainder of the blade length are given $\alpha = 14.5°$ to achieve maximum lift performance. The spanwise twist angle distribution can therefore be seen in Figure 110 and ranges from $69°$ to $21°$ from root to tip. It can be observed that the blade angle distribution is not linear like in the initial design. This allows for the design to be more fine-tuned.

As a propeller is continuous in a non-uniform flow field (Vepa, 2020), an initial twist is usually required and therefore a 'setting angle' can be set initially which essentially provides the propeller profile a pre-twist, with the calculated twist angle added in addition to this. As the twist angle is already quite high along the blade, no setting angle will be added for this case.

The new propeller design was made in *SolidWorks* and can be seen in Figure 111.

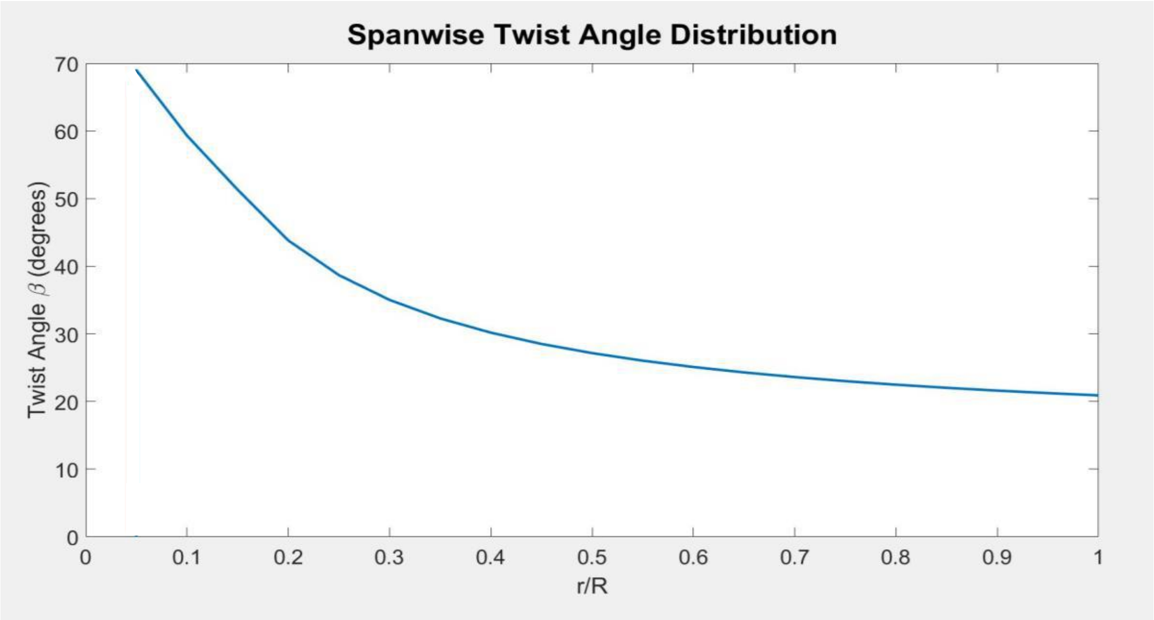

Figure 110: Spanwise twist angle distribution across propeller blade length

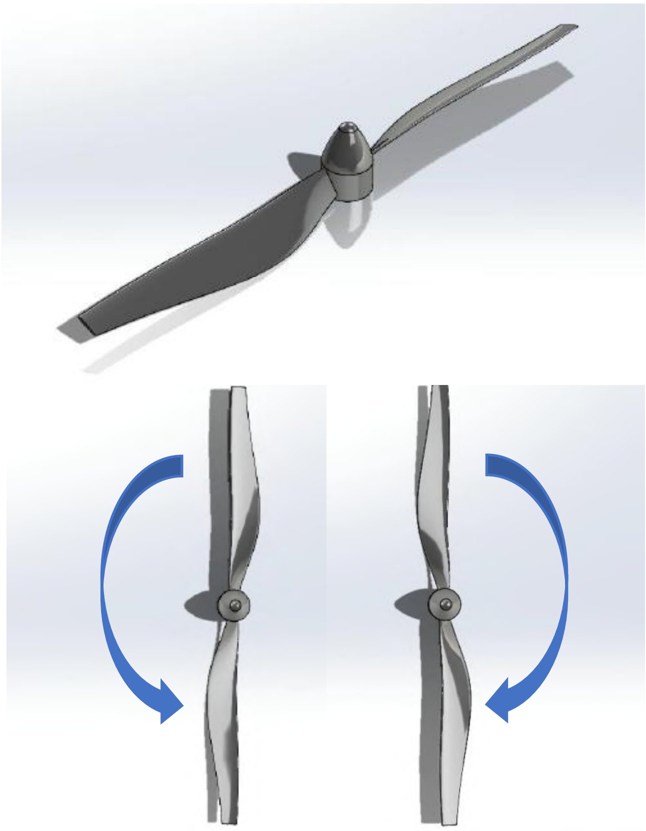

Figure 111: CAD model for new propeller design (Top) isometric view of propeller, (left) anti-clockwise propeller, (right) clockwise propeller

5.2.6.3.4 New Propeller Design Performance Analysis

JBLADE was once again used for the performance analysis of this design and the propeller modelled is shown in Figure 112. The propeller has been split into five sections so that the non-linear twist angle distribution can be modelled more accurately.

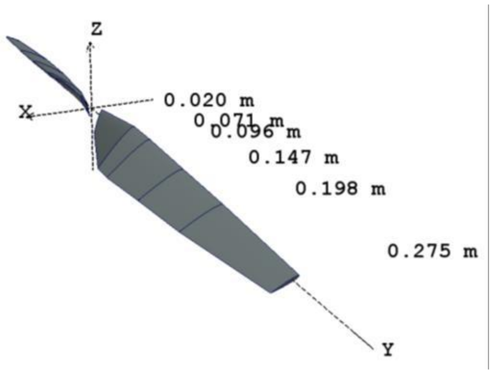

Figure 112: New propeller design modelled in JBLADE

The diameter, chord length variation, and rotational speed for simulation were kept the same for the new design so that the effect of angle distribution on the performance of the propeller could be assessed.

The new propeller design was also replicated for propellers with two, three, four, and five blades, for testing in order to determine if the initial choice of two blades would be reasonable to implement into the design. The latter three propeller designs can be seen in Figure 113.

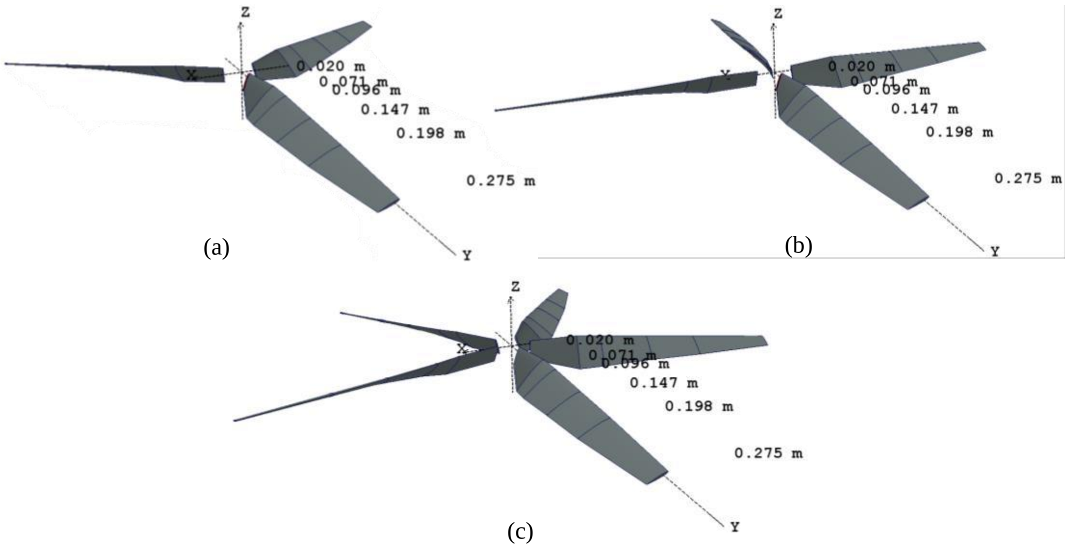

Figure 113: (a) three-bladed (b) four-bladed (c) five bladed propellers tested in JBLADE.

The efficiency curves were plotted for each of these four propellers with the results shown in Figure 114. The efficiency curves did not seem to change with additional blades and therefore the use of two blades would be optimal as this will minimise weight and not compromise efficiency.

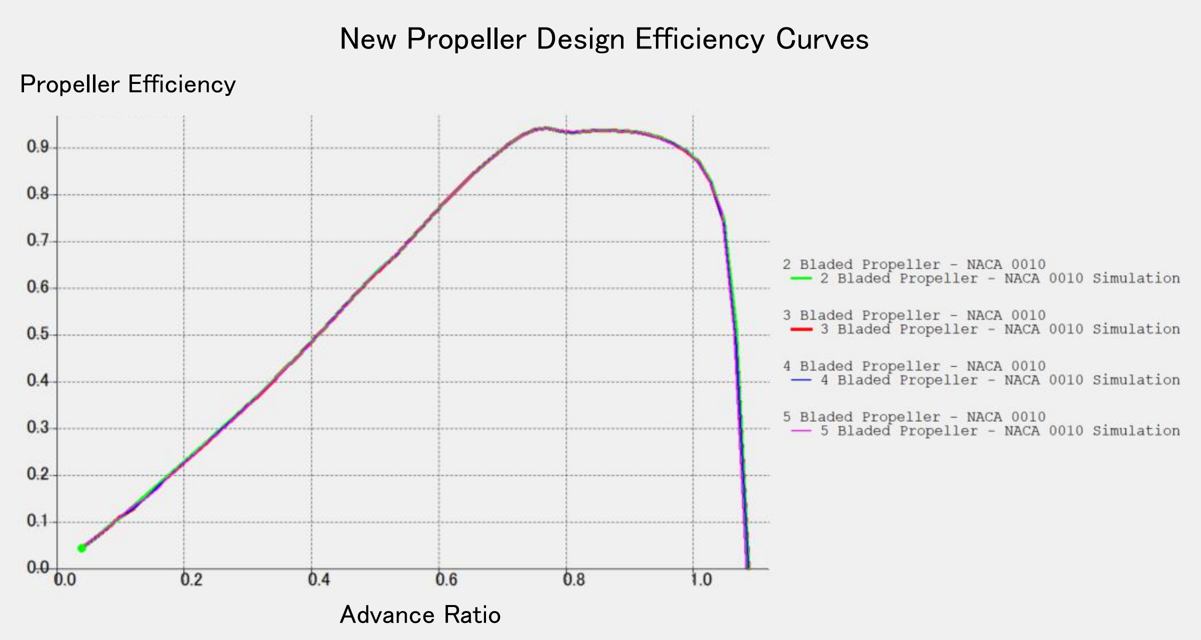

Figure 114: Propeller efficiency against advance ratio for new propeller design with varying number of blades

For the twist distribution calculated, the blade angle at 0.75R is 22°. Comparing the typical efficiency plot for a blade angle of 20° at 0.75R to the efficiency curve produced from the *JBLADE* simulation, although the simulated efficiency curves are not as smooth, the two plots are very similar, with a similar advance ratio ranges and general shape, showing that the calculated results agree quite closely with those typically obtained through literature.

A maximum efficiency of around 0.93 is achieved at an advance ratio of around 0.77 and a similar efficiency is shown for an advance ratio of 0.85. It should be noted that this maximum efficiency is very high and in reality, would not likely be possible to achieve. However, it is possible for propeller designs to have a theoretical efficiency that is this high, like in this case. As previously mentioned, an efficiency above 0.7 is preferable which corresponds to an advance ratio range of $0.55 - 1.05$. Using previous methods, Equation 44 shows that the corresponding rotational speed range is $2900 - 5500\, rpm$, with the advance ratio that corresponds to the highest efficiency relating to a speed of $3900\, rpm$.

$$
\begin{aligned}
J = 0.55 : \ n &= \frac{27.78}{0.58 \times 0.55} \approx 90\, rev/s \approx 5500\, rpm \\
J = 1.05 : \ n &= \frac{27.78}{0.58 \times 1.05} = 50\, rev/s \approx 2900\, rpm
\end{aligned} \tag{122}
$$

$$J = 0.77\ (optimal):\ n = \frac{27.78}{0.58 \times 0.77} = 70\ rev/s \approx 3900\ rpm$$

Figure 115 shows the C_T curve for the new two-bladed propeller design.

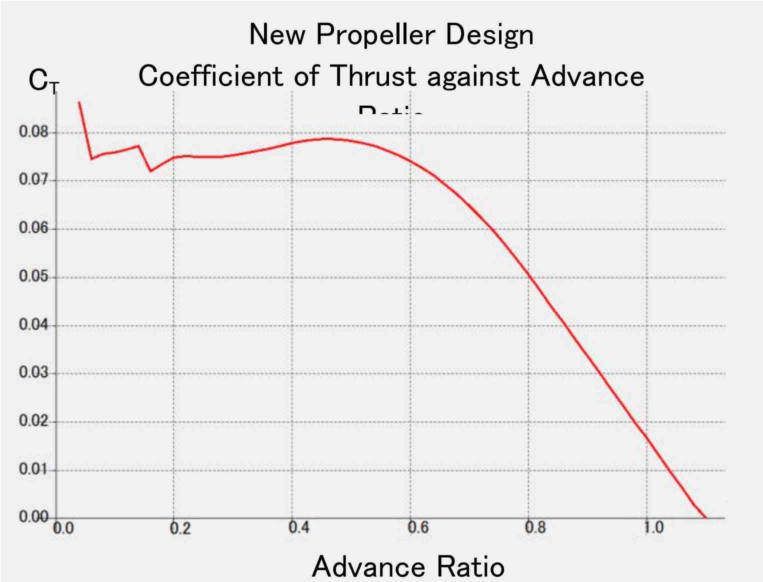

Figure 115: Coefficient of thrust variation with advance ratio for new propeller design

The coefficient of thrust for the new design is reaches a much higher value than the initial design. The initial propeller design had a peak C_T of around 0.65 and for the new design, this peak is close to 0.85, showing that for the same diameter, rotational speed, and air density, the new design is capable of producing more thrust. This supports the notion that the new design is a more optimised one with better performance as it can generate more thrust for the same diameter. This is similarly supported by the efficiency curves of the propeller, with a peak efficiency of 0.93 being achieved with the new design, compared to a peak of 0.8 for the initial design. A peak It can also be noted that the advance ratio ranges for the designs are different, with the new design having a peak efficiency at a higher advance ratio. If the wind speed and diameter of the propeller is the same, a higher advance ratio means that a lower rotational speed is required, as evidence by the optimal rotational speeds of $6600\ rpm$ an $3900\ rpm$ for the initial and new designs respectively. Therefore, the new design does not require a motor with as high of a rotational speed range as the initial design would need.

The C_P curve shown in Figure 116 similarly shows a performance close to the typical curves seen, with a very similar C_P range, peaking at around 0.04.

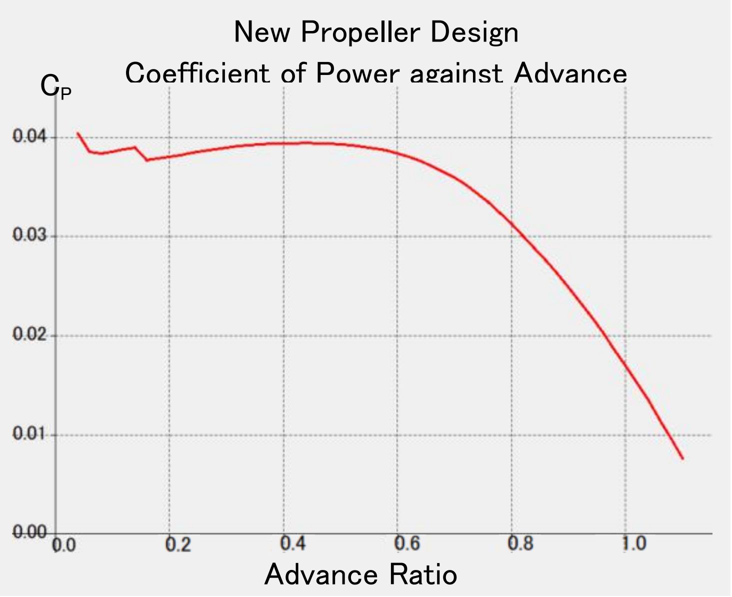

Figure 116: Coefficient of power variation with advance ratio for new propeller design

The thrust curve was also plotted for the new propeller design as shown in Figure 117 which illustrated a peak thrust of $18N$, falling closer to $16N$ before plummeting at higher wind speeds. Recalling that the theoretical thrust per propeller calculated was estimated to be $17N$, the results are agreeable within 5.6% of the theoretical value, once again aiding in the validation of the results.

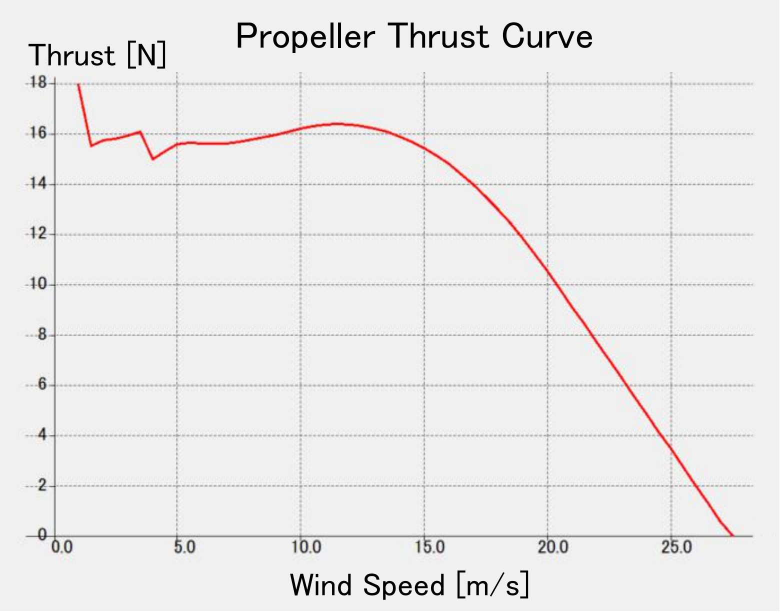

Figure 117: Thrust variation with wind speed for new propeller design

5.2.7 Analysis Limitations

In the first instance of designing the new propeller, the aerofoil lift characteristics were obtained using *XFOIL* which determined the stall angle value. *XFOIL* has limitations including its incapability of modelling flow separation and its assumption of an instantaneous transition from laminar to turbulent flow which leads to deviations in results obtained through *XFOIL* and experimental data (Rab et al., 2018). However, it can predict stall to an extent by utilising empirical formulations and the deviation in results is relatively minimal and thus its accuracy in estimating the maximum lift coefficient is sufficient.

Another shortcoming of this analysis is that the induced velocity was not included in the forward velocity when calculating the inflow angle, making the calculated values smaller than they should be. As this is a first approximation, this change was deemed to be insignificant enough to discount, however as this is not technically correct, the accuracy of the results is limited.

The spanwise twist angle distribution plotted and used in the propeller design does not have a linear variation. Although this is advantageous in terms of providing more accurate angles at each radial position, in both *SolidWorks* and *JBLADE*, it is difficult to model this variation accurately. Between each propeller section specified, the angle distribution is taken as linear and thus for an accurate representation of the true variation in the *JBLADE* simulation, a very large number of sections would need to be created which is incredibly time consuming. For the simulations carried out, the blade was split into five sections in order to try to model the twist more accurately, but this still does not fully model the calculated twist distribution.

Steps may be taken to correct the limitations related to modelling and calculations in the future, and other improvements will be discussed in Section 6.3.9.

5.2.8 Conclusion

Two approaches were carried out in order to design propellers for use on a UAV which delivers aid in natural disasters and their performances were analysed. Sizing calculations were implemented in order to find the required thrust and diameter of each propeller and typical performance data found in literature was used to set preliminary rotational speed for simulations. The first approach involved designing propeller blade angle distribution based on similar VTOL UAV propeller designs, and the second aimed to optimise the design by implementing stall control and aerofoil geometry calculations.

The performance curves of each of the propellers tested very closely follow those shown in literature, aiding in the validation of results. The new propeller design outperformed the initial design in all performance characteristics, with a peak efficiency of 0.93 compared to a peak of 0.82 for the initial design. The new design also reached a peak C_T of 0.85 when compared to the initial design's 0.65, showing more optimal thrust production. The number of blades was found to not have a great effect on the propeller performance, while the blade angle distribution made a great impact. The simulations showed great agreement with the sizing calculations, with the thrust value agreeing within 5.6%. The rotational speed leading to the peak efficiency for the new design was found to be $3900\ rpm$ and thus when considering motor choices, this should be taken into account. The new, two-bladed propeller design is therefore the more optimal design for use on this UAV. Ultimately, the objectives set were carried out and the aims were met successfully.

5.2.9 Future Improvements

There are a few main improvements that can be made for the design of the propellers used for cruise. Firstly, as previously mentioned, the spanwise twist angle distribution was modelled by splitting the propeller blade into five sections. In order to more closely match the true non-linear variation, this number of sections could increase, particularly within the first third of the blade length from the hub as this is where the largest angle variation occurs. The number of sections could also increase towards the tip as even though the angle variation is not as large as closer to the hub, the tip has the largest effect on performance and thus is incredibly important. It can then be assessed how this affects and potentially improves the propeller design and performance.

The induced velocity along the blade could also be calculated in the future through more research into the BEM. This could then be used to calculate a more accurate variation of inflow angle and in turn, spanwise twist angle distribution. Once again, the effects of this on propeller performance can be assessed.

It would also have been an improvement to validate the performance results obtained through *JBLADE* using another software like *MATLAB* for example. A code could be created to plot the same performance curves for each scenario and compare them to the results obtained in order to assess their accuracy. Other propeller design software could similarly be used to see the performance of the propeller design, potentially illustrating even more performance characteristics such as power, and torque variations. Similarly, numerical simulation could also have been carried out to validate the results. The effect of changing the rotational speed of the propeller and pitch angle could also potentially be shown in order to further maximise the performance of the propeller and to assess its performance curves under different conditions. This could potentially reveal a more efficient configuration than considered in this report which could be implemented for the UAV design in the future.

Further simulations could also be carried out on the propellers with different rotational speeds other than the $5500rpm$ tested in order to see how this effects their performance. A range of $2900 - 5500rpm$ could be tested which should still maintain an efficiency of above 0.7 in theory, and a speed of $3900rpm$ as this was calculated to be optimal. The chord length variation along the length of the blade could also be altered and a few different variations could be tested to see how this affects performance.

The effects of using ducted fans instead of open rotors or in combination with each other could also be explored. The sizing calculations and performance characteristics would differ slightly and could be compared with using open rotors only. The blade number analysis carried out only looked at efficiency curves and so in the future, simulations could be run on propellers with a varying number of blades with the aim being to maximise thrust but keep power fixed for example. Additionally, the effects of using a different number of propellers could be tested to see what the optimum number is using CFD for example.

5.3 Propulsion system continued (Emran Rahmat)

5.3.1 Review of previous research

The state of the art report provided an in-depth look into current research developments of the different power sources for the UAV. Since the UAV design requirement is to increase the payload, UAV power supply must provide the required power with reduced weight. The research concluded that Lithium based batteries have the highest energy density, thus, the most suitable for the UAV design. The battery charging methods were also analysed, and battery swap system is the most efficient method.

Mechanical energy converters must meet all the UAV propulsion requirements. The most important parameters in mechanical energy converters are high-power density, efficient and low weight. State of the art report discussed the most recent and advanced research into electric motors in UAV applications. Once the required motor power and torque has been calculated, the range of motors discussed in state of the art report will be evaluated and the most suitable motor will be selected for the UAV. In addition, the required devices to improve UAV performance and technology, such as Insulated Gate Bipolar transistor and electronic speed controller, can also be selected once the motor has been selected.

5.3.2 Battery

5.3.2.1 Battery configuration

The payload will be placed in the basal area of the fuselage to ensure swift payload drop off to target. Therefore, the battery system will be placed in the upper compartment of the fuselage for an efficient battery swap system. The battery will be connected directly to the electric motors to reduce any extra wiring weight. Shorter wires connections will reduce the internal resistance. Ohm’s Law states that V=IR, where V is the voltage drop, I is the current, and R is the wire internal resistance. Lower resistance would also reduce the voltage drop [Carter, 2014].

Since the ideal power source for our design is a battery, the current supplied from a battery is direct. For electric motors to perform full rotations, alternating current supply is required to rotate the magnet. Electronic devices are required to convert these direct currents supplied by the battery into alternating current. The insulated gate bipolar transistor (IGBT) is a successful device used to control the electric energy. The device is a switch used to open and close the path for the current flow, thus changing the current flow direction. IGBT has good switching speed to achieving higher frequencies of AC current [S. Abedinpour, 2011].

Multiple batteries can be used to provide the mission power requirement. Batteries can be wired in series or parallel, depending on the performance requirement. Both parallel and series circuit set up would provide the same power output measured in Wh. Batteries connected in series would result in its voltages added together to provide an overall voltage supply. However, batteries connected in parallel would have its capacity (measured in Ah) added together. Advantage of connecting batteries in series is that thinner wires can be used to connect the system.

5.3.2.2 Battery sizing

(VTOL Power calculation)

The powered required to generate vertical thrust can be calculated using equation 123:

$$P_{req}^{VTOL} = \frac{T \times v_i}{FOM} \tag{123}$$

Where P_{req}^{VTOL} is the power required, T is the thrust required, $v_i$is the vertical velocity (rate of climb) and FOM is the figure of merit. FOM is the rotor efficiency and can vary between 0.7 and 0.8 for helicopter rotors. However, Multi-copter FOM can be lower. Experimental data obtained by Tyan et al. [2017], for 85 motor-propeller, displays FOM ranging between 52-67%. The data obtained presents the model in equation 124:

$$FOM = 0.4742 \times T^{0.0793} \tag{124}$$

The FOM can vary at different stages of the mission depending on the Thrust output required. The FOM for initial vertical take-off, with the payload, can be calculated using equation 2:

$$FOM = 0.4742 \times 327.4^{0.0793} = 0.75$$

Power required for initial vertical take-off can be calculated using Equation 1:

$$P_{req}^{VTOL} = \frac{327.4 \times 2.5}{0.75} = 1091W = 1100W$$

The same steps can be followed to calculate the FoM and subsequently the power requirement for the landing stage with no payload.

(Cruise power calculation)

Equation 1 can be used to calculate the power requirement for cruise stage of the mission:

$$P_{req}^{cruise} = \frac{65.49 \times 27.8}{0.7} = 1774.83W = 1800W$$

(Battery power requirement)

The power required at each stage has been calculated in watts. The maximum mission power requirement can be calculated by obtaining the power required to complete the maximum distance range. For VTOL, the climb rate is 2.5ms^{-1}=9Kmh^{-1}. Since maximum flight altitude is 120m, maximum VTOL time is 48s. Therefore, power required for initial vertical take-off in Wh:

$$P = \frac{1091 \times 48}{3600} = 14.55Wh = 15Wh$$

The same method can be applied to landing stage of the mission:

$$P = \frac{723.6 \times 48}{3600} = 9.65Wh = 10Wh$$

Since cruise velocity=27.8ms^{-1}=100kmh^{-1}, maximum cruise time would be 1hour to cover maximum range of 50Km and return to station. Therefore, the power required for cruise stage is:

$$P = 1800 \times 1 = 1800Wh$$

Therefore, total battery power required for the maximum mission range of 50km:

$$1800 + 10 + 15 = 1825Wh$$

5.3.2.3 Battery selection

Figure 118: Gens Tattu 32000mah 22.8v 10c 6s1p High Voltage LiPo Battery Pack

The SOTA review conducted developed our understanding of current batteries available and any current research developments. It was deduced from the research that LiPo batteries are the most suitable for our design requirements. Lithium Polymer (LiPo) batteries have the highest energy density, therefore, can reduce the UAV weight. Figure 1 displays Tattu 6S 32000mAh 22.8V LiPo battery. It is a high voltage battery, commonly used in UAV applications. The power, measured in Wh, for this battery is:

$$32000 \times 22.8 \times 10^{-3} = 729.6Wh$$

The mission would require 3 × Tattu 6S 32000mAh 22.8V LiPo battery connected in series to give an overall power of 2188.8 Wh. This power would be sufficient for every mission stage, including emergency loiter. Table 25 displays the combined parameters for this battery system.

Table 25: Important parameters for Tattu 6S 32000mAh 22.8V LiPo battery.

3 × Tattu 6S 32000mAh 22.8V LiPo battery	
Voltage (v)	68.4
Minimum capacity (mAh)	32000
Power (Wh)	2188.8
Dimensions (cm) for 1	21.8 length × 12.0 width × 6.1 height
Weight (kg)	10.725

5.3.3 Motor

Initial step is to determine the most suitable motor for our design, with high efficiency and low weight as the main targets. Each propeller will have its individual motor to drive the propulsion system. The research conducted in SOTA recommended that Permanent Magnet Brushless DC motors are suitable for our design, due to high efficiency, low weight and good thermal evacuation attributes. High temperature superconducting motors may also be an alternative candidate as they carry large currents with insignificant losses. They enable high power and torque density for aviation applications. Figure 119 displays the results for the tests carried out on HTS motors and conventional motors ((Masson et al. 2022). Selecting the right motor will depend on the torque and power requirement for VTOL and cruise propellers.

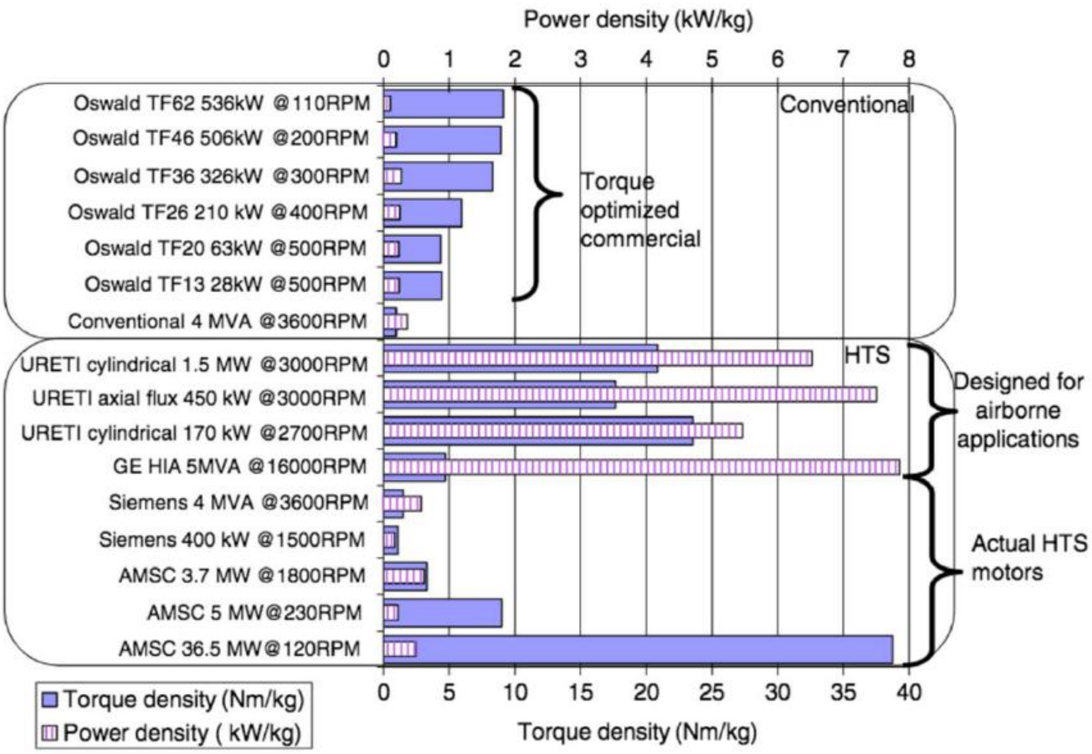

Figure 119: Comparison of electric motors in terms of specific power and torque (Masson et al. 2022).

Dantsker et al., [2020] carried out performance testing of Aero-Naut CAM folding propellers using the Hacker A40-14L 14-pole (355kV) brushless electric motor to rotate propellers with diameter range of 9-13inches. Initially, this motor, shown in figure 120, will be used to drive the propellers.

Figure 120: Hacker A40-14L 14-pole (355kV) brushless electric motor (A40-14L V4 14-Pole kv355, 2022).

Table below displays the important parameters for the electric motors that will be used in the UAV design.

Table 136: Important parameters for Hacker A40-14L 14-pole (355kV) brushless electric motor.

8 × Hacker A40-14L 14-pole (355kV) brushless electric motor	
	Per motor
Power (Wh)	2188.8(15sec)
Dimensions (cm)	5.2 length × 4.17diameter
Weight (kg)	0.275

For aerodynamic and cooling reasons, an internal motor with a shaft connecting the motor to the propeller will be implemented. The shaft must be short as much as possible to avoid parasite vibrations and rotational stiffness (Ragot, Markovic and Perriard, 2006).

5.3.3.1 Motor torque requirement

The torque is the force produced by the motor to rotate the propeller blades about the boss. The torque required to rotate the propeller blades at the required RPM can be calculated using:

$$Q = I\omega \tag{125}$$

Where τ is the torque required, I is the moment of inertia for the propeller, ω is the angular velocity in RPM and t is time in minutes. The moment of inertia of a disk can be derived and applied to the propeller geometry. The blade can be approximated as a rotating disk of mass m and radius r to give the moment of inertia as:

$$I = \frac{1}{2} \times m \times r^2 \tag{126}$$

The mission required torque can be calculated using equation 3 and 4. The VTOL folding propeller mass is obtained from SolidWorks, where m=0.17kg, r= 0.221m, and for initial estimated rotational speed of 1000. The required torque is:

$$Q = \frac{1}{2} \times m \times r^2 \times \omega = \frac{1}{2} \times 0.17 \times 0.221^2 \times 1000 = 4.15Nm$$

The same method can be used to calculate torque requirement for the cruise propellers where m=012, r=0.27 and optimal RPM value of 6000. The required torque for cruise is:

$$Q = \frac{1}{2} \times 0.12 \times 0.27^2 \times 6000 = 52.49Nm$$

UAV motor will have to provide the required torque calculated for both cruise and VTOL propellers.

5.3.3.2 Insulated Gate Bipolar transistor

The electric energy supplied by the battery is a direct current, where electrons flow in one direction. Electric motors require alternating current, where the electron flow change direction, to rotate the motor magnet. A power inverter is required to invert the DC supply from the battery to AC supply for the electric motor. Insulated Gate Bipolar transistor is a successful inverter device, which was introduced in the early 1980s. It is a three-terminal power semiconductor switch used to control the electrical energy. IGBT’s can open and close the switches super-fast to alternate the electron flow directions (Abedinpour and Shenai, 2011). This device will improve the UAVs performance by increasing efficiency through sufficiently alternating the electron flow direction.

5.3.4 VTOL Propeller

The UAV design will utilise the Vertical Take-Off and Landing design using 4 horizontal propellers of same parameters. Commercial smaller drones use similar propeller arrangements called quadcopters to provide the vertical take-off and landing, as well as the lateral movement by adjusting the rotational speed on each propeller (STEM LEARNING, 2022). Similarly, The

UAV VTOL propellers will provide the VTOL thrust, however, cruise propellers will be employed for forward thrust.

Each rotating propeller generate torque, which affects the stability of the UAV. To counteract the torque generated by these propellers, two propellers can rotate clockwise and two anti-clockwise. Figure below shows the propeller rotating in clockwise and anti-clockwise directions to cancel out the produced torque during propeller rotations.

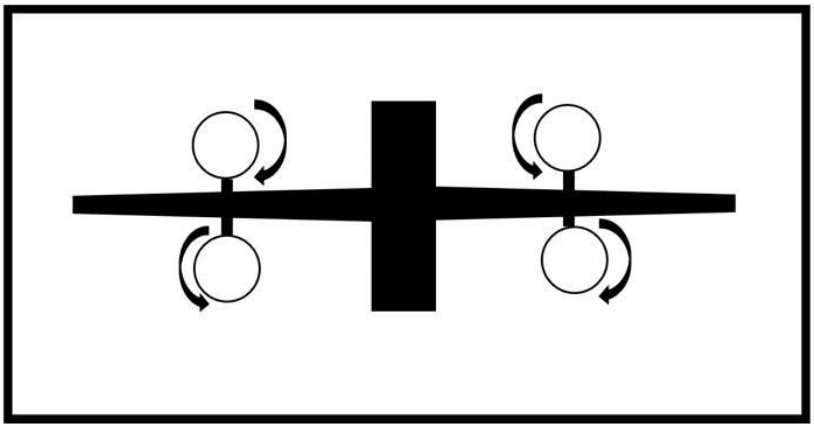

Figure 121: Propeller rotating in different directions to cancel out the torque produced by each propeller.

5.3.4.1 VTOL Propeller diameter calculation

The power required for vertical take of stage is already calculated using equation:

$$P_{req}^{VTOL} = \frac{327.4 \times 2.5}{0.75} = 1091W$$

Since 4 propellers will be designed for vertical take-off, the power required can be split between these propellers, where power for each propeller:

$$P_{req}^{VTOL}\ per\ propeller = 280W$$

The required diameter for each propeller can be calculated using the same equation used for cruise. Where:

$$d = K(P_{inst})^{0.25} = 22\left(\frac{280}{746}\right)^{0.25} = 17.11\ in = 0.43m$$

5.3.4.2 Folding VTOL propeller

Increased UAV payload will result in significantly higher battery power consumption during mission. One design aspect that can be optimised to reduce drag contribution to UAV drag is the VTOL propellers. Significant twist angles in UAV VTOL propellers blades drastically contribute to UAV drag during cruise. Furthermore, VTOL propellers would also contribute to noise generation and vibration during cruise. State of the Art Report introduced recent design developments that can be implemented to reduce VTOL propeller drag contribution.

Introducing a simple folding mechanism that can fold VTOL propellers during cruise is simple yet efficient. The flight performance of the folding VTOL propeller blades, during take-off and landing, are the same as the non-folding VTOL propeller blades. Most recent research has been carried out by NASA into a method for designing conforming folding propellers. The research presents a method for designing folding-blade configurations that conform to the nacelle surface. The method was implemented on propeller with more than 4 blades. This design is not ideal for the UAV 2 blades VTOL propeller; however, the design idea can be optimised to suit the 2 blades VTOL propeller configuration.

5.3.4.3 VTOL Propeller SolidWorks

Initial design requirement for the folded VTOL propeller is ensuring minimal aerodynamic design complication and minimal weight increase to the conventional propeller. This can be achieved by introducing propeller configuration that enables one blade folded into the other. Figure 122 displays the VTOL propeller folding mechanism. The propeller blade can be folded across the propeller boss and parallel to the second propeller to reduce the amount of airflow distorted, consequently, reducing drag contribution. The mechanism requires lightweight servo motor, gear, gear rod and other important mechanical parts. The servo motor will provide the required torque and revolutions to rotate the blade 180 degrees across the propeller boss.

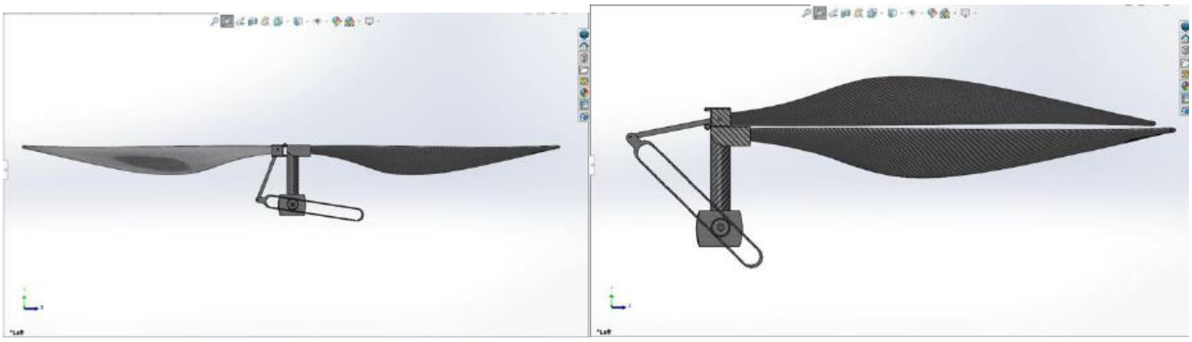

Figure 122: UAV VTOL propeller unfolded (left) and folded (right) mechanism 3D CAD, designed using SolidWorks.

Figure 123 displays the propeller configuration during take-off and landing. As shown, the VTOL propeller gear rod would interfere with the airflow downstream of the propeller, therefore, Computational Fluids Dynamic analysis would be required to investigate how much propeller thrust and lift coefficient would be affected by this folding configuration.

Figure 123: VTOL UAV propeller during vertical take-off and landing in SolidWorks.

Figure 124 displays the VTOL propeller alignment during cruise. As shown in both figures, the propellers blades will be parallel to the supporting rods and the incoming flow. This would significantly reduce airflow distortion. In addition, the folded propeller design has blunt edge features to ensure laminar flow over the propeller body during cruise condition. These features can also be investigated using computational fluids dynamics to analyse the difference in coefficient of drag of VTOL conventional and folded propeller.

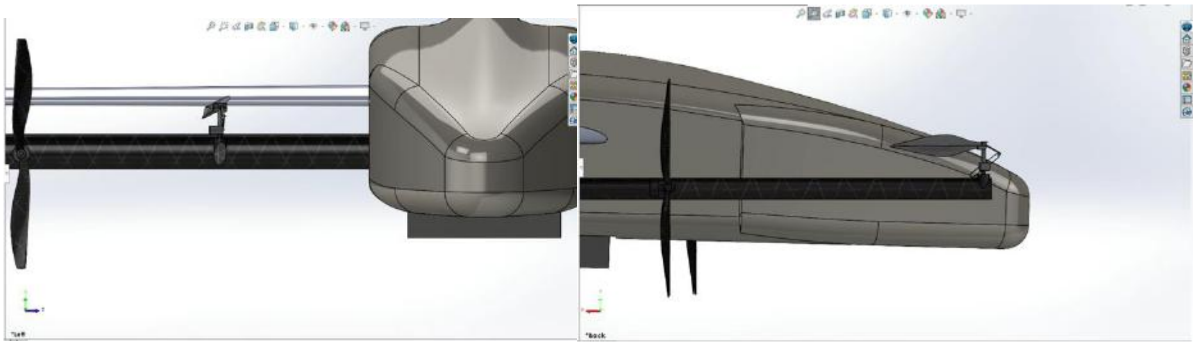

Figure 124: Front view (left) and side view (right) of UAV VTOL propeller, in folded state, during cruise in SolidWorks.

5.3.5 System Configuration

Figure 125 displays the propulsion schematic for the VTOL and cruise propellers. The battery displayed is 3 × Tattu 6S 32000mAh 22.8V LiPo battery as the only power source. The battery is connected to a bus bar to efficiently distribute power to different area of the UAV. The bus bar does not require insulation, thus, allowing sufficient configuration cooling during high current flow.

The direct current flow from the bus bar is transferred to Insulated Gate Bipolar transistor, so the DC is inverted to AC. The power is transferred to the power management and distribution device (PMAD), where the required electric power will be supplied at different flight conditions. The required power supplied to the ESC and motor will drive the motor at the rotational speed communicated by the controls system. Finally, the motor will rotate the propellers and provide the.

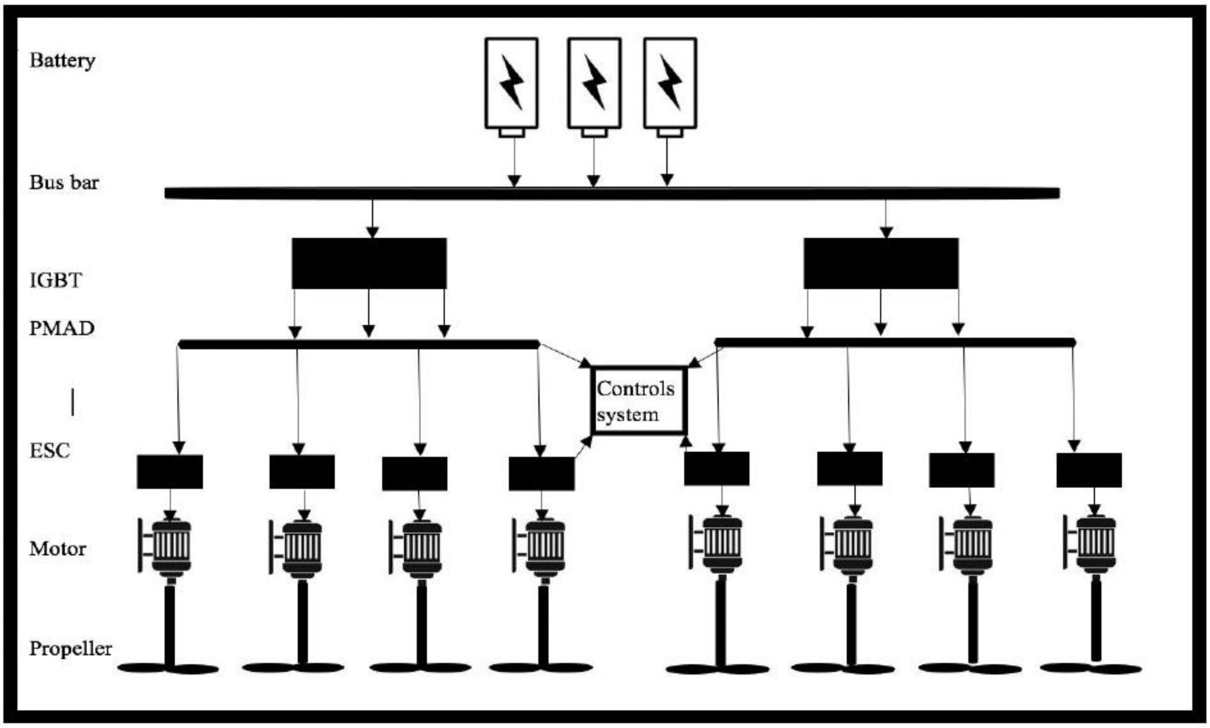

Figure 125:The propulsion system schematic for VTOL and cruise propellers.

5.3.6 Optimisation

Once the initial propeller design configuration has been decided, optimisation using analytical models can be performed to obtain the optimum propeller parameters for different requirements. Analytical model is the ideal method when the number of parameters are high. Therefore, a model that can optimise the design close to realistic values without being too complicated would be preferred.

5.3.6.1 VTOL Propeller optimisation model

5.3.6.1.1Williams Froude's theory

The analytical model that will be used to optimise the propeller is an aerodynamic model based on William Froude's theory. The theory is based on the Bernoulli's equations and momentum theorem [Cam, 2022]. The model is displayed in figure 126. The assumption that the propeller behaves as a thin disk is taken. The stream experiences change in pressure between P_2 and P_3 according to Bernoulli's equation. Thus, the thrust output can be estimated as a result of the pressure drop across the propeller (thin disk):

$$T_{propeller} = A_{disk}(P_3 - P_2) \tag{127}$$

Where $T_{propeller}$ is the propeller thrust output and A_{disk} is the assumed area of the thin disk formed by the propeller. The Bernoulli's equation can be used to substitute the velocity terms for the pressure terms since:

$$\frac{1}{2}\rho({V_3}^2 - {V_2}^2) = (P_3 - P_2) \tag{128}$$

Where V_2 is the inlet velocity (velocity of the UAV) and V_3 is the accelerated exit velocity. Equation 128 can be substituted into equation 127 to give the propeller thrust:

$$T_{propeller} = \frac{1}{2}\rho A_{disk}({V_3}^2 - {V_2}^2) \tag{129}$$

Equation 129 can be rearranged for exit velocity:

$$V_3 = \sqrt{\frac{2T_{propeller}}{\rho A_{disk}} + {V_2}^2} \tag{130}$$

The disk velocity can be calculated using the average of the inlet and exit velocity:

$$V_{disk} = \frac{V_3 + V_2}{2} \tag{131}$$

The propeller velocity (disk velocity) in terms of the inlet velocity is given by:

$$V_{disk} = \frac{\sqrt{\frac{2T_{propeller}}{\rho A_{disk}} + {V_2}^2} + V_2}{2} \tag{132}$$

A new parameter can be introduced that measure how much the inlet velocity has been affected by the propeller (thin disk), called the axial induction factor, a. The propeller velocity (disk velocity) can be expressed in terms of a [(Notre Dame, 2022)]:

$$V_{disk} = V_2(1 + a) \tag{133}$$

The propeller can be optimised using equation 131 and 132 to obtain the optimised disk velocity and axial induction factor for $T_{propeller} = 81.85N$ and inlet velocity of $V_2 = 2.5ms^{-1}$:

$$V_{disk} = \frac{\sqrt{\frac{2 \times 81.85}{1.225 \times \pi \times 0.221^2} + 2.5^2} + 2.5}{2} = 16.93$$

Thus, the axial induction factor:

$$a = \frac{V_{disk}}{V_2} - 1 = 5.52$$

This is the optimised axial induction factor for the required vertical thrust, $T_{propeller} = 81.85N$. The optimised disk velocity can also be used to compare to disk velocity results obtained using Computational Fluids Dynamic simulation.

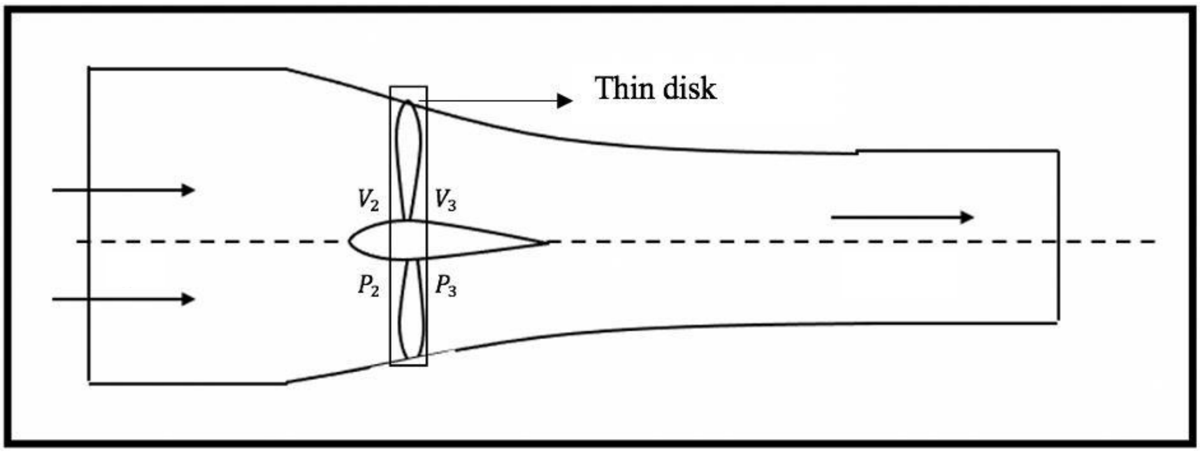

Figure 126: William Froude's theory of propeller with stream tube.

5.3.6.1.2 Blade Element Momentum analysis

The Blade Element Momentum theory (BEM) was introduced by H. Glauert in 1926 to model the aerodynamic interaction between a propeller and incoming fluid flow. It is on the basis of the propeller mechanical and geometric parameters in addition to the characteristics of the incoming flow. BEM model results from combination of two theories: the momentum and blade element theories (Ledoux, Riffo and Salomon, 2021). The momentum theory, also known as actuator disk theory, has been displayed and discussed in Williams Froude's theory.

The blade element theory was also introduced by William Froude to study the propellers from local point of view. The propeller blade is cut into sections called blade elements. This method results in expressions of the applied forces on each blade element, as a function of the incoming flow characteristics and blade geometry. The fundamental quantities are the Lift and Drag coefficients, as a function of the angle of attack. The angle of attack is the angle between the incoming flow and rotating blade. The results are integrated along the blade to obtain global values (Ledoux, Riffo and Salomon, 2021).

JBLADE software will be employed to simulate the Blade Element Momentum analysis on the propeller geometry and optimise using the data obtained. The software is being developed as part of a PhD thesis at Aerospace Sciences Department in University of Beira Interior. The software enables to build and analyse propeller simulations. The software enables BEM analysis with a defined propeller and airflow parameters. The Reynolds number for the simulation can be calculated using the following equation:

$$Reynolds\ number = \frac{\rho u l}{\mu} = \frac{1.225 \times 16.93 \times 0.05}{1.789 \times 10^{-5}} = 57963.24 = 58{,}000$$

Where the air velocity is the propeller blade velocity calculated using Froude's theory, and l is the chord length of the propeller aerofoil. The initial simulation is performed for a range of Reynolds number 50000-100000 values and angle of attack 0-25°. The results obtained have been graphically displayed below for the VTOL propellers:

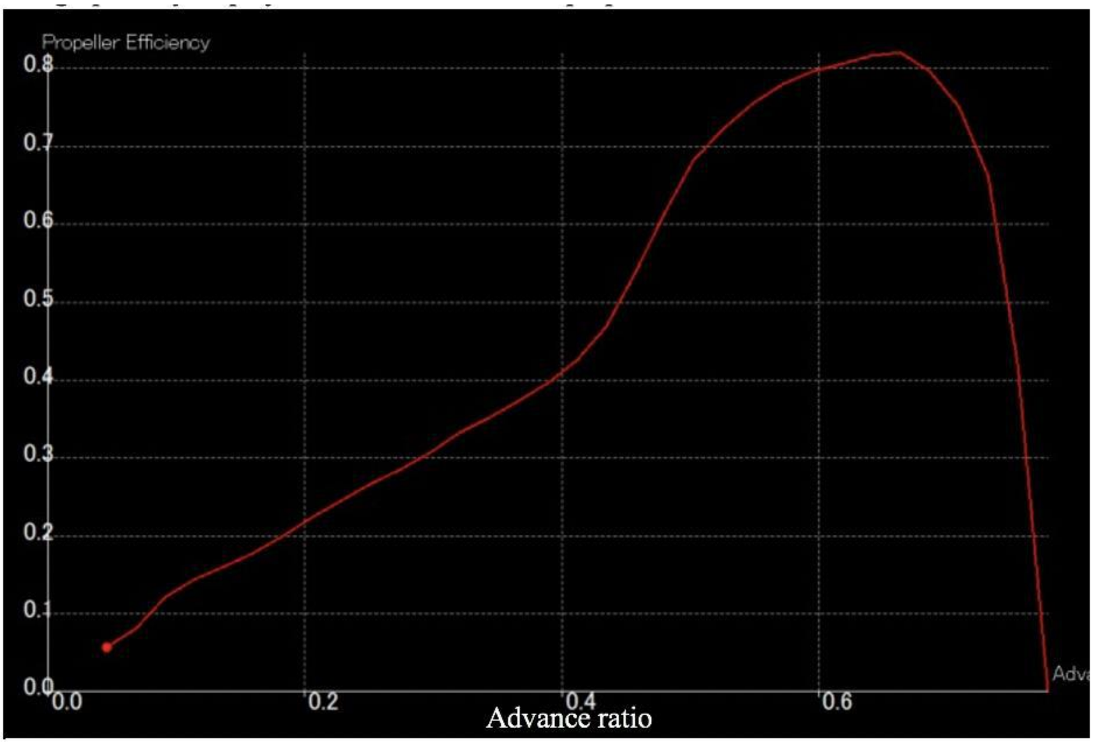

Figure 127: Propeller efficiency against advance ratio of the VTOL propeller.

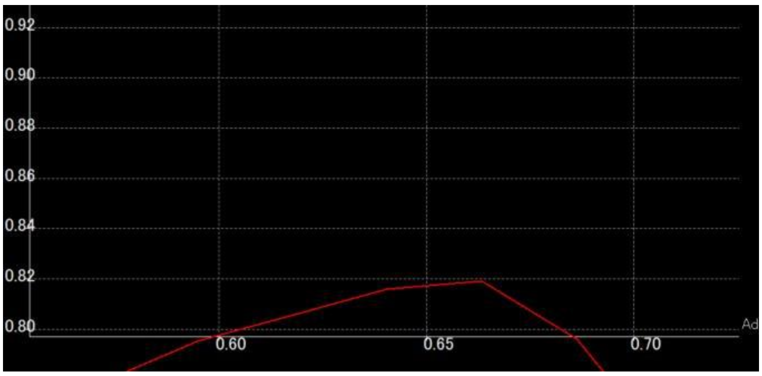

Figure 128: Propeller efficiency against advance ratio for the optimum advance ratio.

Figure above displays the propeller efficiency against advance ratio for the VTOL propeller. The maximum propeller efficiency gives an advance ratio of 0.65. Therefore, the initial propeller rotational speed can be calculated as:

$$n = \frac{V}{dJ} = \frac{2.5}{0.43 \times 0.65} = 10.25revs^{-1} \times 60 = 650rpm$$

The rotational speed obtained above can be used to simulation Computational Fluids Dynamics analysis on the propeller. the simulation can be processed for a range of rotational speeds to obtain the optimal UAV VTOL propeller rotational speed.

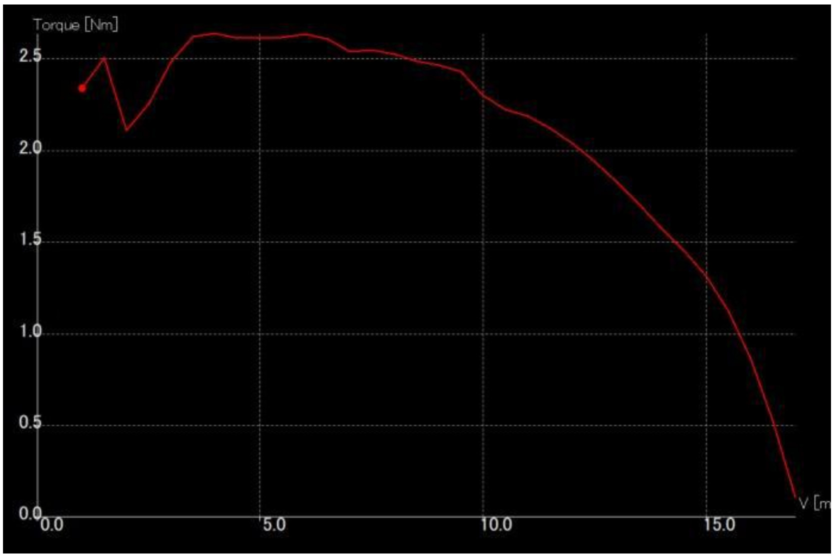

Figure 129: Propeller Torque against airflow velocity for VTOL propeller.

Initially, the torque required to rotate the propeller and provide the specified induced velocity, is high. However, as the velocity reaches 70% of induced velocity, the torque requirement drops. The estimated torque requirement was calculated in chapter 5.3.3.1. The theorical value was calculate at 4.5Nm and the graph displays maximum torque requirement of 2.5Nm, thus, a percentage difference of 44%. The significant percentage difference is because theoretical calculations used the weight for the folding propeller and servo motor which folds the propeller. The simulation confirms the theoretical calculations can be used when selecting the motor to provide the required torque.

5.3.7 Computational Fluids Dynamics analysis

5.3.7.1 Methodology

5.3.7.1.1 Geometry

CFD can be simulated on the propeller using Ansys Fluent flow. The software allows importing geometry created in SolidWorks. Once the geometry is imported, Spaceclaim module can be utilised to prepare the geometry for meshing. Initial step is to specify the interaction between each part of the propeller. Shared topology can be applied to the folded propeller to combine all the overlapping faces and create points of contact. William Froude's assumption of propeller disk behaving as a thin disk can be applied to the geometry. A thin disk, Rotational zone, can be created around the propeller using the closure function. Fluid domain can also be created by creating an enclosure around the rotational zone. If no geometry errors detected, the geometry would be ready for meshing.

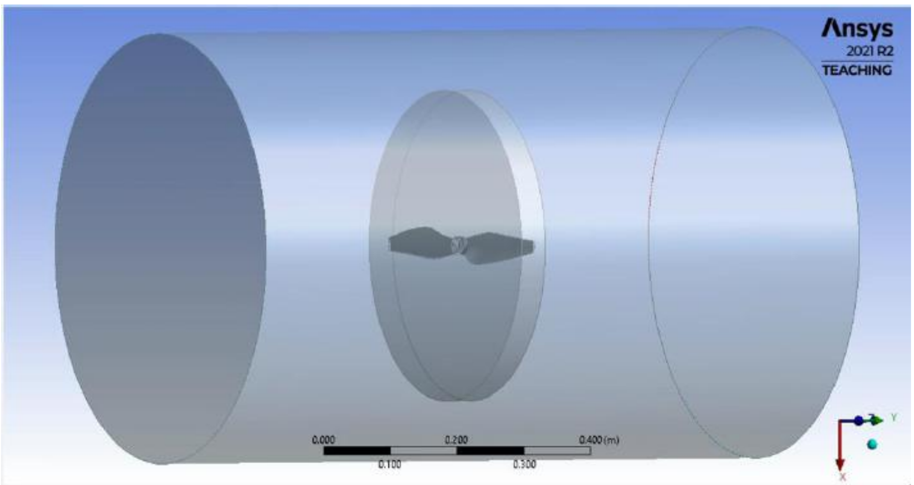

Figure 130: Fluid domain and rotational zone created using Ansys Fluent Workbench Design Modular.

5.3.7.1.2 Meshing

Initially, named selections can be created for the inlet, outlet, rotational zone and propeller. Figure below shows the boundary conditions set for the model. These boundary conditions can later be used to implement simulation boundary conditions such as rotational speed and inlet velocity.

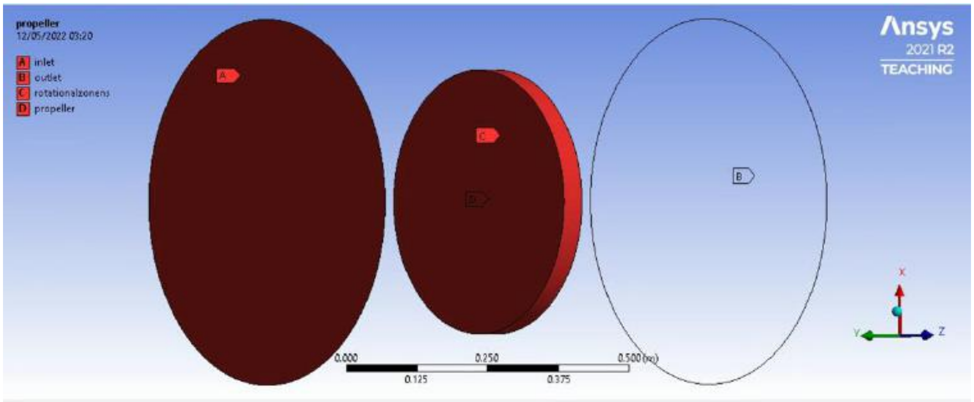

Figure 131: Boundary conditions of the model set before meshing.

Mesh parameters suggested by Ansys Fluent can be generated and later refined. The mesh can be refined by applying Edge sizing to the model to further refine mesh in area near propeller wall. This can significantly improve the thrust force and coefficient of lift values obtained. Capture curvature and proximity are functions that would allow advanced control in geometry regions that contain small holes or curvature. Inflation layer is another function that can be utilised to capture the velocity gradient near wall region due to no-slip condition. These functions can provide a fine mesh for the model to improve the final results obtained. Figure below displays mesh refinement achieved on the model by utilising the functions discussed.

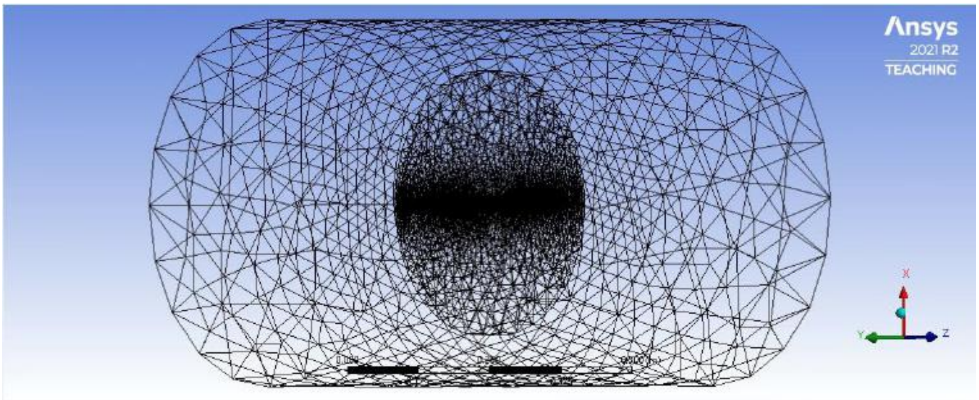

Figure 132: Mesh generation on the fluid domain, rotational zone and the propeller.

In addition, a combination of tetrahedral and hexahedral elements in the same mesh to improve results obtained. Tetrahedral elements can be applied rotational zone, since the propeller has long curve surfaces. As shown in figure below, Hexahedral elements can be utilised near fluid domain wall, where complex flows do not occur (Mesh, 2022).

Scope	
Scoping Method	Geometry Selection
Geometry	1 Body
Definition	
Suppressed	No
Method	Hex Dominant
Element Order	Use Global Setting
Free Face Mesh Type	Quad/Tri
Control Messages	No

Figure 133: Specifying meshing method as Hexahedral around the fluid domain.

5.3.7.1.3 Set up

The next step is to set up the model for simulation. The model will be simulated on pressure based since the velocity is low and the flow is assumed incompressible. First boundary condition in this model is the inlet velocity set as $2.5ms^{-1}$. In addition, since the simulation is based on Vertical Take-off and Landing, gravitational acceleration will also be specified in the negative y direction.

5.3.7.1.3.1 Turbulence model

The most suitable turbulence model needs to be decided for the propeller simulation. The aim of turbulence modelling is to predict the physical behaviour and fluctuations of the turbulent flow properties caused by the geometry. Reynolds-averaged Navier Stokes model (RANS), K-Epsilon and Detached Eddy Simulation are some of the most well-established methods used to predict turbulent flow behaviour. Detached Eddy Simulation was developed for separated flows in the aerodynamic field. The model applies Reynolds-averaged Navier Stokes model (RANS) in the region attached boundary layers close to boundary wall and the Large Eddy Simulations in region where the flow separation has occurred. Detached Eddy Simulation would be the most suitable because the simulation involves turbulent flow interaction with rotating propeller.

The Reynolds-Averaged Navier Stokes model is based on the averaging concept derived by Reynolds (1895) and Navier-Stokes averaged equations of motion. To obtain the Reynolds-averaged time equation, the equations for conservation of mass and momentum has to be considered (Wilcox, 2010, pp.30–41):

$$\rho\frac{\partial u_i}{\partial t}+\rho u_j\frac{\partial u_i}{\partial x_i}=-\frac{\partial p}{\partial x_i}+\frac{\partial t_{ij}}{\partial x_j} \tag{134}$$

$$\frac{\partial u_i}{\partial x_i} = 0 \tag{135}$$

The convective term in conservation can be rewrote and combined with the equation above to obtain the Navier-Stokes averaged equations of motion:

$$\rho \frac{\partial U_i}{\partial t} + \rho \frac{\partial}{\partial x_j}\left(U_i U_j + \overline{u_i' u_j'}\right) = -\frac{\partial P}{\partial x_i} + \frac{\partial}{\partial x_j\left(2\mu S_{ij}\right)} \tag{136}$$

$$\frac{\partial U_i}{\partial x_i} = 0 \tag{137}$$

Detached Eddy Simulation simulates the regions containing attached boundary layers using the equations derived above for the Reynolds-Averaged Navier Stokes model.

Large Eddy simulation was proposed in 1963 by Smagorinsky. The model is more accurate than Reynolds-averaged Navier Stokes model, since it directly models the large scale of turbulent motions directly. The large scale of turbulent motions contains most of the turbulent kinetic energy, therefore, a combination of Large Eddy Simulation and Reynolds-averaged Navier Stokes model makes Detached Eddy Simulation highly suitable for the UAV propeller interactions simulations. Detached Eddy Simulation will be highly computationally demanding, however, the optimal rotational speed achieved would be highly accurate.

Figure below displays the options the specified for the turbulence model. RANS model K-epsilon will be utilised, using the realisable model. The realisable model has presented significant improvement over the standard model for flow features that include rotation, curvature and vortices.

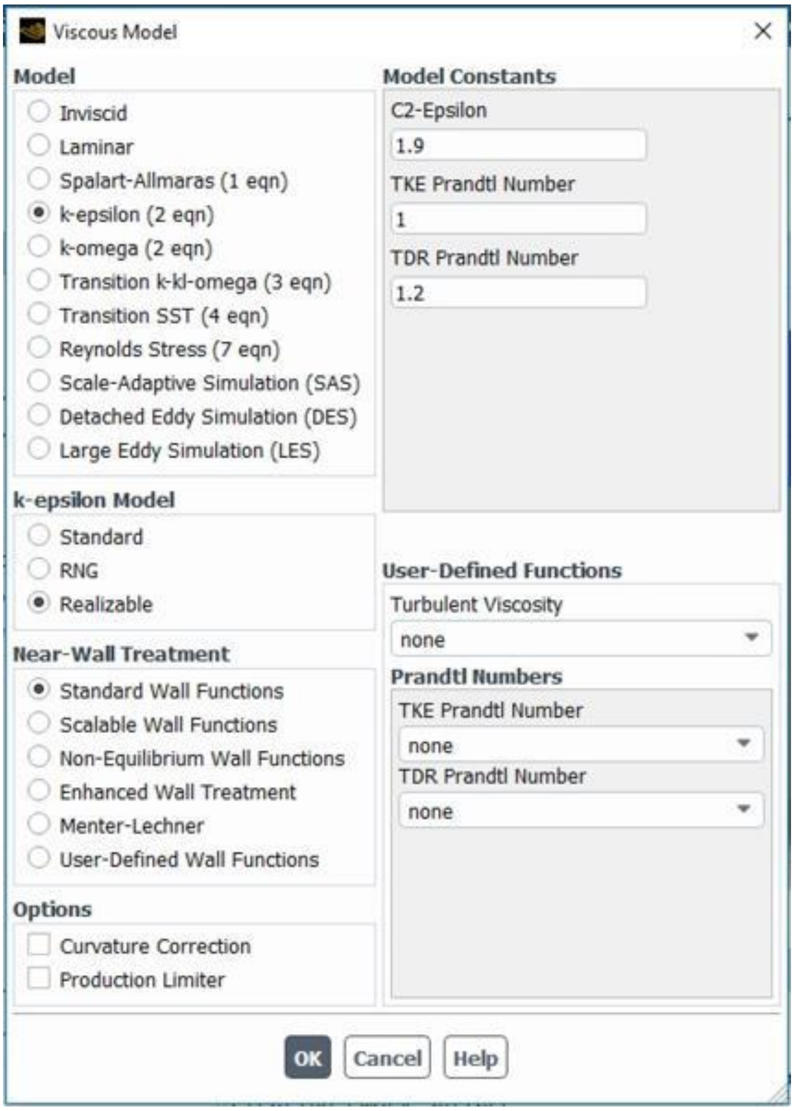

Figure 134: Specification of the Turbulence model for the simulation.

5.3.7.1.3.2 Rotating propeller

Ansys Fluent allows user to rotate propeller using the moving reference frame approach called frame motion. The method involves a thin volumetric mesh created around the propeller, in the rotational zone. The propeller remains stationary and the thin mesh created is rotated around the propeller, during simulation process. This method is preferred for steady simulations, as it is not computationally demanding. Appropriate rotational axis can be specified, and the simulation be processed for a range of rotational velocity. Initially, rotational speed of 650rpm will be simulated and the rotational axis direction towards which the propeller will rotate is the x direction as shown in figure below. The same procedure will be followed to simulate rotational velocity range of 650, 700, 750, 800.

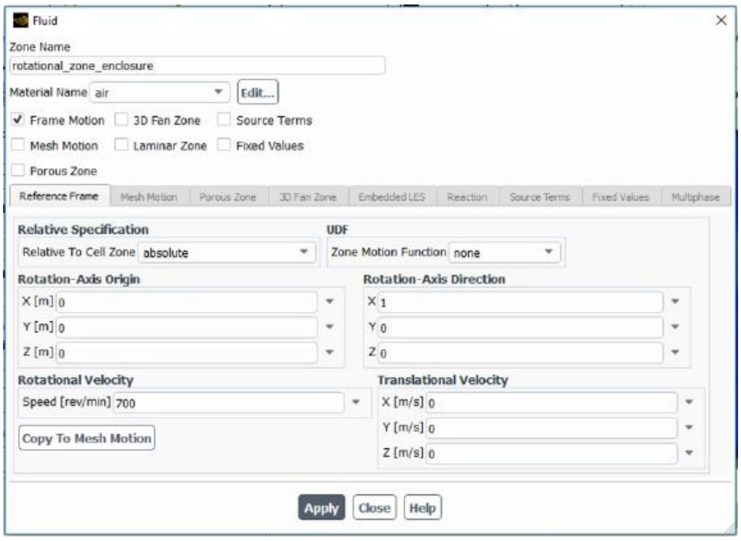

Figure 135: Specification of the rotational zone motion method.

5.3.7.2 Results

5.3.7.2.1 Velocity magnitude across propeller blade position

Results obtained for the velocity magnitude distribution across the propeller blade has been displayed in the table below. The axis displaying the position is the position from root (0m) to the blade tip (0.025m). The results present velocity magnitude increasing from root to tip for every rotational speed. The time constant for one complete revolution across the propeller blade is constant. However, the propeller tip revolution circle has a large circumference than the root, therefore, the velocity would also be greater. This has been demonstrated by the velocity magnitude graphs below.

The simulation boundary conditions were kept constant; however, the rotational speeds were changed obtain different velocity magnitude graphs. The first graph presents the velocity magnitude for the rotational speed of 650rpm. The maximum blade velocity at the tip increases as rotational speed of propeller increases. The blade tip speed for 650rpm and 700rpm are $16ms^{-1}$and $17ms^{-1}$ respectively. Optimal propeller rotational speed has been achieved at 700rpm, where the induced propeller blade velocity is close to the required disk velocity calculated using Froude’s theory in chapter 5.3.6.1.1.

The maximum blade tip velocity is reached before rotational speed of 800rp, thus suggesting that efficiency drops after 750rpm and it is no longer favourable to rotate the propeller at such rotational speeds.

Table 27: Velocity magnitude against propeller blade position for a range of rotational speed.

Rotational speed	Velocity magnitude across propeller blade position graphs:
650rpm	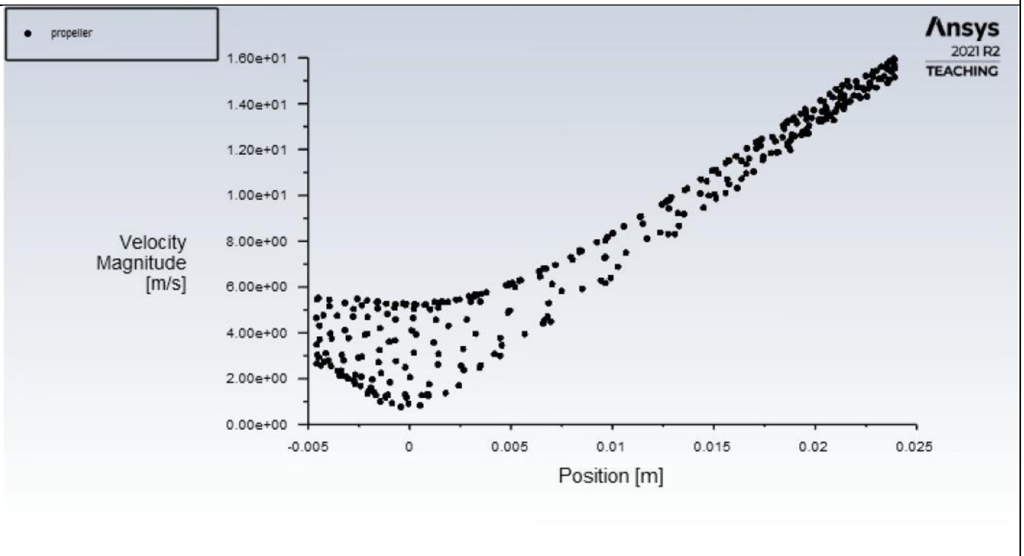
700rpm	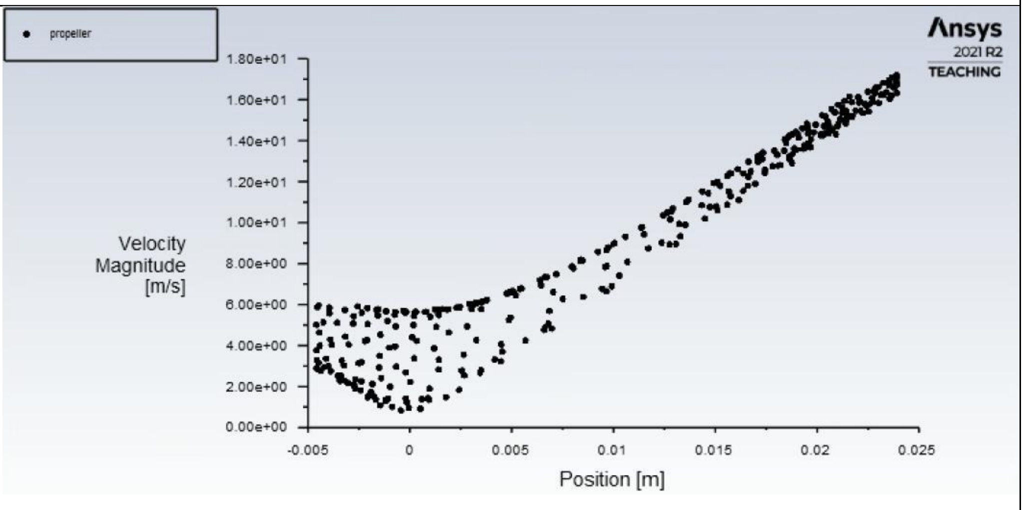
750rpm	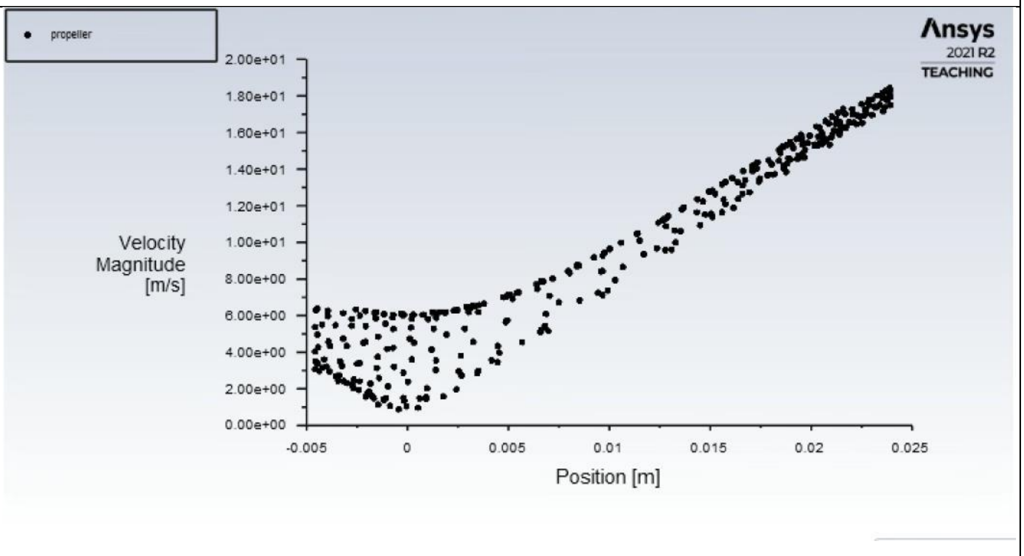

800rpm	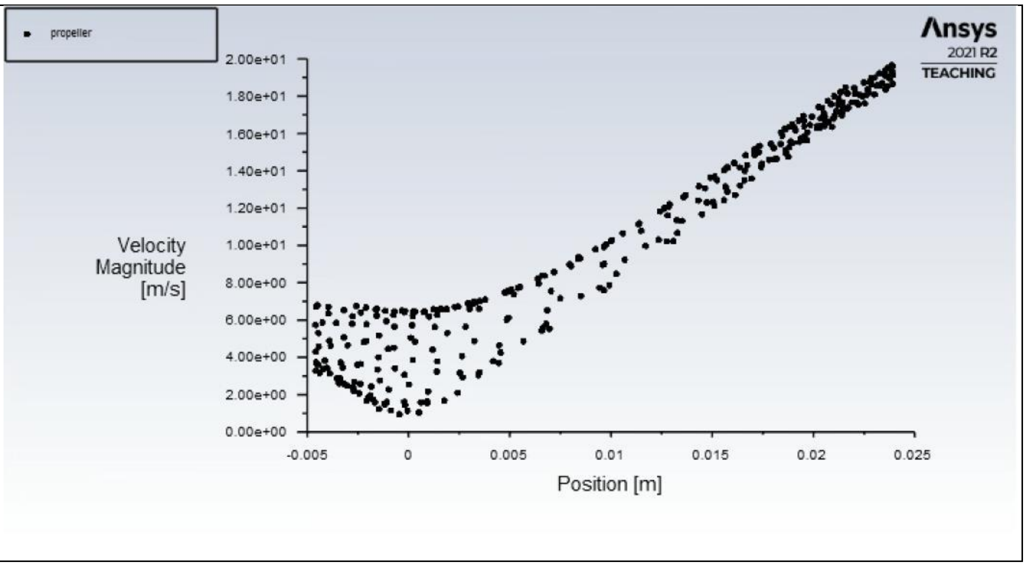

5.3.7.2.2 Static pressure across fluid domain

The Table below displays the static pressure against fluid domain position for the range of propeller rotational speed. Initially, at rotational speed of 650rpm to 700rpm, the static pressure remains constant as flow propagates from the inlet to pressure outlet. However, as the rotational speed increases over 750rpm, the flow becomes highly turbulent and at rotational speed of 800rpm, the turbulent flow intensity increases at the downstream of the fluid domain. Therefore, the propeller stalls after the rotational speed of 750rpm.

Table 28: Static pressure across fluid domain for a range of rotational speed.

Rotational speed	**Static pressure across fluid domain graphs:**
650rpm	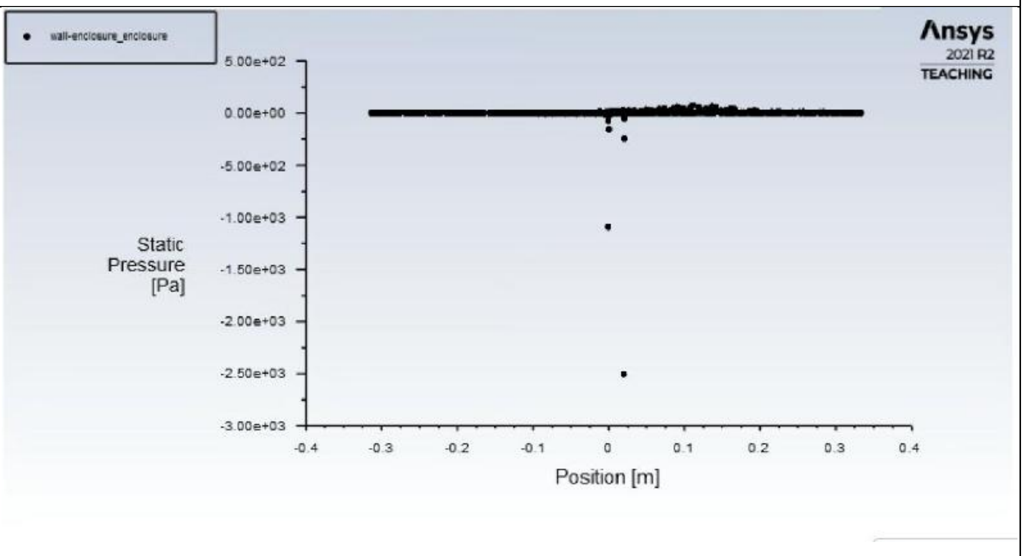

700rpm	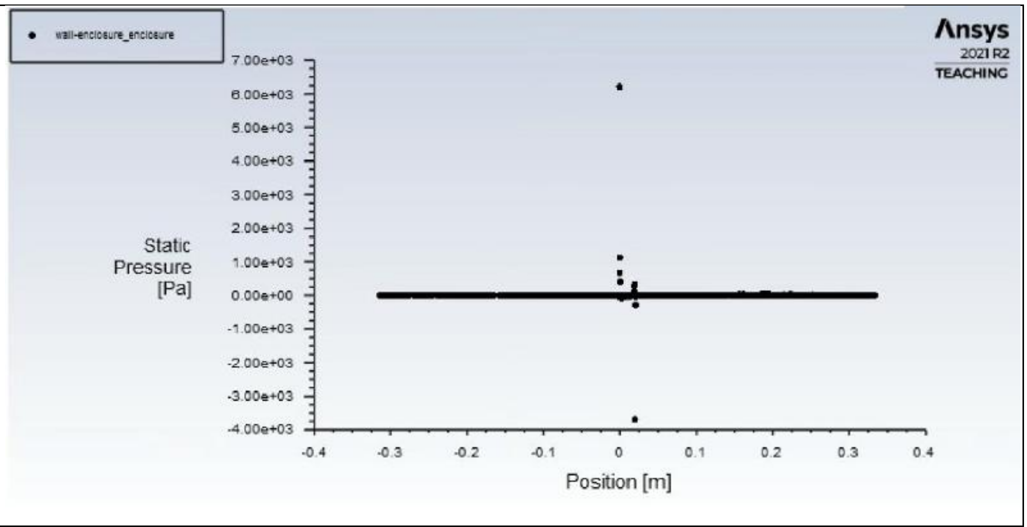
750rpm	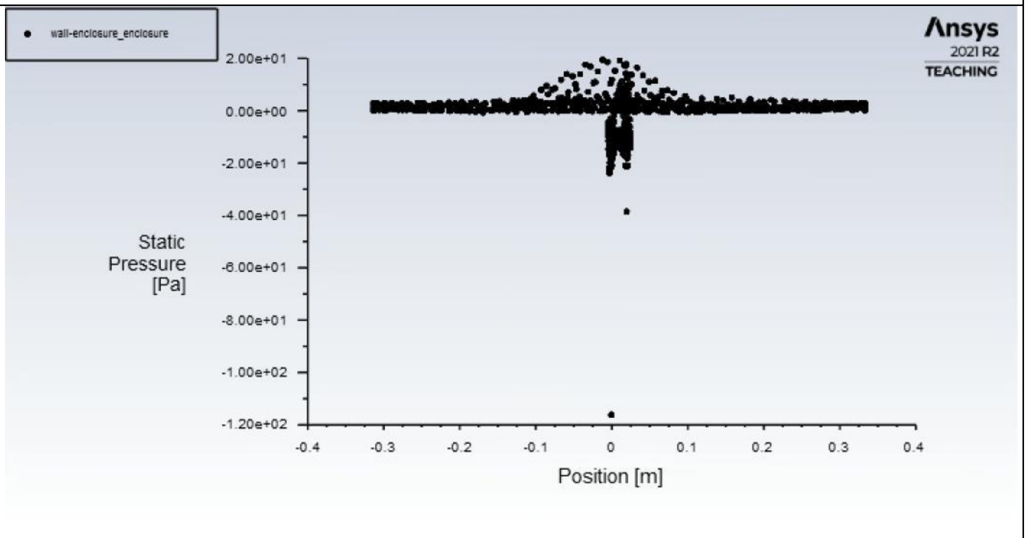
800rpm	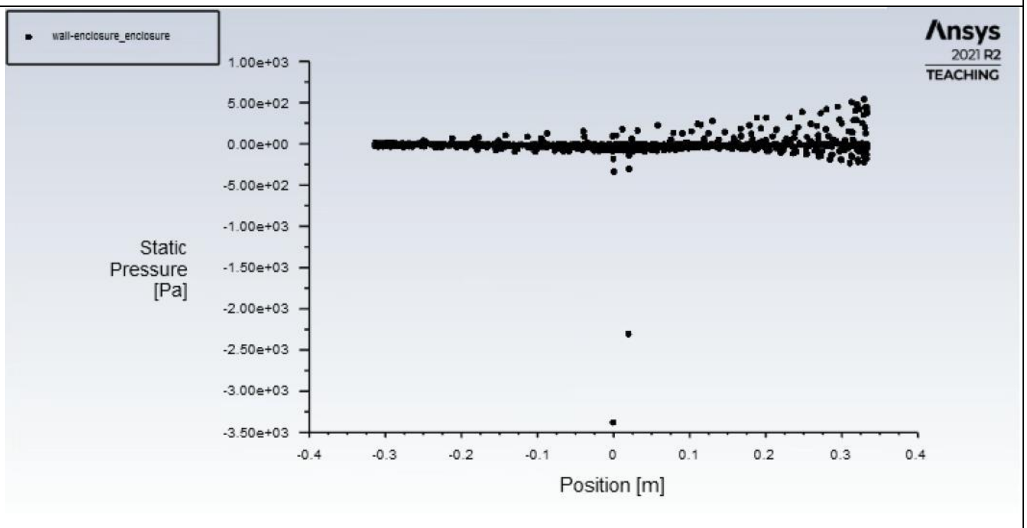

5.3.7.2.3 VTOL propeller thrust force

The propeller thrust results were obtained by plotting the force exerted by the propeller in the y direction. The results obtained have been displayed in the graphs below, for each rotational speed. Turbulent 3D models are computationally demanding, therefore, the converged thrust force values obtained were difficult to obtain. For the optimal rotational speed n=700rpm, thrust force value converged to T= 87.08017608N. This vertical thrust value produced by the propeller is greater than the required thrust value of 81.85N, with a percentage difference of 6.4%. Therefore, propeller rotational speed of 700rpm will provide the UAV with the required vertical thrust for Take-off and landing.

The graphs displaying the thrust force against iterations for the rotational speed above 750rpm showed no signs of convergence. The thrust force value oscillated between impractical values for the rotational values above 750rpm. The oscillating thrust force value suggest propeller blades stall at rotational speeds above 750rpm.

Table 29: Propeller Thrust force for a given rotational speed range.

Rotational speed	**VTOL propeller thrust force graphs:**
650rpm	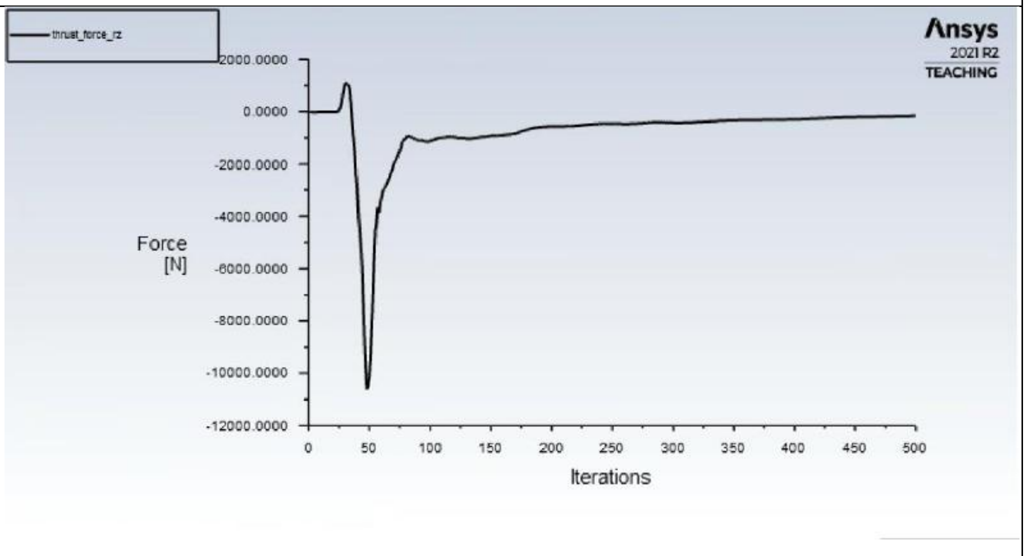

700rpm	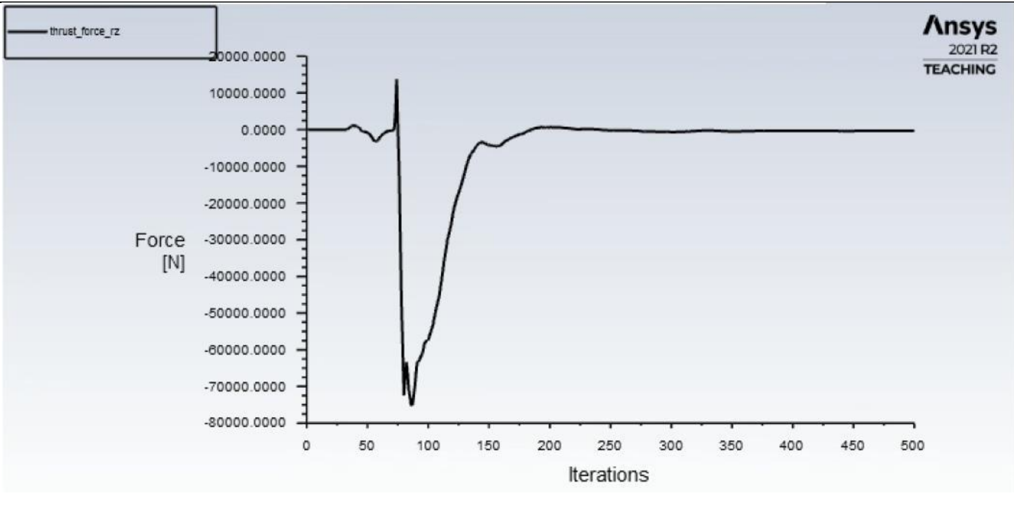
750rpm	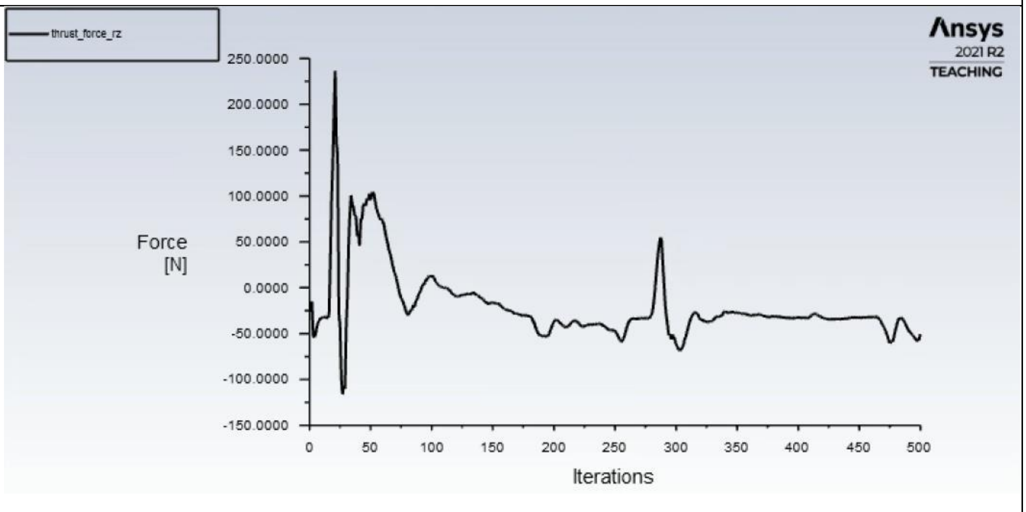
800rpm	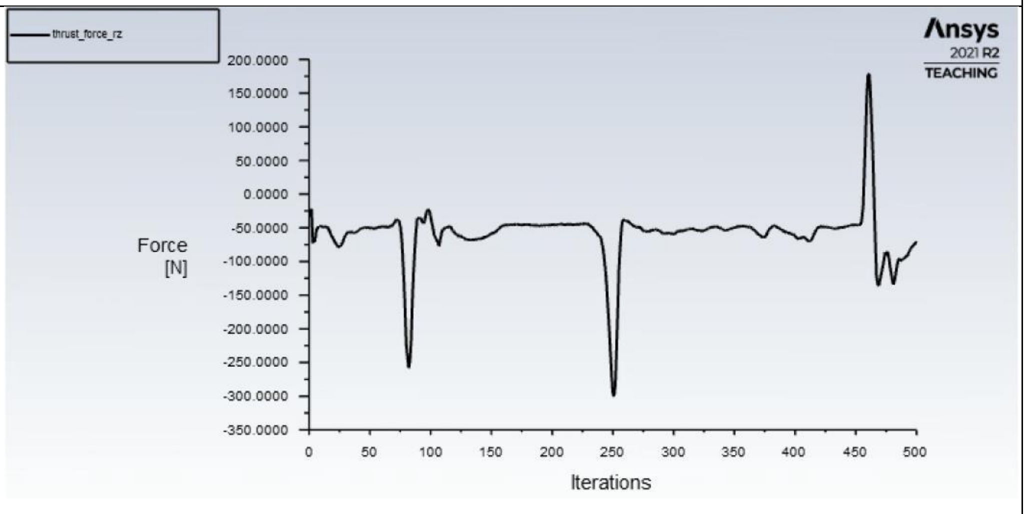

5.3.7.2.4 Graphical Contours for the optimal rotational speed, $\mathrm{n} = 700\mathrm{rpm}$

The figures 19, 20, and 21 below displays the contours for pressure coefficient, turbulence intensity and turbulence kinetic energy respectively. Figure 13 displays pressure coefficient close to propeller blade and lowest near blade root. The figure displays the face of the rotational zone, thus, showing the maximum pressure coefficient. Figure 14 displays the turbulence maximum intensity experienced near the propeller boss. As the propeller rotates, the propeller boss geometry produces highest turbulence intensity. Figure 15 employs a similar pattern as the turbulence kinetic energy is maximum near propeller boss.

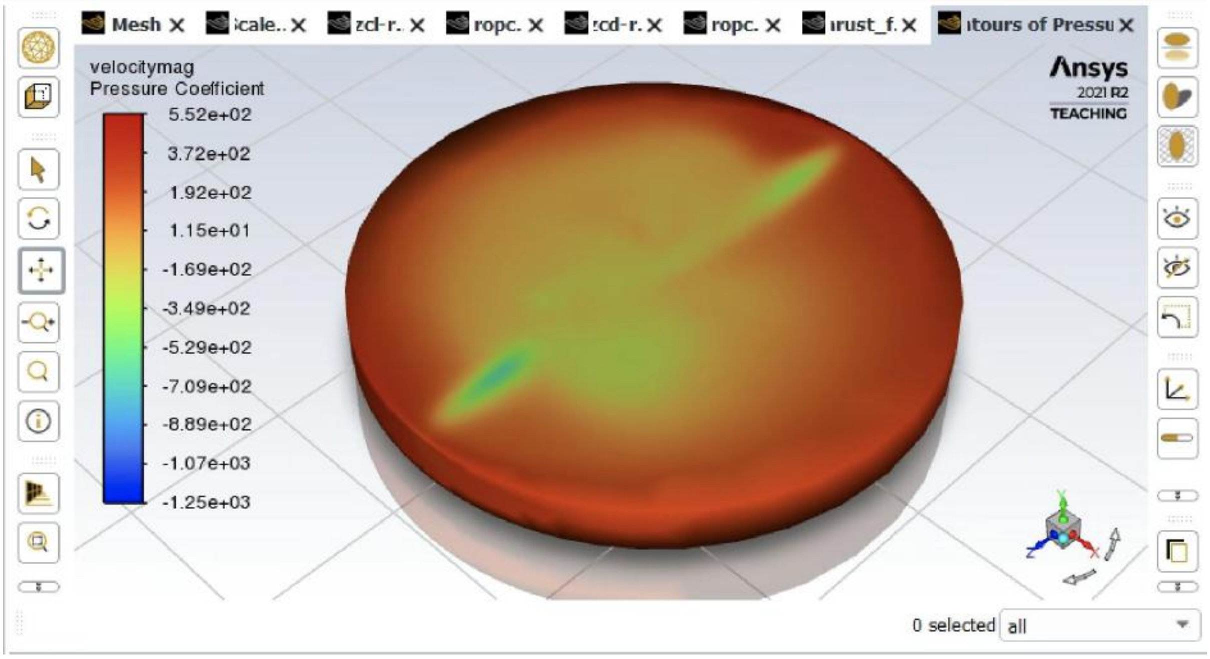

Figure 136: Pressure Coefficient for the propeller and rotational, where rotational speed n=700rpm.

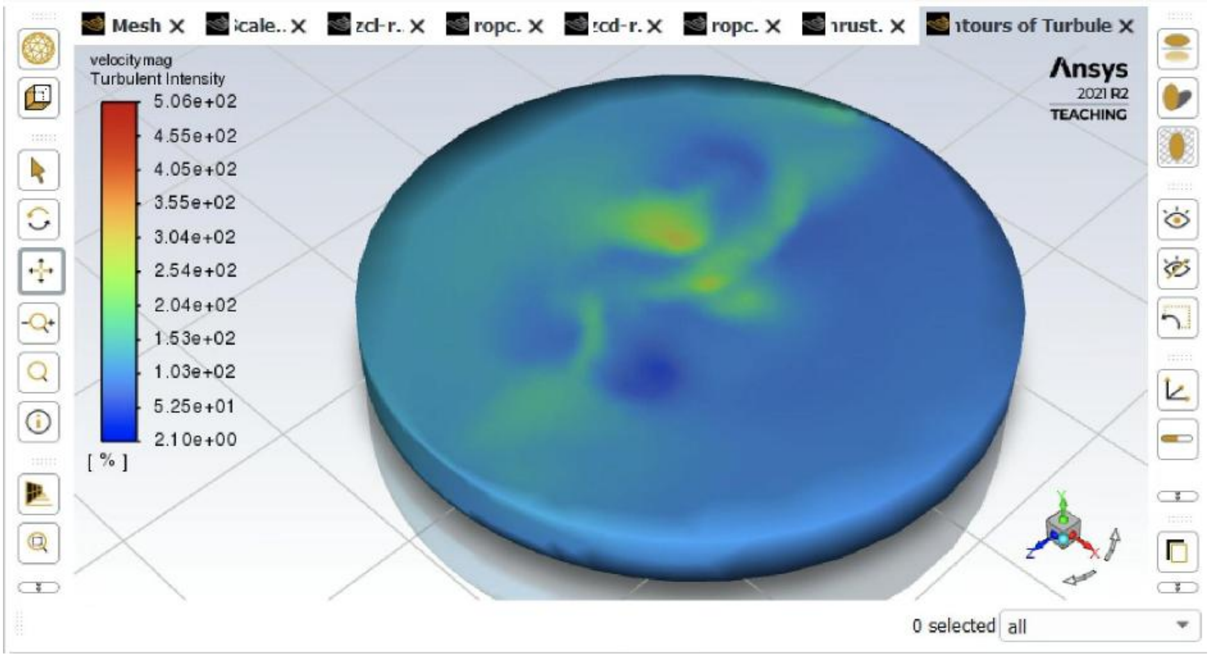

Figure 137: Turbulent Intensity for the propeller and rotational, where rotational speed n=700rpm.

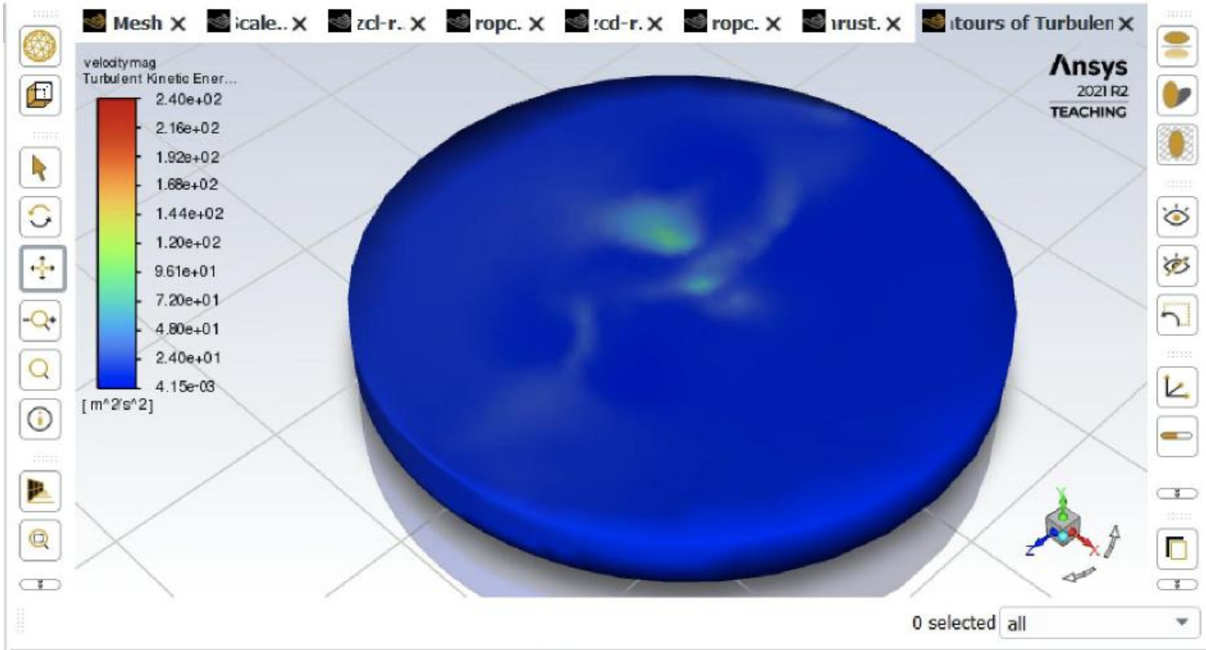

Figure 138: Turbulent Kinetic Energy for the propeller and rotational, where rotational speed n=700rpm.

5.3.8 Discussion

5.3.8.1 Results

The results obtained have all been displayed and discussed in the previous chapter. The velocity magnitude graphs were sufficient to obtain the optimal propeller rotational speed. The propeller thrust force in the y direction also confirmed that the propeller would provide the required thrust for vertical take with the current propeller geometric design. Turbulence model result convergence requires significantly higher number of iterations. As shown the by thrust force results for rotational speed above 750rpm, the turbulence modelling of propeller in those rotational speed regions are computationally demanding.

5.3.8.2 Limitations

Mesh refinement is directly related to obtaining more accurate results. The propeller model mesh could not be refined any further as the maximum number of mesh nodes were reached for Ansys Workbench teaching version. This became apparent when the Thrust force value would not accurately converge. The element size used to mesh this model was 0.12m, reducing the mesh element size would result in failed mesh as further refinement was limited. In addition, computational limitation also resulted in no results obtained for the folded propeller design. Ansys Fluent was unable to mesh the design as it had many holes, curvature and made up of multiple parts. Access to full Ansys fluent license might be able to overcome meshing complicated geometry issues as these geometries require higher number of nodes and advance meshing functions to obtain results. Wind tunnel testing is another method of testing complicated geometry such as the folded propeller.

5.3.8.3 Future work

The UAV design uses 4 propellers for vertical take-off and landing and 4 for cruise. However, the design could be improved in the future by implementing 4 ducted fans for both VTOL and cruise. The ducted fans could initially be vertical to provide the vertical take-off thrust for the UAV to take off at $2.5ms^{-1}$. Once the UAV has reached the required altitude, the ducted fans downstream airflow direction can be changed to horizontal at small angles. The ducted fans can then be rotated at higher rotational speed to provide the required cruise speed. However, this design requires testing to investigate whether the reduced weight of using 4 instead of 8 ducted fans make up for the reduced efficiency compared to propellers.

The propeller design initially involved propeller blades folding parallel across the propeller boss. Further testing is required to investigate whether it provide significant UAV drag reduction. An alternative method of reducing UAV drag during cruise is retracting the propellers into the fuselage. This design was not implemented into the UAV as this would affect the payload compartment in the fuselage. The next step could be introducing fuselage design that maintains the aerodynamic efficiency and payload compartment size while also enabling propeller retraction.

5.3.9 Conclusion

In conclusion, a successful design and research on the electric propulsion system was carried out as the aims and objectives of this design research was achieved. The most suitable power supply, which meets all the mission requirement. LiPo batteries were concluded to be the most suitable because of its high-power density. Brushless DC motors were selected as the mechanical energy converter. However, further research can be carried out into electric motors to design electric motor in the propeller boss. Finally, VTOL propeller optimisation was carried out using different theoretical models and confirmed using simulation results on computational packages. In order to improve the final design suggested, wind tunnel testing could be carried out fold propellers and improved electric motor efficiency.

6. Control System Design – Arisa Supawaree (180035328)

6.1. Introduction

6.1.1. Uses of UAVs

Unmanned aerial vehicles, also known as UAVs, is an aircraft that does not need to have a pilot or an on the ground controller to fly it, they can also be used in a variety of fields. Commonly, UAVs were developed for the military, and can be very useful for these purposes because they do not require personnel on board or people controlling it. UAVs have been used to reduce deaths as there are no people on board and can perform tasks that humans may not want to do such as aerial reconnaissance (Palik and Nagy, 2019). These benefits that have been discussed are the UAVs' most common usage cases, but the benefits seen here are also relevant to this project in its use as a search and rescue drone.

Despite UAVs being mainly used for military purposes, recently, some more developments to review the viability of UAVs for other purposes have been found. For example, Hildmann and Kovacs (2019) have recently reviewed the uses of UAV in urban areas and disaster management. Specially in disaster management, UAVs can be used for most stages of the rescue mission, which ranges from scouting out the terrain and search for survivors to delivery of supplies. The benefits of this would be that UAVs are more portable and can be deployed quicker than manned aircraft, therefore making the relief efforts quicker and more effective. This idea was developed on recently by Munawar, Hammad and Waller (2022) where they developed a drone to be more efficient and able to stretch its operations further for disaster management. In this, the approach of the research was changed slightly to include several drones; working in formation to be more effective and cover a large area, this was optimised to find the best formation with the most efficiency (i.e. least battery consumption and least drones required). These two research papers highlight the importance and demand for the design and implementation plan of a disaster management UAV, in today's world to find modern solutions for events such as natural disasters.

However, there are struggles within the development and deployment of UAVs mainly due to the fact that it is difficult to design and control (Cook, 2007). Therefore, in this project as seen earlier in the overarching aims and objectives, a UAV was designed and implemented with a control system to further current technologies and research in this field.

6.1.2. Morphing Aircraft

In the field of aeronautics, the term morphing aircraft usually talks about a vehicle that can change its shape, specifically, the aircraft is able to change the shape of the wing (Concilio et al., 2018). In terms of morphing wings, there are three main methods of morphing, but this project will focus on one specific way - the folding wing tips. There are usually two main phases for a folding morphing wing, one phase where it is closed and one where the wing is fully extended and open, most folding wings do not have more than two options with no option to have the wing somewhere in between the fully extended and fully closed modes. This idea of a morphing wing could be utilised to enhance the efficiency of the UAV, the morphing mechanism was designed and implemented in the last few sections. In terms of the control system, the morphing must be kept in mind for all the simulations to keep them accurate and applicable for the UAV that has been designed.

6.1.3. Aims and Objectives

As outlined in earlier, the main aim of this project was to design and test a morphing UAV for purposes of aid delivery in the event an earthquake. The physical design of the UAV has been created and optimised earlier, therefore, in this section, the control system design of the UAV will be discussed. Specifically, a control system with the morphing wings in mind was considered and simulated for a response and adjusted so that the UAV will be able to fly and operate autonomously, meaning that it should be able to track, adjust and maintain a given parameter that would change as the flight plan requires.

The software that was used for testing was Matlab Simulink, using this software the response of a control system was simulated and optimised, so that the response was acceptable for the UAV's purpose. The system created should be able to be implemented into a larger autopilot system and the further implementation of the control system created in this paper will be discussed as well. After completing the simulation and analysing the results, the successfulness of the simulation will be compared to a set of criteria to measure the control system's effectiveness. Also, the implementation of the control system (i.e. the transition from software to hardware) will be discussed and practical solutions, and problems of this will be analysed. Using the solutions presented, a final hardware selection will be made, so that UAV can be created in a future project. To summarise, the main aims and objectives of this section is detailed below:

- Create a control system that will track, change, and maintain parameters to reference values autonomously.
- Implement and tune an appropriate controller to help the control system maintain parameters.
- Discuss methods and potential hardware that could be used to move the control system designed onto the UAV.

In this section, the design of a holding control system will be discussed, in terms of a holding system, this means that the control system must be able to adjust certain parameters to match the reference value of a parameter and maintain this until the reference value is changed at which point, the control system should be able to adjust to match the new reference value accordingly. For the hardware, all reasonable and affordable circuit boards will be considered.

6.1.4. Problem Definition

The UAV designed in previous sections was used as the model for the dynamics of the control system. This was important because without the UAV's dimensions, some equations cannot be accurately derived for the control system. Other parameters such as the morphing mechanism and aircraft weight was also used as variables to derive certain constants that needed to be defined for the simulation to run properly. The simulation was run on Simulink and the results were documented and analysed.

6.2. Methodology

6.2.1. Equations for Dynamics

The main goal of the simulation is to create an accurate representation of the control dynamics of the UAV and implement the equations for this into Simulink. This means that the control dynamics equations must be derived before any Simulink work is done. There are two main parts to the Simulink systems that need to be designed, firstly the control system for the morphing wing dynamics, and secondly, the control system for the thrust subsystem. Only the morphing wing dynamic equations and control systems will be discussed here.

6.2.1.1. Orientation Equations

To model the UAV's morphing dynamics, the dynamic equations of motion was derived. The equations for calculating pitch, roll and yaw can be written as (Mills and Ajaj, 2017):

$$\dot{p} = \ddot{\phi} = (c_0 r + c_1 p)q + c_2 \bar{L} + c_3 N - c_4 \frac{m_{tip}}{2m} l_{tip} \left(\left(l_0 - l_{tip}\right) \dot{\delta}_1^2 cos\delta_1 \Delta\delta_1 + \left(l_{tip} - l_0\right) \dot{\delta}_2^2 cos\delta_2 \Delta\delta_2 \right) \tag{138}$$

$$\dot{q} = \ddot{\theta} = c_5 pr - c_6 (p^2 - r^2) + c_7 M \tag{139}$$

$$\dot{r} = \ddot{\Psi} = (c_8 p - c_2 r)q + c_4 \bar{L} + c_9 N \tag{140}$$

Equations 138, 139 and 140, show the ways to calculate p (roll rate), q (pitch rate), and r (yaw rate). It can see seen that these equations also have several constants to define, ranging from c_0 to c_9. These values are defined separately and can be inserted into the equations when necessary. The constants consider the inertia forces acting on a specific plane in a specific direction. Next, the total moment forces within the body frame can be taken into account (Mills and Ajaj, 2017):

$$\bar{L} = \dot{p} I_x - \dot{r} I_{xz} + qr\left(I_z - I_y\right) - pq I_{xz} - \frac{m_{tip}}{2m} l_{tip} \left(\left(l_0 - l_{tip}\right) \dot{\delta}_1^2 cos\delta_1 \Delta\delta_1 + \left(l_{tip} - l_0\right) \dot{\delta}_2^2 cos\delta_2 \Delta\delta_2 \right) \tag{141}$$

$$M = I_y \dot{q} - pr(I_x - I_z) - (p^2 - r^2) I_{xz} \tag{142}$$

$$N = \dot{r} I_z - \dot{p} I_{xz} + pq\left(I_y - I_x\right) + qr I_{xz} \tag{143}$$

Using Equations 141, 142 and 143, the moments for the body frame can be added to the Simulink diagram. Lastly, the last forces in the body frame can be written as (Mills and Ajaj, 2017):

$$\dot{u} = rv + qw + g sin\theta + \frac{F_x}{m} \tag{144}$$

$$\dot{v} = -ur + wp + gcos\theta sin\phi + \frac{F_y}{m} - \frac{m_{tip}l_{tip}}{2m}\left(\dot{\delta}_1^2 sin\delta_1 \Delta\delta_1 + \dot{\delta}_2^2 sin\delta_2 \Delta\delta_2\right) \tag{145}$$

$$\dot{w} = up - vp + gcos\theta cos\phi + \frac{F_z}{m} - \frac{m_{tip}l_{tip}}{2m}\left(\dot{\delta}_1^2 cos\delta_1 \Delta\delta_1 + \dot{\delta}_2^2 cos\delta_2 \Delta\delta_2\right) \tag{146}$$

Using all the equations above (Equations 138 to 146), the control system for simulating the morphing wing can made.

6.2.1.2. Constant Calculations

The constants calculated can be used and applied to all the equations in section 6.2.1. One example of a sample calculation can be detailed below using an equation to work out the constant c_0 (Mills and Ajaj, 2017):

$$c_0 = \left(\frac{\left(I_y - I_z\right)I_z - {I_{xz}}^2}{I_x I_z - {I_{xz}}^2}\right) \tag{147}$$

Moment of inertia values can be calculated as:

$$I_{xz} = \sum(m_i \cdot x_i \cdot z_i) = 6.95m^4 \tag{148}$$

This method that was used in *Equation 70* can be used to calculate all the values of inertia and therefore all the constants can be calculated.

6.2.1.3. Matlab Parameters

Due to the large number of variables that are present in each diagram, there will also be a lot of variables that appear several times in the Simulink diagram. In order to create a coherent diagram, constants are defined as by a parameter (e.g. gravity being represented by the letter g) and all constants are then defined separately in a complementary Matlab file. This ensures that all parameters can be easily tracked in a separate script. This is also useful in the troubleshooting and optimisation stage as constants can be changed quickly and easily. For example, from each constant value, the moment of inertias are worked out and inputted into the Matlab script, and the equations for the constants are transcribed and calculated.

6.2.2. Creating Simulink Diagrams

Using the equations that were derived and presented in section 6.2.1, the control system on Simulink can be drawn. An easy way to understand how to do this is by using an example such as Equation 139 which is repeated below for reference (Mills and Ajaj, 2017):

$$\dot{q} = \ddot{\theta} = c_5 pr - c_6(p^2 - r^2) + c_7 M \tag{139}$$

Equation 139 can be split into several parts to start the simulation drawing. Firstly, the variables that are inputs and outputs. The goal of this system is to find the value of $\dot{q}$ and q, therefore these will be the outputs, Equation 139 is already arranged so that $\dot{q}$ is the subject of the equation so it does not need to be rearranged. As the constants are not variables and have already been defined in a separate Matlab script, the variables that are needed as inputs must be p, r, and M. Firstly, a larger Simulink subsystem is created so that the overall system is easier to look at, this can be seen in Figure 139. This figure also shows the inputs and outputs that were discussed earlier:

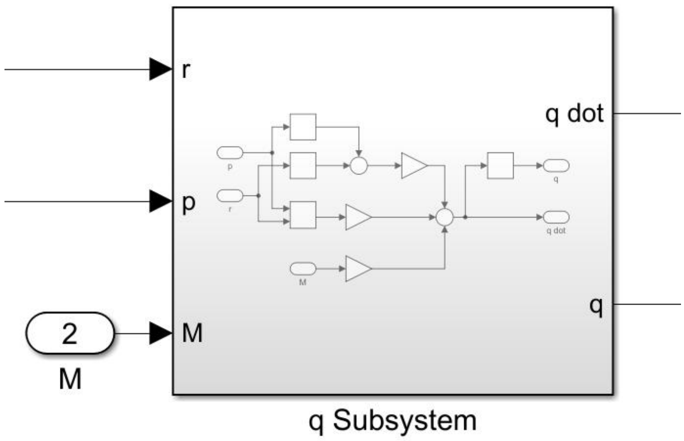

Figure 139: q subsystem with inputs and outputs

Going into more detail, the subsystem can be expanded to see the logic inside:

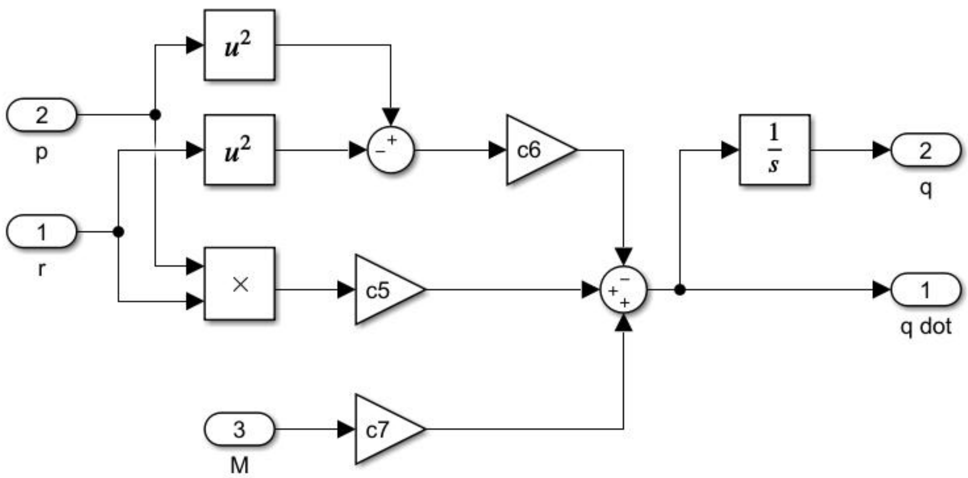

Figure 140: q subsystem expanded

From looking at the routes each input variable's route and the operations it goes through in Figure 140, Equation 139 can be created. The constants c_5, c_6 and c_7 can be used in gain blocks and the variables value can be defined in a separate Matlab file, the gain block multiplies the input signal by a number that the gain block is defined at and creates the results. For the outputs, $\dot{q}$ can be integrated q which is used as an input that can be used for other blocks. Using this method, all the equations of dynamics can be rearranged or transferred to make the whole control system for morphing dynamics.

6.2.3. PID Implementation

A PID controller is one of many ways to moderate a control system's output and alter it so that the output signal is controlled as needed. The PID controller consists of three main parts, a proportional, integral and derivative sections, hence the name PID. Occasionally, it is more advantageous to only use the proportional and integral sections (known as a PI controller) of the controller as the derivate section can amplify noise in some cases (Hun, Tiwari and Sinha, 2016). Altering the values for each section of the controller can change the response of the output. For most process controls, the derivative part is not used at all so most controllers in this instance are a PI controllers (Karl Johan Astrom and Tore Hägglund, 2006).

6.2.3.1. Uses of the PID Controller

PID controllers can be a very versatile tool for control systems, they are able to alter the input to help tune the response for a negative feedback loop. Due to its ability to keep a system at a consistent output value, PID controllers have been implemented for temperature controllers where a basic on and off switch was previously used (Karl Johan Astrom and Tore Hägglund, 2006). It was observed that the PID's ability to control temperature was more effective than the tradition on and off switch system. In a similar vein to this type of application, PID controllers can be used to control temperature in other areas such as baking.

6.2.3.2. Characteristics of a Response Graph

In order to tune the PID controller effectively, it is important to define the parameters that are used to measure the effectiveness of the response of the system. Firstly, the response graph should be shown in comparison with the desired output, this means that the response can be compared. There are four main ways to measure the response of a system that will be focussed on in the analysis of the control system, the rise time, percentage overshoot, settling time and steady state error. Each parameter will be explained, and noteworthy properties discussed.

The first parameter is the rise time, which is the time it takes the system to reach or surpass the desired output. This is important because it shows the speed of the system's response, as is the case with most control systems, the reaction to a new input should not take too long as this could cause the UAV to crash or go off course. Secondly, the percentage overshoot is the difference between the peak value of the output and the set desired output in a percentage, making it easier and fairer to compare between different systems. In some cases, overshoot could lead to instability and therefore should be kept to a minimum when possible. Thirdly, settling time is the amount of time it takes the system to settle within ±1% of its final value. The settling time, along with the rise time can help show the system's responsiveness to changes in the inputs, similarly to the rise time, it is important that the system settles on a value quickly as it makes the UAV more responsive as a whole. Lastly, the steady state error, which is represented by e_{ss}. Steady state error is the difference between the desired output and the settled output of the response, it can be helpful to see how large the steady state error is in many cases as this shows how inaccurate the system's output can be from the desired output indicated by the user or AI system and it should be taken into account if the system needs to have highly accurate outputs.

6.2.3.3. PID Tuning

Changing the values of each parameter in a PID controller can have varying effects. These values need to be tuned between one another in order to create the desired output. There are compromises to be made in each section of the PID controller and changing one part of the PID controller will affect several parameters as mentioned in 6.2.3.2. The effects of the PID controller changing the values of each section can be seen below:

Table 22: PID changes and their affects (adapted from (Livinus et al., 2018)).

PID Parts	Results if K_p, K_i or K_d increased independently			
	Rise Time	% Overshoot	Settling Time	Steady State Error
K_p	Lowers	Rises	Small changes	Lowers
K_i	Lowers	Rises	Rises	Removes
K_d	Small changes	Lowers	Lowers	No effect

Table 22 shows the effects of increasing each part of the PID and it also shows what happens to each measurement of output accuracy. Using this table, the tuning process can happen and compromises in for each of the parameters must be made to create a responsive and accurate control system that can be feasibly used for the UAV's purpose of aid delivery and navigation.

6.3. Simulink Diagrams

6.3.1. Control systems without PID

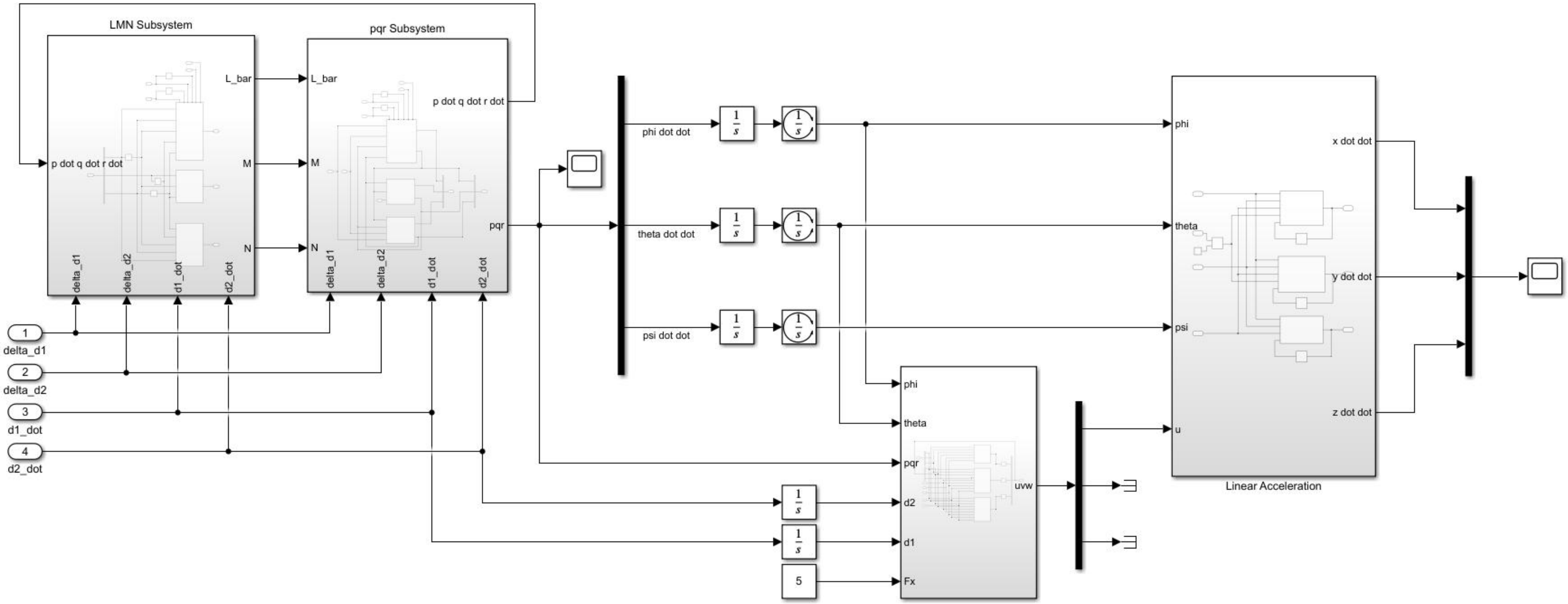

Figure 141: Overall control system diagram

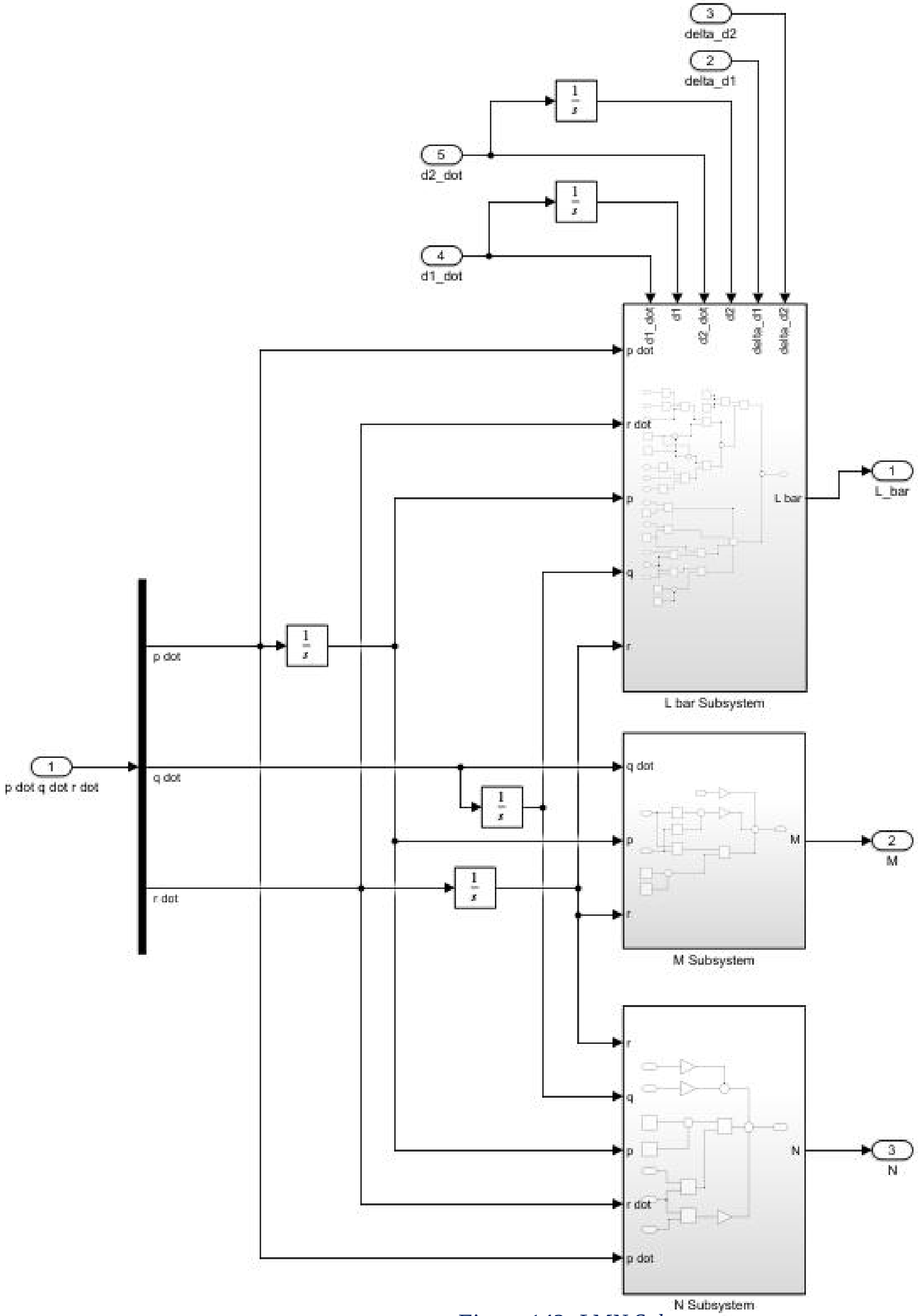

Figure 142: LMN Subsystem

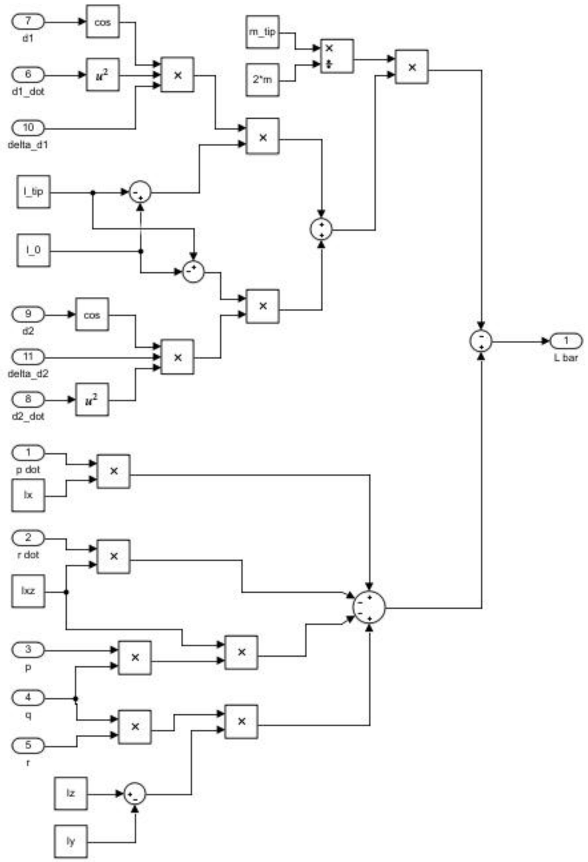

Figure 143: L bar subsystem

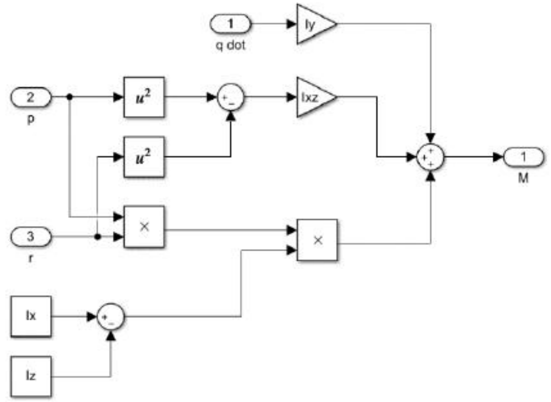

Figure 144: M subsystem

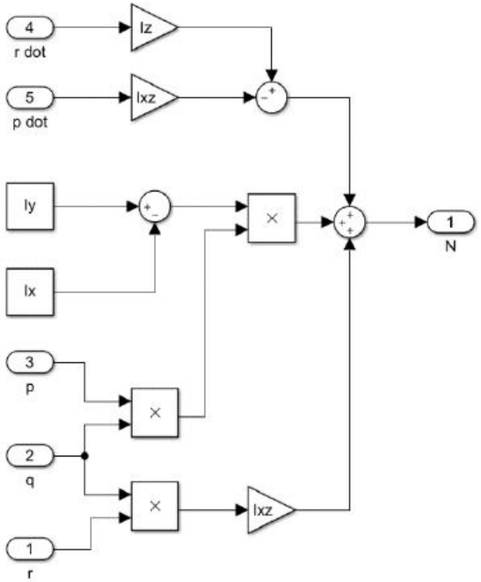

Figure 145: N subsystem

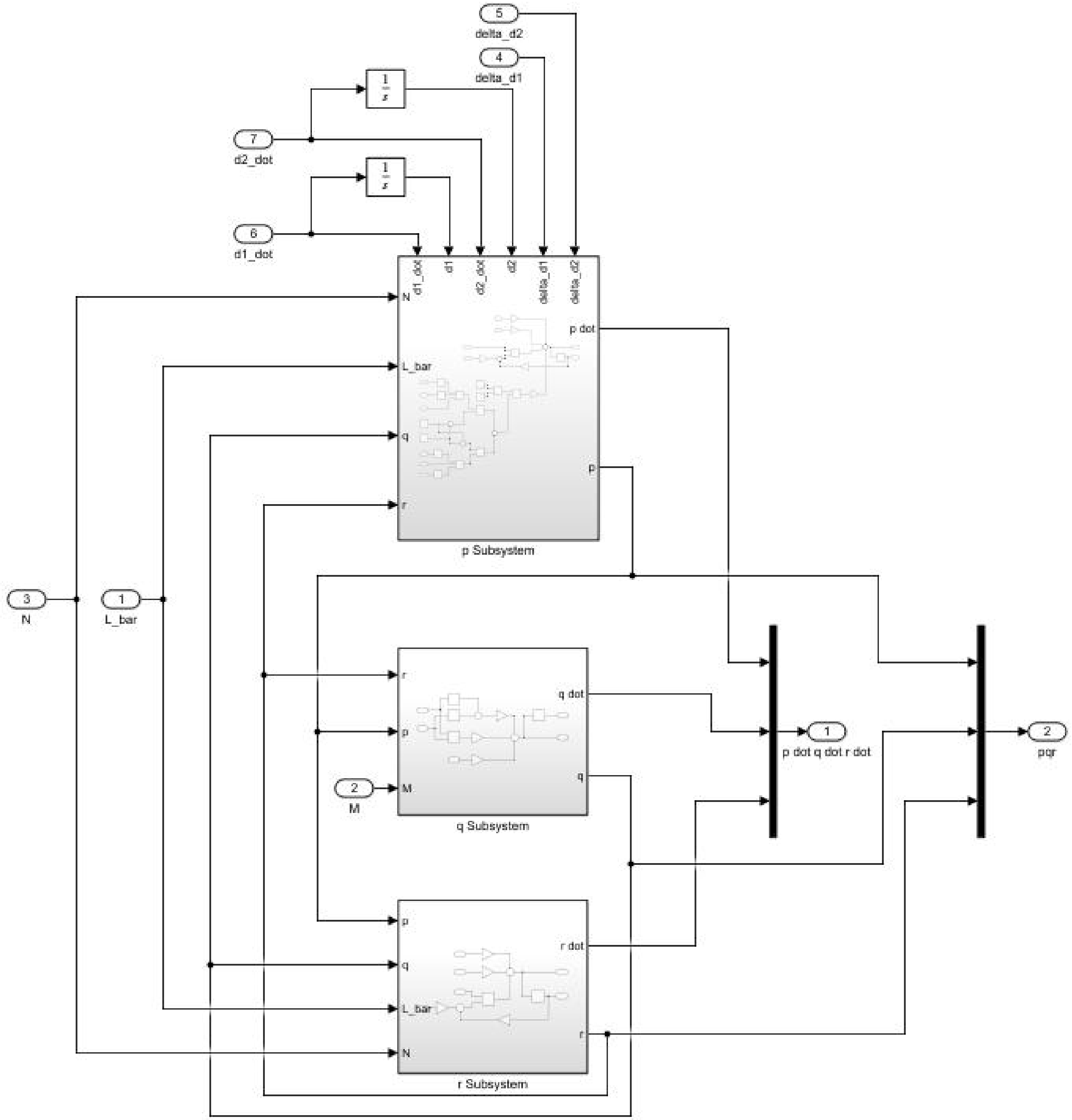

Figure 146: pqr subsystem

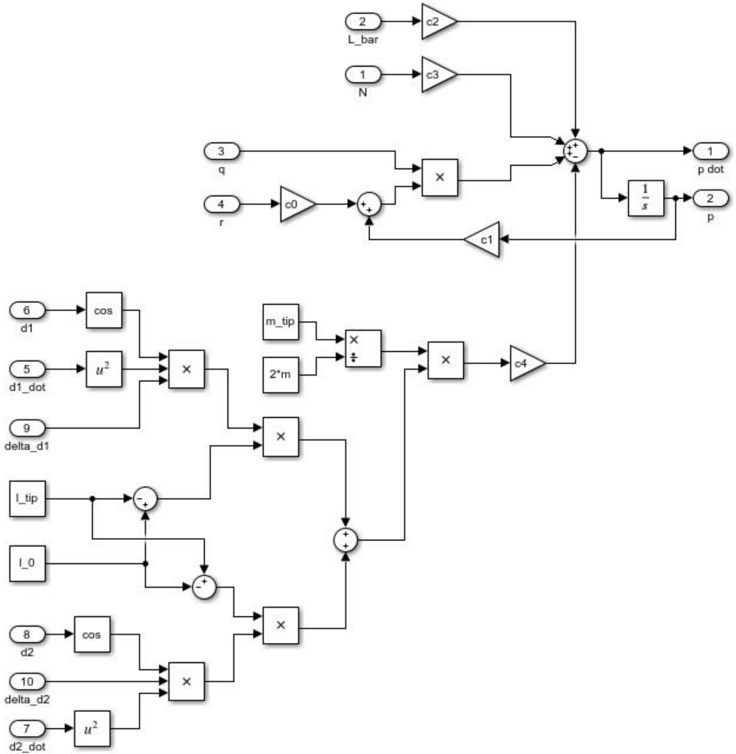

Figure 147: p subsystem

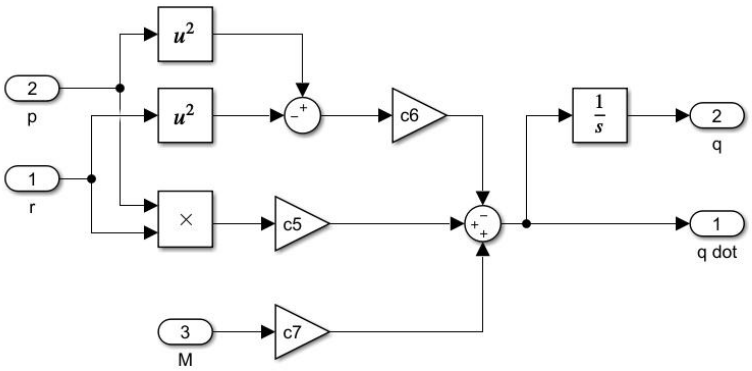

Figure 148: q subsystem

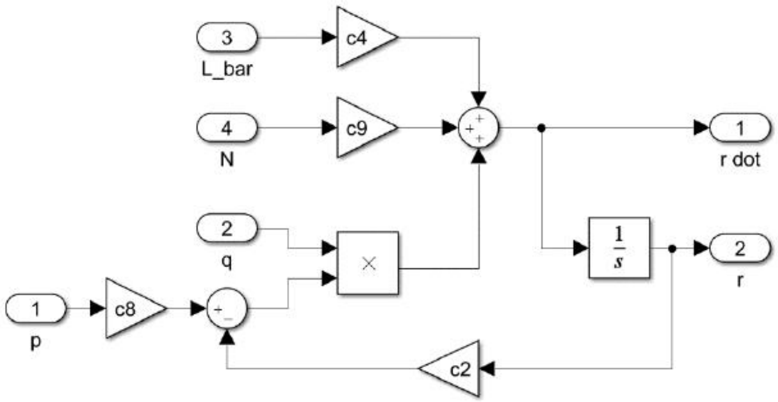

Figure 149: r subsystem

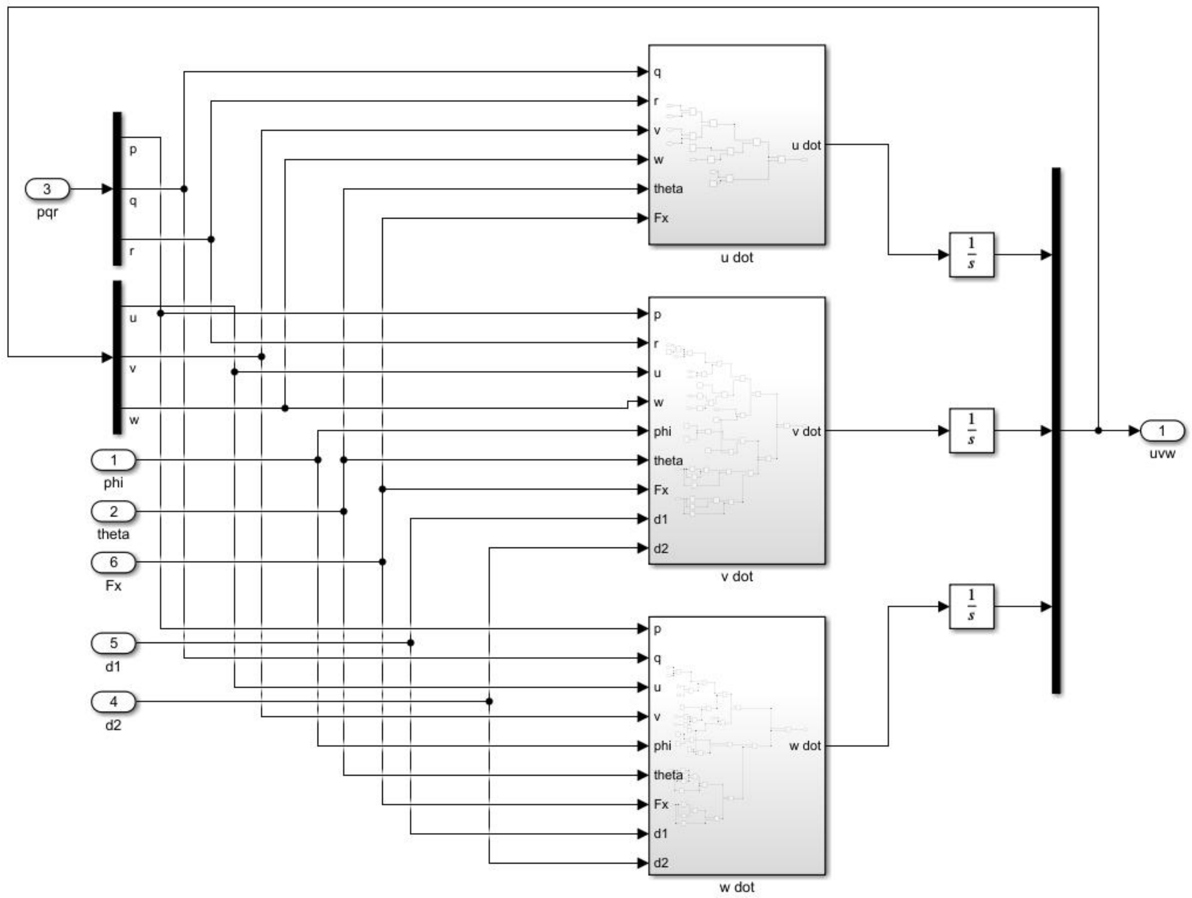

Figure 150: uvw subsystem

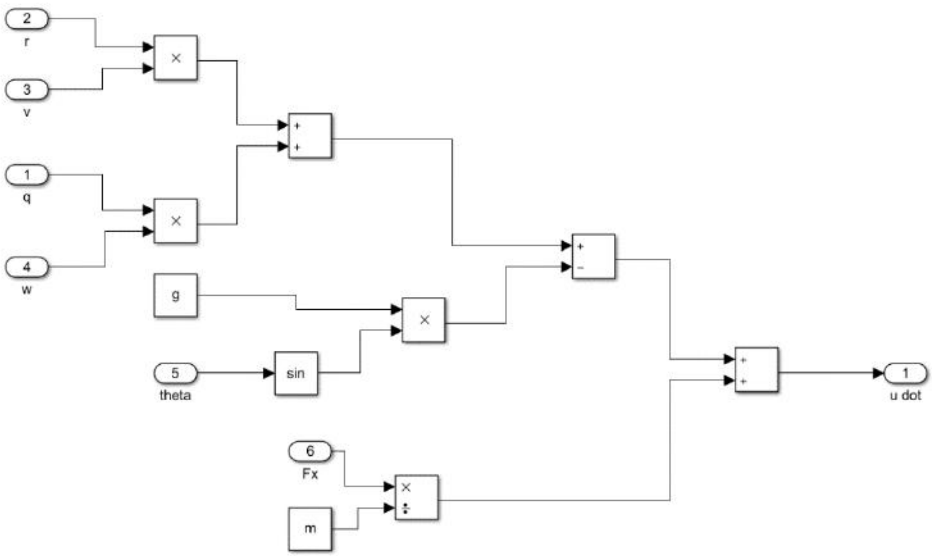

Figure 151: u subsystem

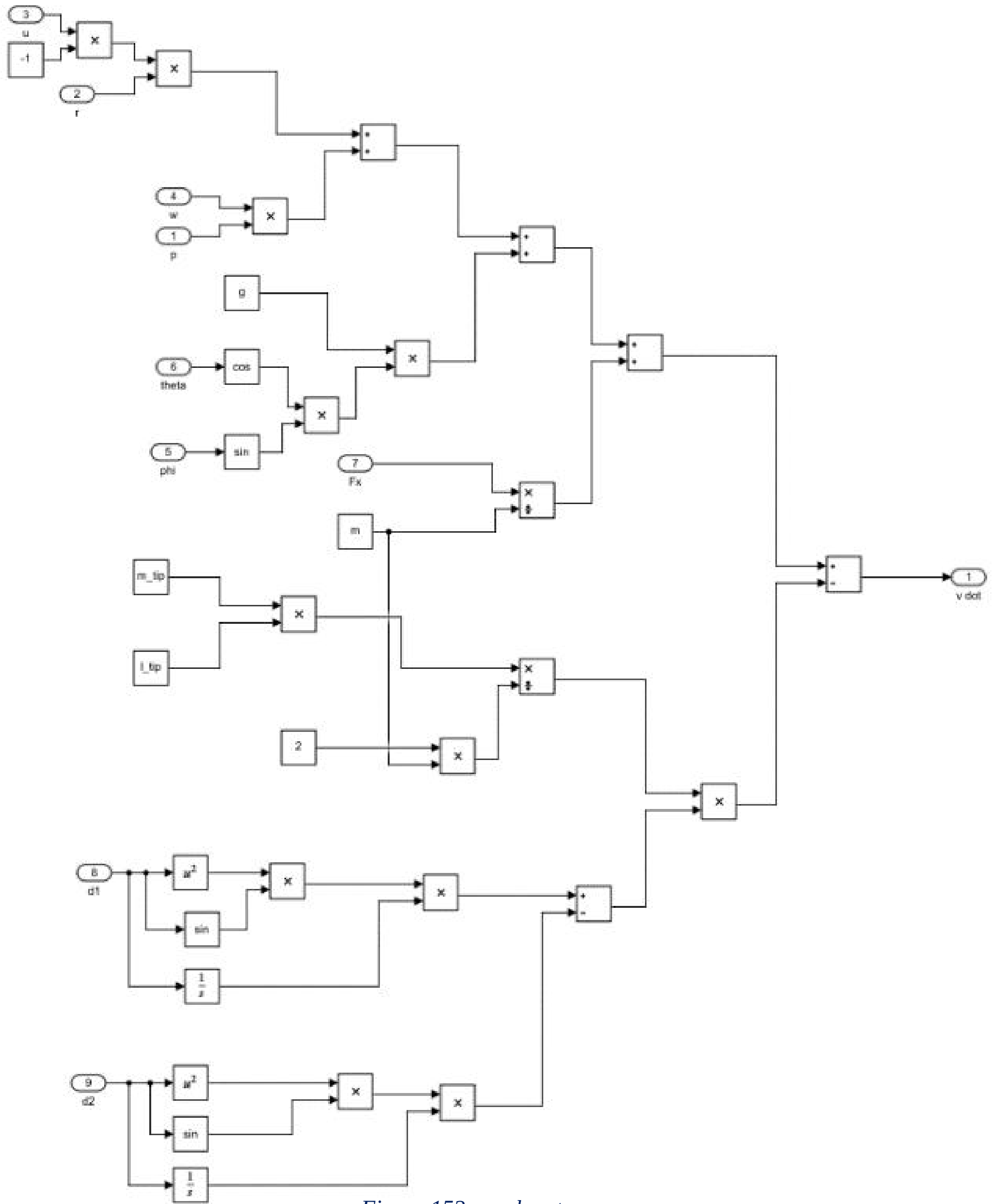

Figure 152: v subsystem

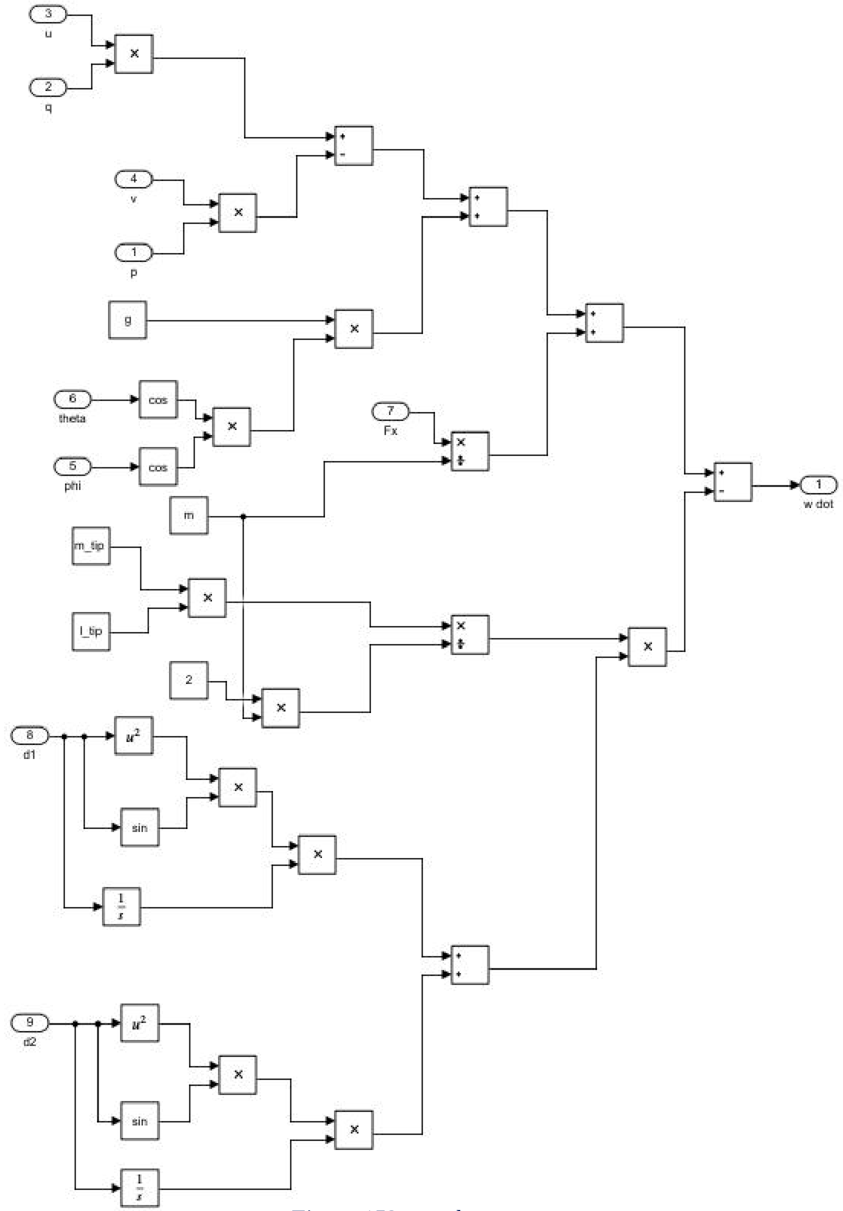

Figure 153: w subsystem

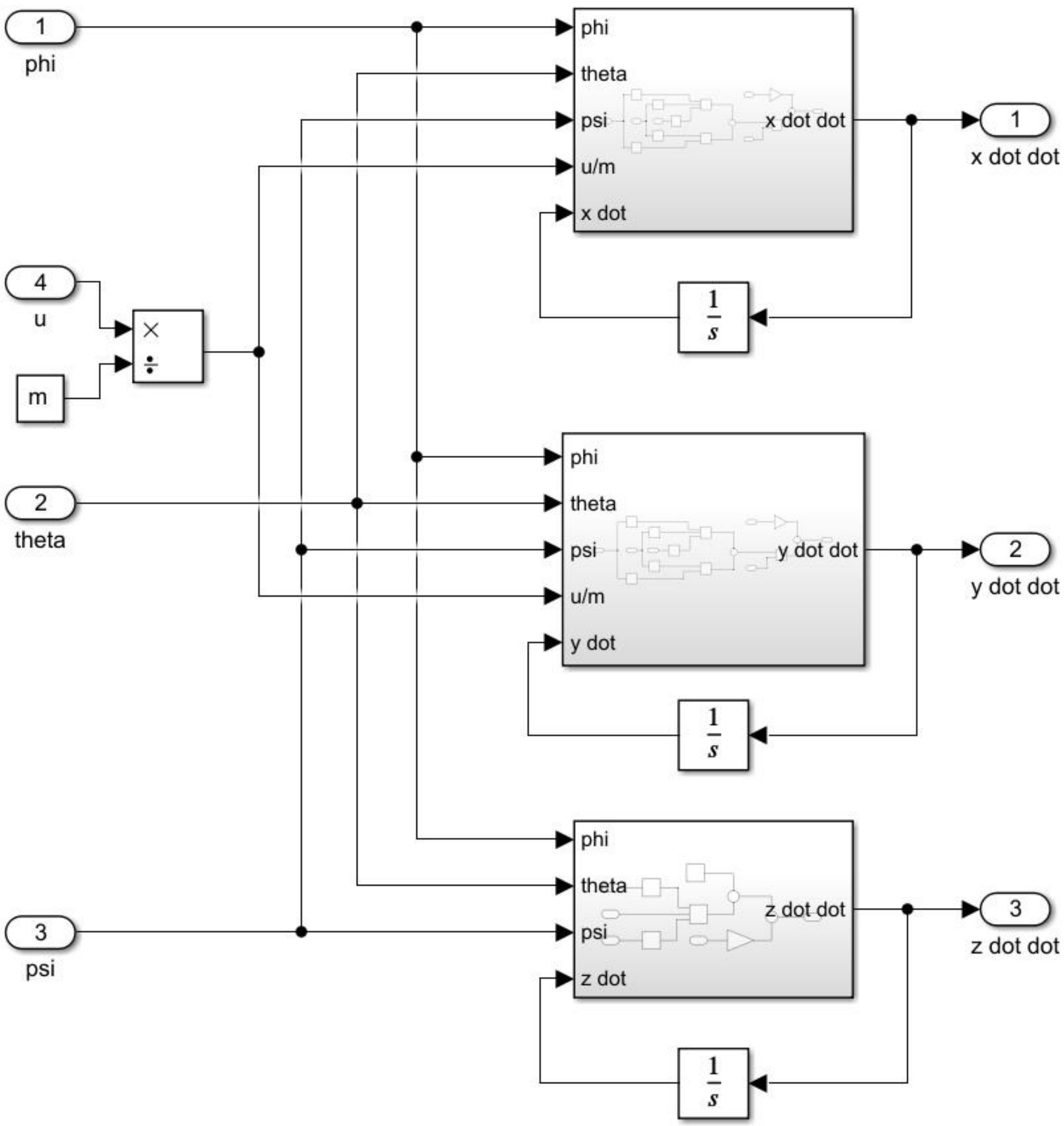

Figure 154: Linear acceleration subsystem

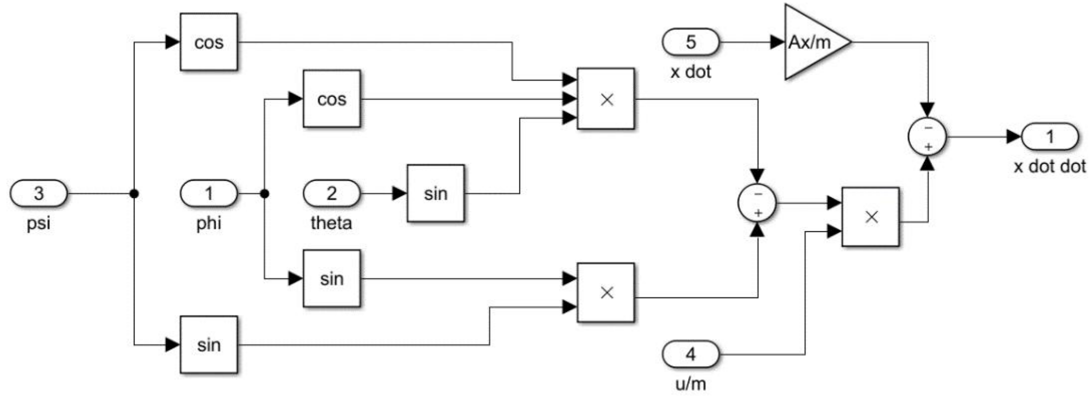

Figure 155: x dot dot subsystem

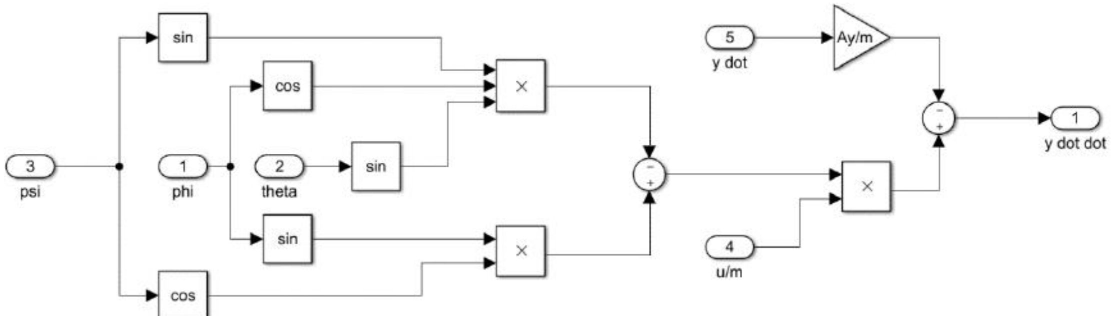

Figure 156: y dot dot subsystem

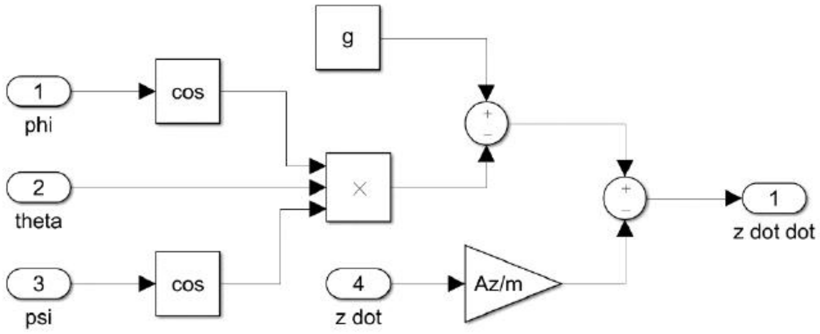

Figure 157: z dot dot subsystem

6.3.2. Control systems with PID

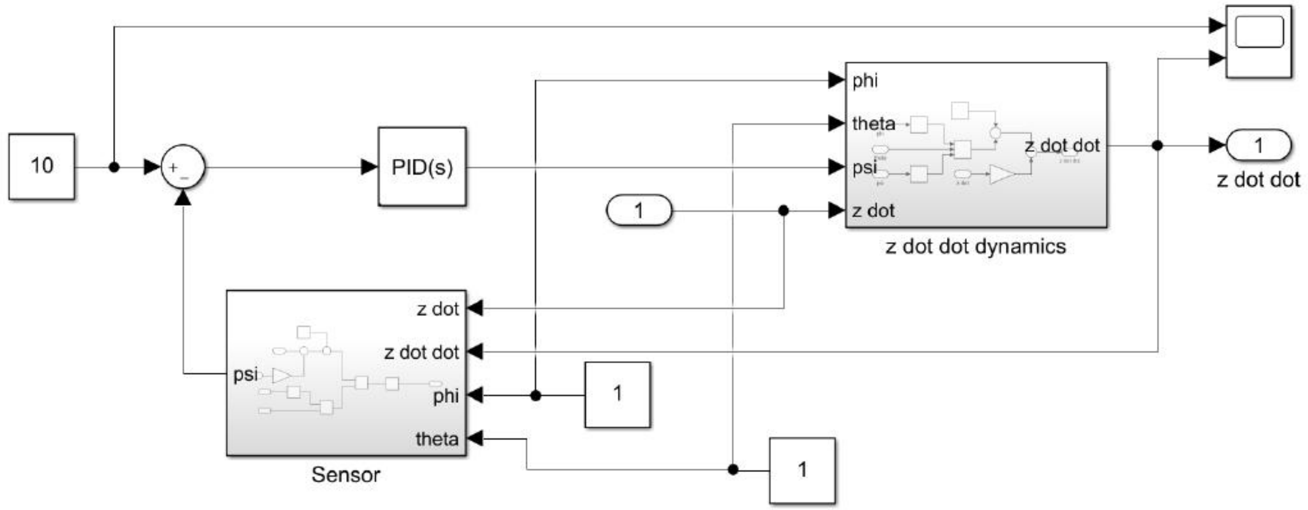

Figure 158: z dot dot with PID control

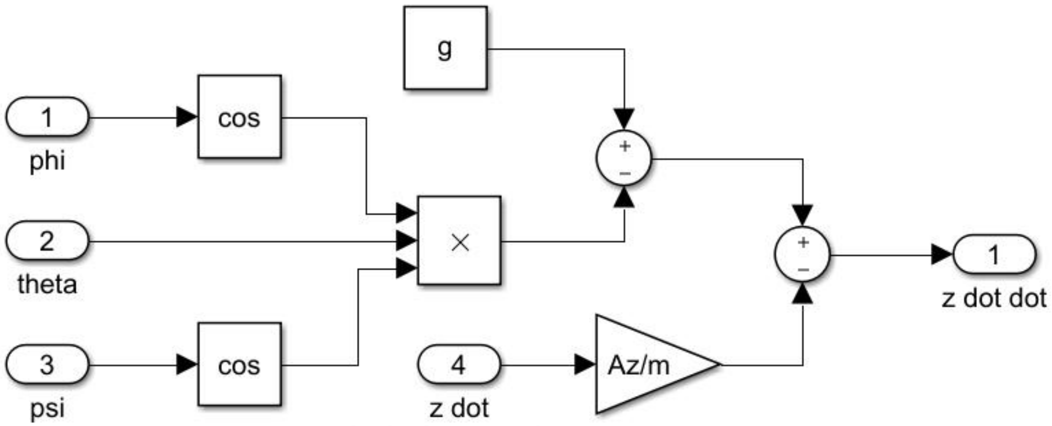

Figure 159: z dot dot dynamics subsystem

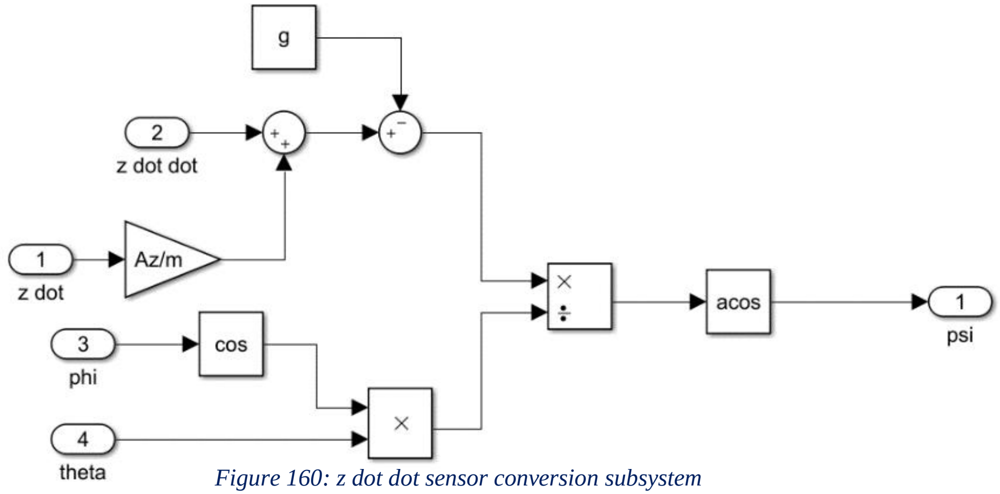

Figure 160: z dot dot sensor conversion subsystem

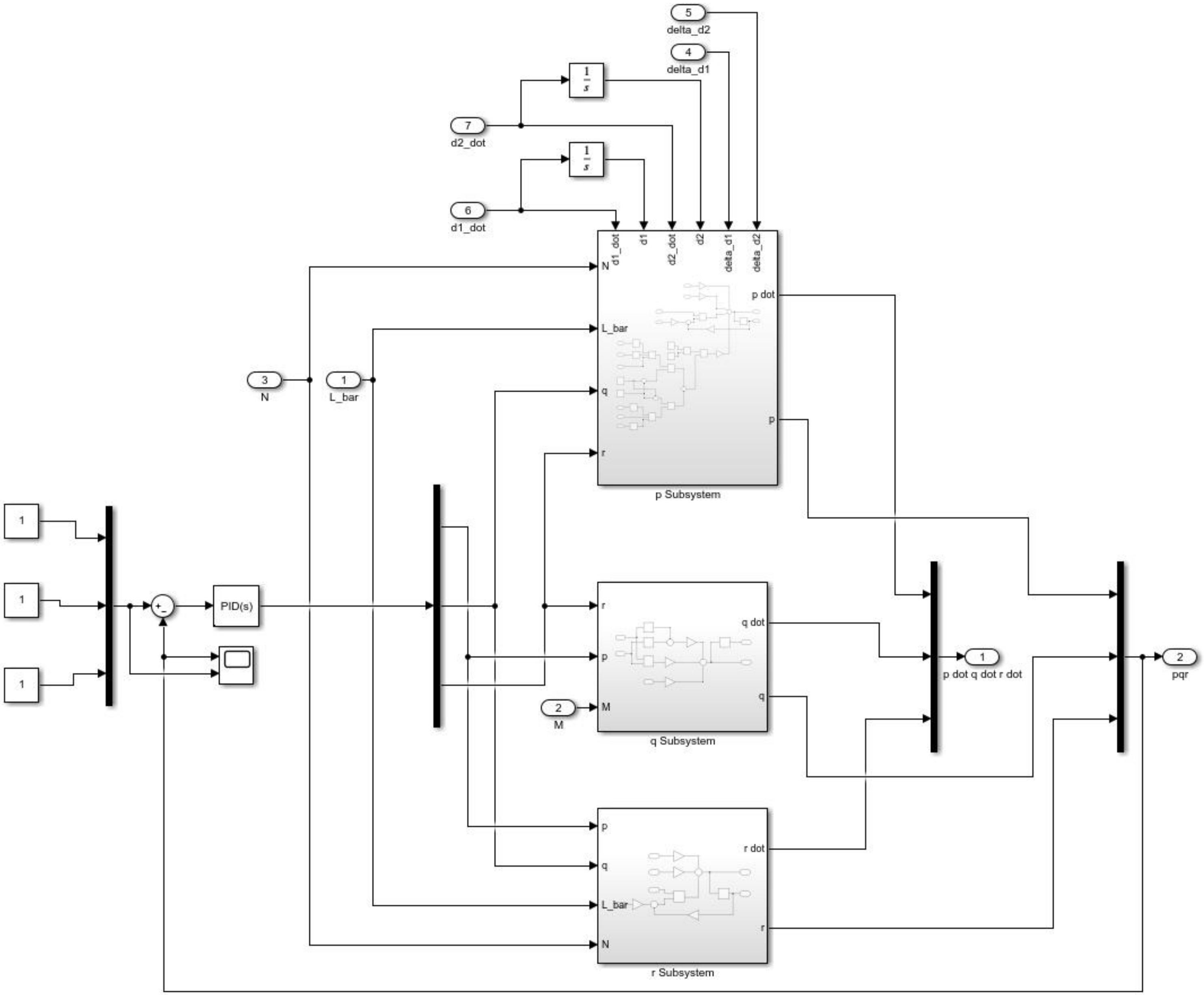

Figure 161: pqr control loop

Note that all subsystems here (p, q and r subsystems are identical inside
to the subsystems shown in figures (pqr) respectively

6.4. Results

6.4.1. Response without PID

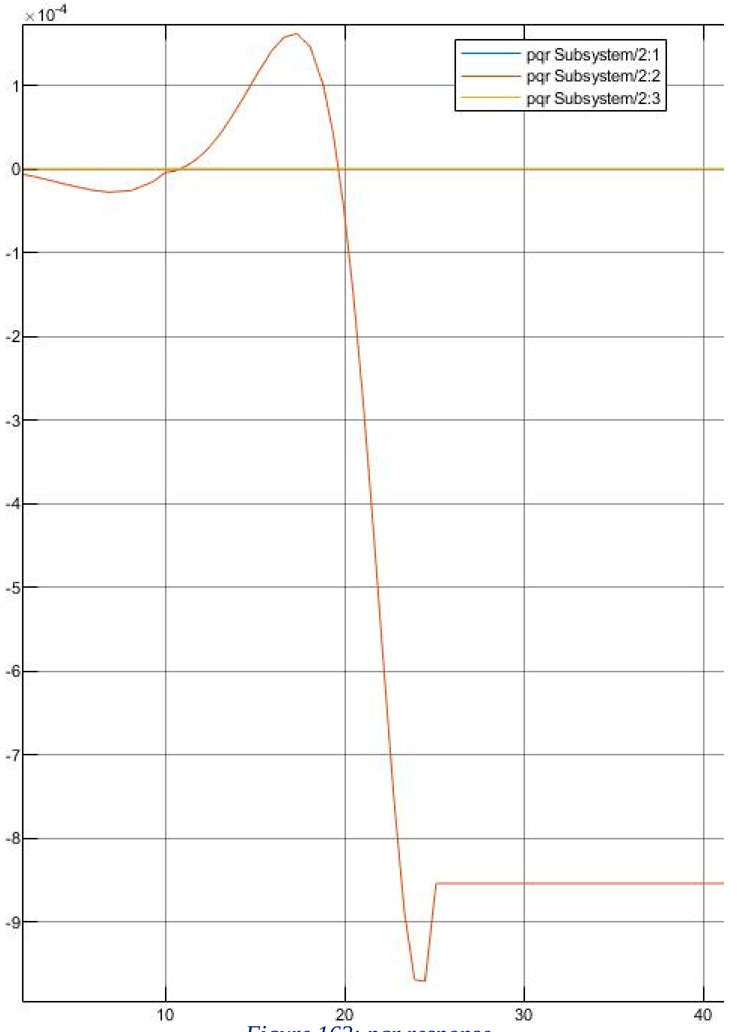

Figure 162: pqr response

(p = blue, q = red, r = yellow)

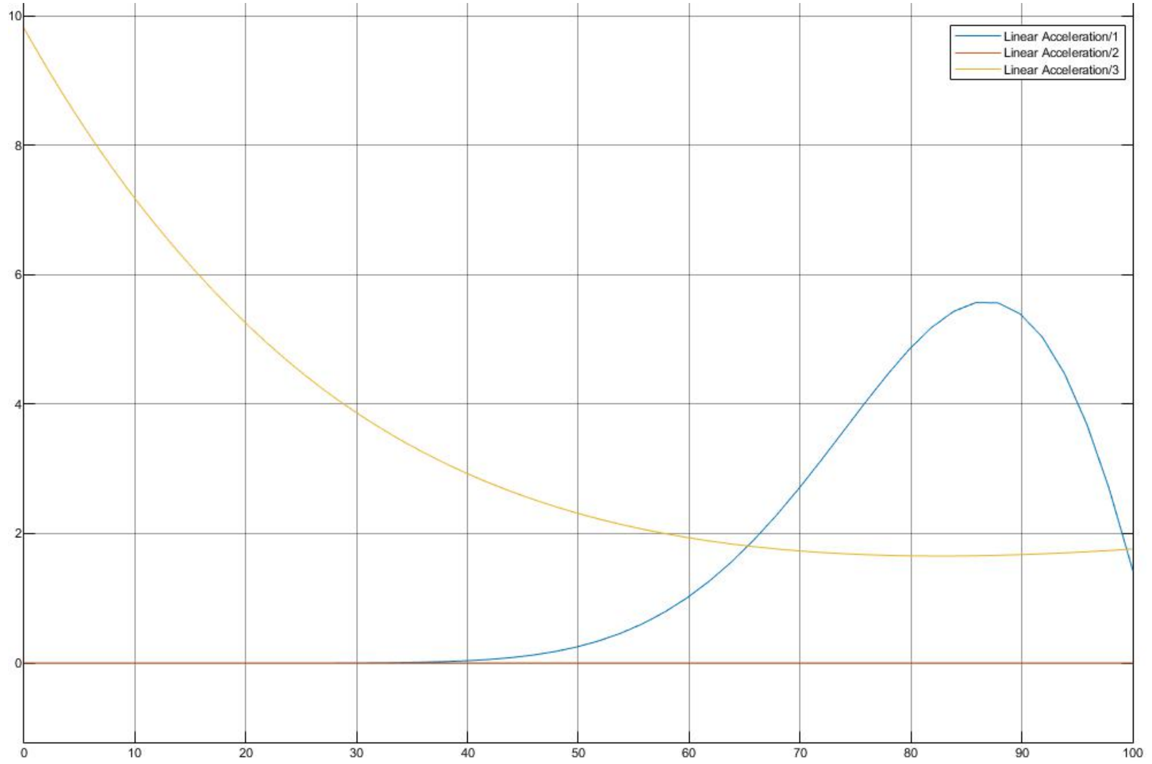

Figure 163: $T = 100s$ $\ddot{x}\ddot{y}\ddot{z}$ response

($\ddot{x}$ = blue, $\ddot{y}$ = red, $\ddot{z}$ = yellow)

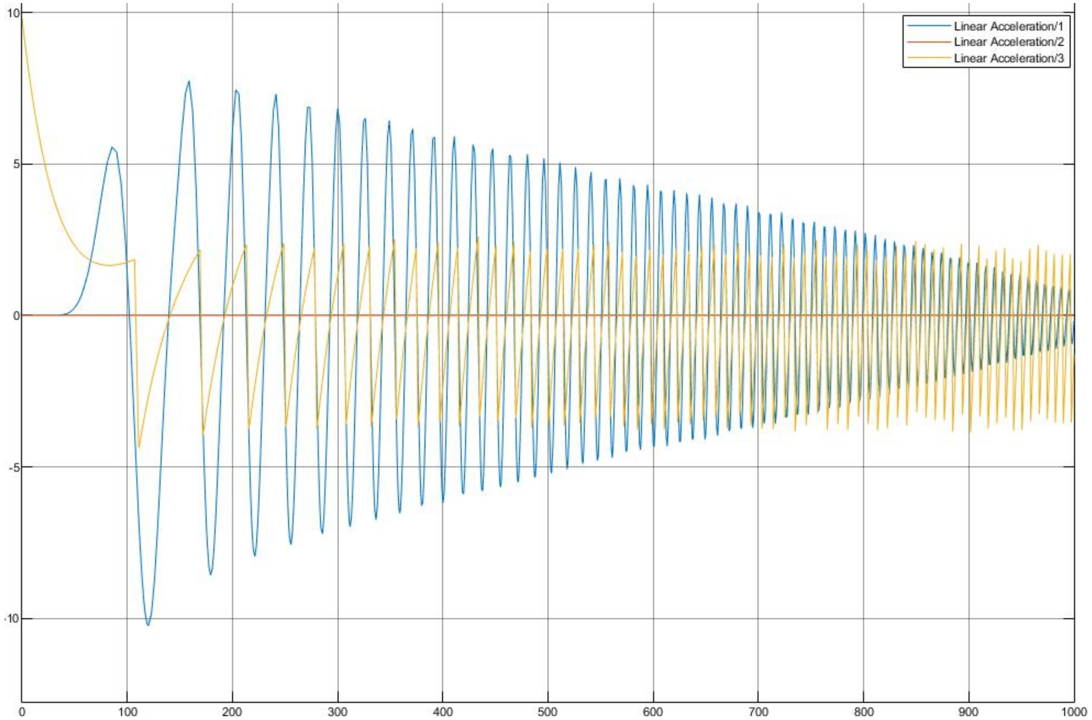

Figure 164: $T = 1000s$ $\ddot{x}\ddot{y}\ddot{z}$ response

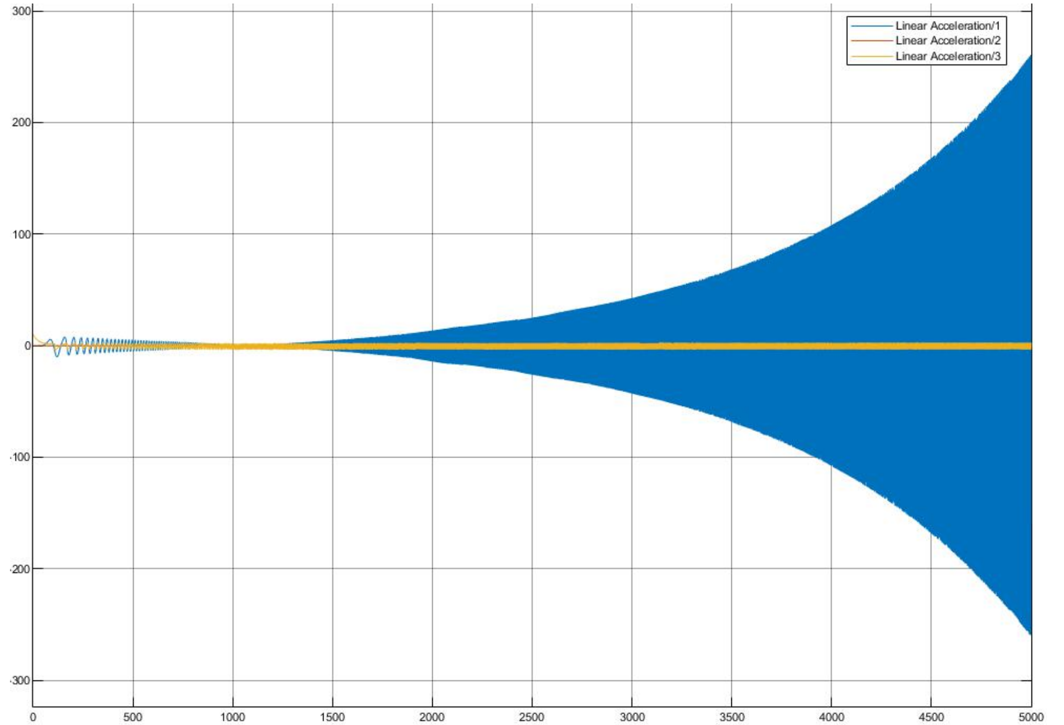

Figure 165: $T = 5000s$ $\ddot{x}\ddot{y}\ddot{z}$ response

Note that: ($\ddot{x}$ = blue, $\ddot{y}$ = red, $\ddot{z}$ = yellow)

6.4.2. Response with PID

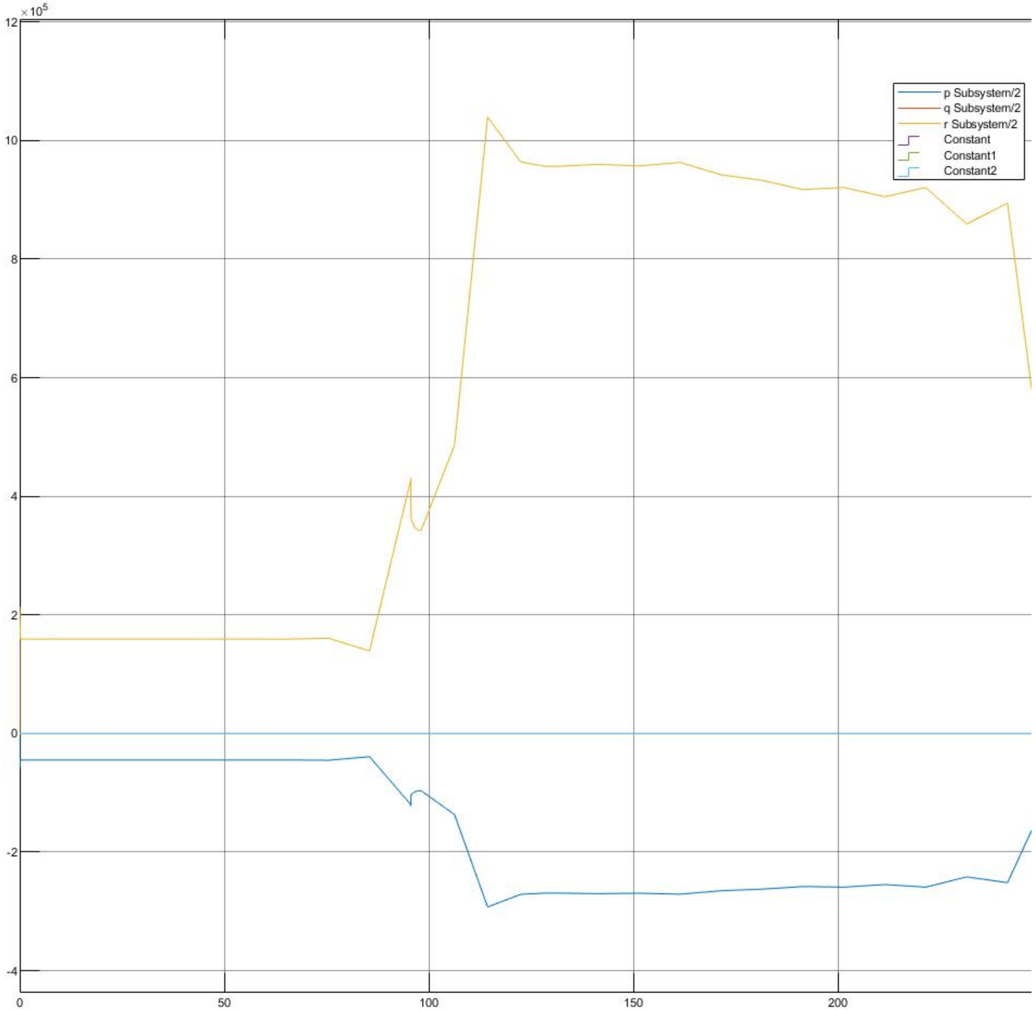

Figure 166: pqr with PID response 1

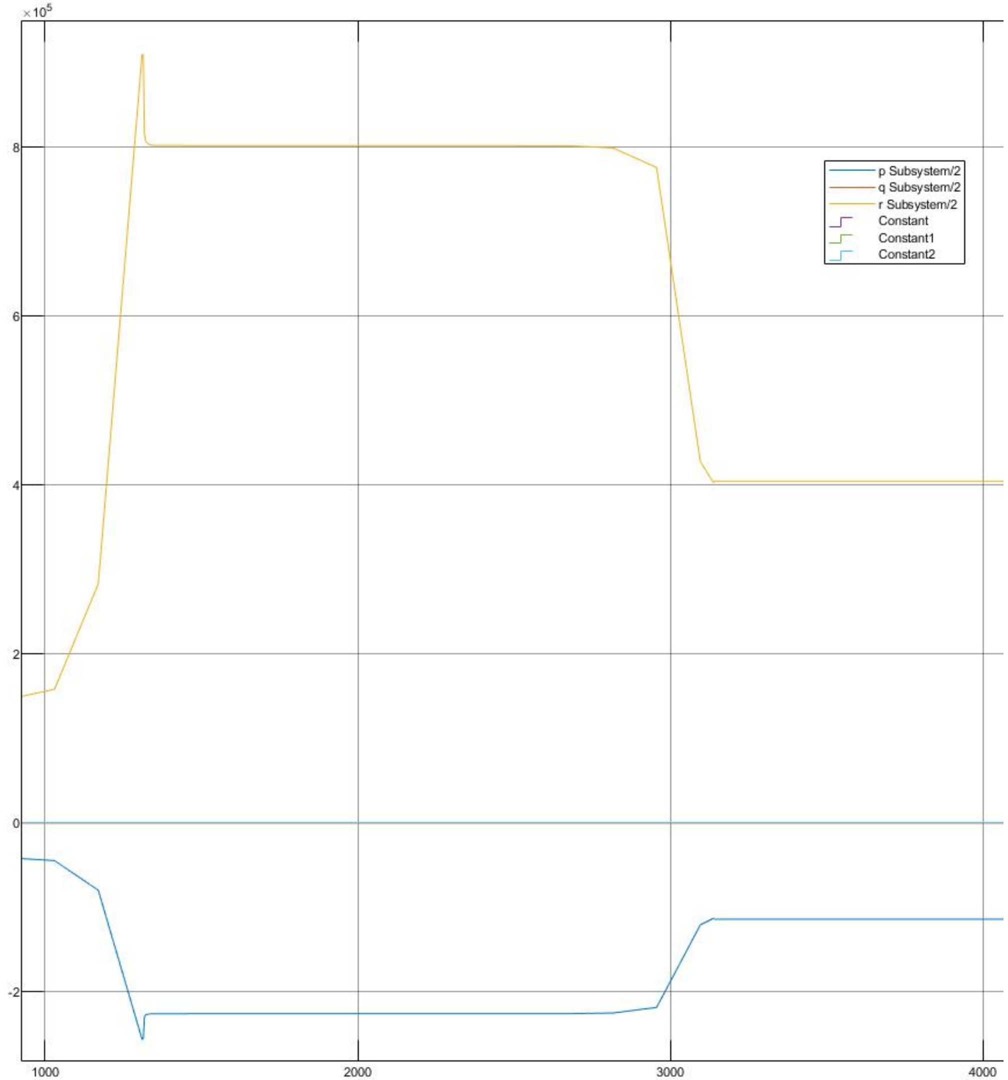

Figure 167: pqr with PID response 2

PID Values: $K_p = 9000, K_i = 7000, K_d = 0.005$

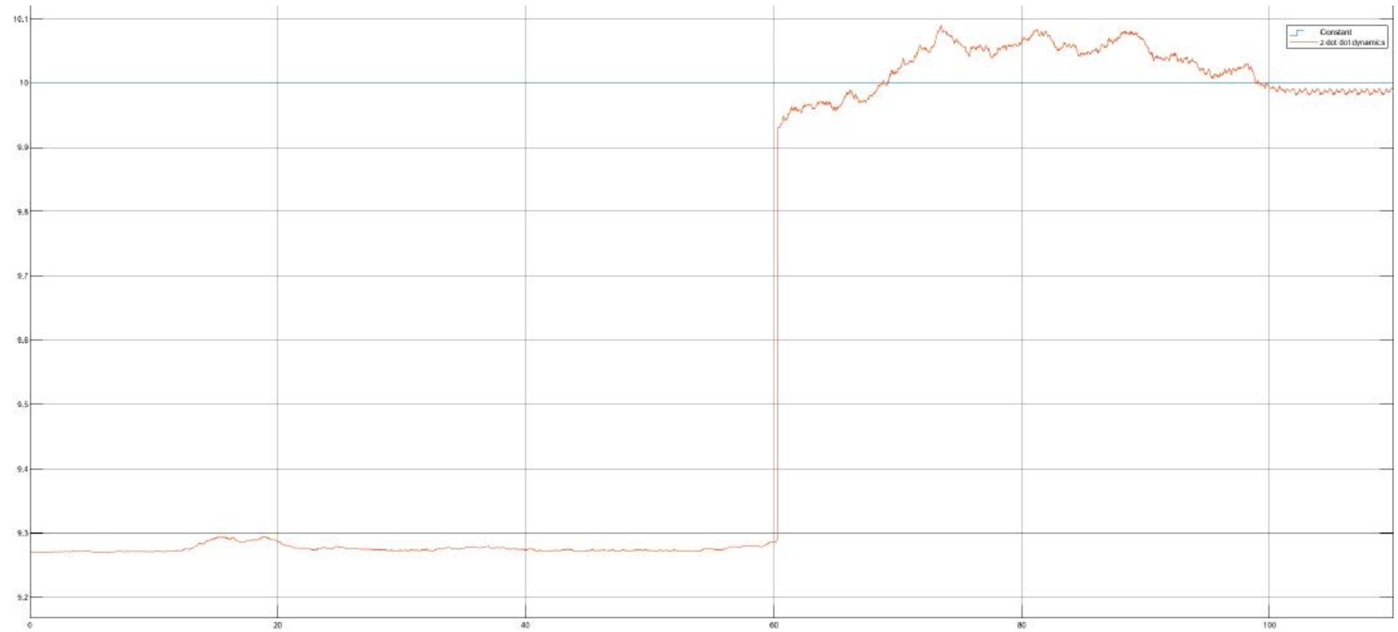

Figure 168: $\ddot{z}$ with PID response 1

PID Values: $K_p = 600$, $K_i = 900$, $K_d = 0.009$

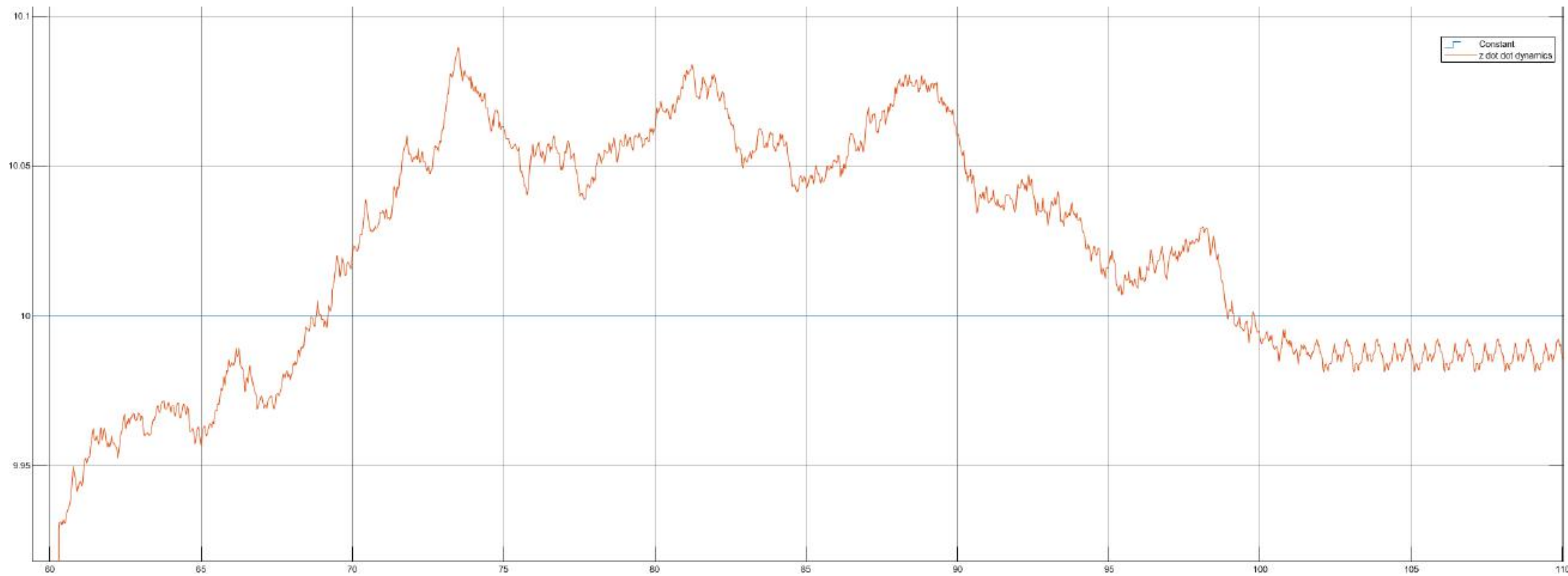

Figure 169: $\ddot{z}$ with PID response 2

6.5. Analysis of Simulation

6.5.1. Effectiveness without PID

To understand how to effectively tune the response, the original results must be analysed first to see what changes need to be made or to see if the system is unstable. Figures 141 to 157, show the arrangement of the equations that were stated in section 6.2 in Simulink diagrams, these were grouped into subsystems to understand the process in the simulation better and compartmentalise each equation and their corresponding equations into their subsequent smaller subsystems. After running the Matlab parameter script and then running the whole system shown in Figure 141, the results for the angular acceleration (pqr subsystem) and linear acceleration subsystems can be analysed. The scope block was used as a point to measure and visualise the results, and the response of the simulation without any controls are seen in Figures 162 to 165.

6.5.1.1. Angular Acceleration

The simpler of the two responses are for the angular acceleration, which is shown in Figure 162. In Figure 162, it can be observed that the roll (represented by p) and yaw (represented by r) are stable and not changing while to simulation runs. However, pitch (represented by q) was varying as the simulation went on. The pitch acceleration rate changes by increasing for a few seconds and then decreases to a lower negative acceleration value until settling at a negative value. This could mean that the pitch acceleration is unstable and cause the UAV to react in an unstable manner. In reaction to the positive acceleration at the beginning of the simulation, the UAV was overcompensating that change with a large negative value of pitch acceleration, causing the pitch is change even more drastically. The value of the pitch acceleration settles on a negative value of -8.5×10^{-4} which is very small but still would cause the pitch angle velocity to decrease for every timestep and would eventually make the UAV unstable.

6.5.1.2. Linear Acceleration

Linear acceleration takes into account all the accelerations in the x, y and z directions and can help show the relationship between these values. The results for the simulation can be seen in Figures 163, 164, and 165, these figures were run for increasingly longer to help see the long-term relationship between the different linear accelerations. Throughout Figures 163, 164, and 165, the value of the acceleration in the y axis does not move and stays at zero. This means that the value of y is not changing throughout the simulation, which was expected in this simulation of the morphing wing dynamics is done assuming cruise condition, steady climb or steady decent, meaning that the altitude should have been maintained throughout the whole simulation for cruise condition or the UAV is in steady climb or steady decent, meaning that the y velocity should be a constant and hence, no changes in acceleration in the y axis for both possibilities.

Since the value of y acceleration can be reasonably ignored, the values of the other two accelerations in the x axis and the z axis can be analysed in relation to one another. Firstly, Figure 163 shows z axis acceleration started at a value just below 10, and starts to fall from there, this means that a UAV with this morphing wing will initially starting with a positive acceleration which reduces at a non-constant pace. In the same Figure 163, the x axis acceleration was different from the z axis acceleration, the x axis acceleration initially starts off at zero, meaning that the UAV is either stationary or moving along the x axis in a constant speed, then the acceleration increases after 35 seconds, meaning that the UAV is speeding up along the x axis then peaks and drops after this. The simulation does not seem to settle yet, therefore it is better to run the simulation for longer to be able to analyse more results which is displayed in Figures 164 and 165.

The longer simulations, Figures 164 and 165, show the simulation response along a longer period of time and this is useful in seeing the true pattern in the response of the graph. It is worth noting before discussing any other value, that both figures show the same constant result for y axis acceleration being zero, this is consistent across Figures 163, 164, and 165 so there were no differences that are needed to be discussed further. Figure 164 shows the shorter time period of the two graphs being discussed here at T=1000s. In this, the x axis acceleration is seen to be oscillating in value but the size of the waves was growing smaller after about 150 seconds of run time and it seems like the x axis acceleration was converging on a final value near to zero. The z axis acceleration seen in the same figure, can be seen to be oscillating but at a somewhat even rate, the waves appear to be uniform and do not seem to be converging or diverging. After analysing Figure 164, the simulation was run for longer to see if the conclusions still hold. Figure 165 was run for the longest and it shows that the conclusion drawn previously on the x axis acceleration was incorrect. Figure 165 shows that the x axis acceleration does not convergence but diverges after 1000 seconds, becoming unstable. The z axis acceleration does stay the same in both figures and the oscillations do not change from Figure 164 to Figure 165. Using these conclusions, the controller can be set up to try and alleviate issues that are currently present in the simulation.

6.5.2. Effect of the PID Controller

6.5.2.1. PID Implementation and Tuning

The PID controller can be applied by following a simple principle:

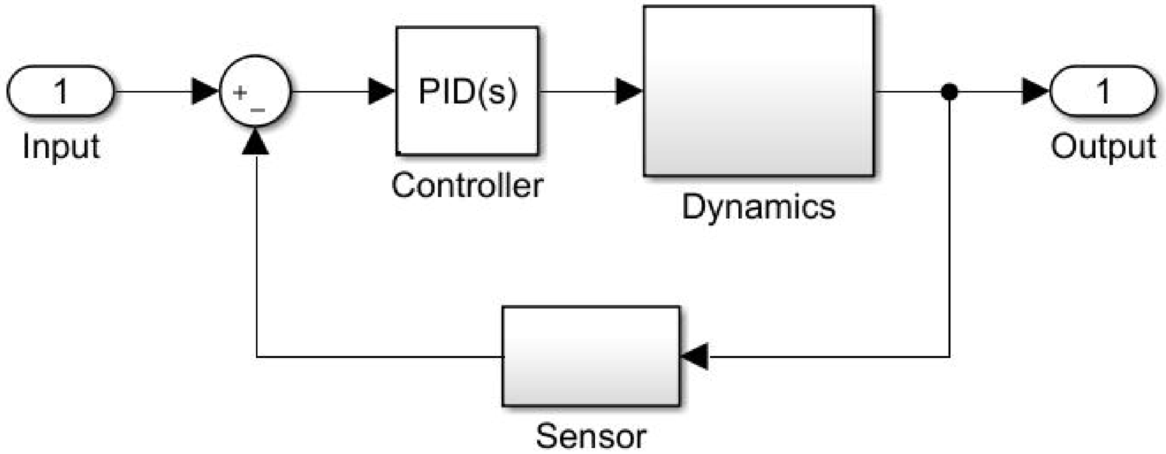

Figure 170: Negative feedback controller design (adapted from Åström and Hägglund, 2006)

Figure 170, shows the basics of creating a PID control system in a feedback loop. The dynamics were already created previously in Figures 141 to 157, these Simulink diagrams were modelling the dynamics of such equations and will be utilised as the dynamic subsystems that are needed to simulate the response of the input. Figures 158, 159, 160 and 161, show the implementation of a negative feedback loop and PID controller into previous dynamic subsystems. Firstly, for the PID simulations, some values of certain dynamics need to be defined and so some inputs have been changed from a typical ‘In’ block to a constant block with a defined value. The sensor seen in Figure 170 was used to simulate the process that a sensor would go through in converting raw measurements into the same parameter as the input to complete the feedback loop (e.g. if the input is given in ampere and the sensor measures voltage, the sensor measurement must be converted back into ampere to complete the negative feedback loop properly). Using this technique, the loops shown in Figures 158, 159, 160 and 161 were be created and run.

PID tuning must be completed for the response to be tuned in a desired manner. The tuning philosophy used will be according to the effects of each PID parameter detailed earlier in section 6.2.3.3. The simulations were run, and the response were altered by changing the PID values until the response was satisfactory for the requirements of the UAV. The results of the PID tuning can be seen in Figures 166, 167, 168 and 169.

6.5.2.2. Analysis of PID Response

Firstly, the control of the pqr subsystem will be discussed. The results of the simulation can be seen in Figures 166 and 167. Figure 166 shows the beginning of the simulation and Figure 167 shows the response of the system when it settles. Both figures show that the acceleration in pitch can be controlled well by the PID controller and matches the reference value quickly. The value of acceleration in yaw frame is always higher than the reference value while acceleration in the roll frame is always lower than the reference value. Both roll and yaw accelerations can settle on a constant value after 3300 timesteps meaning that the eventual steady state error can be found. The advantages of using the PID controller can be seen here as through testing, the steady state error can be used to modify the reference input so that the results are skew in a way that moves both p and r values towards the true reference value. The system is also stable than before in the end, although the overshoot is high for both p and r values, the system is able to recover and land on steady value.

However, there are some drawbacks this particular PID controller, specifically, the percentage overshoot and rise time. The percentage overshoot for both the p and r response is high, meaning that the system is not able to reach and maintain the reference value easily. As this is a simulation, it is hard to see whether if this was implemented in real life, the overshoots here could cause instability which will could cause the UAV to fail. The rise time is a bigger issue than the percentage overshoot as it is more likely to cause problems for the UAV in real life. The response of the UAV does not start for a few timesteps and this could cause issues as the UAV is not able to respond quickly and effectively to outside stimuli. For example, if the UAV detects an obstacle and inputs an appropriate reference value to avoid the object, having a slower rise time means that the gap between the input changing and the UAV's response could be too long that it ends up crashing into the obstacle instead of avoiding it. Steps must be taken to avoid this from happening or the control system would not be able to be implemented in an effective way.

Secondly, the response of the z axis acceleration can be analysed for its own improvements and drawbacks. Figure 168 shows the overall response of the control system, and Figure 169 shows a more detailed result of the z axis acceleration. Figure 169 can be used to analyse overshoot and steady state error, the overshoot is very small, meaning that the system is unlikely to cause in stability in that way. The steady state error is harder to measure as the response of the control system continues to oscillate in a repeatable pattern at the end of the simulation. To find steady state error, an average of these values should be found so that the difference between this found final value and the reference value can be found. Currently the final value can be estimated at 9.98, making the steady state error at 0.02, which is very small, meaning that the steady state could be assumed as zero. This means that the control system works effectively, being able to not overshoot too much as well as settle on a value that was close the reference value, making it a more effective control because it is able to reach the reference value and maintain it accurately.

There are, however, some drawbacks to the PID controller as it is. Namely, the rise time and settling time is very long, taking over 60 seconds to start rising to the reference value and the settling time takes an extra 40 seconds past this to reach a stable value. This would cause a similar issue as the slow rise time for the pqr subsystems, meaning that the UAV may not be able to react in time if something bad were to happen. There could be fixes to this issue, which could involve further tuning of the PID values to reduce the response and settling time. Overall, the z axis acceleration subsystem seems to be able to effectively control the response of the z axis acceleration. The design principle for this one could be used to create other PID controller loops for the x and y axis acceleration controllers too.

6.6. Implementation

6.6.1. Applying Software to Hardware

When the simulations are successful, it is necessary to move the software created into hardware that can be put into the UAV. Considering the work that has been completed so far for this project, it can be assumed that the autopilot AI system will be created using Simulink, therefore for this section, only hardware parts that can be used with Simulink will be considered for implementation.

There are a few important things that need to be noted when looking for a hardware to implement. Firstly, that the hardware can be put onto the UAV designed earlier, this includes factors like weight and number of ports (as there will need to be enough ports for the sensors to input information necessary for the control system to complete its calculations). Secondly, the hardware needs to be able to be accessible enough that the parts can be sourced somewhat easily, therefore no hardware that is no longer in production can be considered. Thirdly, practicalities such as waterproofing and levels of heat that the circuit board can take will be important to consider. Due to the wide variety of potential situations the UAV could be put into as a search and rescue drone, the UAV could be deployed in rainy situations or tropical countries where there is potential for the circuit board to overheat. Therefore, it is important to keep these practicalities in mind otherwise the UAV will not be fit for purpose. This section will present several viable hardware choices, along with their own advantages and disadvantages discussed, the hardware can be compared, and the best hardware presented as the one that would be used for the drone when it is created.

6.6.1.1. Raspberry Pi

Raspberry Pi offer a set of circuit boards and depending on the model, several USB ports and processors that can be coded to run certain programmes. This kind of board can be used to implement the Simulink and Matlab codes onto it so that it can then be transferred to the UAV and used as the UAV's onboard processor. The circuit boards that are most commonly used are affordable specifically, the 4th generation of boards can be customised so some components such as RAM can be changed and this means that the board can be changed to meet the specific requirements of this project. The board's costs starts from £35, depending on what components are added to the board (Raspberry Pi 2020), making it affordable for this project.

Figure 171: Raspberry Pi 4 Model B Board (Raspberry Pi 2020)

One benefit of this board is the high level of Matlab and Simulink compatibility, as Raspberry Pi has its own toolbox that can be downloaded for the Matlab software. This toolbox contains blocks that are already programmed in a way that the circuit board can understand and execute commands effectively. One block in the toolbox can be used to connect Raspberry Pi boards to other boards and iOS (the operating system for Apple devices), which could open new opportunities such as connecting an iPhone to use as a sensor (Mathworks, "Raspberry Pi Support from Simulink"). The board is also able to log data from sensors, this feature could be useful when testing out the model as the data collected can be decompiled and analysed on Matlab for troubleshooting and further development. A disadvantage of the Raspberry Pi board is that it cannot handle many sensors due to its limitations on ports meaning that if all the USB ports are used, there is no way to expand the board to include more. Practicality issues also exist as the board is not waterproof or dust proof, making it hard to rely on when the UAV is put into tougher environments as it may not be able to hold up to the extreme conditions.

6.6.1.2. Arduino Board

In some ways, the Arduino board is very similar to Raspberry Pi. They both provide boards with processors that can be customised, and both are somewhat affordable, although it has to be noted that Arduino boards on the whole are more expensive than Raspberry Pi. One major advantage of Arduino is the number of choices available as it has much bigger than the offerings of Raspberry Pi. Arduino's also offer other modules that can be connected to make a larger system, each one adding something to the overall system. Most notably for the usage in this UAV, a sensor kit is available to purchase along with a larger number of ports and sensors that are designed to work well with the Arduino architecture. This means that there is no limitation of the number of sensors that can be added to Arduino making the creation of the UAV easier.

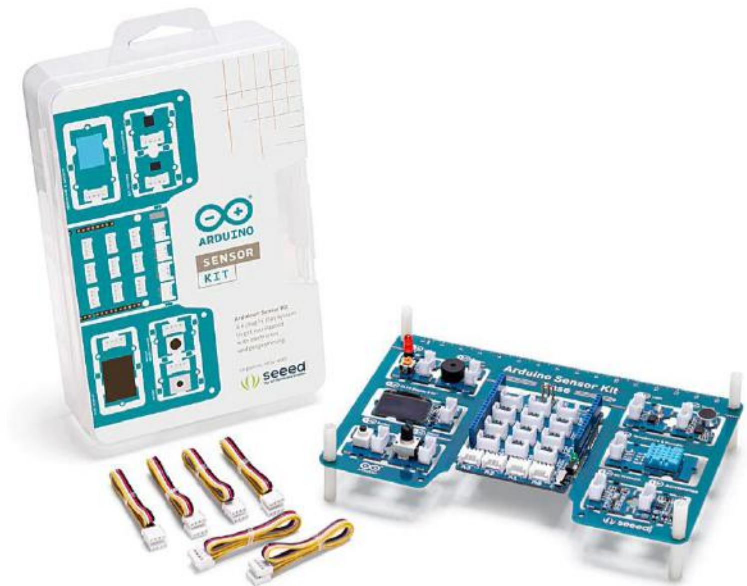

Figure 172: Arduino Sensor Kit (Arduino 2022)

Similarly to Raspberry Pi, Matlab and Simulink offer tailored toolkits that are specific to the Arduino which also allow it to communicate with other boards and the Arduino board can also store data which can be imported to Matlab and analysed. Another benefit of using the Arduino is that it has a built-in ability to connect over Wi-Fi (Mathworks, "Arduino Support from MATLAB"), making it easier to communicate with the board remotely instead if the need to add another module to accommodate communication. However, the Arduino board is not practical as the board is not waterproof or dustproof, it is also not as compact as the Raspberry Pi.

6.6.1.3. Other Hardware Options

There are many options for hardware for the UAV, one common way is to use SoC FPGAs, which are semiconductor devices which have a processor onboard that is codable with programmable logic (Mathworks, "SoC FPGA Development"). SoC FPGAs are more powerful and have much more variety in terms of specs, making it more versatile and suitable for the UAV's purpose and usage. Similarly to the previous hardware options, Matlab also have a SoC set to help transfer the code onto the hardware with ease. There are also limitations with this board, most importantly, it can be difficult to source for an individual process and SoC FPGAs are very expensive when bought from a supplier such as Intel. This board also has the same issues with practicality, but it is the expense that is most difficult challenge to overcome, making it not feasible to use for the UAV model.

6.6.1.4. Hardware Choice

Overall, by weighing up the options that were listed, Arduino boards seem to be the most practical and useful for this project's purpose. Its ability to communicate wirelessly over Wi-Fi and the possible expansions of an additional sensor kit makes it more ideal for this project as it is still evolving and the software is not perfected yet, having the flexibility to troubleshoot and improve the autopilot and AI design is essential. The Arduino board is the hardware interface that offered the most flexibility and options to expand, making it the most ideal hardware of choice. However, it must be mentioned that all the boards will have practicality issues such as waterproofing that must be addressed. Since the body of the drone is waterproof and dustproof, the circuit board must be placed inside of it to alleviate this issue. Further testing needs to be done when the UAV is made to ensure that it can be used in more extreme environments.

6.6.2. Future Improvements

To improve the findings in this project and take it further, suggestions can be made for potential further research into this topic by addressing the issues that rose from the simulation and analysis of the results. The improvements and potential areas of further research can be summarised below:

- Create more dynamic control systems that integrate more parts that link them together.
- Research and test the viability of implementing different controller for negative feedback control.
- Develop a model for all three stages of flight (i.e. take off, cruise and landing) and integrate them all together to work with the thrust subsystem.
- Create a model of the UAV and implement hardware into it using the techniques and choices made in this paper.

6.7. Conclusion

6.7.1. Design Effectiveness

The goal of this part of the project was to research and create a control system that can model the morphing dynamics of the UAV that has been designed in earlier sections. Equations for the dynamics was derived and rearranged for the specific arrangement that was set out in the problem definition. The control system was then created from all the equations of motion and linked to each other to make an interdependent system that can model the UAV. The dynamic response was simulated and analysed to see if the design is unstable and identify areas where control would be needed. Subsequently, a simple negative feedback control loop was introduced along with a PID controller to help manipulate the response to one that was needed from the UAV. The values of each parameter within the controller can be changed in the process of PID tuning and this was modified to help alter the response so that the desired output was achieved. All the results were then compared to each other to help see the difference between the response with and without PID control. The results found that the PID tuning helped the system output a more consistent value as a result but the response have left a lot of room for potential future work where this could be changed or developed further, including areas such as hardware implementation.

Overall, it seems that the project’s aims and objectives were answered effectively, the control system was created and linked together successfully to give some simulation results of which were analysed to identify issues and potential instability. The PID controller was also implemented effectively, helping to control and maintain the response near a set reference value. Further developments were also discussed and the practicalities of buying certain hardware for a future UAV project was discussed.

6.7.2. Future Projects

By taking the conclusions found and research done in this project, some future projects can be done to expand on this idea. The main project idea that could be created from this current project would be to continue to work completed here and create a model of the UAV proposed in this report. More specifically for the control systems section, the software created could be integrated with sensors and implemented into the hardware that was suggested. The control system could also be expanded to include other parts like the AI for autopilot decision making and all dynamic simulations can be integrated into one overall control system.

7. Control Systems and Automation –Saaqib Asif-Jussab (180486988)

7.1. Introduction

Unmanned Ariel Vehicles (UAV) also known as UAVs are now widely used around the world for many uses, from military applications to delivering aid. UAV are vehicles which fly without the need of a pilot. This means that they are controlled from the ground or can also be fully automated using control systems and potentially artificial intelligence (AI). This automation gives these UAVs a wide range of applications making them versatile. The UAVs can be used for photography and delivery to even law enforcement. The integration of UAVs into everyday society increases each year. AI has also been implemented into a lot of modern drones which is a way in which they have been automated. Companies such as DroneSense, Skycatch, and Orby are all implementing AI into their UAVs (Daly, 2018).

This report will look at the design and development of a UAV used for natural disaster management. This section of the report will look at the thrust and navigation subsystem for the UAV and the process of making the UAV autonomous. The different subsystems of the thrust control system will be created using each of the equations need for the desired output. Different types of navigational control systems that can be adapted for use in the UAV will be observed to see what would work best. The automation of the UAV using different systems and sensors will also be observed within this section of the report to see what type would best suit the UAV for the given task. The ability of AI to further help the automation of the UAV will be discussed.

The control systems and research in this section of the report are unique in comparison to the previous years in that the systems within this report are functional and set up so that they can be implemented into a working UAV. The research which has been done within this part of the report can be used to develop the UAV design further and help with the development of a UAV which is automated and can be used for natural disaster management.

7.1.1. Aims

This section aims to design and run suitable control systems for the thrust of the UAV, look at how the navigation of the UAV can be implemented using control systems, look at how the automation of the UAV can be done using various methods and finally how AI could be beneficial towards this.

7.1.2. Objectives

To bring the aims of this section to a successful conclusion the following objectives will have to be met:

- Investigate the equations needed for the thrust control system and use these to create a control system within Simulink which provides the desired output.
- Investigate the different types of navigation systems to see which would be suitable for the UAV and how they can be adapted for the UAV design.
- Look at a range of systems and sensors to see how they work and whether their implementation into the UAV would be beneficial to the given task.
- Look at how AI can be implemented into the UAV design and how it will help with automation.
- Assesses all the findings within this section to see whether they're beneficial to the design of the UAV.

7.2. Methodology

7.2.1. Thrust Control System

For the UAV to perform it needs to manoeuvre, so the thrust produced by it is very important. The thrust also needs to be varied depending on the stage of the mission profile that the UAV has reached. The UAV will have to take off, cruise and land all autonomously. For the UAV to be able to do this effectively a control system which can be adapted to the situation will be needed. This will allow the UAV to vary its trust depending on the phase of its mission profile. To create the control system the following equations were used:

$$T = \frac{1}{2}\rho v^2 \left(C_{D0} + \frac{C_L^2}{\pi A e} + \Delta C_{D0} \right) S \quad (101)$$

$$P_{req}^{VTOL} = \frac{T \times v_i}{FOM} \tag{123}$$

$$\Omega = (V_{in} - I_{in} \times R_a) \times K_V \tag{140}$$

The equations above are used for each of the subsystems within the thrust control system. The equation for thrust required uses the coefficient of drag and lift to calculate the thrust the UAV will need during each phase of the flight. The power required equation takes the thrust input and the rate of climb and combines them to get the desired output. Finally, the rotation speed equations utilise the power required value to get the final output of the thrust control system.

7.2.2. Thrust Simulink

Using the equations above the control system can be created using Simulink and can be seen in the Figure 173 below. The control is made up of three separate subsystems which when combined will calculate the thrust of the UAV. The control system is made up of the thrust required, the power required and the motor subsystem.

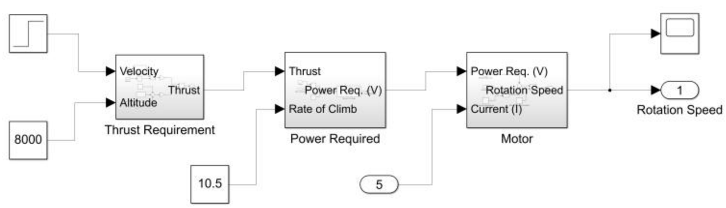

Figure 173: Thrust Control System

The figure 174 shows the thrust required subsystem for the UAV, this is based on the equation 101. This subsystem is made up of all the parameters from the equation above. This subsystem also has another subsystem within it. The subsystem which is with this one can be seen in the Figure 174. This is the atmospheric density subsystem.

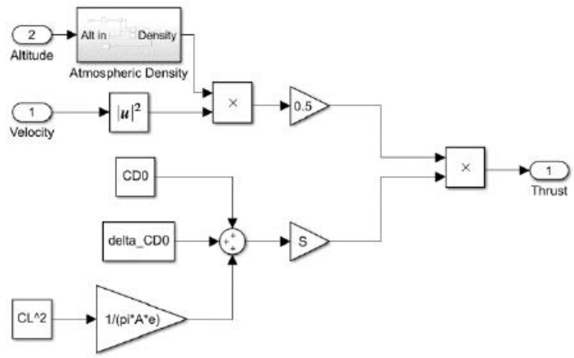

Figure 174: Thrust Requirement Subsystem

The Figure 175 shows the atmospheric density subsystem for the trust control system. This helps to calculate the atmospheric density while the UAV is in motion and changes depending on the altitude of the UAV.

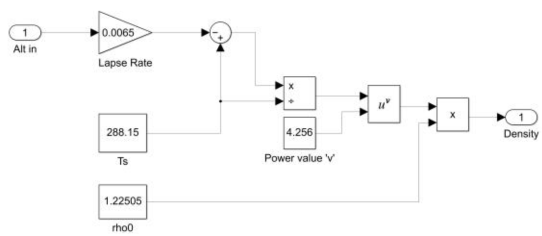

Figure 175: Density Subsystem

The subsystem below is for the power required for thrust in the figure 176 and is based on the equation 123 shown above. This takes the thrust and the rate of climb and uses them to calculate the power required. This subsystem also has another subsystem within it. This is used to convert to voltage.

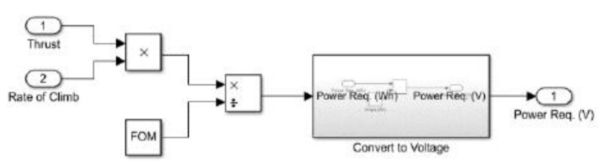

Figure 176: Power Required Subsystem

The figure 177 shows the convert to voltage subsystem which takes the power required in watt-hours and turns it into voltage to get the desired output.

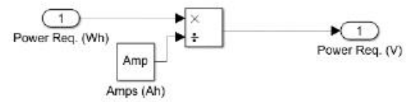

Figure 177: Voltage Converter Subsystem

The final subsystem for the thrust control system is the motor output which uses an equation 140. This can be seen below in the figure 178. This subsystem takes the inputs and converts them into the rotational speed for the propellers of the UAV. It uses the various constants needed for the motors and combines them with the other inputs to get this output.

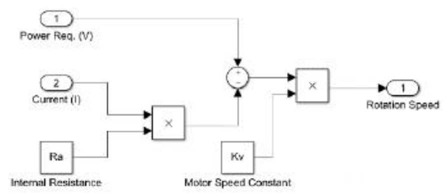

Figure 178: Motor Output Subsystem

7.2.3. Results

When running the thrust control system, the following results were obtained and can be seen in figure 179. The units for the graph are Rotations Per Minute on the y-axis and Seconds on the x-axis. It shows the base result of 800 rotations per minute. The result is seen to drastically increase to the maximum. This shows that the control system works and can be implemented into the UAV.

Figure 179: Initial Thrust Results

7.2.4. PID Simulink for Thrust

The Simulink diagram shown below in figure 180 is for the PID tuning. This is different from the original Simulink as it has a feedback loop which is used to get the optimal result from the control system. This is done by including a PID controller and a sensor.

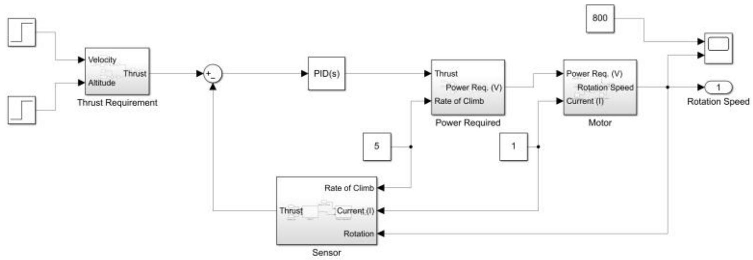

Figure 180: PID Thrust Control System

7.2.5. Thrust PID Tunning

For the PID tuning a feedback loop needs to be created, this allows for the system to cycle until the optimal result is achieved. This is done by first taking the input and running it through the PID controller. The system then will run as normal up until the end of the motor subsystem. It is then cycled through the sensor which detects the new value. The sensor then runs the value back to the beginning. The PID is then used to check the difference between the initial value and final value, so before the value is run through the PID again the final value is subtracted from the initial value. This will repeat as a loop until the difference between the two values is zero. This value will be the optimal result for the control system.

7.2.6. PID Results

The optimal results for this control system can be seen below in the figure 181. These results show that the optimal value of the system is lower than the initial result obtained when running the initial control system. From looking at the data the max optimal value is 795 rotations per minute in comparison to the initials 800. It can also be observed that the result has an exponential increase in comparison to the drastic increase for the initial value.

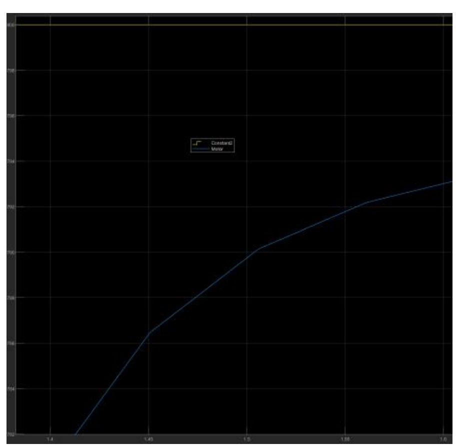

Figure 181: PID Thrust Results

7.3. Navigation System

The UAV is being designed to deal with natural disasters, so it is important for its system to always know its location. There are many ways in which this can be achieved, particularly the use of the Satellite Navigation System (SNS), the Global Positioning System (GPS) and the use of the Synthetic Aperture Radar (SAR) could be implemented. These systems all work in similar but different ways to allow for the global positioning or guidance of an aircraft. These systems could all be helpful to the UAV's navigation system making it easier for the automated system to run. With the RAS working with imaging to help with guidance and the SNS and GPS using satellite signals to get the same output. These will all benefit the UAV by providing data to keep the UAV on track to the right destination when it is in operation.

7.3.1. GPS Signal Simulation

When looking at how the navigation of the UAV could be set up, an article was found on the navigation and GPS link up for UAV security using Matlab/Simulink. The paper is 'Implementation of GPS Signals Simulation for UAV Security using Matlab/Simulink' (Viet et al., 2017). This report looks at the use of digital frequency for a GPS using various mathematical models and how the system uses multiple different signal inputs to generate a GPS location for a UAV. However, the simulated GPS signal in the paper is being used for spoofing and jamming. This gives an insight into how a GPS for a UAV could be done by adapting the system in the report. The control system for this GPS can be seen below in the figure 182. This system can be seen to have three different inputs to get the desired GPS signal.

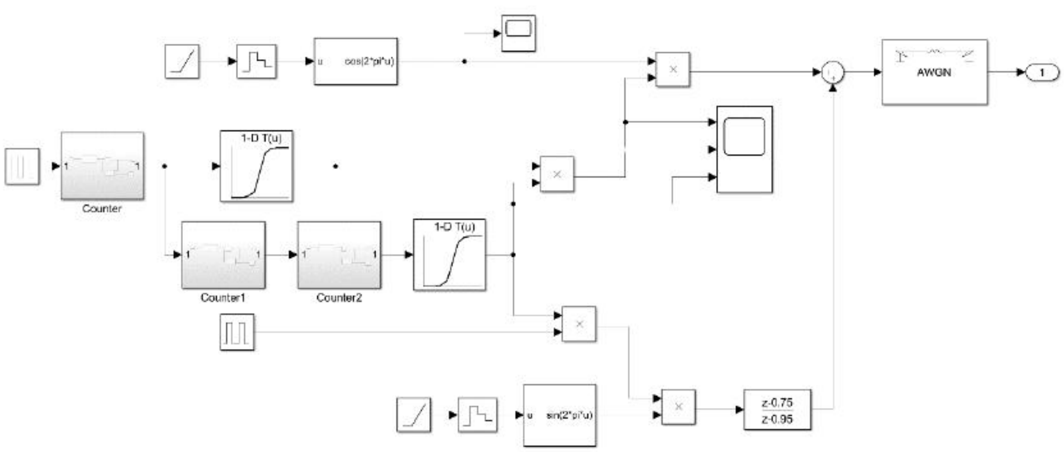

Figure 182: GPS Control System

Looking at the Simulink diagram above its shows that to simulate the GPS signal a couple of different inputs are needed. For the GPS signal to be simulated by this control system a C/A code and P(Y) code are needed and must be generated. In addition to these two codes, Noise is added to complete the signal of the GPS. The C/A and P(Y) codes are generated using an oscillation generator and arrays of data. The C/A code is also used to create the navigation data for the system. This shows that this system for navigation is very complex.

This system can be adapted to create a GPS which instead of jamming and spoofing can be used to get the locations of the UAV by changing the various inputs to receive signals from the UAV and satellites which can then be used to work out the exact location of the UAV at its given point. This would help with the creation of a subsystem that can be inputted into the UAV which will give out a valid GPS signal. This would help with the navigation of the UAV. Theoretically this would be possible however, due to the complexity of this type of system the adaptation would be very difficult and would overcomplicate the control system of the UAV.

7.3.2. Matlab Navigation

The navigation system for the UAV can also solely be run by Matlab using various present blocks within the Simulink software extension (MathWorks, n.d.). This control system is done using an INS (Internal Navigation System), which looks at the position orientation and velocity of a vehicle in relation to its last known location. This paired with a GPS sensor would be perfect for the navigation of the UAV. This sensor would allow the location to be known and help the drone with its automation.

7.4. UAV Automation

The challenge for his UAV is to make it completely automated so that it can provide natural disaster aid without needing any outside inputs after it is set out on its task. Automation can be done in many ways with the use of operating systems and sensors. The operating system would work as a brain and control all the different outputs of the drone allowing it to change and adapt to the situations and tasks it is set out to do. The sensors will allow the UAV to gain all the flight telemetry data to adapt. If the UAV utilised both the operating system and sensors in sync with each other the automation of the UAV would be achieved.

7.4.1. Sensors

With the UAV being tasked to help with the management of natural disasters it will need to adapt to anything which could occur. The use of sensors allows the UAV to detect everything going on while the UAV provides aid. This will allow the UAV to detect any changes in weather conditions and terrain conditions and allows for collision avoidance by changing the flight paths or take-off and landing destinations. The sensors will also allow for all the telemetry data needed by the control systems allowing for adaptation of flight. There are many sensors which can be implemented into the UAV’s design to help with generic flight assistance and automation.

7.4.1.1. Types of Sensors

There are many types of sensors which can be implemented in the UAV’s design to make it fully automated. These sensors will help with stability, navigation, collision avoidance, and many other tasks. The sensor which can be implemented would be LiDAR, Gyroscopes, Accelerometers, Magnetometers, Barometer, and distance sensors. The LiDAR emits light on a surface and uses what bounces back to create an image of what is around the UAV. The use of this would help with image processing for the UAV and help the UAV to survey the area it is flying over to find suitable areas to drop the aid packages during a natural disaster. The LiDAR can also help with collision avoidance which would be key as the UAV is automated. This would help the UAV to navigate through an area where there are skyscrapers and large buildings without colliding with the buildings. The LiDAR will also be key in the automated take-off and landing of the UAV.

The gyroscope is also key as it is used to keep the UAV stable. It will keep the UAV stable during flight, it will also help the UAV stabilise if any external forces are placed on it. This would be very important if the UAV was operating in a country where the weather changes drastically and there might be high winds which can affect the flight patterns of the UAV. The accelerometer will be used by the UAV to see its speed when in flight, this data can be used by many of the systems and is key for the UAV to be automated. It will help with the take-off, cruise and landing of the UAV. The magnetometer will be used on the UAV to measure the earth's magnetic field to help with the UAV orientation. This sensor would work alongside or part of the gyroscope to help the UAV with orientation.

Alongside all the sensors mentioned above, other sensors would be required for the UAV to do the various tasks. The LiDAR is an image processing sensor, as the UAV needs to drop packages and the use of a camera would allow the UAV to drop the packages on the desired target. Along with this basic distance sensor around the UAV would help it with collision avoidance and would be perfect when the UAV is taxing to take off. Also, the implementation of a radar would help the UAV with collision avoidance, take off, landing, and cruise. It will allow the UAV to know if anything is in its surroundings. The sensors which have been mentioned above will all be implemented into the UAV as they all help with the automation. They will all be used because the more sensors which are available will help reduce the chances of any error with the UAV automation.

7.4.1.2. Sensor Implementation

The sensors will be placed around the UAV so they are in the optimum place so they can work effectively and provide the correct data for the UAV to perform. The distance sensors will be placed around the UAV as this will provide better collision avoidance. The image processing sensors will be placed at the bottom and front of the UAV as the camera will need to see the drop-off point for the package and the LiDAR will work most effectively in the front of the UAV. The gyroscope and the various motion sensors will be placed near the centre of gravity of the UAV as this is where it is balanced and will help keep the UAV at equilibrium.

7.4.2. Operating Systems

The UAV will have many systems and sensors to deal with while in flight so the use of an operating system will allow the UAV to control all of them simultaneously, perform and adapt without any delays. This is because the operating system will deal with all the control systems and implement all the changes when they are needed automatically. The operating system will work like a brain for the UAV keeping control of everything.

7.4.2.1. ROS

The ROS (Robot Operating System) are operating systems which are specifically designed for unmanned vehicles and can be used to operate the control system of the UAV. They are set up to control all the different aspects of a UAV to make it all work in coherence. The system is made up of numerous modules also known as nodes which allow the ROS to control all the different aspects of the UAV. To control the UAV the ROS has a specific module - the MAVROS (MAVLink extendable communication node for the ROS with proxy for Ground Control Station) being the main one. This module has the MAVLink (Micro Air Vehicle Communication) protocol within it. These two modules are key as they allow communication between the UAV flight controller and the control system. These operating systems are compatible with many different types of publishing software making them versatile.

For the UAV the implementation of a ROS would be key as the UAV being designed has many different systems and sensors which need to be controlled all at once. The ROS would be a perfect way to combine the control systems and all the sensors for the UAV to be automated. This would mean one system will be controlling the whole UAV making its operation more fluid as the system would be running all through one system. The use of a ROS will also be perfect as it can communicate and work with Matlab/Simulink meaning the integration of the control system with the operating system will be straight forward.

7.4.2.2. Types of ROS

There are many different types of ROS which can be utilised as the operating system for the UAV. Matlab has its own built-in ROS system which uses inbuilt control systems within the software itself. However, there are many ROS which runs separate from Matlab but can be run using its code. FlyOS, Gazebo, and Rosbridge are all ROS which can be run using Matlab codes. FlyOS (Gupta et al., n.d.) is an advanced ROS system which can be used to control UAVs for many different applications, from ariel delivery to emergency response. This ROS works with most programming software from Python to C++. It can integrate a lot of different sensors into its system such as the LiDAR. This ROS is in line with what is needed for the operating system for the UAV however, as the control systems have been set up using Matlab this ROS is not compatible with the software making the combination of the two more difficult.

The next ROS mentioned is the Gazebo which is software which can simulate your entire design. It will take the CAD module, control system, and all the different sensors which are being used by the UAV and model it in 3D and simulate it. This gives a full simulation of how the UAV will perform with real physics active. To get it to work as a ROS, a separate package is needed which makes the software work and run as an operating system. This ROS would give the added benefit of allowing the testing of the UAV design and systems before production. This would allow the simulation of the response of the UAV when it is aiding during a natural disaster.

The Rosbridge ROS (Mace, n.d.) is the last operating system on the list, however, it is not a separate software, it is just a specific protocol which is run through a JSON (JavaScript Object Notation) (Neel. prakash, 2017) API (Application Programming Interface) (Mulesoft, 2018) through a web socket server. This allows the system to run the ROS without any specific software. This ROS also can work with using Matlab using TCP (Transmission Control Protocol), which means the operating system can talk and communicate with the control system and the various sensors needed for the UAV. This would make the control and automation of the UAV less complex as separate software is not needed.

7.4.2.3. Implementation of Operating System

The UAV needs an operating system which can communicate with the control system and all the sensors reliably and straightforwardly. For the UAV the FlyOS would not work as the control system is set up through Matlab which this ROS does not support. The Gazebo ROS would be a good operating system to use for the UAV. This is because it can work as a ROS as well as model and simulate the whole UAV. This would give a visual portrayal of how the UAV would function and work before it is constructed. However, this would be very complicated as to achieve this the Gazebo software would be needed, with its ROS tool. Also, the CAD model and the sensors would have to be inputted into the system to get the most out of this software. The Rosbridge ROS would be very good as the operating software for the UAV. It is very straightforward to set up as no extra software would be needed for it and it can work with Matlab, so it can communicate with the control system. This makes it the best suited as the operating system of the UAV.

7.4.3. AI Implementation and Decision Making

For the UAV to perform autonomously the use of AI (Artificial Intelligence) (BuiltIn, 2017) will help with its performance and decision making. AI is a range of smart machines which can perform like a human brain, making them able to execute the task that a human would normally be able to do. AI can be split into many types such as Reactive Machines, Theory of Mind and even Self Awareness. AI would help with the automation of the UAV as it can be used as an autopilot for the UAV. The AI would be set up so it can control all the aspects of the drone, so the thrust, control surface, sensors, navigation system, and all the features needed for natural disaster management. This would allow the drone to work autonomously and adapt to the situation which is presented to it. This large volume of controls being run by an AI has been looked at in the report 'AI-based adaptive control and design of autopilot system for nonlinear UAV'(YADAV and GAUR, 2014). This report looked at a UAV which has its speed and altitude controlled by AI to create an autopilot. The systems create in this report worked and provided autopilot using AI.

With the UAV being automated it will also have to deal with a lot of obstacles in the areas which have been affected by natural disasters and the AI can be used to deal with this. The University of Zurich has developed a UAV with an inbuilt AI which helps it fly through forests at 25 mph (Parsons, 2021). This was done by the creation of an algorithm that allows the UAV to navigate an area with a large number of obstacles using an autopilot. In the case of the UAV within this report, the AI would have to pilot through areas affected by natural disasters. This could mean large cities with skyscrapers or even areas which are remote and would have natural obstacles such as mountains or trees. With the use of AI and all the sensors within the UAV, the avoidance of such obstacles could be done, further strengthening its automation. Thus, the use and implementation of AI into the UAV would benefit the design and help with its automation.

7.5. Discussion

This section of the report set out to look at parts of the control system and how the UAV would be automated. The thrust control system was produced using the various equations used to calculate propulsion output when the UAV is in motion. The troubleshooting of this control system was also done to get the optimal output of the systems. The application of navigation has been assessed. Multiple types of systems were looked at to see the best way to set up navigation for the UAV. To automate the drone, different systems and sensors are needed alongside the control system. The various types of sensors needed to gain full automation were evaluated to see which would be the best fit for the UAV. The automation of the UAV can be simplified through the use of an operating system. For this application, the use of ROS would be best as they are optimised and have systems specifically for UAVs. Different types of ROS have been evaluated to see the best system for the UAV.

The thrust control system was created within this part of the report. The equations were used to create the control system and are the equations which were used for the sizing calculations in the previous parts of the report. When the control system was first set up the initial result obtained for the thrust output was 800 rpm. When the control system and results were then validated using the PID tuning, the result differed from the initial giving the optimal output of the system. This optimal value was 795 rpm which is not that different from the initial test. The change in the values is due to the losses experienced due to the heat and sound from the motor and other hardware used to output the thrust. This shows that the thrust subsystem is working and giving the correct output. Future development of this will be looked at in the future work section of the report.

The navigation of the UAV was also assessed in this section of the report. Two different navigation systems were looked at to see how they work and if they could be adapted to work within the UAV. The first is form a report 'Implementation of GPS Signals Simulation for UAV Security using Matlab/Simulink' (Viet et al., 2017). This used three different inputs to create a GPS signal for a drone which can be used to jam or spoof the location of a drone for security applications. This system used two different signals which were generated from data and sound to get the signal. This system could be adapted to just create a GPS signal for a UAV which can be used for its navigation. This system also gave an insight into how a Simulink control system can be set up for the navigation of the UAV. The second navigation system looked at was from MathWorks and was a navigation system created using the blocks and systems available within Simulink to create a working INS. This would give a simple solution of a navigation system for the drone and could be integrated into the UAV control system as a subsystem. This will allow it to work with the operating system making everything work in sync. Further development of the navigation system has been discussed within the future work section of the report.

The sensors which need to be implemented into the design of the UAV to aid with the automation have been looked at. All the sensors discussed within this section will be implemented into the UAV design to help with the generic operations of the drone and heavily influence its automation. There are multiple key sensors discussed within this section which are key to the UAV's main application of natural disaster management, such as the visual sensors needed for package delivery and the distance sensory needed for its automation to avoid collisions. Sensors like the LiDAR are key as they will help with the automation of take-off and landings, they will also help with collision avoidance. The use of sensors such as the radar will benefit the UAV's general flight as it will provide data for take-off, cruise, and landing and help with collision avoidance. This sensor is also key for all aircraft as it helps them see other craft flying in the area stopping the chance of in-air collisions. The development of how the sensors will further be worked on has also been discussed in the future work section of this section.

Another aspect of the UAV being assessed in this section of the report is the control systems and sensors which is also a key step towards the automation. For all the different sensors and control systems within the drone to work in sync the use of an operating system would be needed. This helps all these systems and sensors to work smoothly in coherence. For the UAV the operating systems known as ROS are used because they have inbuilt systems specifically for UAVs and make their operation smoother. Three different ROS have been looked at, FlyOS, Gazebo, and Rosbridge. Gazebo and Rosbridge would be best suited for the operating system for the UAV because they both are able to work alongside Matlab, and Simulink has been used for the control system of the UAV making their integration with each other smoother. However, the use of the Rosbridge ROS would be better as it is not a standalone software and is just a plugin which is run remotely which means that the automation using this would be straightforward. This is in comparison to Gazebo which is a standalone software which would complicate the integration. Gazebo does have its benefits as it is able to model and simulate the whole UAV by itself giving the opportunity of virtual testing, with the implementation of physics to see how the final UAV would perform. Further work on the operating system has been discussed as well within the future work section of the report.

The last aspect being observed within this section of the report is how the AI can be implemented and how it will help with the decision making of the UAV. The AI would be used to provide an autopilot system which would help the drone to traverse to the locations in need of help during a natural disaster. The report (YADAV and GAUR, 2014) looked at an AI autopilot system which controls most aspects of a UAV. This report gives an insight into how an autopilot system controlled by AI can be set up and could be adapted for the UAV within this project. The AI would be able to control all the systems the UAV needs to fly and control all the extra features needed for the natural disaster features. This would allow the UAV to be fully automated, achieving one of the main aims of the report. The AI can also further be enhanced by using an algorithm for collision avoidance. This would benefit the design of the UAV as when it is traversing an area which has been affected by a natural disaster it might need to fly through large cities or rural areas with large amounts of natural obstacles. Also the UAV might have to deal with falling rubble due to the natural disaster, this system would allow it to travel without being effected or damaged. The future work in regards to AI would be looking in its implementation into the design of the control system.

7.6. Future Work

To develop upon the work done within this section of the report, further testing of the thrust control system could first be considered. This would be done by changing the values of the parameters to see how the thrust would be affected. Also, the additional results can be taken and compared to see whether there is a way to improve what has already been done within this system, and then looking at how to reduce the losses of the thrust system within the UAV. Furthermore, more types of the navigation system can be investigated to get a better understanding of how they work. The knowledge from this section of the report and the future work can be taken and used to set up a functioning navigation system. This system will have to help the UAV know its location and allow the drone to travel to the location where the natural disaster is. To add to this a navigation subsystem should be set up and worked to integrate the navigation into the UAV so that it can be controlled by the operating system. The sensors being used by the drone should also be tested outside of a simulation to see their different tolerances and error margins. This would help refine the UAV systems making sure that the automation runs with the least number of errors possible. More advanced sensors could be also looked at which could be used for multiple purposes reducing the number of sensors needed for the UAV. This would help with weight reductions helping with the overall efficiency.

To develop the operating system of the UAV more types of ROS systems could be looked into see if there are systems which integrate into the overall design better. Also all the control systems and codes which have been developed throughout this report can be implemented into multiple varying ROS to see which work best and give the desired output needed to get the UAV full automated. This would involve integrating all the sensors into the ROS and can be used to further validate whether sensors work correctly for the UAV. How AI would be incorporated with the operating system could be another thing to be explored as it would increase the reliability and adaptability of the automated system for the UAV. Finally, more control systems which are needed for the UAV operation can be investigated. This would involve looking at the control system for actuators which will be needed with the UAV. These actuators would be used for the flap, slat and rudders needed for flight. Along with this the actuators will be needed for the morphing and cargo bay of the UAV and is a key part of the design. This would help get the design of the drone closer to the overall goal of an automated UAV for natural disaster management.

7.7. Conclusion

This section of the report set out to further develop the control system of the UAV and look at how the automation of it could be achieved. The development and creation of the thrust subsystem of the UAV was the first aspect looked at in this section. The control system was created using the equations used to calculate the thrust output of the UAV. This system was then validated using a PID controller to get the optimal output of this system. This was then used as a validation to see whether the system works correctly. The next aim was to look at different navigation systems to see how they worked and how they could be adapted to work for the UAV. Two navigation systems were looked at to see how they work. Both had aspects that could be adapted to be used within the UAV. These two systems also gave an insight into how a Simulink control system could be set up for navigation and be implemented into the UAV control system. The next two aims were to look at how the automation of the UAV would be done with the use of sensors, operating systems, and AI. The automation was split into two separate sections, one being the sensors and then the other being the operating system that could run the UAV. Multiple sensors were looked at which were needed just for the flight of the UAV and others specifically for its automation. All the sensors looked at in this section would be implemented as they all benefit the UAV's overall performance and help make the automation of the drone more reliable. The second part of the automation was looking at operating systems to run and control the drone. Three different ROSs were looked at to see if they could be used to control the UAV. These two were suitable to be the operating system as they worked with Matlab which was used to create the control system of the drone. The Gazebo ROS was more complex to set up as it had its own software to run. The Rosbridge software did not have its own software and was just a plug-in system which was easier to set up and was the one which would have been chosen for the operating system of the UAV. The final part of the automation was to see how AI could be implemented. The use of AI would provide an autopilot and could also control all the UAV features alongside the operating systems. It would help the drone to adapt to the situations it is in and would further strengthen the automation of the drone. The final objective of this section was to look at how all the findings would be implemented into the UAV’s design. The findings within this section will be implemented into the final design of the UAV as they are a step toward the final goal of the project - to design an automated UAV for natural disaster management.

8.Conclusion

To summarise, the main aim of this project was to create an autonomous UAV capable of delivering aid to areas effected by natural disasters. This main aim was achieved by splitig the project into four different areas of research, topology optimisation, aerodynamics and morphing, propulsion system and control system. All key findings from each category can be detailed below.

Firstly, the topology optimisation was conducted on the wing and the wing ribs using Altair Hyperwork and Optistruct. The optimisation used the minimise compliance methodology, to remove elements that do not contribute to supporting the load path. The Optimisation results were then analysed and interpreted to create a valid and optimised design for the internal structure of the wing.

Secondly, the aerodynamics and morphing section aimed to investigate the flow behaviour at cruise condition to find patterns and interactions present to optimise the aerofoil used for the wing design. The optimisation was completed on XFLR5 and CFD software. Another feature of this UAV was its morphing wingtips and the dynamic response and overall effect of the morphing was analysed by creating a simulation on Matlab Simulink. To support the design decisions made from the simulations, static and model analysis was performed to analyse the structure under applied loads to ensure the integrity of the structure when in flight, and to determine the natural frequency of the structure at different modes and thus, optimise the overall design of the wing. It was found that the NACA 4412 was the most effective aerofoil, the dynamic response of the morphing wingtip provided stable results from the angular and linear velocity. The natural frequency analysis found that mode 5 experience the largest deformation out of all the simulations completed at the natural frequency of 37.924 Hz.

For the propulsion system, lithium polymer batteries and brushless DC motors were determined to be best suited for the UAV. The propellers used during cruise were designed in two different ways, with the optimised design utilising stall control to determine the twist angle distribution. Both designs were analysed using *JBLADE* and it was concluded that the optimised propeller design reached a peak efficiency of 0.93, compared to the peak of 0.82 shown for the initial design. The peak C_T for the optimised design was 0.85 when compared to the initial design's 0.65, showing better thrust production. The number of blades did not have an effect performance and thus the two-bladed optimised propeller design is the one chosen for cruise.

Additionally, to improve aerodynamic efficiency, the VTOL propellers were designed with a folding mechanism on SolidWorks. Numerical optimisation and simulation were used to optimise the VTOL propellers, with Froude's Theory and *Ansys Fluent* being utilised to achieve optimisation. The theoretical rotational speed was $650\ rpm$, with the *Ansys* simulation displaying an optimal rotational speed of $700\ rmp$, which shows a percentage difference of 7.14%.

Finally, the dynamic equations and thrust equations were used to model control systems in Matlab and Simulink. The systems functioned properly and were proved to work with PID tuning. It was discovered that introducing the PID controller assisted to successfully modify the system's reaction, allowing the control systems to be included into the UAV model in the future. The simulations without PID controllers produced intriguing results on the stability of the current system. The UAV is currently not stable in x-axis acceleration, which could be considered in the future when a model is generated. Overall, the Simulink control system results were successful since the response could be altered effectively such that the UAV could stabilise itself around a reference value. This was because a PID controller was implemented and tuned.

9. References

A Y N Sofla, Meguid, S.A., Tan, K.T. and Yeo, W.K. (2010). *Shape morphing of aircraft wing: Status and challenges*. [online] ResearchGate. Available at: https://www.researchgate.net/publication/248465102_Shape_morphing_of_aircraft_wing_Status_and_challenges [Accessed 23 Apr. 2022].

A40-14L V4 14-Pole kv355. (2022). *A40-14L V4 14-Pole kv355 | A40-14-Pole | Hacker A40 | Hacker Outrunner | Brushless Motors*. [online] Hacker-motor-shop.com. Available at: https://www.hacker-motor-shop.com/Brushless-Motors/Hacker-Outrunner/Hacker-A40/A40-14-Pole/A40-14L-V4-14-Pole-kv355.htm?shop=hacker_e&SessionId=&a=article&ProdNr=33726616&p=310 [Accessed 10 May 2022].

Aabid, A., Zakuan, M., Khan, S. and Ibrahim, Y. (2021). *Structural analysis of three-dimensional wings using finite element method*. [online] Available at: https://link.springer.com/content/pdf/10.1007/s42401-021-00114-w.pdf [Accessed 10 May 2022].

Abbott I.H. and Doenhoff A.E.V. (1959). 'Theory of Wing Sections,' Dover... [online] ResearchGate. Available at: https://www.researchgate.net/figure/Abbott-IH-and-Doenhoff-AEV-1959-Theory-of-Wing-Sections-Dover-Publications-Inc_fig2_266095940 [Accessed 11 May 2022].

Abdul, N. and Mousa, R. (2014). Proposed Modification to Increase Main Swept Back Wing Efficiency for Aircraft Aermacchi Siai S211 المقترح التعديل كفاءة لسيادة ال لطائرة الخلف الى المتراجع جناح : Aermacchi Siai S211. Journal of Engineering, [online] 20. Available at .https://www.iasj.net/iasj/download/533dc7b4629e7af7. [Accessed 12 May 2022]

Abedinpour, S. and Shenai, K. (2011). Insulated Gate Bipolar Transistor. *Power Electronics Handbook*, [online] pp.73–90. Available at: https://www.sciencedirect.com/science/article/pii/B9780123820365000057 [Accessed 30 Apr. 2022].

Abedinpour, S. Ph.D. and Shenai, K. Ph.D, Rashid, M. (2011). *POWER ELECTRONICS HANDBOOK*. 3rd ed. Butterworth-Heinemann, pp.73-90.

Ackroyd, J. (2013). The Spitfire Wing Planform: A Suggestion. [online] Available at: https://www.aerosociety.com/media/4843/the-spitfire-wing-planform-a-suggestion.pdf. [Accessed 12 May 2022].

Ahmad., Bici, M. and Campana, F., 2021. Guidelines for Topology Optimization as Concept Design Tool and Their Application for the Mechanical Design of the Inner Frame to Support an Ancient Bronze Statue. *Applied Sciences*, 11(17), p.7834.

Airfoiltools.com. (2022). *NACA 0010 (naca0010-il)*. [online] Available at: http://airfoiltools.com/airfoil/details?airfoil=naca0010-il [Accessed 18 Apr. 2022].

Airfoiltools.com. (2022). *NACA 4412 (naca4412-il)*. [online] Airfoiltools.com. Available at: <http://airfoiltools.com/airfoil/details?airfoil=naca4412-il> [Accessed 11 May 2022].

Airfoiltools.com. (2022). *NACA 6412 (naca6412-il)*. [online] Available at: http://airfoiltools.com/airfoil/details?airfoil=naca6412-il [Accessed 18 Apr. 2022].

Ajaj, R.M., Michael Ian Friswell, Saavedra, E.I. and Isikveren, A.T. (2012). *Span Morphing: A Conceptual Design Study*. [online] ResearchGate. Available at: https://www.researchgate.net/publication/268478785_Span_Morphing_A_Conceptual_Design_Study [Accessed 25 Apr. 2022].

Alejandro, E., Hugo, V. and Darío Rodríguez. (2018). Parametric modelling for aerodynamic assessment of a fixed wing UAV implemented for Site Specific Management. [online] ResearchGate. Available at: https://www.researchgate.net/publication/322311195_Parametric_modelling_for_aerodynamic_assessment_of_a_fixed_wing_UAV_implemented_for_Site_Specific_Management [Accessed 11 May 2022].

All About CFD... (2017). Understanding The Spalart-Allmaras Turbulence Model. [online] Available at: https://cfdisrael.blog/2017/04/26/understanding-the-spalart-allmaras-model/ [Accessed 12 May 2022].

Altair Engineering Inc. (2011). *Application of Topology, Sizing and Shape Optimization Method to Optimal Design of Aircraft Components*. Bristol, pp.1-11.

Ameduri, S. and Concilio, A. (2020). Morphing wings review: aims, challenges, and current open issues of a technology. *Proceedings of the Institution of Mechanical Engineers, Part C: Journal of Mechanical Engineering Science*, [online] p.095440622094442. Available at: <https://journals.sagepub.com/doi/10.1177/0954406220944423> [Accessed 27 April 2022].

Anderson, J., & John, D. (2001). Fundamentals of Aerodynamics, 3rd Edition. New York: McGraw-Hill.

Andersson, O. and Wilkman, D. (2020). *Propulsion system for a small unmanned aerial vehicle*. [online] Available at: https://www.diva-portal.org/smash/get/diva2:1438252/FULLTEXT01.pdf [Accessed 12 Jan. 2022].

Ansys. (2021). *Modal Analysis | Ansys Innovation Courses*. [online] ANSYS Innovation Courses. Available at: https://courses.ansys.com/index.php/courses/modal-analysis/ [Accessed 12 May 2022].

Ansys. (2022). *Governing Equations for Modal Analysis | Ansys Courses*. [online] ANSYS Innovation Courses. Available at: https://courses.ansys.com/index.php/courses/modal-analysis/lessons/governing-equations-of-modal-analysis-lesson-2/ [Accessed 10 May 2022].

Arduino. (n.d.). *Arduino Sensor Kit - Base*. [online] Arduino Official Store. Available at: https://store.arduino.cc/products/arduino-sensor-kit-base?_gl=1 [Accessed 10 May 2022].

Arvind, P. (2013). CFD ANALYSIS OF STATIC PRESSURE AND DYNAMIC PRESSURE FOR NACA 4412 .

Åström, K.J. and Hägglund, T. (2006). *Advanced PID Control - 1.3.1 On-off Control*. [online] International Society of Automation (ISA). Available at: https://app.knovel.com/hotlink/pdf/id:kt007W3EK2/advanced-pid-control/on-off-control.

Atmeh, G.M., Hasan, Z. and Darwish, F. (2010). *Design and Stress Analysis of a General Aviation Aircraft Wing*. [online] Available at: https://www.comsol.com/paper/download/114853/atmeh_paper.pdf.

Austin, F., Rossi, M.J., Van Nostrand, W. and Knowles, G. (1994). Static Shape Control for Adaptive Wings. *AIAA Journal*, 32(9).

Barbarino, S., Bilgen, O., Ajaj, R.M., Friswell, M.I. and Inman, D.J. (2011). A Review of Morphing Aircraft. Journal of Intelligent Material Systems and Structures, [online] 22(9), pp.823–877. Available at:https://journals.sagepub.com/doi/abs/10.1177/1045389X11414084?casa_token=KYmaciWvo_UAAAAA%3AMTkyIGHB6iH6blcG7SOY1ovaH-QOUrhqRcZKXRo0u9O_suaCuLuQQo2RJNh54iJ88HdnlGudKEaV& [Accessed 11 May. 2022].

Barbarino, S., Bilgen, O., Ajaj, R.M., Friswell, M.I. and Inman, D.J. (2011). A Review of Morphing Aircraft. *Journal of Intelligent Material Systems and Structures*, [online] 22(9), pp.823–877. doi:10.1177/1045389x11414084.

Bendsøe, M. and Sigmund, O. (2003). *Topology optimization*. Berlin: Springer.

Bil, C., Massey, K. and Abdullah, E.J. (2013). Wing morphing control with shape memory alloy actuators. Journal of Intelligent Material Systems and Structures, [online] 24(7), pp.879–898. doi:10.1177/1045389x12471866.

Bontoft, E. and Toropov, V. (2018). Topology Optimisation of Multi-Element Wingtip Devices. *2018 AIAA/ASCE/AHS/ASC Structures, Structural Dynamics, and Materials Conference*,.

Bristeau, P.-J., Callou, F., Vissière, D. and Petit, N. (2011). The Navigation and Control technology inside the AR.Drone micro UAV. *IFAC Proceedings Volumes*, 44(1), pp.1477–1484. doi:10.3182/20110828-6-it-1002.02327.

Bronz, M., Moschetta, J.M. and Hattenberger, G. (2012). *Multi-Point Optimisation of a Propulsion Set as Applied to a Multi-Tasking MAV*. [online] ResearchGate. Available at: https://www.researchgate.net/publication/281946347_Multi-Point_Optimisation_of_a_Propulsion_Set_as_Applied_to_a_Multi-Tasking_MAV [Accessed 16 Apr. 2022]

Brunton, S.L. and Rowley, C.W. (2013). Empirical state-space representations for Theodorsen's lift model. *Journal of Fluids and Structures*, [online] 38, pp.174–186. doi:10.1016/j.jfluidstructs.2012.10.005.

BuiltIn. (2017). *What Is Artificial Intelligence? How Does AI Work? | Built in*. [online] Builtin. Available at: https://builtin.com/artificial-intelligence [Accessed 22 Apr. 2022].

Cam.ac.uk. (2022). *Froude's Propeller Theory*. [online] Available at: http://www-mdp.eng.cam.ac.uk/web/library/enginfo/aerothermal_dvd_only/aero/fprops/cvanalysis/node50.html [Accessed 22 Apr. 2022].

Carter, B. (2014). *Op Amps for Everyone*. 4th ed. pp.7-17.

Chang, P.K. (1970). Characteristics of Separated Flows. Separation of Flow, [online] pp.272–335. doi:10.1016/b978-0-08-013441-3.50011-3.

Christensen, J., Bastien, C. and Blundell, M. (2015). *Topology Optimisation of Structures Exposed to Large (non-linear) Deformations*. [online] Coventry: Research Gate. Available at: <https://www.researchgate.net/publication/284419329_Topology_Optimisation_of_Structures_Exposed_to_Large_non-linear_Deformations> [Accessed 11 May 2022].

Concilio, A., Ignazio Dimino, Lecce, L. and Pecora, R. (2018). *Morphing wing technologies : large commercial aircraft and civil helicopters*. [online] Oxford ; Cambridge, Ma: Butterworth-Heinemann, An Imprint Of Elsevier. Available at: https://app.knovel.com/hotlink/pdf/id:kt011FXQD1/morphing-wing-technologies/ [Accessed 3 May 2022].

Cook, K.L.B. (2007). The silent force multiplier: The history and role of UAVs in warfare. In: *2007 IEEE Aerospace Conference*. [online] pp.1–7. doi:10.1109/AERO.2007.352737.

Corda, S. (1958). Introduction to aerospace engineering with a flight test perspective

Crawford, C. (2016). *6 Awesome Ways Drones Are Being Used Today*. [online] Lifehack. Available at: https://www.lifehack.org/403615/6-awesome-ways-drones-are-being-used-today [Accessed Apr. 12AD].

Crivellini, A., D'Alessandro, V., Di Benedetto, D., Montelpare, S. and Ricci, R. (2014). Study of laminar separation bubble on low Reynolds number operating airfoils: RANS modelling by means of an high-accuracy solver and experimental verification. Journal of Physics:

Conference Series, [online] 501, p.012024. doi:10.1088/1742-6596/501/1/012024. [Accessed 11 May 2022].

Daly, S. (2018). *Fighting fires and saving elephants: How 12 companies are using the AI drone to solve big problems*. [online] Built In. Available at: https://builtin.com/artificial-intelligence/drones-ai-companies [Accessed 5 Apr. 2022].

Dantsker, O., Caccamo, M., Deters, R.W. and Selig, M.S. (2020). Performance Testing of Aero-Naut CAM Folding Propellers. *AIAA AVIATION 2020 FORUM*. doi:10.2514/6.2020-2762.

Das, S.K. and Roy, S. (2018). *Finite element analysis of aircraft wing using carbon fiber reinforced polymer and glass fiber reinforced polymer*. [online] Available at: https://iopscience.iop.org/article/10.1088/1757-899X/402/1/012077/pdf#:~:text=Static%20structural%20analysis%20of%20the,the%20noise%20and%20avoid%20vibration. [Accessed 10 May 2022].

Dassault Systèmes. (2020). *SIMP Method for Topology Optimization*. Topology Study. [online] Vélizy-Villacoublay: Dassault Systèmes. Available at: <https://help.solidworks.com/2019/English/SolidWorks/cworks/c_simp_method_topology.htm> [Accessed 29 April 2022].

Detrick, M. and Washington, G. (2012). *Modeling and Design of a Morphing Wing for Micro Unmanned Aerial Vehicles via Active Twist | 48th AIAA/ASME/ASCE/AHS/ASC Structures, Structural Dynamics, and Materials Conference*. [online] Structures, Structural Dynamics, and Materials and Co-located Conferences. Available at: https://arc.aiaa.org/doi/abs/10.2514/6.2007-1788 [Accessed 27 Apr. 2022].

Devos, A., Smaulel Malik Ebeid, E. and Manooonpong, P. (2018). Development of Autonomous Drones for Adaptive Obstacle Avoidance in Real World Environments. In: *2018 21st Euromicro Conference on Digital System Design (DSD) Authors:* University of South Denmark.

Dongli, M., Zhao Yanping, Qiao Yuhang and Guanxiong, L. (2015). Effects of relative thickness on aerodynamic characteristics of airfoil at a low Reynolds number. [online] ResearchGate. Available at: https://www.researchgate.net/publication/279069359_Effects_of_relative_thickness_on_aerodynamic_characteristics_of_airfoil_at_a_low_Reynolds_number [Accessed 12 May 2022].

El Khchine, Y. and Sriti, M. (2016). *Performance prediction of a horizontal axis wind turbine using BEM and CFD methods*. [online] ResearchGate. Available at: https://www.researchgate.net/publication/298431164_Performance_prediction_of_a_horizontal_axis_wind_turbine_using_BEM_and_CFD_methods [Accessed 23 Apr. 2022].

Elelwi, M., Botez, R. and Dao, T. (2021). Structural Sizing and Topology Optimization Based on Weight Minimization of a Variable Tapered Span-Morphing Wing for Aerodynamic Performance Improvements. *Biomimetics*, 6(4), p.55.

Enea.it. (2022). ANSYS FLUENT 12.0 User's Guide - 26.1 Overview of Using the Solver. [online] Available at: https://www.afs.enea.it/project/neptunius/docs/fluent/html/ug/node776.htm [Accessed 12 May 2022].

Enea.it. (2022). ANSYS FLUENT 12.0 User's Guide - 26.4.1 Changing the Courant Number. [online] Available at: https://www.afs.enea.it/project/neptunius/docs/fluent/html/ug/node789.htm [Accessed 12 May 2022].

Etches, J., Potter, K., Bond, I.P. and Weaver, P.M. (2008). Morphing skins. *Aeronautical Journal*.

Federal Aviation Administration. (2008). *FEDERAL AVIATION REGULATIONS: Sec. 25.303 — Factor of safety.*. [online] Washington: US Congress. Available at: <https://www.risingup.com/fars/info/part25-303-FAR.shtml#:~:text=25.303%20%E2%80%94%20Factor%20of%20safety.,be%20applied%20unless%20otherwise%20specified.> [Accessed 5 May 2022].

Fehrm, B. (2017). Aircraft drag reduction. Leeham News and Analysis.

Findlay, S.J. and Harrison, N.D. (2002). Why aircraft fail. Materials Today, 5(11), pp.18–25.

Friswell, M. and Inman, D. (2006). *Morphing Concepts for UAVs Morphing Concepts for UAVs*. [online] Available at: http://michael.friswell.com/PDF_Files/C205.pdf.

Galantai, V. (2010). Design and Analysis of Morphing Wing for Unmanned Aerial Vehicles. [online] Available at: https://tspace.library.utoronto.ca/bitstream/1807/33722/3/Galantai_Vlad_P_201011_MASc_thesis.pdf.

Gamboa, P., Aleixo, P., Lobo, J. and Suleman, A. (2007). *Design and Testing of a Morphing Wing for an Experimental UAV.* [online] ResearchGate. Available at: https://www.researchgate.net/publication/235211095_Design_and_Testing_of_a_Morphing_Wing_for_an_Experimental_UAV [Accessed 23 Apr. 2022].

Geometriccae Engineering Services. (2018). AIRFOIL TERMINOLOGY - Geometriccae Engineering Services - Medium. [online] Medium. Available at: https://geometriccae.medium.com/airfoil-terminology-423c79d5ed8 [Accessed 11 May 2022].

Gupta, N., Gala, K., Dhula, D., Das, S. and Negi, A. (n.d.). *FlytOS: Operating System for Drones*. [online] flytbase.com. Available at: https://flytbase.com/flytos/ [Accessed 22 Apr. 2022].

Hanleyinnovations.com. (2014). UAV Design Calculations. [online] Available at: https://www.hanleyinnovations.com/uavdesign.html [Accessed 11 May 2022].

Harish, A. (2016). *What Is Modal Analysis and Why Is It Necessary?* [online] SimScale. Available at: https://www.simscale.com/blog/2016/12/what-is-modal-analysis/ [Accessed 12 May 2022].

Hartman, E. and Biermann, D. (1938). The Aerodynamic Characteristics of Full-Scale Propellers Having 2, 3, and 4 Blades of Clark Y and R.A.F. 6 Aerofoil Sections. *Core.ac.uk*. [online] Available at: https://core.ac.uk/reader/42794680 [Accessed 23 Jan. 2022].

Hee, K.H. (2012). *DESIGNING MORPHING AIRFOILS FOR IMPROVING THE AERODYNAMIC CHARACTERISTICS*. [online] Available at: https://core.ac.uk/download/48655936.pdf [Accessed 25 Apr. 2022].

Heinzen, S., Hall Jr, C. and Gopalarathnam, A. (2015). *Development and Testing of a Passive Variable-Pitch Propeller | Journal of Aircraft*. [online] Journal of Aircraft. Available at: https://arc.aiaa.org/doi/abs/10.2514/1.C032595?casa_token=o0VmnCR6QEkAAAAA%3A7bRtkgBjVIOmjqp3Ffpb3kkhbCgHpJVLnzGgRL5HVil9dgLkQoH7DdDvejRjHjj2thqL7zKS3Rjv&journalCode=ja [Accessed 19 Jan. 2022].

Hicks, R. and Henne, P. (1978). Wing Design by Numerical Optimization. *Journal of Aircraft*, [online] 15(7), pp.407-412. Available at: <https://arc.aiaa.org/doi/10.2514/3.58379> [Accessed 27 April 2022].

Hildmann, H. and Kovacs, E. (2019). Review: Using Unmanned Aerial Vehicles (UAVs) as Mobile Sensing Platforms (MSPs) for Disaster Response, Civil Security and Public Safety. *Drones*, 3(3), p.59. doi:10.3390/drones3030059.

Hoang, V. (2015). *SIMPLIFIED DESIGN OF A COMMERCIAL AIRCRAFT WING MADE OF CARBON FIBER*. [online] Madrid: DEPARTMENT OF CONTINUUM MECHANICS AND STRUCTURAL ANALYSIS. Available at: <https://core.ac.uk/download/pdf/44311196.pdf> [Accessed 27 April 2022].

Hsu, J., Koenig, N. and Colemen, D. (2019). *Simulate before You Build*. [online] Gazebo. Available at: https://gazebosim.org/features [Accessed 27 Apr. 2022].

Hun, R., Tiwari, A. and Sinha, N.K. (2016). Design and Simulation of Autopilot Control System for Stratospheric Airship. *IFAC-PapersOnLine*, 49(1), pp.712–717. doi:10.1016/j.ifacol.2016.03.140.

Hyperwork, A. (2022). *HyperWorks Solvers*. [online] 2017.help.altair.com. Available at: <https://2017.help.altair.com/2017/hwsolvers/hwsolvers.htm?minimum_member_size_control_.htm> [Accessed 3 May 2022].

Ibrahim, H G. Yüksel, E, Mehmet, H D. (2018) Effects of Taper Ratio on Aircraft Wing Aerodynamic Parameters: A Comperative Study [online] Available at: https://dergipark.org.tr/tr/download/article-file/629766 [Accessed 12 May 2022].

Illinois.edu. (2015). *UIUC Propeller Data Site*. [online] Available at: https://m-selig.ae.illinois.edu/props/propDB.html [Accessed 1 May 2022].

International Medical Corps (2021). *2021 Haiti Earthquake Situation Report #2* - September 10, 2021 - Haiti. [online] ReliefWeb. Available at: https://reliefweb.int/report/haiti/2021-haiti-earthquake-situation-report-2-september-10-2021 [Accessed 17 Apr. 2022].

Jain, S., Sitaram, N. and Krishnaswamy, S. (2015). Effect of Reynolds Number on Aerodynamics of Airfoil with Gurney Flap. International Journal of Rotating Machinery, [online] 2015, pp.1–10. doi:10.1155/2015/628632. [Accessed 12 May 2022].

Jameco (n.d.). *How it Works: The Drone in Flight - Gyroscopes, Sensors and Computerized Positioning Systems*. [online] www.jameco.com. Available at: https://www.jameco.com/Jameco/workshop/ProductNews/howitworks-drone.html#:~:text=A%20gyroscope%20measures%20the%20rate [Accessed 14 May 2022].

Joom.com. (2022). *Gemfan 9047 Carbon Nylon CW/CCW Propeller For DJI RC Multirotor-buy at a low prices on Joom e-commerce platform*. [online] Available at: https://www.joom.com/en/products/1491389977527638584-13-1-26312-921861799 [Accessed 01 May 2022].

Jose Rodolfo Chreim. (2016). EXTENDED LIFTING-LINE THEORY FOR VISCOUS EFFECTS. [online] ResearchGate. Available at: https://www.researchgate.net/publication/341668932_EXTENDED_LIFTING-LINE_THEORY_FOR_VISCOUS_EFFECTS [Accessed 11 May 2022].

Juan Carlos Gomez and Garcia, E. (2011). *Morphing unmanned aerial vehicles*. [online] ResearchGate. Available at: https://www.researchgate.net/publication/231152758_Morphing_unmanned_aerial_vehicles [Accessed 23 Apr. 2022].

Kammermann, J., Bolvashenkov, I., Tran, K., Herzog, H. and Frenkel, I. (2020). Feasibility Study for a Full-Electric Aircraft Considering Weight, Volume, and Reliability Requirements. *2020 International Conference on Electrotechnical Complexes and Systems (ICOECS)*, [online] Available at: <https://ieeexplore.ieee.org/stamp/stamp.jsp?tp=&arnumber=9278461> [Accessed 27 April 2022].

Karabulut, B. S. (2021). *What Is Modal Analysis and How is It Interpreted*. [online] Mechead.com.

Available at: https://www.mechead.com/ansys-modal-analysis/ [Accessed 10 May 2022].

Karl Johan Astrom and Tore Hägglund (2006). *Advanced PID control*. [online] Research Triangle Park, N.C.: Isa. Available at: https://app.knovel.com/hotlink/pdf/id:kt007W3EH2/advanced-pid-control/introduction- [Accessed 3 May 2022].

Khan, A.M., Adams, D.O., Dayal, V. and Vogel, J. (2000). *Effects of Bend–Twist Coupling on Composite Propeller Performance*. [online] ResearchGate. Available at: https://www.researchgate.net/publication/263192930_Effects_of_Bend-Twist_Coupling_on_Composite_Propeller_Performance [Accessed 02 May 2022].

Kidane, B. S. (2019). *Aeroelastic Model Development for Folding Winglet Design using Aerodynamic Actuation*. [online] ResearchGate. Available at: https://www.researchgate.net/publication/328902306_Aeroelastic_Model_Development_for_Folding_Winglet_Design_using_Aerodynamic_Actuation [Accessed 21 Apr. 2022].

Kidane, B. S. and Troiani, E. (2020). *Static Aeroelastic Beam Model Development for Folding Winglet Design*. [online] ResearchGate. Available at: https://www.researchgate.net/publication/343232904_Static_Aeroelastic_Beam_Model_Development_for_Folding_Winglet_Design [Accessed 24 Apr. 2022].

Kim, H.D., Perry, A.T. and Ansell, P.J. (2018). A Review of Distributed Electric Propulsion Concepts for Air Vehicle Technology. *2018 AIAA/IEEE Electric Aircraft Technologies Symposium*. [online] Available at: https://www1.grc.nasa.gov/wp-content/uploads/2018EATS-Review-of-DEP-Hyun-D.-6.2018-4998.pdf.

Kundu, A. (2010). *Aircraft Design*. Cambridge: Cambridge University Press (Cambridge Aerospace Series), p.356.

Ledoux, J., Riffo, S. and Salomon, J. (2021). Analysis of the Blade Element Momentum Theory. *SIAM Journal on Applied Mathematics*, [online] 81(6), pp.2596–2621. doi:10.1137/20m133542x.

Li, D., Zhao, S., Da Ronch, A., Xiang, J., Drofelnik, J., Li, Y., Zhang, L., Wu, Y., Kintscher, M., Monner, H.P., Rudenko, A., Guo, S., Yin, W., Kirn, J., Storm, S. and Breuker, R.D. (2018). A review of modelling and analysis of morphing wings. Progress in Aerospace Sciences, [online] 100, pp.46–62. doi:10.1016/j.paerosci.2018.06.002.

Litherland, B.L., Patterson, M.D., Derlaga, J.M. and Borer, N.K. (2017). A Method for Designing Conforming Folding Propellers. *17th AIAA Aviation Technology, Integration, and Operations Conference*. doi:10.2514/6.2017-3781.

Liu, S., Li, Q., Liu, J., Chen, W. and Zhang, Y. (2018). A Realization Method for Transforming a Topology Optimization Design into Additive Manufacturing Structures. *Engineering*, [online] 4(2), pp.277-285. Available:https://reader.elsevier.com/reader/sd/pii/S2095809917302059?token=CC1568AE3F8BE576F8EA9E4347CFD8F61CE457627E3E439107F4C2C3FA19558F4CF36C10E6EC6D0F13104631C0DE329E&originRegion=eu-west-1&originCreation=20220514131035

Livinus, U.T., Zagorodna, N., Tamunomiebaka, D., Friz and Longinus, U.E. (2018). Effects of a PID Controller in Closed Loop Feedback System. *International Journal of Scientific & Engineering Research*, [online] 9(4). Available at: https://www.ijser.org/researchpaper/Effects-of-a-PID-Controller-in-Closed-Loop-Feedback-System.pdf [Accessed 10 May 2022].

Mace, J. (n.d.). *rosbridge_suite - ROS Wiki*. [online] wiki.ros.org. Available at: http://wiki.ros.org/rosbridge_suite [Accessed 24 Apr. 2022].

Martinez, I. (2014). *Propellers*., lecture notes, The Technical University of Madrid, delivered 3 August 2014.

Massachusetts Institute of Technology. (2013). *Topology Optimisation: Material Interpolation*. [online] Cambridge: Massachusetts Institute of Technology. Available at: <https://abaqus-docs.mit.edu/2017/English/TsoUserMap/tso-c-user-TopOpt-Sett-Sensi-MatInt.htm> [Accessed 29 April 2022].

Mathworks. (n.d.). *Arduino Support from MATLAB*. [online] uk.mathworks.com. Available at: https://uk.mathworks.com/hardware-support/arduino-matlab.html?s_tid=srchtitle [Accessed 10 May 2022].

MathWorks. (n.d.). *Inertial Navigation System*. [online] uk.mathworks.com. Available at: https://uk.mathworks.com/discovery/inertial-navigation-system.html [Accessed 16 Apr. 2022].

Mathworks. (n.d.). *Raspberry Pi Support from Simulink*. [online] uk.mathworks.com. Available at: https://uk.mathworks.com/hardware-support/raspberry-pi-simulink.html.

Mathworks. (n.d.). *SoC FPGA Development*. [online] uk.mathworks.com. Available at: https://uk.mathworks.com/discovery/soc-fpga.html [Accessed 10 May 2022].

Megson, T. (2017). *Aircraft structures for engineering students*. 6th ed. Oxford: Elsevier.

Megson, T.H. (1990). Aircraft structures for engineering students 4th edition. Amsterdam Elsevier.

Mesh, H. (2022). *Hexahedral Mesh vs. Tetrahedral: Comparing High-Quality Meshing*. [online] Cadence.com. Available at: https://resources.system-analysis.cadence.com/blog/msa2022-hexahedral-mesh-vs-tetrahedral-comparing-high-quality-meshing [Accessed 12 May 2022].

Messina, M. (2018). *SHM Open Database*. [online] shm.ing.unibo.it. Available at: http://shm.ing.unibo.it/.

Mh-aerotools.de. (2018). *JavaProp - the Applet*. [online] Available at: https://www.mh-aerotools.de/airfoils/jp_validation.htm [Accessed 02 May 2022].

Mills, J. and Ajaj, R. (2017). Flight Dynamics and Control Using Folding Wingtips: An Experimental Study. *Aerospace*, 4(2), p.19. doi:10.3390/aerospace4020019.

Mills, J. and Ajaj, R. (2017). Flight Dynamics and Control Using Folding Wingtips: An Experimental Study. *Aerospace*, 4(2), p.19. doi:10.3390/aerospace4020019.

Milne-Thomson, L. M. (1973). Theoretical aerodynamics, 4th Editions. New York: Dover Publications.

Mit.edu. (2022). *11.7 Performance of Propellers*. [online] Available at: https://web.mit.edu/16.unified/www/FALL/thermodynamics/notes/node86.html [Accessed 1 May 2022].

Muelaner, J. (2013). *UAV 4th Year Project*. [ebook] Available at: <https://projects.exeter.ac.uk/uav/j_muelaner> [Accessed 29 January 2022].

Mulesoft. (2018). *What is an API? (Application Programming Interface)*. [online] MuleSoft. Available at: https://www.mulesoft.com/resources/api/what-is-an-api [Accessed 18 Mar. 2022].

Munawar, H.S., Hammad, A.W.A. and Waller, S.T. (2022). Disaster Region Coverage Using Drones: Maximum Area Coverage and Minimum Resource Utilisation. *Drones*, 6(4), p.96. doi:10.3390/drones6040096.

NASA. (2009). *Modern Lift Equation*. Glenn Research Centre. [online] Washington, D.C.: NASA. Available at: <https://wright.nasa.gov/airplane/lifteq.html> [Accessed 5 May 2022].

Nasa.gov. (2021). *The Lift Equation*. [online] Available at: https://www.grc.nasa.gov/www/k-12/airplane/lifteq.html [Accessed 6 May 2022].

neel.prakash (2017). *What Is JSON API? Overview of JSON API: Text-based Data Exchange*. [online] Valuebound.com. Available at: https://www.valuebound.com/resources/blog/overview-of-json-api [Accessed 20 Apr. 2022].

Notre Dame. (2022). *Aerodynamic Performance*. [online] Available at: https://www3.nd.edu/~tcorke/w.WindTurbineCourse/Aerodynamics_Presentation.pdf [Accessed 22 Mar. 2022].

Palaia, G., Cipolla, V., Binante, V. and Rizzo, E. (2019). *Preliminary Design and Testing of a VTOL Light UAV Based on a Boxwing Configuration*. Pisa, Italy: Aircraft Engineering and Aerospace Technology, p.9.

Palik, M. and Nagy, M. (2019). Brief history of UAV development. *Repüléstudományi Közlemények*, [online] 31(1), pp.155–166. doi:10.32560/rk.2019.1.13.

Parsons, J. (2021). *Artificial intelligence means drones can dodge through forests at 25mph*. [online] Metro. Available at: https://metro.co.uk/2021/10/11/artificial-intelligence-means-drones-can-fly-through-a-forest-at-25mph-15399832/ [Accessed 28 Apr. 2022].

Phillips, W. F., & Snyder, D. O. (2000). Modern Adaptation of Prandtl's Classic Lifting-Line Theory. JOURNAL OF AIRCRAFT, Vol. 37, No. 4, 662-663.

Prabhakar, N., Prazenica, R.J. and Gudmundsson, S. (2015). Dynamic analysis of a variable-span, variable-sweep morphing UAV. *2015 IEEE Aerospace Conference*. [online] doi:10.1109/aero.2015.7119089.

Rab, M.F.U., Alam, M.J., Akhlaque, A. and Mahrukh, M. (2018). COMPARATIVE ANALYSIS OF HIGH-LIFT AIRFOILS FOR MOTORSPORTS APPLICATIONS. *Advances in Fluid Mechanics XII*. [online] doi:10.2495/afm180171.

Ragot, P., Markovic, M. and Perriard, Y. (2006). Optimization of electric motor for a solar airplane application. *IEEE Transactions on Industry Applications*, [online] 42(4), pp.1053–1061. doi:10.1109/tia.2006.876073.

Raspberry Pi (Trading) Ltd. (n.d.). *Buy a Raspberry Pi 4 Model B*. [online] Raspberry Pi. Available at: https://www.raspberrypi.com/products/raspberry-pi-4-model-b/ [Accessed 10 May 2022].

Ravi, J., Usman, M. (2018). CFD Approach of Joukowski Airfoil (T=12%), Comparison of its Aerodynamic Performance with NACA Airfoils Using k-ε Turbulence Model with 3 Million Reynolds Number [online] Available at: https://www.irjet.net/archives/V5/i10/IRJET-V5I10270.pdf [Accessed 12 May 2022].

Reid, J. (2020). A General Approach to Lifting-Line Theory, Applied to Wings with A General Approach to Lifting-Line Theory, Applied to Wings with Sweep Sweep. [online] Available at: https://digitalcommons.usu.edu/cgi/viewcontent.cgi?article=8982&context=etd. [Accessed 11 May 2022].

Rogers, J. (2018). Finite Element Analysis of 3D Printed Aircraft Wing. [online] doi:10.15760/honors.543.

Roskam, J. (1997). *Airplane design*. Lawrence, Kansas: DAR Corporation, pp.118,121,122,127.

Rozvany, G. (2007). A critical review of established methods of structural topology optimisation. *Structural and Multidisciplinary Optimization*, [online] 37, pp.217-238. Available at: <https://link.springer.com/content/pdf/10.1007/s00158-007-0217-0.pdf> [Accessed 29 April 2022].

Sandhiya. K, S. and Sankar. V, S. (2016). Ribs Strength and Topology Optimization with Low Weight. *International Journal of Engineering Research and*, [online] V5(05). Available at: <https://www.ijert.org/research/ribs-strength-and-topology-optimization-with-low-weight-IJERTV5IS050846.pdf>.

Segarra, A. (2014). *Study of numerical techniques for structural optimization in aeronautics*. [online] Barcelona: Universidad Politécnica de Cataluña. Available at: <http://alexcortiella.com/assets/downloads/BS_THESIS_MEMORY.pdf> [Accessed 5 May 2022].

Sforza, P. (2014). Aircraft Performance. *Commercial Airplane Design Principles*, [online] pp.405–452. Available at: https://www.sciencedirect.com/science/article/pii/B9780124199538000103?via%3Dihub [Accessed 25 Mar. 2022].

SimuTech Group. (2020). *Why is Ansys Meshing Important for Structural FEA and Fluid CFD Simulations?* [online] Available at: https://simutechgroup.com/why-is-meshing-important-for-fea-fluid-simulations/ [Accessed 15 May 2022].

Smith, H. (2020). *Introduction — Aircraft Flight Mechanics by Harry Smith, PhD*. [online] Aircraftflightmechanics.com. Available at: https://www.aircraftflightmechanics.com/EoMs/Introduction.html [Accessed 21 Apr. 2022].

Smyczyński, P., Starzec, Ł. and Granosik, G. (2017). Autonomous drone control system for object tracking: Flexible system design with implementation example. In: *International Conference on Methods and Models in Automation and Robotics*.

Sofla, A.Y.N., Meguid, S.A., Tan, K.T. and Yeo, W.K. (2010). Shape morphing of aircraft wing: Status and challenges. Materials & Design, [online] 31(3), pp.1284–1292. Available at: https://www.sciencedirect.com/science/article/abs/pii/S0261306909004968 [Accessed 10 May. 2022]

Somers, D. (2005). Effects of Airfoil Thickness and Maximum Lift Coefficient on Roughness Sensitivity. [online] Available at: https://www.nrel.gov/docs/fy05osti/36336.pdf. [Accessed 12 May 2022].

Soundarya, S., Sathiyavani, S. and Arun, K. (2018). Topology Optimisation of Wing Ribs. *International Journal Of Research In Aeronautical and Mechanical Engineering*, [online] 6(3), pp.7-17. Available at: <http://www.ijrame.com/wp-content/uploads/2019/03/V6i303.pdf> [Accessed 7 May 2022].

Stanford. (n.d) Simulation of Turbulent Flows From the Navier-Stokes to the RANS equations Turbulence modeling k-ε model(s) Near-wall turbulence modeling Examples and guidelines. (n.d.). [online] Available at: https://web.stanford.edu/class/me469b/handouts/turbulence.pdf. [Accessed 12 May 2022].

STEM LEARNING: Advanced Air Mobility: The Science Behind Quadcopters Reader-Student Guide. (n.d.). [online] Available at: https://www.nasa.gov/sites/default/files/atoms/files/aam-science-behind-quadcopters-reader-student-guide_0.pdf.

Sun, J., Guan, Q., Liu, Y. and Leng, J. (2016). Morphing aircraft based on smart materials and structures: A state-of-the-art review. *Journal of Intelligent Material Systems and Structures*, [online] 27(17), pp.2289–2312. doi:10.1177/1045389x16629569.

Toropov, V. and Muller, J. (2022). *DEN7026 Numerical Optimisation in Engineering Design*. Numerical Optimisation in Engineering Design. [online] London: Queen Mary University of London. Available at: <https://qmplus.qmul.ac.uk/course/view.php?id=17616> [Accessed 28 April 2022].

Transportation Electrification Community, I. (2015). *Challenges in More Electric Aircraft (MEA) - IEEE Transportation Electrification Community*. [online] Tec.ieee.org. Available at: <https://tec.ieee.org/newsletter/july-august-2015/challenges-in-more-electric-aircraft-mea> [Accessed 27 April 2022].

Tyan, M., Nguyen, N.V., Kim, S. and Lee, J.-W. (2017). Comprehensive preliminary sizing/resizing method for a fixed wing – VTOL electric UAV. *Aerospace Science and Technology*, [online] 71, pp.30–41. Available at: https://www.sciencedirect.com/science/article/pii/S1270963817300871 [Accessed 26 Mar. 2022].

Vepa, R. (2020). *Electric Aircraft Dynamics*. [online] First edition. | Boca Raton, FL : CRC Press, 2020.: CRC Press. doi:10.1201/9780429202315.

Viet, H.N., Kwon, K.-R., Kwon, S.-K., Lee, E.-J., Lee, S.-H. and Kim, C.-Y. (2017). Implementation of GPS signal simulation for drone security using Matlab/Simulink. *2017 IEEE XXIV International Conference on Electronics, Electrical Engineering and Computing (INTERCON)*. [online] doi:10.1109/intercon.2017.8079647.

Walker, D., Liu, D. and Jennings, A. (2013). Topology Optimization of An Aircraft Wing. *Air Force Institute of Technology*, [online] Available at: <https://www.i3dmfg.com/wp-content/uploads/2015/07/Walker-and-Liu-Wing-optimization.pdf> [Accessed 23 April 2022].

Wang, C., Khodaparast, H.H., Friswell, M., Shaw, A.D., Xia, Y. and Walters, P. (2016). *Development of a morphing wingtip based on compliant structures*. [online] Available at: file:///Users/marklapitan/Downloads/JIMSS_Smart2017_accepted.pdf [Accessed 1 May 2022].

Wilcox, D.C. (2010). *Turbulence modeling for CFD*. 3rd ed. La Cañada, Calif. Dcw Industries, pp.30–41.

Winslow, J., Otsuka, H., Govindarajan, B. and Chopra, I. (2018). Basic Understanding of Airfoil Characteristics at Low Reynolds Numbers (104–105). Journal of Aircraft, 55(3), pp.1050–1061. doi:10.2514/1.c034415.

Wiratama, C. (2021). Pemilihan Desain Airfoil Pesawat Terbang – Aeroengineering.co.id. [online] Aeroengineering.co.id. Available at: https://www.aeroengineering.co.id/2021/03/pemilihan-desain-airfoil-pesawat-terbang/ [Accessed 12 May 2022].

Worldbank.org. (2020). *World Bank Climate Change Knowledge Portal*. [online] Available at: https://climateknowledgeportal.worldbank.org/country/philippines/climate-data-historical [Accessed 25 Mar. 2022].

YADAV, A.K. and GAUR, P. (2014). AI-based adaptive control and design of autopilot system for nonlinear UAV. *Sadhana*, 39(4), pp.765–783. doi:10.1007/s12046-014-0275-0.

Yang, J., Wen, L., Jiang, B. and Wang, Z. (2020). Dynamic Modeling and Flight Simulation of a Folding Wing-Tip UAV. *2020 Chinese Control And Decision Conference (CCDC)*. [online] doi:10.1109/ccdc49329.2020.9164095.

Zaini, H. and Ismail, N. (2016). *A Review of Morphing Wing*. [online] ResearchGate. Available at: https://www.researchgate.net/publication/308647301_A_Review_of_Morphing_Wing [Accessed 26 Apr. 2022].

Zakuan, M.A., Aabid, A. and Khan, A. (2019). Modelling and Structural Analysis of Three-Dimensional Wing. *International Journal of Engineering and Advanced Technology*, [online] 9(1), pp.6820–6828. doi:10.35940/ijeat.a2983.109119.

Zhang, J. and Bisagni, C. (2021). Buckling-driven mechanisms for twisting control in adaptive composite wings. Aerospace Science and Technology, [online] 118, p.107006. doi:10.1016/j.ast.2021.107006.

Zhou, M., Fleury, R., Patten, S. and Stannard, N. (2011). *Topology Optimisation- Practical Aspects for Industrial Application*. Shizuoka, Japan: Altair Engineering, pp.1-9.

10. Appendix

Min 50 max 200 simulation results

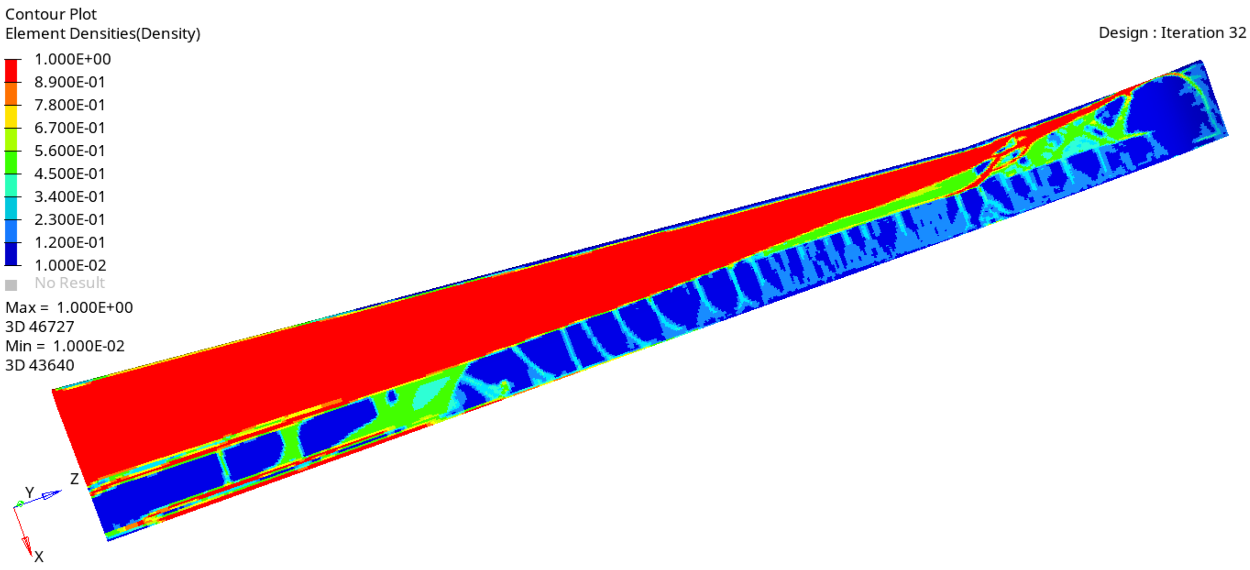

Data from XFLR5

y-span	Cl	L
0	1.051466	257.6092
0.1764	1.071695	262.5653
0.3522	1.08383	265.5384
0.5265	1.092949	267.7725
0.6988	1.09983	269.4584
0.8683	1.105189	270.7713
1.0344	1.109217	271.7582
1.1964	1.112154	272.4777
1.3537	1.114002	272.9305
1.5057	1.114788	273.1231
1.6517	1.114379	273.0229
1.7912	1.112623	272.5926
1.9236	1.109212	271.7569
2.0484	1.103748	270.4183
2.1651	1.095608	268.424
2.2733	1.084023	265.5856
2.3726	1.067928	261.6424
2.4624	1.044827	255.9826
2.5426	1.010436	247.5568
2.6127	0.961864	235.6567
2.6725	0.89464	219.1868
2.7217	0.799103	195.7802
2.7602	0.66799	163.6576
2.7878	0.491346	120.3798
2.8045	0.26457	64.81965

Co-ordinates of aerofoil to create wing rib

X	Y	Z
1	0.0013	0
0.95	0.0147	0
0.9	0.0271	0
0.8	0.0489	0
0.7	0.0669	0
0.6	0.0814	0
0.5	0.0919	0
0.4	0.098	0
0.3	0.0976	0
0.25	0.0941	0
0.2	0.088	0
0.15	0.0789	0
0.1	0.0659	0
0.075	0.0576	0
0.05	0.0473	0
0.025	0.0339	0
0.0125	0.0244	0
0	0	0
0.0125	-0.0143	0
0.025	-0.0195	0
0.05	-0.0249	0
0.075	-0.0274	0
0.1	-0.0286	0
0.15	-0.0288	0
0.2	-0.0274	0
0.25	-0.025	0
0.3	-0.0226	0
0.4	-0.018	0
0.5	-0.014	0
0.6	-0.01	0
0.7	-0.0065	0
0.8	-0.0039	0
0.9	-0.0022	0
0.95	-0.0016	0
1	-0.0013	0

Unused results for TO of wing rib

No Constraints

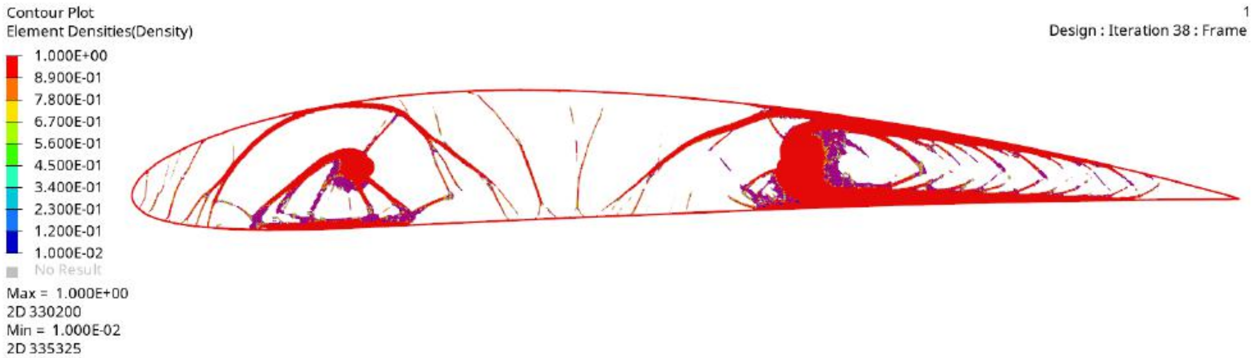

4mm

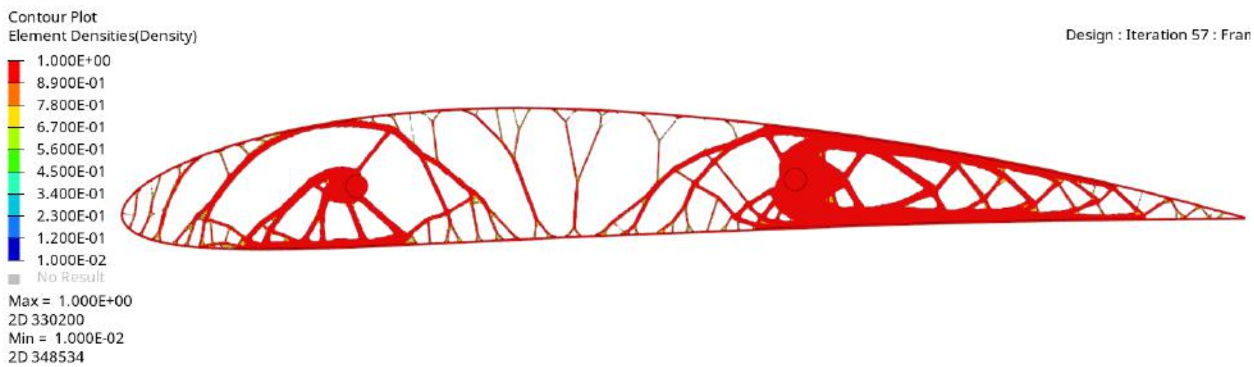

16mm

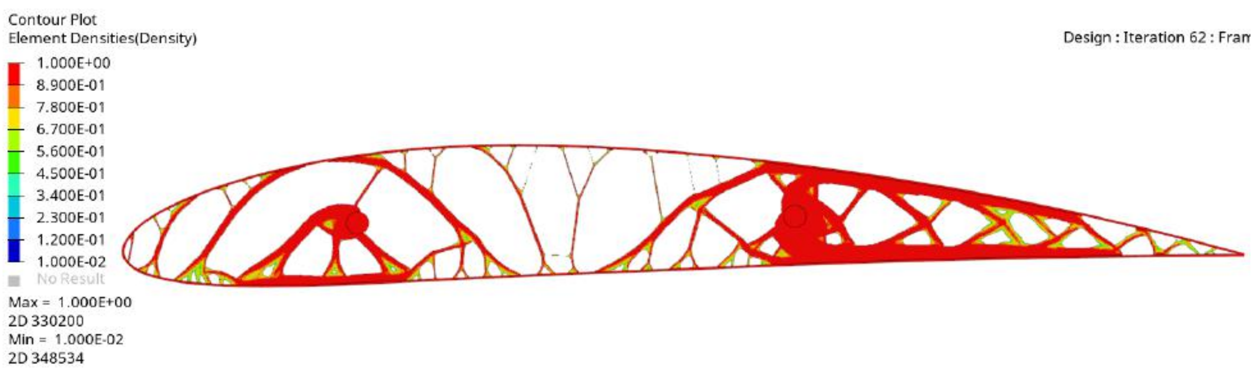

32mm

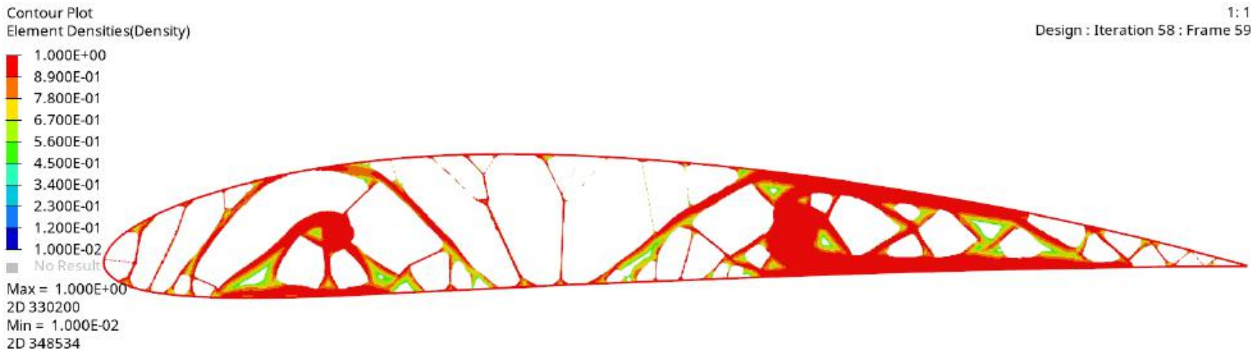

Wing rib (OSSmooth)

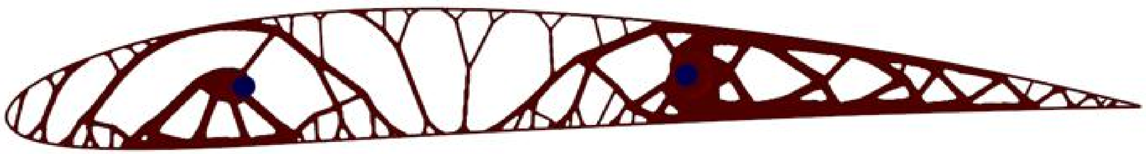

Modified XYZ Coordinates for NACA 4412 with chord length of 0.56m

X - Coordinates	Y - Coordinates	Z - Coordinates
0.56	0.000728	0
0.56	-0.000728	0
0.532	0.008232	0
0.532	-0.000896	0
0.504	0.015176	0
0.504	-0.001232	0
0.448	0.027384	0
0.448	-0.002184	0
0.392	0.037464	0
0.392	-0.00364	0
0.336	0.045584	0
0.336	-0.0056	0
0.28	0.051464	0
0.28	-0.00784	0
0.224	0.05488	0
0.224	-0.01008	0
0.168	0.054656	0
0.168	-0.012656	0
0.14	0.052696	0
0.14	-0.014	0
0.112	0.04928	0
0.112	-0.015344	0
0.084	0.044184	0
0.084	-0.016128	0
0.056	0.036904	0
0.056	-0.016016	0
0.042	0.032256	0
0.042	-0.015344	0
0.028	0.026488	0
0.028	-0.013944	0
0.014	0.018984	0
0.014	-0.01092	0
0.007	0.013664	0
0.007	-0.008008	0
0	0	0